

Enhanced Ocean Scatterometry

Proefschrift

ter verkrijging van de graad van doctor
aan de Technische Universiteit Delft,
op gezag van de Rector Magnificus prof. prof. ir. K.C.A.M. Luyben;
voorzitter van het College voor Promoties,
in het openbaar te verdedigen op
woensdag 18, november 2015 om 12:30 uur

Door

Franco FOIS

Doctor of Philosophy in Geoscience & Remote Sensing, Faculty of Civil Engineering and
Geosciences

Delft University of Technology

geboren te Sassari, Italië

This dissertation has been approved by the

promotor: Prof.ir. P. Hoogeboom

Composition of the doctoral committee:

Rector Magnificus

Prof.ir. P. Hoogeboom

Prof.dr. F. Le Chevalier

Dr. A. Stoffelen,

Instituut

Technische Universiteit Delft, promotor

Technische Universiteit Delft

Koninklijk Nederlands Meteorologisch

Independent members:

Prof.dr.ir. H.W.J. Russchenberg

Prof.dr.ir. P.N.A.M. Visser

Prof.dr.ir. N. Pierdicca

Dr. N. Floury

Technische Universiteit Delft

Technische Universiteit Delft

Sapienza University of Rome

European Space Agency

Franco FOIS received the Master of Science degree (with distinction) in Electronics Engineering from the University of Rome La Sapienza, Italy.

SUPPORT

The research leading to these results has received support from the Koninklijk Nederlands Meteorologisch Instituut (KNMI), the European Space Agency (ESA/ESTEC) and RHEA Systems s.a.

ISBN/EAN: 978-94-6259-883-6

Printed in the Netherlands by IPSKAMP Drukkers

©2015 Franco Fois

All rights reserved. No part of the material protected by this copyright notice may be reproduced or utilized in any form or by any means, electronic or mechanical, including photocopying, recording or by any information storage and retrieval system, without written permission from the author.

*To Beatrice and my little
miss sunshine Martina*

Summary	6
Samenvatting.....	9
1 Introduction to Ocean Scatterometry.....	12
1.1 Principles of Scatterometry	12
1.2 Scatterometer Missions.....	16
1.3 Main Challenges and Future Prospective	20
1.3.1 Empirical versus Physical Based Scattering Models	22
1.3.2 The Need for simultaneous Observation of Ocean Wind and Ocean Motion Vectors...	25
1.4 Aim and Overview of the Thesis.....	25
2 Electromagnetic Interaction of Microwaves with the Ocean Surface	28
2.1 Introduction.....	28
2.2 Ocean Modelling	29
2.2.1 An Overview of Ocean Surface Wave Spectra	29
2.2.2 Breaking Waves and Foam.....	31
2.2.3 Linear and Non-Linear Sea Surface Representation	32
2.3 Approximate Scattering Models	33
2.3.1 Scattering Geometry, Notations And Definitions.....	33
2.3.2 Kirchhoff Approximation	35
2.3.3 Geometrical Optics.....	36
2.3.4 Small-Perturbation Method	37
2.3.5 Two-Scale Scattering Model	37
2.3.6 Unified Models	38
2.3.7 Trade-offs between Models.....	42
2.4 Comparison with Experimental Data	44
2.4.1 Inclusion of Steep Breaking Waves.....	46
2.4.2 Wave Height Spectrum Optimization.....	49
2.5 Comparison with Measurements	50
2.5.1 Measurements Data Sets	50
2.5.2 Numerical Results.....	52
2.6 Conclusions	58
3 On the Use of Cross-Polar Scattering to Observe Very High Winds.....	61
3.1 Introduction.....	61
3.2 Properties of the Ocean Sea Surface	63
3.2.1 Properties of the rough ocean surface.....	63
3.2.2 Properties of the sea foam.....	64
3.3 Description of the Scattering Model.....	67
3.3.1 Scattering from a Rough Ocean Surface.....	67
3.3.2 Scattering from Sea Foam	69
3.3.3 Complete Scattering Model.....	71
3.4 Observing Systems and Measurement Campaigns.....	73
3.4.1 RADARSAT-2 Hurricane Campaigns.....	73
3.5 Numerical Results and Comparison with Measurements.....	74
3.5.1 Wind Speed Dependence.....	74
3.5.2 Wind Direction Dependence.....	75
3.5.3 The Importance of 2nd Order Bragg Effects.....	78
3.5.4 Full-polarimetric Signal Saturation.....	78
3.5.5 Future Improvements of the Model.....	79
3.6 Conclusions	81

4	The Sea Surface Doppler Signature.....	83
4.1	Need for Ocean Motion Data.....	83
4.2	Properties of the Sea Surface Doppler Spectra.....	86
4.2.1	Linear Sea Surface Representation.....	87
4.2.2	Non-Linear Sea Surface Representation.....	88
4.2.3	Statistical Properties of the Sea Surface.....	89
4.2.4	Spectral Undressing.....	91
4.3	The microwave full polarimetric sea surface Doppler signature.....	93
4.3.1	Second Order SSA for the Linear Sea Surface.....	93
4.3.2	Second Order SSA for the Non-Linear Sea Surface.....	94
4.3.3	Doppler Central Frequency and Doppler Spread.....	95
4.3.4	Derivation of Special Scattering Cases.....	96
4.4	Observing Systems and Measurement Campaigns.....	99
4.4.1	The SAXON-FPN Campaign.....	99
4.4.2	The ENVISAT-ASAR Data Sets.....	100
4.5	Numerical Results and Comparison with Measurements.....	101
4.5.1	Linear versus Nonlinear Sea Surface.....	101
4.5.2	Comparison with measurements and empirical GMFs.....	104
4.6	Conclusions.....	107
5	Toward the Definition of a Future Mission Concept.....	110
5.1	User Requirements and Observing System Specifications.....	112
5.1.1	Background.....	112
5.1.2	User Product Requirements.....	115
5.1.3	Observing System Specifications.....	115
5.2	Measurement System Concept.....	121
5.2.1	Orbit Selection and Geometry of Observation.....	122
5.2.2	Observation Principle.....	122
5.2.3	Instrument Concept.....	125
5.2.4	Instrument Subsystems.....	128
5.2.5	Level-1 Data Processing.....	129
5.2.6	Scientific Data Processing.....	134
5.2.7	End-to-End System Calibration and Characterization.....	135
5.3	Performance Estimation.....	137
5.3.1	End-to-End Simulator.....	137
5.3.2	Level-1 Performance.....	140
5.3.3	Level-2 Performance.....	144
5.4	Conclusions.....	147
6	Conclusions and Recommendations.....	149
6.1	Conclusions.....	149
6.2	Recommendations.....	153
	Acronyms.....	154
	Appendix.....	155
	Acknowledgments.....	181
	Curriculum Vitae.....	182
	List of Publications.....	183
	References.....	184

Summary

An ocean scatterometer is an active microwave instrument which is designed to determine the normalized radar cross section (NRCS) of the sea surface. Scatterometers transmit pulses towards the sea surface and measure the reflected energy. The primary objective of spaceborne scatterometers is to measure near-surface winds over the ocean. This is made possible by observing the ocean with different azimuth views and by using a geophysical model function (GMF) which relates wind and backscatter. Nowadays satellites measure wind fields over the oceans worldwide on a daily basis to improve weather forecasts.

Current Geophysical Model Functions are derived either from collocated backscatter and buoy-based wind measurements or by empirically fitting satellite data and NWP (Numerical Weather Prediction) model winds. These functions have been shown to be accurate to approximately ± 1.5 m/s for winds within the range 5–15 m/s. The characterization of an empirically derived relationship between normalized radar cross-section and wind vector strongly depends on the data set from which such a relationship is derived. This limits the domain of validity of the model to a specific frequency, a specific polarization of the electromagnetic wave, and a confined range of incidence angles and wind speeds. In particular, given the low probability of having scatterometer observations and collocated independent wind vector measurements during high-wind events (such as hurricanes and typhoons), current empirical models are not well defined for high winds. Furthermore, the relatively coarse spatial resolution of existing spaceborne scatterometers (50 km x 50 km) results in the averaging of high and moderate surface winds within the cell. Nowadays, wind dependent correction terms are used, operationally, by the European Centre for Medium-Range Weather Forecasts (ECMWF) to overcome the underestimation of high wind speeds resulting from the CMOD geophysical model function.

In addition, being measurement-dependent, the use of empirical functions makes it very difficult to distinguish errors associated with uncertainties of the observing system from errors associated with uncertainties of the models. In some cases, receive chain saturations of the observing systems are confused with limited sensitivity of normalized radar cross section to wind speed. In other cases, poor cross-talk performance of the instrument generates wrong polarization relationships between VV, HH and VH scattering products.

Today, there is no integrated approach valid across different frequencies, polarizations, incidence angles and wind speeds that is used operationally to model the relationship between ocean scattering and wind vector. This represents the key objective of the present thesis.

Radar backscatter models, based on a description of the underlying physical phenomenon, have the big potential of providing a more general and understandable relation between measured microwave backscatter and surface wind field than the empirical models.

The growing interest in achieving a better understanding of the physics that governs the scattering of microwave radiation from sea is triggered by extremely rich and varied data sets collected by microwave sensors on numerous space-borne satellite missions. Additional missions with advanced microwave sensors are planned for launch in the near future; they ask not only for better spatial resolution, radiometric resolution and stability but also for wider swaths and multi-polarisation observation capabilities. Higher spatial resolutions, can better describe the spatial variations in hurricanes and coastal wind fields, whereas wider swaths can sensibly reduce the time between consecutive observations of the same area on the Earth. Wider swaths imply wider ranges of incidence angles to be explored, and then new challenges arise in the modelling of the interaction of the electromagnetic and oceanic waves.

Current operating scatterometers use only co-polar scattering (VV or HH) to retrieve wind speeds and directions. The main reason behind this design choice is associated with the fact that the Signal-to-Noise Ratio (SNR) in co-polarization is expected to be higher than in cross-polarization for most winds. However, airborne measurements over hurricanes, performed at C-band and Ku-band, have confirmed that co-polar scattering suffers from problems of incidence- and azimuth angle-dependent signal saturation and dampening, which make it only weakly sensitive to wind speed variations above 25 m/s. This shortcoming impairs the ability to provide accurate hurricane warnings. Errors in wind sometimes prevent communities from correctly identifying the most vulnerable regions where emergency preparations are needed.

The addition of VH polarisation to the standard VV and HH polarisations, can significantly improve the retrieval of the wind speed in case of extreme weather events, such as hurricanes. Analysis of RADARSAT-2 quad-polarisation data with collocated in situ ocean wind measurements has recently revealed that the cross-polarised radar backscatter does not saturate at high wind speeds. As a result, the wind speed retrieved with cross-polarised backscattering is much more accurate than that retrieved with co-polarised data in hazardous storm conditions.

In this thesis, we present an analytical physical model for accurate simulation of full-polarimetric microwave sea-surface scattering and Doppler signatures. This model combines an adequate sea surface description with advanced electromagnetic theories to simulate both monostatic and bistatic scattering over a wide range of wind speeds, radar frequencies, incidence angles, different polarisations and arbitrary radar look direction with respect to the wind direction. Results will be compared with real measurements from ASAR, Sentinel-1, Radarsat-2, ASCAT and well established empirical Geophysical Model Functions showing good agreement. Being capable of simulating full-polarimetric Doppler spectra of microwave backscatter from ocean surface, this model will be used to explore ocean surface motion retrievals, thus supporting the definition of future ocean Doppler scatterometers, capable of simultaneous measurement of Ocean Vector Wind (OVW) and Ocean Vector Motion (OVM) on a global scale.

Measurements of powerful, complex and highly variable ocean surface currents are fundamental for a variety of applications, such as the monitoring of changes in coastal regions, risk management for coastal and off-shore structures, ship routing, anthropogenic and natural pollution and offshore renewable energy monitoring. Ocean surface currents are complex and, in coastal areas, highly dynamic, and therefore need to be monitored with short time sampling (possible on a daily basis) on a global scale. To this aim, Ocean Doppler scatterometry provides simultaneous and accurate measurements of wind fields and ocean motion vectors that can be used to generate global surface ocean current maps at a spatial resolution of 25 km (i.e. 12.5 km spatial sampling) on a daily basis (thanks to the very large swath illuminated). These maps will allow gaining some insights on the upper ocean dynamics at mesoscale.

Samenvatting

Een verstrooiingsmeter of scatterometer voor de oceaan is een actief instrument werkend in het microgolfgebied dat is ontworpen om de genormaliseerde radardoorsnede (NRCS) van het zeeoppervlak te meten. Een scatterometer zendt microgolfpulsen naar het zeeoppervlak en meet vervolgens de terug verstrooide energie. Het hoofddoel van een scatterometer aan boord van een satelliet is het bepalen van de windsterkte en –richting vlak boven het zeeoppervlak. Dit kan worden gedaan door de microgolf terugverstrooiing van het zeeoppervlak onder verschillende kijkrichtingen ten opzichte van de windrichting te meten en vervolgens een geofysisch model (GMF) te gebruiken dat deze metingen aan de wind relateert. Satelliet scatterometers meten tegenwoordig dagelijks windvelden over de wereldzeeën om de weersvoorspellingen te verbeteren.

De huidige geofysische modellen zijn afgeleid, of uit een in tijd en locatie bij elkaar passende set van microgolfverstrooiingsmetingen en windmetingen van boeien, of door het empirisch passend maken van satelliet gegevens en NWP (Numerieke Weer Voorspelling) modelwinden. Het is aangetoond dat deze modellen een nauwkeurigheid hebben van ongeveer ± 1.5 m/s voor windsnelheden tussen 5 en 15 m/s. Een empirisch bepaald model tussen de genormaliseerde radardoorsnede en de windvector hangt sterk af van de gegevens welke zijn gebruikt om de relatie af te leiden. Dit beperkt het geldigheidsgebied van het betreffende model tot de gebruikte microgolf frequentie en polarisatie van de elektromagnetische golf, en tot een begrensd bereik van invalshoeken en windsnelheden. In het bijzonder zijn hedendaagse empirische modellen niet goed geschikt voor het voorspellen van hoge windsnelheden, vanwege de lage waarschijnlijkheid om in tijd en locatie bij elkaar passende sets van microgolfverstrooiingsmetingen en onafhankelijke windvectormetingen te verkrijgen gedurende perioden van hoge windsnelheden (zoals bij orkanen en tyfoons). Bovendien zorgt de relatief lage ruimtelijke resolutie van hedendaagse satelliet scatterometers (50 km x 50 km) voor een middeling van hoge en gematigde oppervlaktewinden in een resolutie cel. Tegenwoordig worden in operationele toepassingen windafhankelijke correctietermen gebruikt bij het Europese Centrum voor Middellange Termijn Weersvoorspellingen (ECMWF) om de onderschatting, van de door middel van het zogenaamde CMOD geofysisch model bepaalde hoge windsnelheden, te verbeteren.

Daarnaast is het bij het gebruik van empirische functies, door de afhankelijkheid van metingen, moeilijk om fouten welke samenhangen met onnauwkeurigheden in het observatiesysteem te onderscheiden van fouten welke door modelon nauwkeurigheden worden veroorzaakt. In sommige gevallen is verzadiging in de ontvanger van het

observatiesysteem verward met een beperkte gevoeligheid van de genormaliseerde radardoorsnede voor windsnelheid. In andere gevallen zijn door een grote polarisatie overspraak in het instrument verkeerde relaties gelegd tussen de VV, HH en VH verstrooiingsproducten.

Op dit moment is er geen integraal model dat voor verschillende frequenties, polarisaties, invalshoeken en windsnelheden de relatie met de verstrooiing door het zeeoppervlak beschrijft. Radar verstrooiingsmodellen, welke gebaseerd zijn op een beschrijving van het onderliggende fysische fenomeen, hebben een hoge potentie om een meer generieke en begrijpbare relatie tussen de gemeten microgolfverstrooiing en het oppervlakte windveld te geven dan de empirische modellen. Het afleiden van zo'n model vertegenwoordigt het hoofddoel van dit proefschrift.

De groeiende interesse voor een beter inzicht in de fysica, welke de verstrooiing van microgolven aan het zeeoppervlak beschrijft, wordt gestimuleerd door de overvloedige en gevarieerde gegevensverzameling met microgolf sensoren van een groot aantal ruimte missies. Additionele missies met nog geavanceerdere microgolf sensoren zullen om in de nabije toekomst gelanceerd worden; met niet alleen betere ruimtelijke resolutie, radiometrische resolutie en stabiliteit, maar ook een bredere opnamestrook en multi-polarisatie observatie mogelijkheden. Een betere ruimtelijke resolutie kan leiden tot een betere beschrijving van de ruimtelijke variaties in orkanen en windvelden in kustgebieden, terwijl een bredere bedekking de tijd tussen twee opeenvolgende observaties van hetzelfde gebied op aarde kan verkleinen. Een bredere bedekking houdt tegelijkertijd in dat met een groter bereik van invalshoeken wordt gemeten, er ontstaan dan nieuwe uitdagingen voor de modellering van de interactie van elektromagnetische en oceaan golven.

De huidige generatie van operationele satelliet scatterometers gebruikt alleen de microgolfverstrooiing met gelijke polarisatie (VV of HH) om de windsnelheid en – richting te bepalen. De hoofdoorzaak achter deze ontwerpkeuze is gelegen in het feit dat voor de meeste windsnelheden de signaal-ruis verhouding (SNR) voor gelijke polarisatie hoger is dan voor kruispolarisatie (VH of HV). Metingen in de C- en Ku-band met behulp van scatterometers aan boord van een vliegtuig hebben echter bevestigd dat bij gelijke polarisatie, invalshoek en azimuthhoek afhankelijke verzadiging en demping van het signaal optreedt, waardoor de gevoeligheid voor windsnelheidsveranderingen boven de 25 m/s minder wordt. Deze tekortkoming verkleint de mogelijkheid om nauwkeurige stormwaarschuwingen te genereren. Fouten in windvoorspellingen verhinderen soms het identificeren van de meest bedreigde regio's.

De toevoeging van metingen met VH polarisatie, naast de standaard VV en HH polarisatie metingen, kan de bepaling van de windsnelheid in het geval van extreem weer, zoals bij orkanen, significant verbeteren. De analyse van zogenaamde quad-polarisatie data opgenomen met RADARSAT-2 tezamen met in tijd en locatie passende lokale windmetingen heeft recent laten zien dat de kruispolarisatie verstrooiingsmetingen niet verzadigen bij hoge windsnelheden. Het gevolg is dat de windsnelheid bepaald aan de hand van kruis polarisatie terug-verstrooiing nauwkeuriger is dan welke bepaald is met gelijke polarisatie metingen in het geval van gevaarlijke storm condities.

In dit proefschrift wordt een analytisch fysisch model geïntroduceerd waarmee nauwkeurig de microgolhverstrooiing van het zeeoppervlak voor alle polarisatie combinaties en bijbehorende Doppler signatuur kan worden gesimuleerd. Dit model combineert een adequate beschrijving van het zeeoppervlak met geavanceerde elektromagnetische theorieën om zowel mono-statische als bi-statische verstrooiing over een groot bereik aan windsnelheden, radarfrequenties, invalshoeken, verschillende polarisaties en willekeurige radar kijkhoeken ten opzichte van de windrichting te simuleren. De simulatie resultaten zijn vergeleken met echte metingen verkregen met ASAR, Sentinel-1, Radarsat-2, ASCAT en met geaccepteerde empirische geofysische modellen. De overeenkomst is goed. Omdat het model in staat is om de volledige polarisatie Doppler spectra van de microgolhverstrooiing van het zeeoppervlak te simuleren, wordt het model gebruikt om de bepaling van de beweging van het zeeoppervlak te onderzoeken. Hiermee is een definitiestudie uitgevoerd voor toekomstige Doppler scatterometers, welke in staat zijn om gelijktijdig de windvector boven en de beweging van het zeeoppervlak op een wereldwijde schaal te meten.

Metingen van sterke, complexe en zeer variabele stromingen aan het zeeoppervlak zijn fundamenteel voor een variëteit aan toepassingen, zoals het monitoren van de veranderingen in kustgebieden, risico management voor kust en offshore constructies, scheepsroutes, antropogene en natuurlijke vervuiling en het monitoren van installaties voor offshore duurzame energie. De oppervlakte stromingen van de zee zijn complex en in kustgebieden zeer dynamisch. Ze moeten daarom wereldwijd frequent (indien mogelijk dagelijks) gemonitord worden. De Doppler scatterometer techniek levert simultane en nauwkeurige metingen van windvelden en stroomrichtingen van het zeeoppervlak die kunnen worden gebruikt om dagelijks (dankzij de zeer brede opnamestrook) wereldwijd stromingskaarten van het zeeoppervlak te maken met een ruimtelijke resolutie van 25 km (dit betekent 12.5 ruimtelijke sampling). Deze kaarten zullen de inzichten in de dynamiek van het zeeoppervlak op mesoschaal kunnen helpen vergroten.

1 Introduction to Ocean Scatterometry

Winds drive the ocean circulation. By changing the small scale geometry of the sea surface, winds influence the exchanges of gases, heat, moisture, energy and momentum between atmosphere and ocean. Nowadays, the Numerical Weather Prediction (NWP) provides global wind fields every six hours. The accuracy of the prediction is limited by the knowledge of the physical processes and the availability of data. Space-borne microwave scatterometers represent a unique tool to measure wind fields (i.e. both wind speed and direction) under clear and cloudy conditions, day and night. The inclusion of these ocean wind fields led to significant improvements in accuracy of the numerical weather forecasts.

This introductory chapter provides the principles of ocean scatterometry and explains the physical mechanisms ruling the microwave scattering from ocean. In section 2, an overview of past, current and future scatterometer missions is provided. Section 3 addresses the capabilities of existing space-based systems and highlights the main challenges for future missions. Section 4 deals with the importance of physical based scattering models as opposed to empirical geophysical model functions. Section 5 focuses on the need for simultaneous observation of ocean wind and ocean motion vectors. An overview of the thesis concludes this chapter.

1.1 Principles of Scatterometry

The scatterometer sends microwave pulses to the Earth's surface and measures the power backscattered from the surface roughness. Over the ocean, the scattering process at moderate incidence angles is a resonant or nearly Bragg mechanism, in which the scattering elements on the surface have just about the same wavelength as the microwave radiation. The small scale roughness elements on the sea surface are also called gravity capillary waves. The fundamental assumption, which is empirically known in scatterometry, is that the small scale scattering elements on the sea surface are in local equilibrium with the wind, almost instantaneously. This means that the amplitudes and the directional distributions of these small scale centimetric waves on the sea surface are a sensitive function of the local wind speed and the local wind direction.

The capability of measuring both wind speed and direction is the major, unique characteristic of the scatterometer. This measurement capability is affected by three main sources of uncertainty (see Fig.1.1):

- the influence of wind and waves on small scale sea surface roughness,
- the relation between small scale sea surface roughness and backscatter power,
- the effect of precipitation.

The fundamental scatterometer wind retrieval is based on an empirical model function:

$$\sigma^0 = f(U, \phi, \theta_{inc}, p, \lambda), \quad (1.1)$$

The model function is the relationship between the Normalized Radar Cross Section (NRCS), also called backscattering coefficient (σ^0), the wind speed (U), the relative wind direction (ϕ), the incidence angle (θ_{inc}), the polarization of the radiation (p) and its wavelength (λ). The NRCS refers to how much radar power is reflected back to the scatterometer. The function (1.1) is empirical because of the fact that we lack complete understanding the physics behind the above mentioned sources of uncertainty.

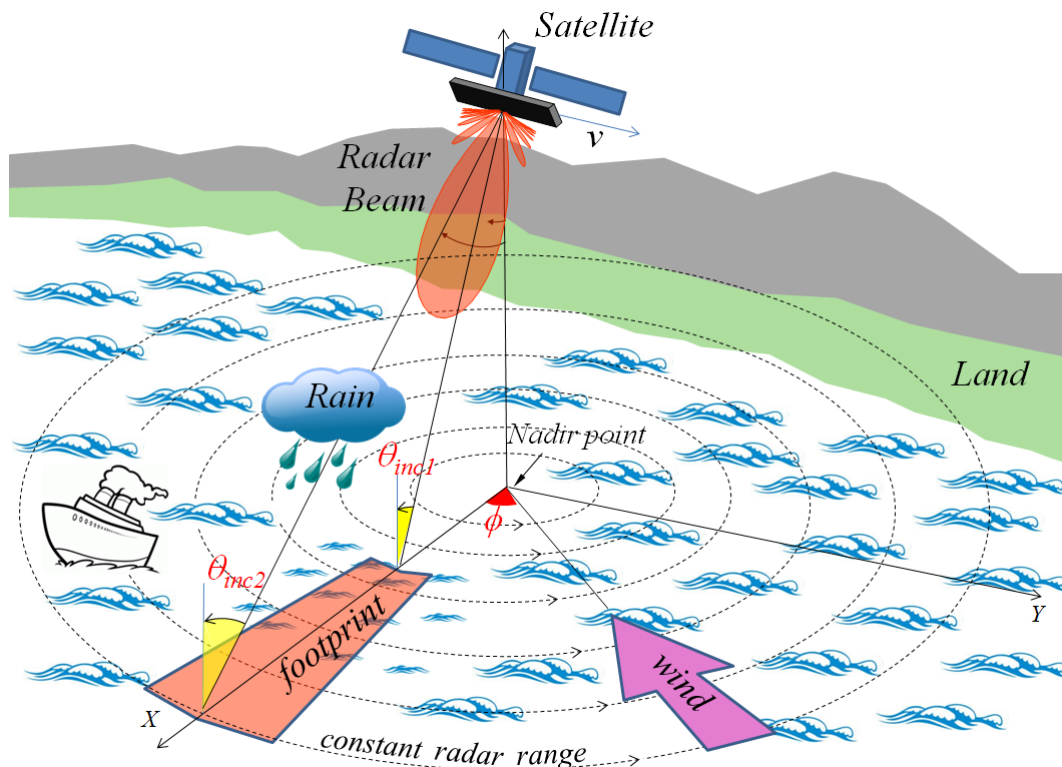


Fig. 1.1 Geometry of observation of a wind scatterometer.

The model is, in fact, generated from backscatter measurements collected from airborne or spaceborne platforms over areas of the ocean where wind fields are available from in situ buoys or other independent sources. One can use observations collected in different environmental conditions to derive an empirical relationship between the NRCS and the wind vector. The empirical models typically express the backscatter cross section as a Fourier series, where the NRCS is a function of viewing geometry (θ_{inc}, ϕ) and wind speed, independent of wind direction:

$$\sigma^0 = A_0(U; \theta_{inc}, p, \lambda) + A_1(U; \theta_{inc}, p, \lambda) \cos(\phi) + A_2(U; \theta_{inc}, p, \lambda) \cos(2\phi), \quad (1.2)$$

In (1.2), ϕ is the relative angle (azimuth), in the horizontal plane, formed by the look angle of the radar and the relative wind direction, whereas θ_{inc} is the angle formed by the local vertical and the radar look direction. The parameters A_0 , A_1 and A_2 are generally functions of incidence angle, radar frequency and polarization. σ^0 is a symmetric function of the wind direction and, for fixed ϕ , is an increasing function of the wind speed.

The parameter A_0 is the direction averaged mean value of the normalized radar cross section. The quantity $A_0 + A_2 \cos(2\phi)$ represents the largest modulation of NRCS as a function of the wind direction: the cosine function makes the backscatter cross section largest when looking upwind ($\phi=0^\circ$) and downwind ($\phi=180^\circ$), smallest when looking crosswind ($\phi=90^\circ$). The term $A_1 \cos(\phi)$ represents a relatively small modulation with the relative azimuth angle, that is maximum in upwind and minimum in downwind. As shown in Fig. 1.2a, adding up the three contributions on the right side of equation (1.2) yields a function that is highest upwind and almost as high downwind (upwind/downwind differences can be in the order of 1 dB). In Fig. 1.2b, we plot the NRCS in dB from the C-band empirical geophysical model function CMOD5n [Verhoef *et al.*, 2008], as a function of the relative wind direction for an incidence angle of 40° , four wind speeds (5, 10, 15, 20 m/s) and VV-polarization.

The relationship between wind speed and the normalized radar cross section varies as a function of the incidence angle. At higher incidence angles (i.e. when we look more grazing toward the surface) backscatter cross sections are, in general, smaller but they have a higher sensitivity to wind speed than they do at lower incidence angles (i.e. when we look almost straight down from the satellite), where cross sections are larger but weakly sensitive to wind speed. Figures 1.3a-b show the NRCS at C-band, provided by CMOD5n [Verhoef *et al.*, 2008], and at Ku-band, by SaSS-II [Wentz, 1984] empirical model functions.

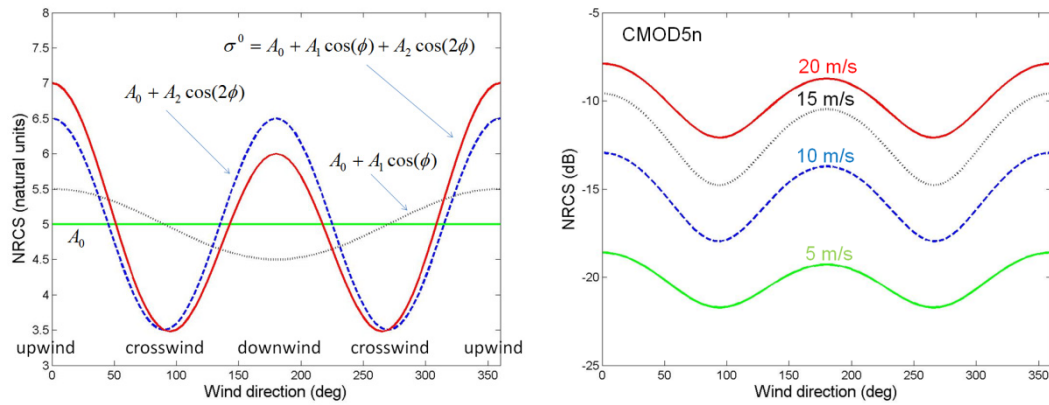


Fig. 1.2 a) The three main contributions of equation (1.2); b) CMOD5n NRCS as a function of the relative wind direction for an incidence angle of 40° . Four wind speeds are plotted: 5, 10, 15 and 20 m/s.

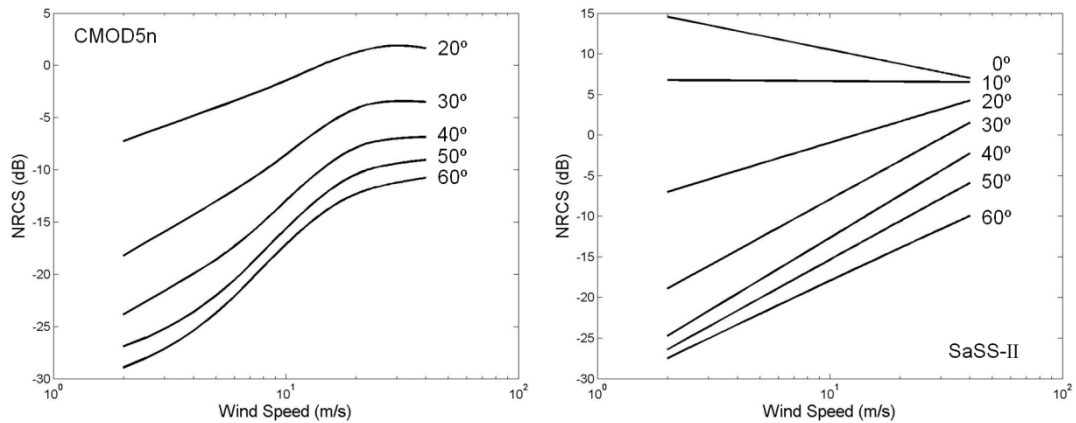


Fig. 1.3 a) CMOD5n C-band NRCS versus the wind speed for 20° , 30° , 40° , 50° and 60° incidence angles; b) SaSS-II Ku-band NRCS versus the wind speed for 0° , 10° , 20° , 30° , 40° , 50° and 60° incidence angles.

The backscatter cross section, on the vertical axis, is plotted versus the wind speed, on the horizontal axis. At Ku-band (14 GHz), the relationship between NRCS and wind speed at moderate incidence angles (30° - 40°) is about a wind speed squared relationship. At C-band and for the same angles the relationship is about linear within the wind speed range 7 - 20 m/s. The objective of ocean scatterometry is to retrieve wind speed and wind direction (vector variable) from backscatter cross section measurements (scalar variable). In order to measure vector quantities from scalar quantities, we need to acquire multiple measurements of σ^0 of nearly the same place on the ocean's surface at nearly the same time with different viewing geometries. The use of this data together with the model function allows calculating wind speed and direction.

1.2 Scatterometer Missions

Table 1.1 lists the operating characteristics of the main, past and present, spaceborne wind scatterometers. The two approaches commonly used to collect multiple measurements of σ^0 are: the fan beam geometry and the pencil beam rotating antenna. The fan beam geometry was used for the European AMI scatterometer, for the MetOp Advanced SCATterometer, ASCAT, and also for the NASA scatterometers SASS and NSCAT. Figure 1.4 (a, b, d, e) show how the measurements of a fan beam scatterometer are made. Different antennas send out long, narrow radar beams on the sea surface. Range-Doppler processing allows gaining resolution in the long-beam directions. Each of the fan beams acquires a continuous image of the ocean's NRCS. In SASS, NSCAT and ASCAT both sides of the sub-satellite track are imaged, each with two (SASS) or three (NSCAT and ASCAT) azimuth views. For each azimuth view, independent looks are summed in both across and along-track direction, in order to meet the specified radiometric resolution requirements.

Table 1.1 Spaceborne scatterometers

	SASS	AMI	NSCAT	Seawinds	ASCAT-A	ASCAT-B	Oceansat-2 SCAT	HY-2A
Time Period	July – Sept. 1978	1992 - 2007	Sept. 1996 - June 1997	July 1999 – Nov. 2009	October 2006- present	Sept. 2012- present	Sept. 2009- present	August 2011 - present
Frequency	14.6 GHz	5.3 GHz	14.0 GHz	13.4 GHz	5.225 GHz	5.225 GHz	13.5 GHz	13.25 GHz
Antennas	Four fixed	Three fixed	Six fixed	1 m diameter rotating dish	Six fixed	Six fixed	1 m diameter rotating dish	Rotating dish
Polarizations	V-H, V-H	V Only	V, V-H, V	V-outer beam /H- inner beam	V Only	V Only	V-outer beam /H- inner beam	V-outer beam /H- inner beam
Resolution	50/100 km	25/50 km	25/50 km	25 x 6 km ²	25/50 km	25/50 km	12.5 x 12.5 km ²	25 x 25 km ²
Swath width	750 km	500 km	600 km	1400 km/1800 km	2 x 550 km	2 x 550 km	1400 km (inner) /1840 km (outer)	1350 km (inner) /1750 km (outer)
Incidence Angles	0 - 70°	18 - 59°	17 - 60°	46 (inner) , 54° (outer)	25 - 54°	25 - 54°	48.90° (inner), 57.60° (outer)	41° (inner), 48° (outer)
Orbit (SSO)	810 km alt. 106° incl.	780 km alt. 98.52° incl.	805 km alt. 98.7° incl.	803 km alt. 98.6° incl.	817 km alt. 98.7° incl.	817 km alt. 98.7° incl.	728 km alt. 98.27° incl.	973 km alt. 99.3° incl.
Coverage	Variable	< 41% in 24h	78% in 24h	92% in 24h	97% in 48h	97% in 48h	92% in 24h	92% in 24h

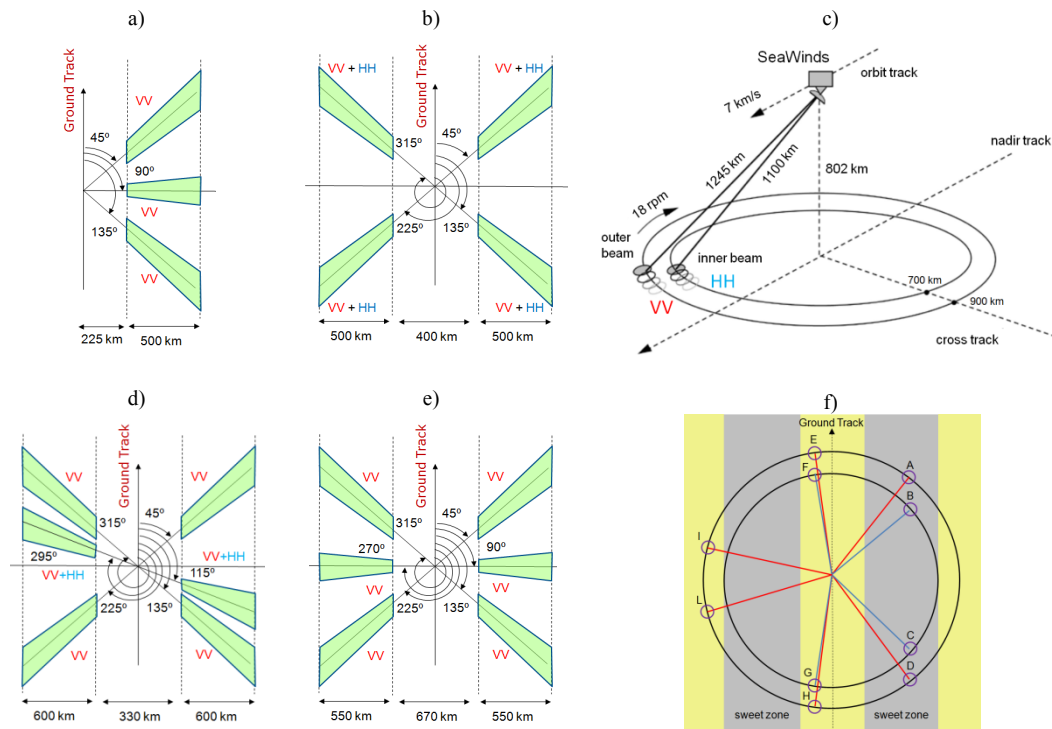


Fig. 1.4 Sketch of the microwave illumination patterns of: a) AMI (ERS-1/2); b) SASS (SeaSat-A); c) and f) SeaWinds, Oceansat-2 SCAT and HY-2A; d) NSCAT; e) MetOp ASCAT-A and B. The case a), b), d) and e) correspond to a fan beam geometry whereas c) and f) correspond to a pencil beam geometry.

The first space-borne scatterometer was the NASA SeaSat-A Scatterometer System, SASS, launched in 1978 and operative for only three months. SASS had four antennas (two on both sides of the satellite) pointing at 45° , 135° , 225° and 315° with respect to the ground-track, as depicted in Fig.1.4b. A point in the swath was first observed by the fore beam, and a few minutes later by the aft beam. Basically, each point in the swath was observed twice with 90° difference in the azimuth view angle. A single measurement of backscatter cross section plugged into the model function provides a locus of all possible wind speeds (vertical axis in Fig.1.5a) and relative wind directions (horizontal axis in Fig.1.5a) which could correspond to that single measurement of backscatter cross section. This locus of possible wind speeds and direction is depicted in dashed blue line in Fig.1.5a. By taking another measurement of σ° from the same incidence angle and a different azimuth viewing geometry, that is 90° away, we can trace out the locus of all possible wind speeds and directions which correspond to the new measurement. This locus of points is plotted with a dash-dot red line in Fig.1.5a. In a noise-free case (perfect knowledge of the model function and perfect σ° measurement) the only possible wind speeds and wind directions would be where the dash blue curve and the dash-dot red curve intersect. The intersection points are called A, B, C and D in Fig. 1.5a.

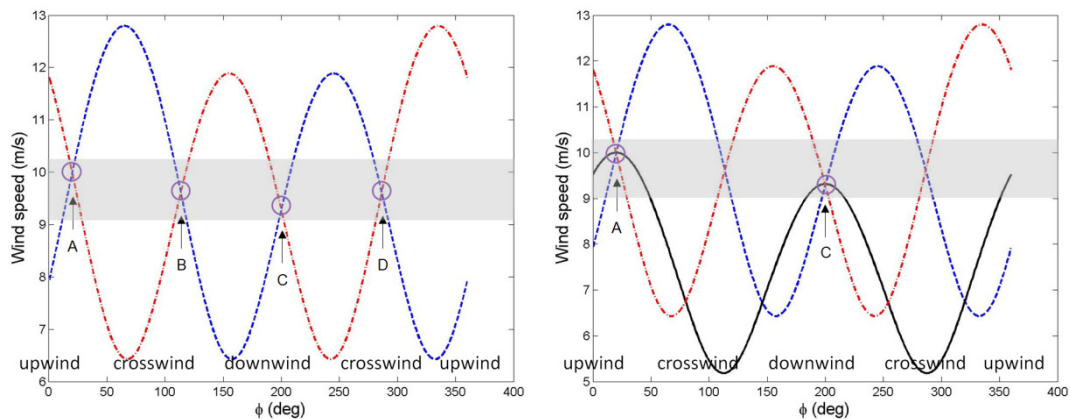


Fig. 1.5 a) Wind speed as a function of wind direction for a fore and aft beam measurement of backscatter. The arrows indicate the four possible solutions; b) locus of possible wind speeds and wind directions for fore (dash-blue line), aft (dash-dot red line) and mid (solid black line) beam measurement

Taking measurements 90° apart in relative azimuth angle, the four solutions of the two coupled equations have about the same wind speeds (spanning within the grey area in Fig. 1.5a) but different wind directions. In ocean scatterometry, this phenomenon is called directional ambiguity. The directional ambiguity was a big problem limiting the accuracy of the SASS wind data and major efforts were needed to obtain acceptable wind products [Peteherych *et al.*, 1984; Stoffelen & Cats, 1991].

The European Remote Sensing (ERS) scatterometers were launched by ESA in 1991 and 1995. As shown in Fig.1.4a, the ERS scatterometers cover a swath of 500 km. Only one side of the satellite ground track is illuminated. Measurements are made only in vertical polarization at three azimuth angles, 45° , 90° , and 135° . The ERS scatterometers provided wind products over only 41% of the global ocean on a daily basis. For the fore beam the incidence angle ranges between 22° and 59° , whereas for the aft beam it goes from 18° to 51° . Measurements of the backscattering coefficients are collected with 50 km spatial resolution and a spatial sampling of 25 km. Thanks to the three measurements of backscatter cross section with 45° , 90° and 135° azimuth angles, in the noise-free case, there is only one wind speed and one wind direction, corresponding to point A in Fig.1.5b, where all of the lines perfectly intersect. Point C in the same figure, represents a near solution (i.e. the curves do not intersect exactly at the same point), which is 180° away. The near solution is generated by the small difference in backscattering between upwind and downwind cases. In particular, for high upwind/downwind ratios false ambiguities, 180° away, are easier to identify.

In a follow-on design of SASS made by NASA, called NSCAT, a beam was added between the fore and aft beams as shown in Fig. 1.4d. The mid beams had both VV and HH measurement capability. The side antennas only used VV polarization. It is worth

noting that in HH polarization, the relationship between backscatter cross section and wind speed is different from VV. In this respect, HH polarization measurements can provide complementary information to retrieve wind fields (especially wind directions) from scatterometer data. The two additional mid antennas help resolving the directional ambiguity issue of SASS by providing a unique solution for the wind vector. However, an azimuth view angle of the mid beam in between the azimuth view angles of the fore and aft beams (as for ERS scatterometers) would have better sampled the harmonic wind direction dependency. This was not done for technical reasons. NSCAT was launched in 1996, aboard the Advanced Earth Observing Satellite (ADEOS), a mission of the National Space Development Agency of Japan. After only nine months with useful NSCAT data, the National Space Development Agency of Japan lost control of the satellite.

The European MetOp Advanced Scatterometers, ASCAT-A and B, represent an evolution of the ERS scatterometers. ASCAT-A and B were launched in 2006 and 2012 and they are currently working. As shown in Fig.1.4e, two sets of three antennas measure the ocean NRCS over two swaths of 550 km. On each side of the satellite ground track, the three antennas are oriented to 45°, 90° and 135°. In this way 97% of the global ocean is covered within 48 hours.

In fan beam geometry the azimuth angle for each beam is fixed (i.e. it does not change along the swaths), whereas the incidence angle varies along the swath, thus we have to know the model function at all incidence angles to retrieve wind vectors from σ^0 measurements. The problem of fan beam scatterometers is the nadir gap between right and left swaths: practically, we cannot measure wind speed and wind direction right under the satellite, because backscatter cross section is nearly insensitive to wind speed and direction at small incidence angles. For NSCAT the nadir gap was 330 km whereas for ASCAT-A and B is about 670 km. The size of the nadir gap also depends on the limited accuracy of the instrument measurements at low incidence angles (i.e. limited radiometric resolution performance). This point will be further discuss in chapter 5.

The NASA QuikSCAT (Quick Scatterometer) was a "quick recovery" mission replacing the NASA Scatterometer (NSCAT), after its premature failure. QuikSCAT was an Earth observation satellite carrying the SeaWinds scatterometer. It used a rotating 1m-dish antenna sending two pencil beams at about 40° and 46° incidence to generate multiple σ^0 measurements. The geometry of observation is shown in Fig. 1.4c. As the antenna spins around and the spacecraft flies along its orbit, the scatterometer images nearly the same place on the ocean's surface at nearly the same time with different azimuth views. A point on the sea surface will be first seen, at a particular azimuth angle,

by the outer forward pencil beam (point A in Fig.1.4f). As the spacecraft moves in its orbit, the same point will be then imaged by the inner pencil beam at a slightly different incidence angle and a different azimuth angle (point B in Fig.1.4f). When the satellite propagates even further, the same point will be imaged by the inner beam looking aft and then imaged by the outer beam looking aft (points C and D in Fig.1.4f). The rotating or conical scanning strategy avoids nadir gaps because the antenna never measures straight down but always measures at a constant incidence angle. The problem of a scanning pencil beam is that along the swaths the azimuth angle changes, and some angles are not ideal for calculating wind speed and direction. To explain the concept we can refer to Fig. 1.4f. The grey area in the figure is called “sweet zone” as it provides nearly optimum viewing geometry: in fact, four measurements spanning a nearly optimum range of azimuth angles are collected (e.g. points A, B, C and D). Near nadir track of the satellite, four measurements are still available (e.g. points E, F, G and H) but the azimuth angles are too similar (nearly 180° apart) to provide unambiguous data. Far swath areas, outside the range of the inner beam, only get two measurements instead of four (e.g. points I and L in Fig.1.4f). This azimuthal diversity over the swath leads to variations in the accuracy of wind speed and direction estimates as a function of across-track distance.

SASS, NSCAT, QuikSCAT, and SeaWinds work with a carrier frequency of 14.6 GHz (i.e. Ku-band) which is seriously affected by atmospheric attenuation. In addition, rain droplets distort the gravity-capillary waves, which are the main contributors to the microwave scattering. Therefore, deriving a relationship between wind vector and backscatter becomes far more difficult. Latter effects become substantially smaller for lower carrier frequencies. To avoid such effects, the ERS and ASCAT scatterometers use a carrier frequency of 5.3 GHz (i.e. C-band).

1.3 Main Challenges and Future Prospective

The measurements of oceanic quantities and air-sea interaction processes play a key role in weather and ocean state forecasting, as well as in oceanography and climate research. Satellite scatterometers are, and will continue to be, an important component of the ocean observing systems. Since 1978, when SeaSat-A was launched, scatterometers have demonstrated the ability to obtain meaningful, accurate measurements of key ocean forcing and response quantities on space and time scales that were inaccessible using only data from in-situ observing systems. Although, in the last 37 years significant progress has been made in the observation of the ocean, some important challenges remain. These

challenges include the need for better temporal sampling and spatial resolution than is possible with individual satellite missions and present instruments.

The wide range of oceanic time and space scales, and their intrinsic coupling, represents the most challenging problem in justifying, designing, and implementing a new ocean observing system [Freilich, 2002]. Large scale, long-period phenomena spanning over thousands of kilometres and occurring annually or inter-annually, are very often strictly coupled with small-scale, short-period variations in atmospheric forces and oceanic processes. High resolution and frequent temporal sampling is particularly required over coastal areas, where several factors, such as the presence of the coast as a boundary to flow, the shallowness of the water, river runoff and the effects of continental air masses flowing out over the sea [Pickard & Emery, 1989], challenge the performance of future ocean observing systems.

Future ocean scatterometers shall measure small scale processes globally and over multi-decadal periods to provide both adequate frequency resolution and adequate statistics for analysis of ocean and climate processes. The observation of these processes poses implicit constraints on the accuracy of such measurements.

In practice, to be scientifically valid a future missions shall ask not only for better spatial resolution, radiometric resolution and stability but also for wider swaths, long life-time and multi-polarisation observation capabilities. The high spatial resolution, can better describe the spatial variations in hurricanes and coastal wind fields; whereas, wider swaths can sensibly reduce the time between consecutive observations of the same area on the ocean. Requiring wide swaths implies exploring wide ranges of incidence angles and then facing new challenges in the modelling of the interaction of the electromagnetic and oceanic waves. The use of HH (horizontal transmit horizontal receive) and VH (horizontal transmit vertical receive or vertical transmit horizontal receive) polarizations in addition to the standard VV (vertical transmit vertical receive) polarization, can improve the retrieval of the wind vectors. As a matter of fact, the sensitivity of HH and VH to wind speed and wind direction is different from the sensitivity of VV. The VV polarization is dominated by the Bragg resonance scattering mechanism, whereas HH and VH contain nontrivial non-Bragg contributions mainly produced by steep breaking waves and foam. A main limitation of the current scatterometers is their inability to retrieve very high wind speeds. Current scatterometers only use co-polar signals (i.e. VV-polarization or HH-polarization) to derive wind speeds and directions: such signals suffer from problems of incidence and azimuth angle-dependent signal saturations and dampening, which make them weakly sensitive above 25 m/s. On the contrary, the cross-polarized signals showed no evident loss of sensitivity as the wind-speed increased from 20 m/s up

to 45 m/s. On the basis of these considerations, there are good reasons to think that the cross-polarized data can be a valuable tool for the retrieval of strong-to-severe wind speeds for future scatterometers. Improved modelling of the cross-polar microwave sea-surface scattering thus becomes imperative for accurate retrieval of wind speeds in case of extreme weather events, such as hurricanes and typhoons.

Analytical models of ocean scattering in VH-polarization are very complex as they have to include non-Bragg effects and volume scattering effects in case of very high-winds. One of the purpose of this thesis is to develop accurate analytical scattering models with emphasis on high wind speed behaviour.

The accuracy of the wind field estimates can also be improved by performing simultaneous measurements of the ocean backscattering at different frequencies, such as 14 GHz (Ku-band) and 5.3 GHz (C-band). Observations at Ku and C-band are, in fact, complementary: Ku-band is more sensitive to small scale roughness changes by wind than C-band, whereas scattering at C-band is less sensitive to rain than at Ku-band.

1.3.1 Empirical versus Physical Based Scattering Models

As anticipated in the previous section, ocean scatterometry makes the assumption that the ocean normalized radar cross section is correlated with the local wind vector. Practically, the wind vector retrieval is based on existing data sets of collocated in-situ wind measurements and scatterometric NRCS measurements. Assuming a strong correlation between the surface wind vector and the measured NRCS works well for moderate and uniform winds, as demonstrated by the success of various empirical geophysical model functions such as SASS, CMOD and NSCAT [Jones *et al.*, 1982; Wentz *et al.*, 1984; Bentamy *et al.*, 1999; Wentz, 1999; Stoffelen & Portabella, 2006].

However, the ocean backscattering depends also on the wind and wave history as well as on the wind and atmospheric variability, size of the fetch, wave age and other parameters (such as long wave spectrum, viscosity, sea water temperature, surface tension) [Voronovich & Zavorotny, 2001]. Recently RADARSAT-2 measurements showed that these models fail at high wind speeds, especially in hurricane conditions where current GMFs significantly underestimate the true surface wind field. In addition empirical models have always a limited validity in terms of incidence angles, polarizations and frequencies. Therefore, relying entirely on empirical model functions in the design of future scatterometric missions is not advisable and should, in principle, be avoided.

As opposed to empirical model functions, radar backscatter models, based on a description of the underlying physical phenomenon, have the capability of providing an understandable relation between measured microwave backscatter and surface wind field. Examples of advanced backscattering models for ocean surface are the model by Holliday *et al.* [1987], which is based on the so-called Kirchhoff approximation of the Stratton-Chu integral [Stratton *et al.*, 1941], and the model by Apel [1994], which applies the quasi-specular and Bragg scattering approximation. These investigations show that the microwave ocean backscattering can be described as product of a Kirchhoff integral by a coefficient which depends on the dielectric constant of the medium and on the incidence angle. Other attempts to describe microwave backscattering from the ocean have used the Bragg scattering mechanism in combination with quasi-specular scattering at low incidence angles. However, most of the “physical” imaging models have not been optimized for the reproduction of absolute NRCS values and their dependence on various parameters, like the radar frequency and the wind speed. In addition, very often, other fundamental aspects, like the dependence of the normalized radar cross section on the polarization or the fact that the observed ocean is not a perfectly conductive surface, are neglected. Further improved models are rather complex (like the one by Chen *et al.* [1992]), or they require very detailed sets of input parameters (like the composite surface model by Donelan and Pierson [1987]). Such models are not ideally suited for general applications. The same apply to the approach by Snoeij *et al.* [1992], who have tried to explain details of wind scatterometer measurements by dedicated wave model calculations. Aside from the fact that it is difficult to use their model for general applications, Donelan and Pierson [1987] have demonstrated that it is feasible to develop a calibrated “physical” model for NRCS calculations within the frame of the composite surface theory. Using detailed expressions for the long wave (gravity wave) region of the ocean wave spectrum, Donelan and Pierson were able to find a good match between their model and scatterometer measurements at Ku-band. For general applications it is desirable to have a model which is applicable to a wide range of environmental conditions, radar wavelengths, different polarizations and geometries of observation. The formulation of the model should be “physical” and the mathematical formulation for the input ocean wave spectrum should be continuous and differentiable, in order to avoid numerical problems. In addition, the use of tuning parameters should be avoided.

The composite surface model presented by Romeiser and Alpers [1997] was one of the first attempts to meet all these specifications. This model is based on Bragg scattering theory in combination with a two dimensional Taylor expansion of the NRCS, that

represents a first approximation for the hydrodynamic modulation of the Bragg waves by longer waves.

If we couple the recent advances in modelling microwave backscatter from ocean with the speed of modern computers, we can also follow an alternative approach to solve the scattering problem. Individual realizations of the ocean surface can be generated from one of the available surface wave height spectra [e.g., Donelan and Pierson, 1987; Elfouhaly *et al.*, 1997]. The Kirchhoff integral can then be computed to locally derive the backscatter from individual facets of the ocean surface. Mean backscattering cross sections can finally be obtained by ensemble averages over the facets of the stochastically rough, long wave surface [Plant, 2002].

The mechanisms responsible for microwave ocean scattering at low incidence angles ($<20^\circ$) are different from those at mid incidence angles. Bragg scattering is the major contributor at mid incidence angles. At low incidence, close to nadir, the scattering is dominated by the geometric optics and physical optics mechanisms. In this region, a quasi-specular scattering model is often used to describe the radar cross-section [Hesany *et al.*, 2000]. At near vertical incidence, the strongest backscattering would occur with a perfectly flat surface or a gently undulating one. As the surface gets rougher, more of the vertically incident energy is scattered away from the radar look direction. Hence, the radar backscatter decreases with increasing wind speed and wave height near vertical, whereas it increases with increasing wind speed at angles beyond about 12° . Near grazing incidence, the backscattering mechanism is dominated by non-Bragg scattering events, with backscattering cross-section of horizontal polarization exceeding that of vertical polarization of about 20-40 dB [Plant, 1997; Hwang *et al.*, 2008]. This level of difference is much larger than that we expect from tilting modulation of Bragg roughness, and it can be better associated with steep wave features possibly going through wave-breaking process, with or without the generation of whitecap. Portions of the wave, near grazing, may be shadowed by waves between the radar and the wave being observed. Furthermore, both constructive and destructive interference may take place between the direct electromagnetic wave, striking the ocean, and the electromagnetic wave reflected off the surface. Shadowing and interference effects tend to cause a more rapid decrease in scattering coefficient with angle of incidence than what predicted by the theory of Bragg scattering.

1.3.2 The Need for simultaneous Observation of Ocean Wind and Ocean Motion Vectors

In the last few years, the potential of scatterometer instruments for simultaneous Ocean Vector Wind (OVW) and sea surface current retrievals has gained considerable interest [Stoffelen *et al.*, 2011; Fabry *et al.*, 2013]. Existing scatterometer data are being used with new signal processing techniques to explore ocean surface motion retrievals. Based on this, an optimized scatterometer concept might be developed, maintaining OVW capability, but extended with Doppler shift estimation capability with sufficient accuracy for surface current estimation. Sea surface current signature is one component of ocean surface motion. Several recent studies [Chapron *et al.*, 2005; Johannessen *et al.*, 2008; Collard *et al.*, 2008] have explored SAR Doppler velocity measurements in relation to sea state. Wind-generated and breaking roughness elements ride on larger and fast moving waves, which thus contribute strongly to the measured Doppler shift. The simultaneous measurement of OVW and OVM (Ocean Vector Motion) on a global scale may allow for the determination of open ocean currents and improved understanding of ocean waves, wave-current interaction and air-sea interaction. In this context, an analytical model which is capable of estimating both scattering and Doppler spectra of microwave backscatter from ocean surface would be of paramount importance in studying and designing future spaceborne Doppler scatterometric missions.

1.4 Aim and Overview of the Thesis

The aim of this thesis is to derive a unified theory for the description of both microwave scattering and Doppler signature of the ocean, for use in meteorological applications and for supporting the definition and design of new ocean observing systems. It is clear that an understanding of the relationship between the scattered field and sea surface shape is necessary for the proper interpretation of data collected by existing scatterometers and for the design of future families of ocean scatterometers. Although this thesis focuses mainly on scatterometry applications, the basic physics is applicable to other microwave sensors both active and passive. The thesis comprises this introductory first chapter and 4 subsequent chapters.

Chapter 2 presents a survey of some of the most common analytical approximate models that are used to describe the microwave sea surface scattering. However, in order to extract geophysical information from the data collected by microwave sensors, one must understand not only the scattering physics, but also the sea surface behaviour. An adequate representation of the sea surface is, in fact, necessary in order to properly apply

the electromagnetic boundary conditions. A convenient way to describe the sea surface is through the wave height spectral density. In chapter 2, the properties of the wave height spectrum are discussed and three spectral models are examined. Strengths and weaknesses of the various spectral models and scattering theories are reviewed. Theoretical calculations for co-polar and cross-polar signals at C-band and Ku-band are compared with empirical Geophysical Model Functions (GMF) and real data (from Envisat/ASAR and Sentinel-1), to verify the adequacy of both scattering models and sea surface descriptions at different frequencies, observation angles and wind conditions.

Chapter 3 investigates the potential of cross-polarization (VH) to measure very high wind speeds. To this aim, an innovative analytical model for the full polarimetric scattering of the microwave radiation from ocean is developed. The model combines the 2nd order Small Slope Approximation Theory with the Vector Radiative Transfer Theory to obtain a statistical expression of the ocean scattering. The model is verified against RADARSAT-2 C-band SAR observations and collocated/time-coincident SFMR (Stepped-Frequency Microwave Radiometer) wind measurements by NOAA's hurricane-hunter aircraft. The validity of the model will be also proved against ECMWF (European Centre for Medium-range Forecasts) forecasted winds. Numerical results suggest that the present scattering model can be a powerful tool for understanding the full polarimetric ocean scattering at very high wind speeds, especially in hurricane conditions where existing empirical model functions fail predicting the relationship between NRCS and wind fields (i.e. wind speeds and directions).

In chapter 4, we extend the analytical physical model to provide not only accurate estimates of the full-polarimetric microwave sea-surface scattering but also accurate estimates of the ocean Doppler signatures. The model combines an adequate non-linear sea surface description, based on the Choppy Wave Model (CWM), with 2nd order Small-Slope-Approximation (SSA) wave scattering theory to simulate both scattering and Doppler spectra over a wide range of wind speeds, radar frequencies, incidence angles, different polarizations and arbitrary radar look direction with respect to the wind direction. The model is validated against real measurements from Envisat-ASAR (C-band radar), the well-established Empirical Geophysical Model Function CDOP [Mouche et al., 2012], and data collected at Ku band during the SAXON-FPN campaign [Plant and Alpers, 1994; Plant et al., 1994]. The same model will be used, in chapter 5, to explore ocean surface motion retrievals, thus supporting the definition of future scatterometers capable of simultaneous measurement of Ocean Vector Wind (OVW) and Ocean Vector Motion (OVM) on a global scale.

Drawing on arguments presented in the previous chapters, chapter 5 presents an

innovative microwave mission concept, called DopSCAT (Doppler Scatterometer), capable of resolving mesoscale features and their variations in time and space, with the objective of providing simultaneous worldwide measurements of Ocean Wind Vector and Ocean Motion Vector for operational use in weather and marine forecasting. Chapter 5 provides the background and scientific issues to be addressed by Ocean Doppler Scatterometry. It also provides a justification for the mission and identifies the potential “delta” that the mission could provide. Starting from the outlined research objectives and mission requirements, chapter 5 provides an overview of the observing system elements, including instrument design, principle of observation, data processing and calibration. It makes a comparison of expected versus required performance and ability to fulfill the research/observational objectives based upon the documented system concept.

2 Electromagnetic Interaction of Microwaves with the Ocean Surface

In this chapter, we present a survey of some of the most common analytical approximate models that are used to describe the microwave sea surface scattering. The main strengths and weaknesses of the various methods are identified and critically discussed. Such models combine an adequate sea surface description with advanced electromagnetic theories to simulate both monostatic and bistatic scattering for a wide range of wind speeds, radar frequencies, incidence angles, different polarizations and arbitrary radar look direction with respect to the wind direction. Theoretical calculations for co-polar and cross-polar signals at C-band and Ku-band are compared with empirical Geophysical Model Functions (GMF) and real data from Envisat/ASAR and Sentinel-1. The survey shall support the review of the scattering theories best adapted to the description of the electromagnetic interaction of microwaves with the ocean surface.

This chapter is based on the results published by the authors in [Fois *et al.*, 2014a] and [Hwang & Fois, 2015].

2.1 Introduction

In the last decades, the need for an improved understanding of the microwave scattering from ocean has gained considerable interest. This interest is largely motivated by the increased number of space-borne microwave instruments observing the ocean. Radar backscattering from the ocean surface has been used, in an operative way, to measure wind speed and direction over the ocean. These measurements constitute an important input to global and regional Numerical Weather Prediction (NWP), and, at the same time, provide valuable information for tracking of extreme weather events. Past attempts to develop physical models of microwave backscatter from the ocean surface have relied on Bragg scattering. This mechanism is generally used to describe scattering from the ocean when the electromagnetic waves are in resonance with sea waves of comparable wavelengths, the so-called Bragg waves. The radar wavelengths normally used for the observation of the ocean are resonant to components of the sea surface that are either very short gravity waves or surface-tension waves. To first order, the backscattered power is proportional to the wave height spectral density. On the other

hand, it is well known that neither the measured absolute NRCS values, for some combination of radar parameters and environmental conditions, nor their observed relative variations can be explained satisfactorily by pure Bragg scattering theory. The interpretation of the data from wind scatterometers requires, nowadays, a simple algorithm for the mapping of measured normalized radar cross sections into wind vectors at a given height. The level-2 processing of the ASCAT-MetOp scatterometer [Figa-Saldaña *et al.*, 2002], the Seasat scatterometer [Long *et al.*, 1993] and the ERS scatterometers [Lecomte, 1998] makes use of completely empirical models which are basically free of explicit physical assumptions. In contrast to this, radar backscattering models, based on a description of the scattering phenomenon, have the big capability of clarifying the physical relation between measured microwave backscatter and surface wind field. Several authors have developed sophisticated “physical” models, which account not only for pure Bragg scattering but for the impact of the complete ocean wave spectrum on the backscattered power. Crucial in these models is the accurate description of the ocean wave spectrum, as this is the link between microwave backscatter and wind.

2.2 Ocean Modelling

2.2.1 An Overview of Ocean Surface Wave Spectra

The 2-dimensional properties of the sea surface determine the characteristics of the measured NRCS. In this section, we focus our attention on the properties of the surface wave spectrum and how they depend on environmental parameters such as the local wind vector. Evaluation of the wave height variance spectrum over the footprint of a microwave radar is extremely challenging. This is not only because of the broad range of roughness scales present on the sea surface, from millimetre wavelengths to wavelengths on the order of 300 meters, but also because no single technique is able to determine wave height variance spectral densities over the entire range of wavelength, due to resolution and dynamic range limitations. Most routine measurements of the sea surface are limited to the height and directional characteristics of the wave field collected from a wave buoy at a single position in space as function of time.

Many studies in the recent literature have tried to assimilate such measurements into models for the sea surface wave spectra. These models generally characterize the measured properties of the sea surface through the spectral moments. Today, one of the most well known and accepted spectral models is the Elfouhaily unified spectrum [Elfouhaily *et al.*, 1997]. The development of this spectrum was based on available field and wave-tank measurements along with physical arguments. It is fully consistent with

Donelan spectrum [Donelan *et al.*, 1985] for the long wave part, whereas, for the short wave part, it is consistent with the optical tank measurements by Jähne [1990].

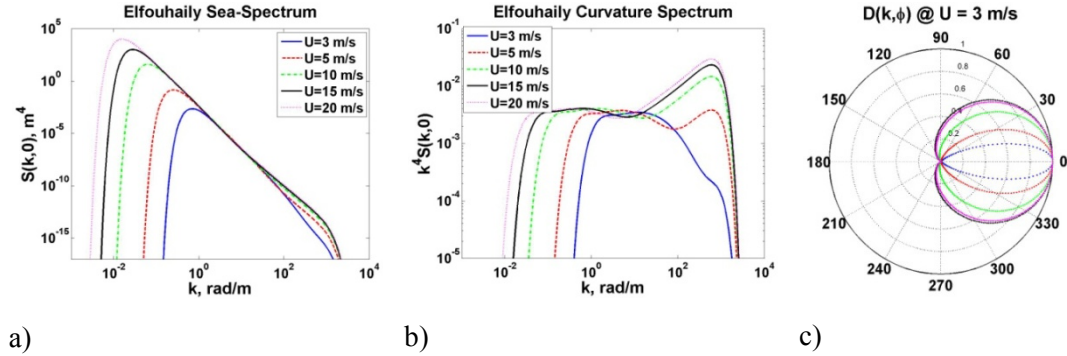


Fig. 2.1 Elfouhaily spectrum at various wind speeds and fetches of $9.7U^2$ km. a) The wave height variance spectral density in the direction of the wind; b) the curvature spectrum in the wind direction; c) the angular part of the spectrum, $D(k,\Phi)$. The different lines, here, show, in order of increasing loop size $k/k_p=1, 3, 10, 50$, while the line in magenta corresponds to $k/k_p=1000$.

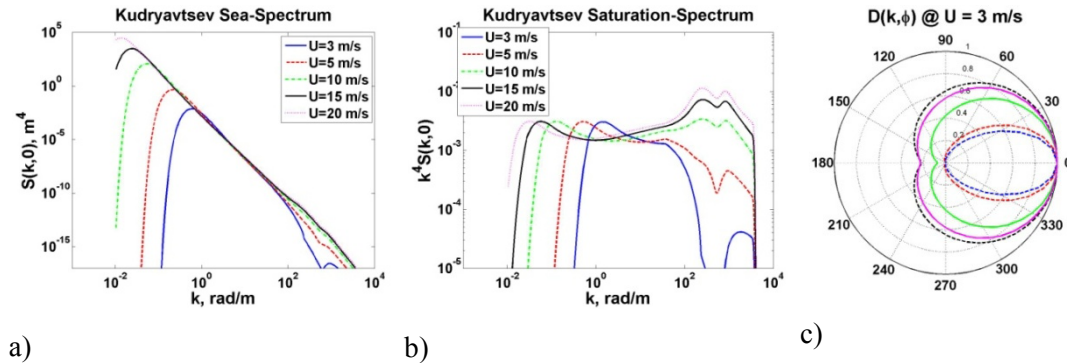


Fig. 2.2 Kudryavtsev spectrum at various wind speeds and fetches of $9.7U^2$ km. a) The wave height variance spectral density in the direction of the wind; b) the curvature spectrum in the wind direction; c) the angular part of the spectrum, $D(k,\Phi)$.

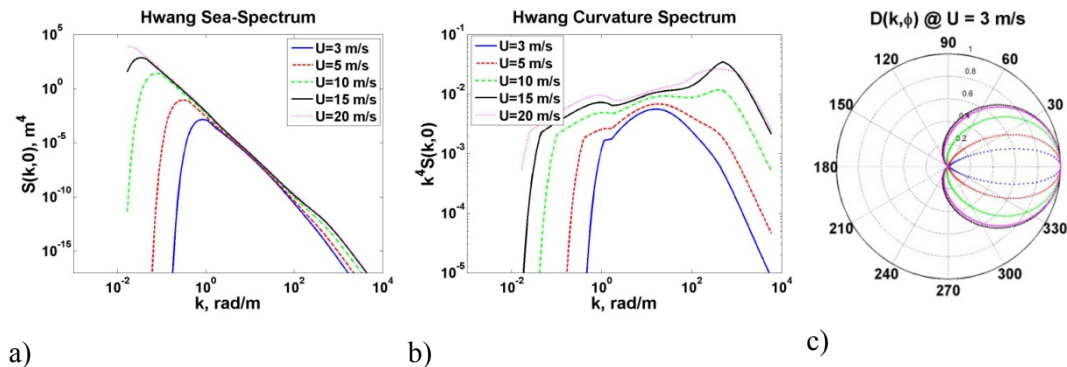


Fig. 2.3 As for Fig. 2.2 but for Hwang spectrum. Please note that the same directional spectrum $D(k,\Phi)$ of Elfouhaily is used.

The reader can refer to the original paper in order to obtain the explicit expression of the wave height variance spectral density. For convenience, Fig. 2.1 shows the Elfouhaily spectrum at various wind speeds and fetches.

The ocean surface wave spectrum by Kudryavtsev *et al.*, [1999], which is recently become quite popular, has improved the modelling of short-gravity and capillary waves. The spectral shape results from the solution of the energy spectral density balance equation. In the original paper, Kudryavtsev demonstrated that the measured statistical properties of the sea surface related to the short waves, such as the spectral shape of omni-directional and up-wind spectra, their wind speed dependence and angular spreading and the wind speed dependence of integral mean square slope and skewness parameters, are well reproduced by the model. Fig. 2.2 provides, from the left to the right hand side, the wave variance spectrum, the curvature (or saturation) spectrum and the directional part of the Kudryavtsev spectrum respectively.

Very recently, an improved spectral model for short-waves has been proposed in [Hwang *et al.*, 2013; Hwang & Fois, 2015], where a method is developed to obtain the short scale properties of ocean surface roughness and wave breaking from Ku, C and L band polarimetric sea returns. The results are used for quantitative evaluation of the ocean surface roughness spectral models and for deriving understanding of the breaking contribution important to microwave ocean remote sensing, in particular its dependence on wind speed, microwave frequency and incidence angle. The Hwang ocean wave height and curvature spectra are depicted in Fig. 2.3a-b, whereas the spreading function in Fig. 2.3c is the same of Elfouhaily *et al.* [1997].

2.2.2 Breaking Waves and Foam

Foam and whitecaps generated by breaking waves, at wind speeds higher than 7 m/s, can affect the scattering from the sea surface. Very often foam is described by its covered (or sheltered) area. Many empirical models express the whitecap coverage as a function of the wind friction velocity, the wind speed and the wind stress [Anguelova & Webster, 2006]. A key parameter in the description and characterisation of the breaking waves, is the *cumulative fraction of the sheltered surface*, describing the cumulative contribution of breaking wind waves to the sheltered zones. As suggested by Kudryavtsev & Makin [2007], there is a cascade sheltering process occurring at high wind speeds: the air-flow separation from the crest of long breaking waves may shelter the shorter waves and thus prevents the generation of small scale roughness. As a direct consequence, the microwave scattering is reduced. This mechanism can be taken into account in the model of the wave

height spectrum, by reducing the rate of wind waves growth [Kudryavtsev & Makin, 2007]; the objective is to overcome some inaccuracies of the Elfouhaily and Kudryavtsev models of sea roughness at high wind speeds.

2.2.3 Linear and Non-Linear Sea Surface Representation

In remote sensing applications the sea surface height is often modelled with Gaussian statistics. This representation of the ocean sea surface is called linear. However, non-linear surface waves can have an important impact on the interpretation of scattering data. The deviations from the Gaussian law of the slope distribution [Cox & Munk, 1954] may have a visible impact on the radar returns.

Non linear hydrodynamics link the motion of the large and small waves and modify both shape and statistical characteristics of the ocean sea surface. Hydrodynamic modulations of short waves by large waves are identified [Plant, 2002] as one of the reasons for the directional variation of the radar return and the observed difference among upwind and downwind measured NRCS.

Most of the non-linear models [Hasselmann, 1962; Loguet-Higgins, 1963] are only applicable to long gravity waves. For shorter waves, instead, wave-wave interactions to higher-order become non-negligible and must be accounted for. A theory that captures the lowest-order non-linear behaviour of surface waves was proposed by Creamer *et al.* [1989]. It represents the non-linearity of the wave field by using a special canonical transformation method and by expanding the surface wave Hamiltonian to the third-order.

The main limitation of this theory is that no statistical formulation exists and the numerical implementation of this theory is highly time-consuming especially for two-dimensional surfaces simulations.

A numerically efficient weakly non-linear model was developed recently to overcome these limitations [Nouguier *et al.*, 2009]. It is called Choppy Wave Model (CWM) and is based on the non-linear transformation of a reference linear surface. This transformation is performed through a horizontal shifting process of waves that makes them look choppy. The model provides a statistical formulation of the ocean surface in terms of sea surface height/ slope distributions, associated higher-order moments and joint-probabilities.

2.3 Approximate Scattering Models

2.3.1 Scattering Geometry, Notations And Definitions

Let us choose the right Cartesian coordinate system as depicted in Fig. 2.4. The sea surface $z = h(\mathbf{r})$, with $\mathbf{r} = x\hat{\mathbf{x}} + y\hat{\mathbf{y}}$, separates two homogeneous half spaces with permittivities ε_1 (upper half-space, $z > 0$) and ε_2 (lower half-space, $z < 0$). In the following, we will consider waves of frequency ω and the time dependence $\exp[-i\omega t]$ will be omitted. The sea-rough surface is illuminated by a monochromatic plane-wave coming from the upper half-space, impinging on the surface at incidence angle θ_i . The incident direction is defined by the wave vector $\mathbf{K}_i = \mathbf{k}_i - q_{ki}\hat{\mathbf{z}}$, with $\mathbf{k}_i = k_{ix}\hat{\mathbf{x}} + k_{iy}\hat{\mathbf{y}}$ and $q_{ki} = \sqrt{K_1^2 - k_i^2}$, where the wave number K_1 in the upper half-space is given by $K_1 = \sqrt{\mu_1\varepsilon_1} 2\pi/\lambda$, being λ the wavelength in the vacuum. The incident plane wave is given by:

$$\mathbf{E}_i = \frac{1}{\sqrt{q_{ki}}} \exp(i\mathbf{k}_i \cdot \mathbf{r} - iq_{ki}z) \mathbf{e}_{\alpha_i}^i(\mathbf{k}_i), \quad (2.1)$$

where $\mathbf{e}_{\alpha_i}^i(\mathbf{k}_i)$ is the unit vector defining the polarization of the incident plane wave. Here, $\alpha_i=1, 2$ is the index describing the vertical and horizontal polarizations of the electromagnetic wave, respectively. In particular, we can express $\mathbf{e}_{\alpha_i}^i(\mathbf{k}_i)$ in the following way:

$$\mathbf{e}_1^i(\mathbf{k}_i) = -\frac{(k_i^2\hat{\mathbf{z}} + q_{ki}\mathbf{k}_i)}{K_1k_i}, \quad \mathbf{e}_2^i(\mathbf{k}_i) = \frac{(\hat{\mathbf{z}} \times \mathbf{k}_i)}{k_i}. \quad (2.2)$$

The incident field \mathbf{E}_i gives rise to a scattered field \mathbf{E}_s in the upper half-space, moving in the direction $\mathbf{K}_s = \mathbf{k}_s + q_{ks}\hat{\mathbf{z}}$, with $\mathbf{k}_s = k_{sx}\hat{\mathbf{x}} + k_{sy}\hat{\mathbf{y}}$ and $q_{ks} = \sqrt{K_1^2 - k_s^2}$. Following the Rayleigh decomposition, the scattered field can be written as superposition of outgoing plane waves:

$$\mathbf{E}_s = \sum_{\alpha_s=1,2} \int \frac{d\mathbf{k}_s}{\sqrt{q_{ks}}} S_{\alpha_s\alpha_i}(\mathbf{k}_s, \mathbf{k}_i) \exp(i\mathbf{k}_s \cdot \mathbf{r} + iq_{ks}z) \mathbf{e}_{\alpha_s}^s(\mathbf{k}_s), \quad (2.3)$$

where $S_{\alpha_s \alpha_i}(\mathbf{k}_s, \mathbf{k}_i)$ is the so called scattering amplitude (SA) and $\mathbf{e}_{\alpha_s}^s(\mathbf{k}_s)$ is the scattered polarization given, for $\alpha_s=1, 2$, by:

$$\mathbf{e}_1^s(\mathbf{k}_s) = -\frac{(k_s^2 \hat{\mathbf{z}} + q_{ks} \mathbf{k}_i)}{K_1 k_s}, \quad \mathbf{e}_2^s(\mathbf{k}_s) = \frac{(\hat{\mathbf{z}} \times \mathbf{k}_s)}{k_s}. \quad (2.4)$$

With reference to the four polarization coefficients, $\alpha_i=1, 2$ and $\alpha_s=1, 2$, the scattering process can be described by the following 2×2 matrix:

$$\mathbf{S}(\mathbf{k}_s, \mathbf{k}_i) = \begin{bmatrix} S_{11}(\mathbf{k}_s, \mathbf{k}_i) & S_{12}(\mathbf{k}_s, \mathbf{k}_i) \\ S_{21}(\mathbf{k}_s, \mathbf{k}_i) & S_{22}(\mathbf{k}_s, \mathbf{k}_i) \end{bmatrix}. \quad (2.5)$$

Some more quantities must be defined to better describe the scattering from the sea surface, such as the scattered power ensemble averaged moments. The first-order moment, also known as the *coherent scattered amplitude*, is defined as:

$$V_{\alpha_s \alpha_i}(\mathbf{k}_s, \mathbf{k}_i) = \langle S_{\alpha_s \alpha_i}(\mathbf{k}_s, \mathbf{k}_i) \rangle. \quad (2.6)$$

The incoherent second order moment or *scattering cross-section* of the rough surface is:

$$\sigma_{\alpha_s \alpha_i}(\mathbf{k}_s, \mathbf{k}_i) = \left\langle \left| S_{\alpha_s \alpha_i}(\mathbf{k}_s, \mathbf{k}_i) - \langle S_{\alpha_s \alpha_i}(\mathbf{k}_s, \mathbf{k}_i) \rangle \right|^2 \right\rangle. \quad (2.7)$$

For distributed targets, the common quantity used in remote sensing is the *normalised radar cross section* (NRCS), which is defined as:

$$\sigma_{\alpha_s \alpha_i}^0(\mathbf{k}_s, \mathbf{k}_i) = \lim_{A \rightarrow \infty} \frac{4\pi \left\langle \left| S_{\alpha_s \alpha_i}(\mathbf{k}_s, \mathbf{k}_i) - \langle S_{\alpha_s \alpha_i}(\mathbf{k}_s, \mathbf{k}_i) \rangle \right|^2 \right\rangle}{A}, \quad (2.8)$$

where A is the area illuminated by transmit antenna pattern. Only normalized radar cross sections will be reported in this work.

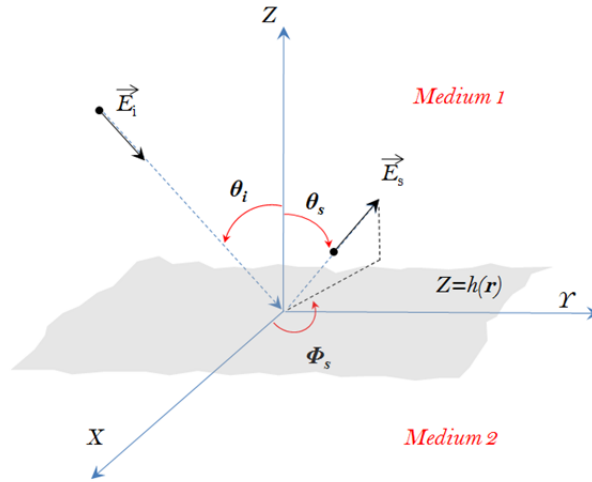


Fig. 2.4. Geometry of the scattering problem.

2.3.2 Kirchhoff Approximation

The formulation of the Kirchhoff method is based upon the *Green's theorem*, which states that the scattered field at any point within a source free region, bounded by a closed surface, can be expressed in terms of tangential fields on the surface [Ulaby *et al.*, 1990]. This approximation, known as *Tangent-Plane Approximation* or *Kirchhoff Approximation*, is valid when the observed target (body or surface) has a radius of curvature large compared to the wavelength of radiated signal. The procedure to compute the scattering fields by means of the tangent-plane approximation is denoted as *physical optics* or *Kirchhoff method* in scattering. The *physical optics* provides a high-frequency solution to the scattering problem. This solution becomes exact for the limiting case $\lambda \rightarrow 0$ (*geometrical optics* limit), being λ the wavelength of the *e.m.* radiation, and $A \rightarrow \infty$ so that no edge effects exist. The condition for the applicability of the *physical optics* was given, for the first time, by Brehkovskikh [1952] in the following form

$$r_c \cdot K_1 \cos^3 \theta_i \gg 1, \quad (2.9)$$

where θ_i is the angle of incidence of the *e.m.* radiation with respect to the normal surface, and r_c is the radius of curvature. For processes with Gaussian correlation coefficient $r_c = l^2 / (2.76 \sigma)$, with l is the correlation length and σ is the standard deviation of height. Among the many surface-scattering theories, the *Kirchhoff* or the *physical optics* formulation is one of the most widely used. The evaluation of the scattering amplitude in the *Kirchhoff Approximation* writes:

$$\mathbf{S}^{KA}(\mathbf{k}_s, \mathbf{k}_i) = \frac{\mathbf{K}_{\alpha_s \alpha_i}(\mathbf{k}_s, \mathbf{k}_i)}{Q_z} \int \frac{d\mathbf{r}}{(2\pi)^2} \exp[i\mathbf{Q}_H \cdot \mathbf{r} + iQ_z h(\mathbf{r})], \quad (2.10)$$

where $Q_z = q_{ks} + q_{ki}$, $\mathbf{Q}_H = \mathbf{k}_s - \mathbf{k}_i$, $Q_H = |\mathbf{k}_s - \mathbf{k}_i|$, $h(\mathbf{r})$ is the sea surface shape and $\mathbf{K}(\mathbf{k}_s, \mathbf{k}_i)$ is the Kirchhoff kernel. The reader can refer to appendix-A for its general expression. To simplify the notation the dependency on α_s and α_i will be often omitted. Starting from (2.8), we can derive the statistical determination of the normalised radar cross-section, which for linear surface cases writes:

$$\sigma_{\alpha_s \alpha_i}^0(\mathbf{k}_s, \mathbf{k}_i) \Big|_{KA} = \frac{1}{\pi} \left| \frac{\mathbf{K}_{\alpha_s \alpha_i}(\mathbf{k}_s, \mathbf{k}_i)}{Q_z} \right|^2 \exp[-Q_z^2 C(0)] \times \int d\mathbf{r} \left\{ \exp[Q_z^2 C(\mathbf{r})] - 1 \right\} \exp[i\mathbf{Q}_H \cdot \mathbf{r}] \quad (2.11)$$

where

$$C(\mathbf{r}) = \langle h(\boldsymbol{\rho} + \mathbf{r}) h^*(\boldsymbol{\rho}) \rangle = \int d\xi S(\xi) \exp(i\xi \cdot \mathbf{r}), \quad (2.12)$$

being $S(\xi)$ the spectrum of roughness. As it appears clear in equation (2.9), the Kirchhoff method is valid in a limited angular region around the specular direction and thus, in a monostatic configuration, it works only at small incidence angles. At intermediate angles, the present method has no sensitivity to polarization (i.e. the polarization ratio $\sigma_{11}^0 / \sigma_{22}^0$ is equal to 1). In addition, the horizontal polarization is very poorly described and it predicts null cross-polarized signal in the plane of incidence, being a single scattering theory.

2.3.3 Geometrical Optics

The validity of the Kirchhoff approximation depends on the radar wavelength: in particular this approximation becomes exact for the limiting case $\lambda \rightarrow 0$, *geometrical optics* limit (GO). In this specific case, the normalized cross-section can be written as [Voronovich, 1999]:

$$\sigma_{\alpha_s, \alpha_i}^0(\mathbf{k}_s, \mathbf{k}_i)|_{GO} = \left| \frac{K_{\alpha_s, \alpha_i}(\mathbf{k}_s, \mathbf{k}_i)}{Q_z^2} \right|^2 \frac{R_0}{2\pi \text{mss}} \exp\left[-\frac{|\mathbf{k}_s - \mathbf{k}_i|^2}{2Q_z^2 \text{mss}}\right], \quad (2.13)$$

where mss corresponds to the mean squared slope of the surface and R_0 is a reflectivity factor.

2.3.4 Small-Perturbation Method

In the previous sections, we have highlighted that the Kirchhoff method can be only applied to surfaces with horizontal roughness scale and average radius of curvature larger than the electromagnetic wavelength. When both the surface standard deviation and correlation length are smaller than the wavelength, a different method must be used. One standard approach is the *small-perturbation method* (SPM) [Ulaby *et al.*, 1990], which requires the surface standard deviation to be less than about 5 percent of the electromagnetic wavelength. In addition to the standard-deviation requirement, the average slope of the surface should be of the same order of magnitude as the wave number, times the standard deviation; mathematically

$$K_1 \sigma < 0.3, \quad (2.14)$$

$$\sqrt{2} \sigma / l < 0.3. \quad (2.15)$$

These conditions should be viewed only as a guideline for applying the SPM. The main differences between the Kirchhoff approximation and the small perturbation method (SPM), can be summarized in the following two points:

- The Kirchhoff approximation is valid for long wavelengths and small slopes. This approximation correctly reproduces quasi-specular scattering, but does not provide any polarisation sensitivity.
- The SPM is valid for short wavelengths and small slopes. It provides polarisation sensitivity, but does not include the effects of long-scale features of the ocean nor the effects of specular scattering.

2.3.5 Two-Scale Scattering Model

In the previous sections, two different scales of surface roughness were considered. The surface roughness was either large or small when compared with the incidence

wavelength. Natural surfaces not only include both scales of roughness but, more in general, present a continuous distribution of roughness. Analytically, there is no simple method to treat surfaces with a continuous distribution of roughness. However, for two-scale surfaces, a simple approximate treatment of the scattering problem is possible. Wright in [1968] formulated, for the first time, the so called *composite-surface scattering model*. In this model, the sea surface is assumed to be made of an infinite number of slightly rough patches. The backscattered power from a single patch is the result of an average over the distribution of slopes of long waves of the ocean. When this type of model is combined, for small incidence angles, with the physical optics approximation, then we speak of a *two-scale model* (TSM). As it is well known, the main weakness of the classical TSM is the arbitrariness of the separation scale between small and large waves. The two scale model is unable to correctly predict the cross-polar signal in the plane of incidence, and it sensibly underestimates the scattering at large incidence angles. In addition, the TSM does not provide a scattering matrix, thus it is not adequate to perform a deterministic calculation of the NRCS nor of the Doppler spectrum of a time evolving sea surface.

2.3.6 Unified Models

In this section, we present scattering calculations based on *unified scattering models*, which do not have the above-mentioned drawback. They, in fact, replace the two-scale description of the scattering process with a unique expression of the scattering amplitude with a smooth dynamical transition between the two regimes, namely GO and SPM.

1st-Order Small-Slope Approximation (SSA1)

The small slope approximation does not invoke any arbitrary scale-dividing parameter separating small and large scale components of the roughness. The SSA can be applied to an arbitrary wavelength, provided that the tangent of grazing angles of incident/scattered radiation sufficiently exceeds the RMS slope of roughness [Voronovich, 1994]. Its validity domain is defined by the following equation:

$$K_1 s \sigma < 1, \quad (2.17)$$

with s and σ being the slope and height RMS, respectively. The slopes of sea-surfaces are generally small except for steep breaking waves which represent a relatively small percentage. The small slope approximation is adequate for the computation of scattering

from both large (the Kirchhoff regime), intermediate and small scale (the Bragg regime) roughness. Being the result of a regular expansion with respect to powers of slope, it allows the evaluation of the effect of higher-order corrections on its results. We refer now to the lowest order approximation, named SSA1; the next order approximation, SSA2, will be discussed at the end of section 2.3.6. The explicit expression for the scattering amplitude is:

$$\mathbf{S}^{SSA-1}(\mathbf{k}_s, \mathbf{k}_i) = \frac{B_{\alpha_s \alpha_i}(\mathbf{k}_s, \mathbf{k}_i)}{Q_z} \int \frac{d\mathbf{r}}{(2\pi)^2} \exp[-i\mathbf{Q}_H \cdot \mathbf{r} + iQ_z h(\mathbf{r})], \quad (2.18)$$

where $B(\mathbf{k}_s, \mathbf{k}_i)$ is the Bragg kernel. The general expression for the kernel function is reported in appendix-B, see also [Voronovich, 2001] for details. The normalized radar cross-section, for linear surface cases, can be then written as:

$$\begin{aligned} \sigma_{\alpha_s \alpha_i}^0(\mathbf{k}_s, \mathbf{k}_i) \Big|_{SSA-1} &= \frac{1}{\pi} \left| \frac{B_{\alpha_s \alpha_i}(\mathbf{k}_s, \mathbf{k}_i)}{Q_z} \right|^2 \exp[-Q_z^2 C(0)] \\ &\times \int d\mathbf{r} \left\{ \exp[Q_z^2 C(\mathbf{r})] - 1 \right\} \exp[i\mathbf{Q}_H \cdot \mathbf{r}] \end{aligned}, \quad (2.19)$$

A drawback of the SSA1 model is that the polarization ratio is not sensitive to surface roughness. This limits the domain of validity of the model to low wind-speeds and low microwave frequencies. As for KA also for SSA1, the model predicts null cross-polarization in the plane of incidence, as SSA1 is based on a single scattering theory. Though in many papers the SSA1 is used up-to very high incidence and scattering angles, the model should be limited in angle, since SSA1 does not account for shadowing effects.

Weighted Curvature Approximation

In [2004], Elfouhaily *et al.* derived a model named the *Weighted Curvature Approximation* (WCA). They arrived at a scattering amplitude which is a correction to the tangent plane approximation in a form of a Kirchhoff integral with a local unknown kernel. They developed such a kernel with all desirable properties (reciprocity, shift and tilt invariance, compatibility with SPM and KA limits). The WCA writes as:

$$\begin{aligned} \mathbf{S}^{WCA}(\mathbf{k}_s, \mathbf{k}_i) = & \mathbf{S}^{KA}(\mathbf{k}_s, \mathbf{k}_i) + i \frac{\mathbf{B}(\mathbf{k}_s, \mathbf{k}_i) - \mathbf{K}(\mathbf{k}_s, \mathbf{k}_i)}{Q_H^2} \\ & \times \int \frac{d\mathbf{r}}{(2\pi)^2} \Delta h(\mathbf{r}) \exp[-i\mathbf{Q}_H \cdot \mathbf{r} + iQ_z h(\mathbf{r})] \end{aligned} \quad (2.20)$$

where $\Delta h(\mathbf{r}) = \nabla \cdot \nabla h(\mathbf{r})$ is the Laplace operator of the sea surface. From equation (2.20), we see that the correction of the Kirchhoff integral involves second order spatial derivatives of the surface $h(\mathbf{r})$. As alternative, the WCA can be written as a correction to the SSA1 scattered amplitude, that is:

$$\begin{aligned} \mathbf{S}^{WCA}(\mathbf{k}_s, \mathbf{k}_i) = & \mathbf{S}^{SSA-1}(\mathbf{k}_s, \mathbf{k}_i) - \frac{Q_z[\mathbf{B}(\mathbf{k}_s, \mathbf{k}_i) - \mathbf{K}(\mathbf{k}_s, \mathbf{k}_i)]}{Q_H^4} \\ & \times \int \frac{d\mathbf{r}}{(2\pi)^2} [\mathbf{Q}_H \cdot \nabla h(\mathbf{r})]^2 \exp[-i\mathbf{Q}_H \cdot \mathbf{r} + iQ_z h(\mathbf{r})] \end{aligned} \quad (2.21)$$

After simple but tedious manipulations one finds the normalized radar cross-section:

$$\begin{aligned} \sigma_{\alpha_s, \alpha_i}^0(\mathbf{k}_s, \mathbf{k}_i) \Big|_{WCA} = & \sigma_{\alpha_s, \alpha_i}^0(\mathbf{k}_s, \mathbf{k}_i) \Big|_{SSA-1} \\ & + \frac{2}{\pi Q_H^2} \text{Re}[\mathbf{B}_{\alpha_s, \alpha_i}^* (\mathbf{B}_{\alpha_s, \alpha_i} - \mathbf{K}_{\alpha_s, \alpha_i})] \times \int d\mathbf{r} e^{-Q_z^2(C(0)-C(\mathbf{r}))} e^{-i\mathbf{Q}_H \cdot \mathbf{r}} A(\mathbf{r}) \\ & + \frac{Q_z^2 |\mathbf{B}_{\alpha_s, \alpha_i} - \mathbf{K}_{\alpha_s, \alpha_i}|^2}{\pi Q_H^4} \times \int d\mathbf{r} e^{-Q_z^2(C(0)-C(\mathbf{r}))} e^{-i\mathbf{Q}_H \cdot \mathbf{r}} [W(\mathbf{r}) + A^2(\mathbf{r})] \end{aligned} \quad (2.22)$$

The kernels $A(\mathbf{r})$ and $W(\mathbf{r})$ are provided in appendix-B. In [Elfouhaily *et al.*, 2004], it was shown that the WCA is able to improve both KA and SSA1, in some range of moderate roughness and in co-polarization. For sea surface scattering, the WCA is more accurate than the SSA1 and can work at larger incidence angles; in particular, it improves the horizontal polarization estimates. Being a single scattering theory, as for the KA and SSA1, the WCA predicts null cross-polarization in the plane of incidence.

2nd -Order Small-Slope Approximation (SSA2)

The aforementioned unified models have a main limitation, which is their inability to estimate cross-polarized scattering components in the plane of incidence. The cross-polarization in the incidence plane is essentially due to multiple-scattering mechanisms and it can properly be estimated either by solving numerically the electromagnetic

equations via Method of Moments [Tsang *et al*, 1994; Johnson, 1996], or by second-order perturbation theory (SPM2) [Valenzuela, 1978] and its extension (SSA2) [Voronovich, 1994]. Statistically tractable formulae for the sea spectra can only be obtained for SPM2 and SSA2. The SPM2 model is only valid for very small roughness, whereas SSA2 has a more extended domain of validity. The computation of SSA2 scattering amplitude is very complicated as it requires the calculation of four-fold integrals with oscillating functions. The SSA2 presents the following expression of the scattering amplitude:

$$\begin{aligned} \mathbf{S}_{\alpha_s, \alpha_i}^{SSA2}(\mathbf{k}_s, \mathbf{k}_i, t) &= \frac{1}{Q_z} \int \frac{d\mathbf{r}}{(2\pi)^2} \exp[-i\mathbf{Q}_H \cdot \mathbf{r} + iQ_z h(\mathbf{r}, t)] \\ &\times \left[\mathbf{B}_{\alpha_s, \alpha_i}(\mathbf{k}_s, \mathbf{k}_i) - \frac{i}{4} \int M_{\alpha_s, \alpha_i}(\mathbf{k}_s, \mathbf{k}_i, \xi) \hat{h}(\xi, t) e^{i\xi \cdot \mathbf{r}} d\xi \right] \end{aligned} \quad (2.23)$$

where

$$\begin{aligned} M_{\alpha_s, \alpha_i}(\mathbf{k}_s, \mathbf{k}_i, \xi) &= \mathbf{B}_2(\mathbf{k}_s, \mathbf{k}_i, \mathbf{k}_s - \xi) + \\ &\mathbf{B}_2(\mathbf{k}_s, \mathbf{k}_i, \mathbf{k}_i + \xi) + 2Q_z \mathbf{B}_{\alpha_s, \alpha_i}(\mathbf{k}_s, \mathbf{k}_i) \end{aligned} \quad (2.24)$$

In equation (2.23) we have also added the time variable t in order to make the expression of the scattering amplitude more general. The function

$$\hat{h}(\xi, t) = \frac{1}{(2\pi)^2} \int d\mathbf{r} e^{-i\xi \cdot \mathbf{r}} h(\mathbf{r}, t). \quad (2.25)$$

is the two-dimensional spatial transform of the linear surface. We call A the area illuminated by the transmit antenna pattern. The spatiotemporal covariance function is the limit of the statistical average:

$$\begin{aligned} \text{Cov}(\mathbf{k}_s, \mathbf{k}_i; t) \Big|_{Lim.} &= \\ \lim_{A \rightarrow \infty} \frac{4\pi \left\langle \left| \mathbf{S}_{\alpha_s, \alpha_i}^{SSA2}(\mathbf{k}_s, \mathbf{k}_i, t) - \left\langle \mathbf{S}_{\alpha_s, \alpha_i}^{SSA2}(\mathbf{k}_s, \mathbf{k}_i, t) \right\rangle \right|^2 \right\rangle}{A} & \end{aligned} \quad (2.26)$$

for an infinitely illuminated area A . After tedious manipulations and assuming Gaussian statistics of roughness, the following expression can be found:

$$\begin{aligned} \text{Cov}(\mathbf{k}_s, \mathbf{k}_i; t) = \\ \frac{4\pi}{Q_z^2} \int \frac{d\mathbf{r}}{(2\pi)^2} R_{\alpha_s \alpha_i}(\mathbf{k}_s, \mathbf{k}_i; \mathbf{r}, t) \exp[-i\mathbf{Q}_H \cdot \mathbf{r}] \end{aligned} \quad (2.27)$$

where

$$\begin{aligned} R_{\alpha_s \alpha_i}(\mathbf{k}_s, \mathbf{k}_i; \mathbf{r}, t) = \\ -e^{-Q_z^2 C(0,0)} |B_{\alpha_s \alpha_i}(\mathbf{k}_s, \mathbf{k}_i) - F_{\alpha_s \alpha_i}(\mathbf{k}_s, \mathbf{k}_i; 0)|^2 + \\ e^{-Q_z^2 (C(0,0) - C(\mathbf{r}, t))} \left[\frac{1}{16} \int |M_{\alpha_s \alpha_i}(\mathbf{k}_s, \mathbf{k}_i; \xi)|^2 S(\xi, t) e^{i\xi \cdot \mathbf{r}} d\xi + \right. \\ (B_{\alpha_s \alpha_i}(\mathbf{k}_s, \mathbf{k}_i) - F_{\alpha_s \alpha_i}(\mathbf{k}_s, \mathbf{k}_i; 0, t) + F_{\alpha_s \alpha_i}(\mathbf{k}_s, \mathbf{k}_i; \mathbf{r}, t)) \times \\ \left. (B_{\alpha_s \alpha_i}(\mathbf{k}_s, \mathbf{k}_i) - F_{\alpha_s \alpha_i}(\mathbf{k}_s, \mathbf{k}_i; 0, t) + F_{\alpha_s \alpha_i}(\mathbf{k}_s, \mathbf{k}_i; -\mathbf{r}, t))^* \right] \end{aligned} \quad (2.28)$$

with

$$F_{\alpha_s \alpha_i}(\mathbf{k}_s, \mathbf{k}_i; \mathbf{r}, t) = -\frac{Q_z}{4} \int M_{\alpha_s \alpha_i}(\mathbf{k}_s, \mathbf{k}_i; \xi) S(\xi, t) e^{i\xi \cdot \mathbf{r}} d\xi. \quad (2.29)$$

and

$$C(\mathbf{r}, t) = \langle h(\mathbf{r}, t) h(\mathbf{0}, 0) \rangle = \int d\xi S(\xi, t) \exp(i\xi \cdot \mathbf{r}). \quad (2.30)$$

being $S(\xi, t)$ the spectrum of roughness. Note that the spatiotemporal covariance function computed at the time $t=0$ provides the Normalized Radar Cross Section, σ^0 , that is:

$$\sigma_{\alpha_s \alpha_i}^0(\mathbf{k}_s, \mathbf{k}_i) = \text{Cov}(\mathbf{k}_s, \mathbf{k}_i; 0). \quad (2.31)$$

2.3.7 Trade-offs between Models

Following the example of Elfouhaily & Guerin [2004], we use a synthetic table to summarize the major properties of the approximate scattering models discussed in the previous sections of this work. Among the properties listed in table 2.1 are: reciprocity, shift invariance, tilt invariance. The *reciprocity* expresses the invariance of scattering amplitude at reciprocal incidence and scattering angles:

$$\mathbf{S}(\mathbf{k}_s, \mathbf{k}_i) = \mathbf{S}^T(-\mathbf{k}_s, -\mathbf{k}_i). \quad (2.32)$$

where the superscript T stands for the transposed dyad (or matrix). The *shift invariance* refers to the phase-shifting (delays in the time domain) that results from horizontal and vertical translations of the surface:

$$\mathbf{S}(\mathbf{k}_s, \mathbf{k}_i) \Big|_{h(\mathbf{r}-\mathbf{d})+D} = e^{-i\mathbf{Q}_H \cdot \mathbf{d}} e^{-iQ_z \cdot D} \mathbf{S}(\mathbf{k}_s, \mathbf{k}_i) \Big|_{h(\mathbf{r})}. \quad (2.33)$$

The *tilt invariance* expresses the fact that the scattering amplitude should not depend on the choice of the reference plane and the reference coordinate system. Satisfying these properties does not ensure that the method will be accurate in various roughness scenarios, but it is an efficient criterion to see whether an approximation can be a good candidate for a given type of surface.

Table 2.1 Properties of the scattering models [Elfouhaily & Guerin, 2004].

Property	1	2	3a	3b	3c	4	5	6	7	8a	8b	9a	9b	10
SPM1	▲	▲	□	⊗	⊗	▲	▲	□	⊗	▲	⊗	⊗	⊗	⊗
KA-HF	▲	▲	□	▲	▲	▲	▲	⊗	▲	⊗	□	⊗	⊗	⊗
GO1	▲	▲	□	-	□	▲	▲	⊗	▲	⊗	▲	⊗	⊗	⊗
SSA1	▲	▲	▲	▲	⊗	▲	▲	▲	▲	▲	⊗	⊗	⊗	⊗
WCA	▲	▲	▲	▲	▲	▲	□	□	▲	▲	▲	⊗	⊗	⊗
SPM2	▲	▲	□	⊗	⊗	▲	□	▲	⊗	-	⊗	▲	-	▲
KA2-HF	▲	▲	▲	□	□	□	□	⊗	▲	⊗	-	⊗	□	□
GO2	▲	▲	□	-	□	▲	▲	⊗	▲	⊗	-	⊗	▲	□
SSA2	▲	▲	▲	▲	□	⊗	□	▲	▲	▲	◆	▲	⊗	▲

1. All types of surfaces (dielectric, conducting, acoustic).
2. Full two-dimensional surfaces.
3. a. Reciprocal, b. Shift Invariant, c. Tilt invariant.
4. Numerically fast and stable while easy to implement.
5. Statistical formulae already available or easily derivable.
6. Not restricted to large correlation length.
7. Not restricted to small surface height.
8. a. SPM1 limit, b. GO1 limit.
9. a. SPM2 limit, b. GO2 limit
10. Can predict cross-polarization in the plane of incidence.

- ▲ = Satisfied by construction;
- = Satisfied upon inspection;
- ◆ = Satisfied upon special conditions;
- ⊗ = Not satisfied;
- = Irrelevant.

A further property is that the method satisfies the fundamental high and low-frequency limits, namely GO and SPM, and possibly extends beyond the validity domain of *Small Perturbation Method* and *Geometrical Optics*. The existence of statistical formulae for the cross-section represents a fundamental criterion in trading off the different methods.

The numerical implementation should be fast, stable and easy. By ‘fast’ we mean essentially an analytical expression that involves a limited number of integrations and FFTs. By ‘stable’ we mean that the integration procedure does not include oscillating functions or singularities. By ‘easy’, we mean that the scattering model is based on a simple-to-implement formula. Finally, the model should be able to predict a correct cross-polarization in the incidence plane. With reference to table 2.1 [Elfouhaily & Guerin, 2004], any ‘positive’ feature of a method is marked as a box or a triangle. Elfouhaily & Guerin make a distinction between properties that are inherent to the model (satisfied ‘by construction’) and those which are a suitable but not necessary outcome (satisfied ‘upon inspection’). Empty squares are used when the models satisfy a property only partially or under special conditions. This table should guide us in identifying those models that best suit our needs. To this aim, it is worth noting that not necessarily the best scattering method is the one having more boxes or triangles.

2.4 Comparison with Experimental Data

We have made a detailed comparison between the scattering models, presented in section 2.3, and Geophysical Model Functions (GMF), for three different frequencies (Ku, X and C-band), three values of wind speeds (5, 10 and 15 m/s) and two wind directions (upwind and crosswind). Figures 2.5-2.8 are just an extract of our simulations: here, we only show the results for two bands (C and Ku) and two wind speeds (5 m/s and 15 m/s upwind and crosswind). Except for the Ku-band case at high wind speed, the WCA method agrees very well with the SSA2, for both VV and HH-polarizations. All these plots are generated by using the Elfouhaily *et al.* [1997] sea spectrum model. Averaged experimental data for Ku (14 GHz) and C (5.3 GHz) bands are obtained by using SASS-II [Wentz, 1984] and CMOD5n [Hersbach, 2010] empirical GMFs. The choice of the incidence angles (0° - 60° , for SASS-II, 20° - 60° for CMOD) is determined by the validity range of the empirical models. For Gaussian statistics of roughness, backscattering in the opposite directions (i.e. for negative angles of backscattering) is the same and theoretical curves, calculated according to SSA, WCA and KA, coincide. Since CMOD5 does not provide the NRCS in HH-polarization, this value is obtained by computing the polarization ratio (PR) as proposed in [Thompson *et al.*, 1998]:

$$PR = \frac{\sigma_{VV}^0}{\sigma_{HH}^0} = \frac{[1 + 2(\tan \theta)^2]^2}{[1 + \alpha(\tan \theta)^2]^2}, \quad (2.34)$$

where $\alpha = 0.6$ at C-band and $\alpha = 1.729$ at X-band. In general, we can say that there is a fair agreement between the theory and the experimental results; however, the HH-polarization is severely underestimated for large incidence, in the upwind direction, with the error growing with the wind speed. The HH-polarization for cross-wind directions is in much better agreement with the experimental data than for up-wind directions; whereas, the VV-polarization is slightly overestimated. At C-band, both WCA and SSA can accurately predict the NRCS in VV-polarization for all the upwind cases investigated. In the cross-wind direction, instead, such an agreement is weaker. On the contrary, WCA and SSA prediction of the HH-polarization is more accurate in cross-wind than in up-wind direction. At X-band, we did not manage to find any accurate agreement between the scattering models and the empirical geophysical model function X-MOD [Ren *et al.*, 2012]. We believe that such a discrepancy is mainly due to the fact that X-MOD is a relatively new geophysical model and needs more time and data to be well tuned. In order to justify the differences occurring between scattering models and empirical models, we need to make a remark on the way both sea-roughness spectrum and empirical models are obtained. Practically, they are the results of averaging over broad ensembles of environmental situations corresponding to a given wind.

The variability of environmental conditions over a single resolution cell could have a non-negligible impact in the wind retrieval. The backscattering cross section is, in fact, a non-linear function of the roughness spectrum S and thus [Voronovich & Zavorotny, 2001]:

$$\langle \sigma(S) \rangle \neq \sigma \langle S \rangle, \quad (2.35)$$

where $\langle \dots \rangle$ denotes averaging over different environmental conditions with a given wind. On the basis of these considerations and remembering that the derivation of the Elfouhaily spectrum was not based on remote sensing data and that we have not used any adjustable parameter in the scattering models, the overall agreement between theoretical calculations and experimental data is remarkable. If we want to further improve the agreement between theoretical calculations and experimental data we need to work in two different directions: on one hand, by improving the scattering models with the inclusion of steep breaking waves, and, on the other, by improving the Elfouhaily wave height spectrum.

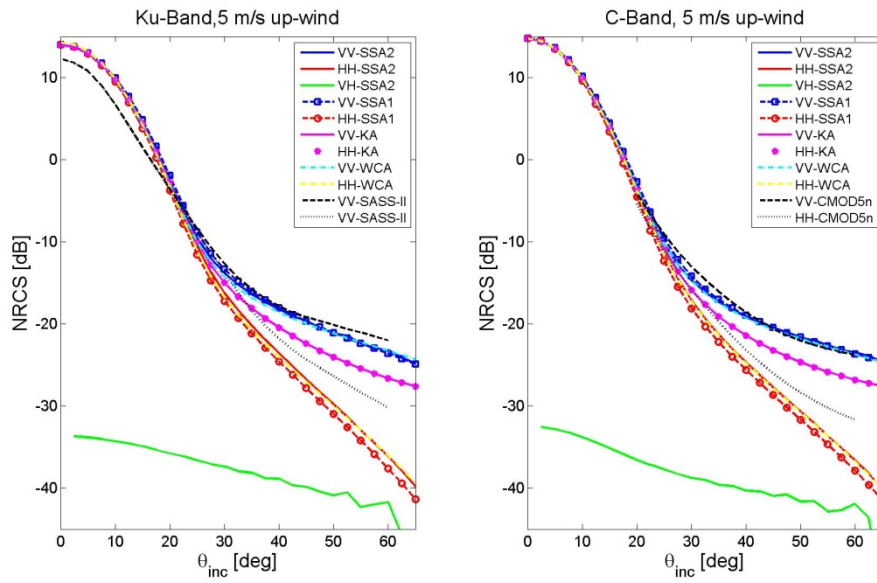


Fig. 2.5 Normalized radar cross section (NRCS) at Ku and C-band for 5 m/s wind speed, in up-wind direction. Experimental data are computed according to SASS-II and CMOD5n geophysical model functions.

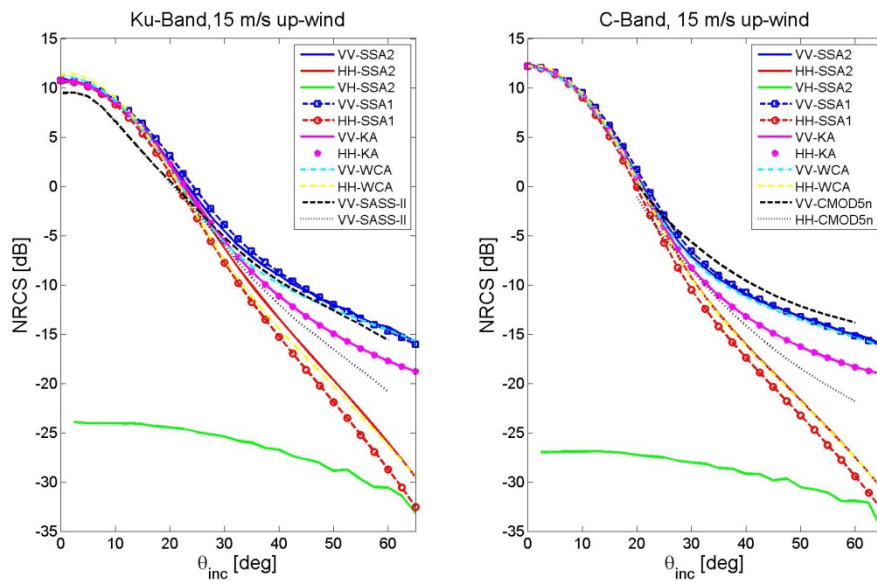


Fig. 2.6 Same as Fig.2.5 but for 15 m/s up-wind.

2.4.1 Inclusion of Steep Breaking Waves

The importance of steep breaking waves for polarization behaviour of microwave backscattering has been acknowledged by many authors [Voronovich & Zavorotny, 2001; Chapron *et al.*, 2000; Smirnov & Zavorotny, 1995]. The inclusion of steep breaking waves into the backscattering model is needed to properly estimate the HH-polarization at high incidence angles and thus the polarization ratio PR.

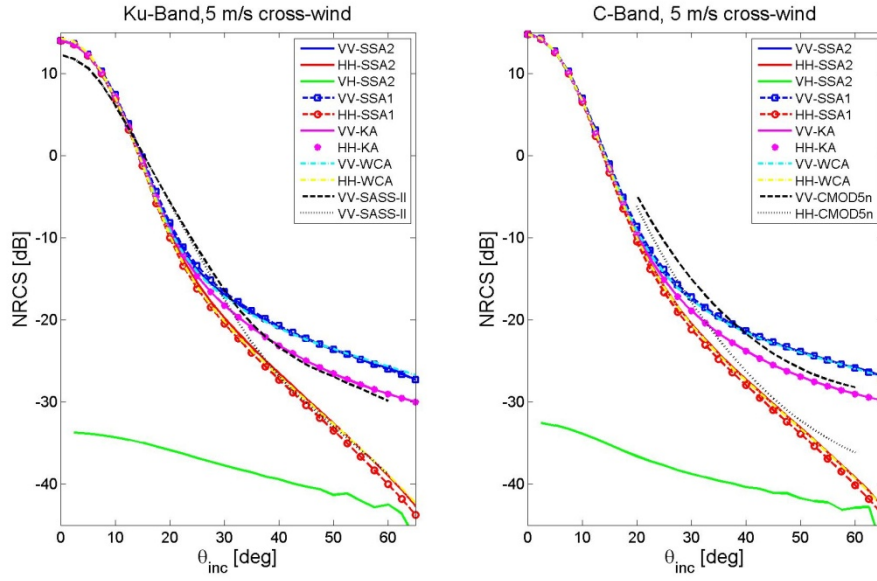


Fig. 2.7 Normalized radar cross section (NRCS) at Ku and C-band for 5 m/s wind speed, in cross-wind direction. Experimental data are computed according to SASS-II and CMOD5n geophysical model functions.

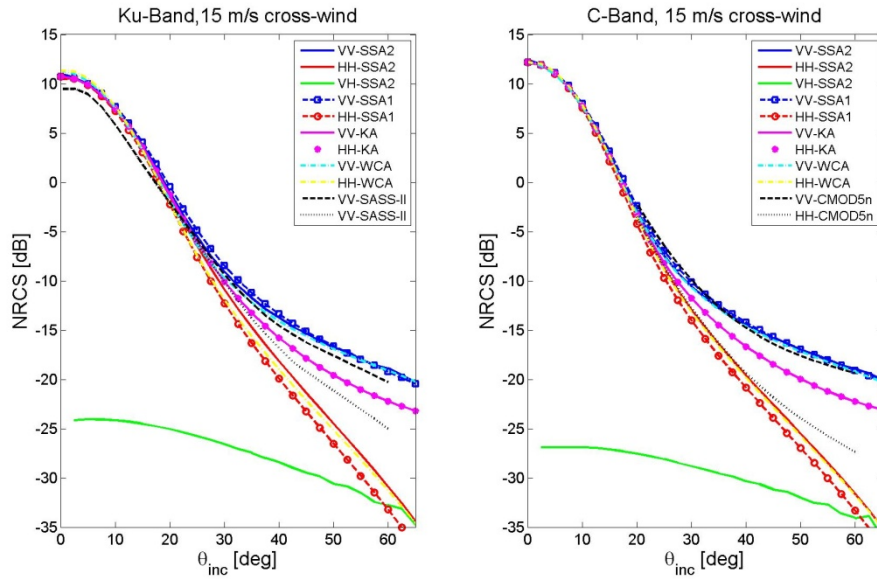


Fig. 2.8 Same as Fig.2.7 but for 15 m/s cross-wind.

Specular reflection and scattering from breaking waves, randomly distributed on the sea surface, are statistically independent of Bragg scattering. Hence, the total NRCS can be expressed as a sum of two contributions: one including Bragg scattering and specular reflections and the other including non-Bragg scattering from breaking waves:

$$\sigma_{pq}^0(\theta, \varphi) = \sigma_{pq}^0 \Big|_{WCA \text{ or } SSA2}(\theta, \varphi) \cdot (1 - q) + \sigma^0 \Big|_{WB}(\theta, \varphi). \quad (2.36)$$

Both specular and wave breaking contributions are independent of polarization. Bragg scattering and specular reflections can be taken into account by either the SSA2 or the WCA model. As discussed in [Kudryavtsev *et al.*, 2003], some hypothesis are necessary to simplify the NRCS model: a) only breakers with scales exceeding the radar wavelength can contribute to the increased radar returns; b) a cut-off wave number k_{nb} is fixed to compute the backscattering. By using the same notation as in [Kudryavtsev *et al.*, 2003], we get:

$$\sigma^0 \Big|_{WB}(\theta, \varphi) = \sigma^0 \Big|_{WB}(\theta) \cdot (1 + M_{iWB} \bar{\theta}_{WB} A_{WB}(\varphi)) \cdot q, \quad (2.37)$$

where M_{iWB} is the tilting transfer function and $\bar{\theta}_{WB}$ is a mean tilt of non-Bragg scattering areas. The NRCS $\sigma^0 \Big|_{WB}(\theta, \varphi)$ is, in practice, the multiplication of two terms: one incidence angle dependent and the other azimuth angle dependent. The quantity q is the fraction of sea surface covered by plumes and can be written as:

$$q = c_q \int_{\varphi} \int_{k < k_{nb}} \left[\frac{1}{2k} \left(\frac{B(k, \varphi)}{\alpha} \right)^{n+1} \right] d\varphi dk, \quad (2.38)$$

where $B(k, \varphi)$ is the curvature spectrum, c_q is a constant defining the fraction of sea surface covered by breaking waves, whereas α and n are functions of k/k_γ where $k_\gamma = \sqrt{g/\gamma}$, being γ the surface tension and g the gravity acceleration. The term $\sigma^0 \Big|_{WB}(\theta)$ can be estimated by using the *geometrical optics* with the addition of the contribution to the NRCS from the sides of the plume:

$$\sigma^0 \Big|_{WB}(\theta) = (\sec^4 \theta / s_{WB}^2) \exp(-\tan^2 \theta / s_{WB}^2) + \varepsilon_{WB} / s_{WB}^2, \quad (2.39)$$

The quantity ε_{WB} is a constant which represents the ratio of the breaker thickness to its length. The quantity s_{WB}^2 is the mean square slope of enhanced roughness (assumed isotropic) of the wave breaking zone. On the basis of experimental measurements, we can fix the constants: $\bar{\theta}_{WB} = 0.05$, $s_{WB}^2 = 0.19$, $c_q = 10.5$, $\varepsilon_{WB} = 0.005$ [Kudryavtsev *et al.*, 2003]. Figure 2.9 shows the polarization ratio at Ku-band as function of the wind speed for 3 different incidence angles (30°, 45°, 60°) and two different wind directions, up-wind

and cross-wind. Blue lines correspond to the NSCAT GMF by Wentz & Smith [1999], black lines refer to WCA model with Elfouhaily-spectrum applied, green dash lines correspond to WCA with Kudryavtsev-spectrum applied and, finally, the red circles are obtained by adding to the WCA model the breaking contributions. The improvement in the prediction of the polarization ratio obtained through the inclusion of wave-breaking is remarkable across the full range of wind-speeds and directions analyzed.

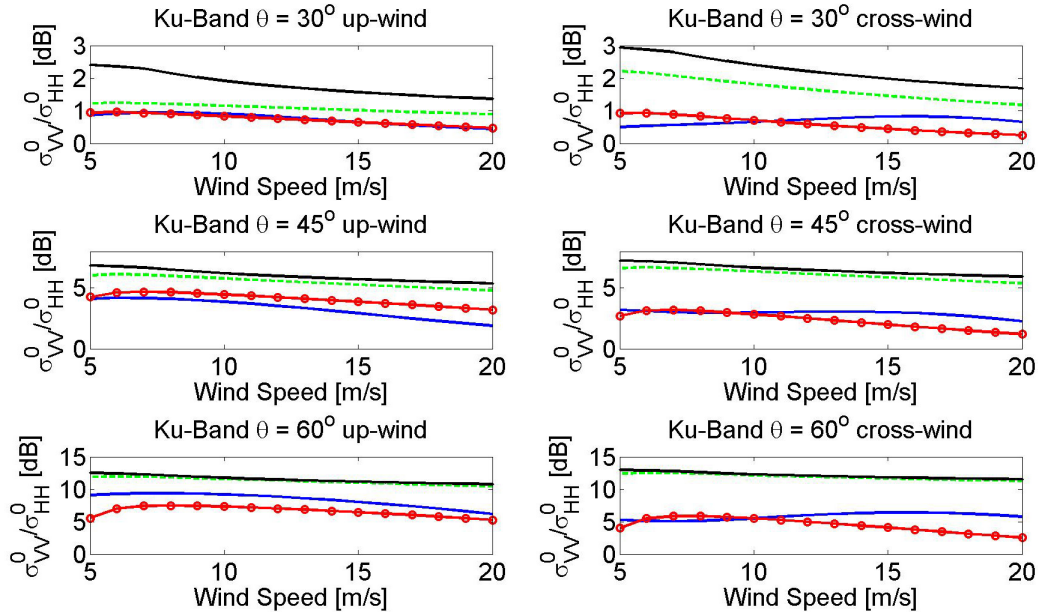


Fig. 2.9 Polarization ratio at Ku-band as function of the wind speed for 3 different incidence angles (30° , 45° , 60°) and two different wind directions up-wind and cross-wind. Blue lines correspond to the NSCAT GMF by Wentz and Smith [1999], black lines refer to WCA model with Elfouhaily spectrum applied, green dash lines correspond to WCA with Kudryavtsev spectrum applied and red circles are obtained by adding to the WCA model the breaking contributions.

2.4.2 Wave Height Spectrum Optimization

As mentioned in section 2.4, an alternative way to improve the accuracy of the NRCS, at different frequencies, incidence angles and polarizations, is to correct the omnidirectional sea surface spectrum to better match the experimental data. Microwave backscattering from the sea surface contains valuable information of the ocean surface roughness and wave breaking that is very difficult to measure using conventional oceanographic instruments. Making use of the property that VV, HH and VH respond to roughness and breaking differently, a method to extract the quantitative roughness and breaking properties is outlined in [Hwang & Fois, 2015]. Basically, the GMFs established from global NRCS measurements are treated as field data of roughness and wave breaking reflected in the interaction of microwave and the sea surface. Theoretical solutions of the Bragg resonance scattering from the surface roughness contributions for

VV, HH and VH are computed using the SSA2. The VV return is dominated by Bragg resonance scattering; therefore the comparison between the GMF and the SSA2 is useful for refining the ocean surface roughness spectral model. Once a satisfactory roughness model is obtained, the differences between the GMF and SSA2 solutions is used to derive the information of small scale surface wave breaking properties. The information is useful for microwave applications as well as air-sea interaction research in areas such as gas transfer and sea spray aerosol production. It's important to point out that the results regarding the dependence on frequency, incidence angle and wind speed as presented in [Hwang & Fois, 2015] are based on the still-evolving GMFs and roughness models. We expect further refinement in the future with improved accuracy of the surface roughness models and GMFs. The refined Hwang spectrum is used in the following section to compare the backscattering coefficient obtained by the second order small slope approximation solution (SSA2) with real measurements from Sentinel-1 and Envisat-ASAR data sets.

2.5 Comparison with Measurements

In this section, the validation of the scattering models is performed through comparison with real measurements from different data sets, namely Sentinel-1 cross-polar data sets and Envisat-ASAR co-polar data sets. A short description of the observing systems and their products is provided in the following sub-section.

2.5.1 Measurements Data Sets

Sentinel-1 Extra Wide Swath Ocean Data Set

The ESA Sentinel-1 satellite [Torres *et al.*, 2012] carries a C-band (5.404 GHz) synthetic aperture radar instrument to provide an all-weather day-and-night supply of imagery of Earth's surface. The Extra Wide (EW) swath mode employs the TOPSAR technique [De Zan & Guarnieri, 2006] to acquire data over a very large area using five sub-swaths. EW mode acquires data over a 400 km swath at 20 m by 40 m spatial resolution. The TOPSAR imaging is a form of ScanSAR imaging (the antenna beam is switched cyclically among the five sub-swaths) where, for each burst, the beam is electronically steered from backward to forward in the azimuth direction. This leads to uniform NESZ and ambiguity levels within the scan bursts, resulting in a higher quality image. The EW mode is a TOPSAR single sweep mode [Aulard-Macler, 2011]; the radar beam switching has been chosen to provide one azimuth look per beam for all points. The azimuth steering angle is $\pm 0.8^\circ$. The polarization can be either single (VV or HH) or dual

(VV+VH or HH+HV). EW Single Look Complex (SLC) products contain one image per sub-swath and one per polarisation channel. The five sub-swaths cover an incidence angle range which goes from 18.9° up to 47°. Table 2.2 provides the precise incidence angle ranges corresponding to the minimum orbit height satellite positions (~698 km) and the corresponding NESZ values. The instrument cross-talk is estimated being better than -35 dB. The EW mode is aimed primarily for use over sea-ice, polar zones and certain maritime areas, in particular for ice, oil spill monitoring and security services. In this chapter, Normalized Radar Cross Sections, in VH or HV polarizations, from Sentinel-1 data are used in combination with ECMWF forecasted winds to validate our scattering model.

Tab. 2.2 Incidence Angles and NESZ for Extra Wide Swath Beams

Beams	EW1	EW2	EW3	EW4	EW5
Incidence angles	20.00°-29.20°	29.15°-34.47°	34.41°-39.66°	39.60°-43.89°	43.86°-46.97°
NESZ	-28dB ÷ -23dB	-30dB ÷ -27dB	-32dB ÷ -27dB	-34dB ÷ -26dB	-33dB ÷ -30dB

ASAR/Envisat Ocean Data Set

As a complement to the RADARSAT-2 and Sentinel-1 data sets, the ASAR/Envisat [Desnos *et al.*, 2000] data in VV and HH polarizations are also used to verify and validate the proposed analytical scattering model. Envisat (“Environmental Satellite”) is an inoperative Earth-observing satellite still in orbit. It was launched on 1 March 2002 and ended its mission on 9 May 2012.

The Advanced Synthetic Aperture Radar (ASAR) aboard Envisat is a C-band (5.331 GHz) high resolution imaging radar. Before the end of the Envisat mission, ASAR was operated in 5 distinct measurement modes [Kult, 2012]: Image Mode (IM), Alternating Polarization mode (AP), Wide Swath mode (WS), Global Monitoring mode (GM), and Wave mode (WV). Within each mode, several different imaged swaths were used. The Image Mode provided data with 30 m spatial resolution. The observed area was selected among seven possible swaths spanning the incidence angle range 15° to 45°. The Wave Mode generated vignettes of 5 km by 5 km, spaced 100 km along-track. The Wide Swath and Global Monitoring modes were based on the ScanSAR technique. Five sub-swaths, were used to cover 400 km swath with spatial resolutions of 150 m for the Wide Swath mode and 1000 m for the Global Monitoring mode. These four modes used either HH or VV polarization. The Alternating Polarisation mode allowed alternating the instrument polarisation among HH and VV, HH and HV or VV and VH. The Noise Equivalent Sigma Zero of the ASAR products is much higher (2 ÷ 4 dB) than the NESZ of RADARSAT-2 and Sentinel-1, resulting in a very limited Signal-to-Noise Ratio over the

ocean, particularly in cross-polarisation. This explains why only VV and HH polarisations have been mainly used for ocean applications.

2.5.2 Numerical Results

Figures 2.10-2.11 show the cloud of ASAR normalized radar cross section measurements in VV polarization versus collocated (close enough in space and time to be representative) wind speed measurements provided by the MetOp-ASCAT scatterometer. The following incidence angles are analyzed: 17°, 20°, 24°, 28°, 33.5°, 34.5°, 38.5° and 39.5°. For each wind speed the NRCS values associated with all possible wind directions are plotted. The different colours in the two figures represent the frequency of the observations. Black and grey lines represent the NRCS computed by using the SSA2 model in combination with Hwang and Elfouhaily sea surface spectrum respectively. The magenta lines show the backscattering coefficients given by the geophysical model function CMOD5n. Solid and dashed lines correspond to up-wind and cross-wind cases respectively. Figures 2.12-2.13 show the same information as Fig. 2.10-2.11 but for HH-polarization. Considering that no geophysical model function at C-band in HH polarization exists, the magenta lines are obtained by combining CMOD5n with the polarization ratio given by equation (2.34). The wind speed sensitivity of co-polar backscattering measurements increases with the incidence angle. This feature is more evident in HH-pol than in VV-pol. The behaviour of HH and VV-NRCS are similar for 17°, 20° and 24° incidence, whereas some differences emerge beyond 30 degrees. These differences increase with the incidence angle. The above mentioned characteristics of the co-polar backscattering coefficients are also confirmed by the numerical implementation of the SSA2 model. The use of the Hwang spectrum over estimates the VV-pol NRCS of about 1÷2 dB at low incidence angles (< 20°) and wind speeds above 10 m/s.

Although the Elfouhaily unified directional wave spectrum matches better the ASAR data in up-wind cases, it under-estimates the cross-wind cases of about 1÷3 dB within the wind speed range 3÷15 m/s. The CMOD5n geophysical model function should well represent the transfer between vector wind and backscattering coefficient of the ocean, as it is built on the basis of MetOp-ASCAT backscatter triplets and collocated ECMWF forecasted winds. However, some discrepancies are visible at both 17° and 20° incidence. In fact, CMOD5n seems to under-estimate the NRCS of 1÷2 dB in up-wind cases. These discrepancies can be justified by the fact that the GMF is valid within the incidence angle range 25°÷55°, corresponding to near and far swath of the ASCAT scatterometer.

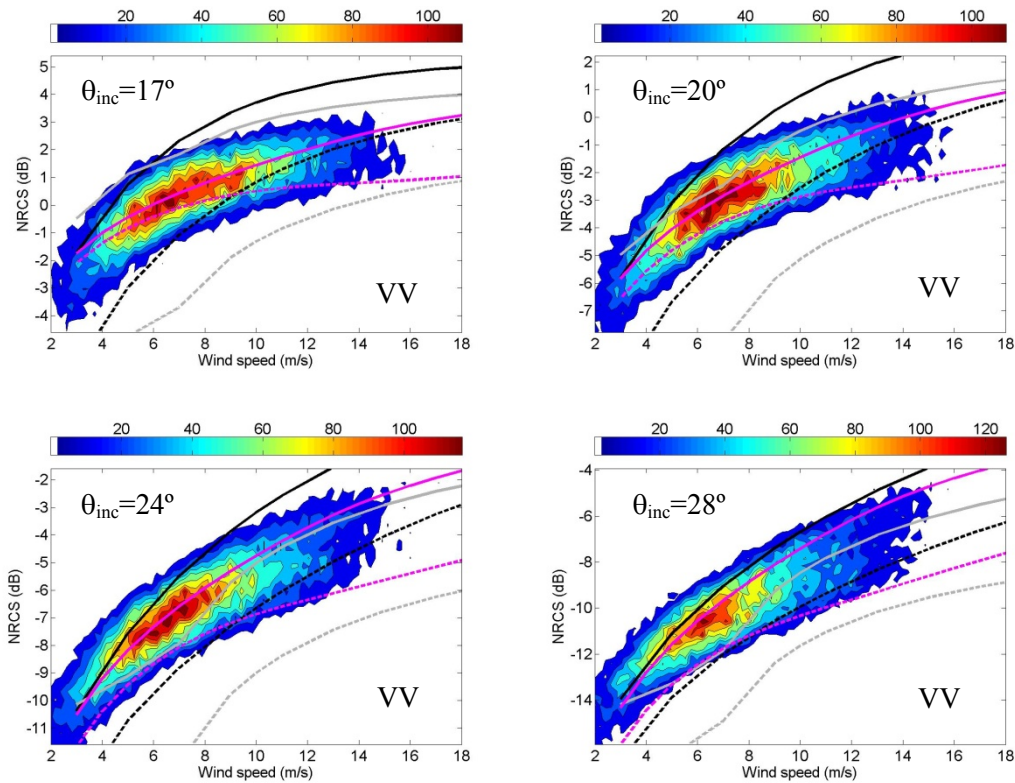


Fig. 2.10 Two-dimensional histogram of the NRCS in VV polarization versus wind speed for different incidence angles (17° , 20° , 24° , 28°). Black curves correspond to numerical calculations performed with SSA2 and Hwang spectrum. Grey curves correspond to SSA2 and Elfouhaily spectrum. Magenta curves correspond to CMOD5n geophysical model function. Solid lines depict up-wind cases whereas dashed lines depict cross-wind cases.

For incidence angles higher than 20° (see Fig. 2.10-2.11) the agreement between the SSA2 model and the cloud of VV-polar measurements significantly improves and the differences between model and measurements are in the order of 1 dB or less, except for very low wind speeds (<4 m/s) for which the measurement accuracy is affected by the limited radiometric resolution. Figures 2.12-2.13, provide the same information as Fig. 2.10 and 2.11 for the case of HH-polarization. At low incidence angles ($\leq 20^\circ$) the behaviour of HH-NRCS and VV-NRCS is very similar. This is also confirmed by the Kirchhoff approximation of the scattering fields, which holds at low angles of incidence. Above 20° , the correlation between HH and VV ocean backscattering decreases. The SSA2 model underestimates the HH normalized radar cross section of about 1–3 dB within the range of incidence angles 24° – 40° and wind speeds between 5 and 15 m/s. Similar differences are also found between the measurements and CMOD5n geophysical model function combined with the Thompson polarization ratio.

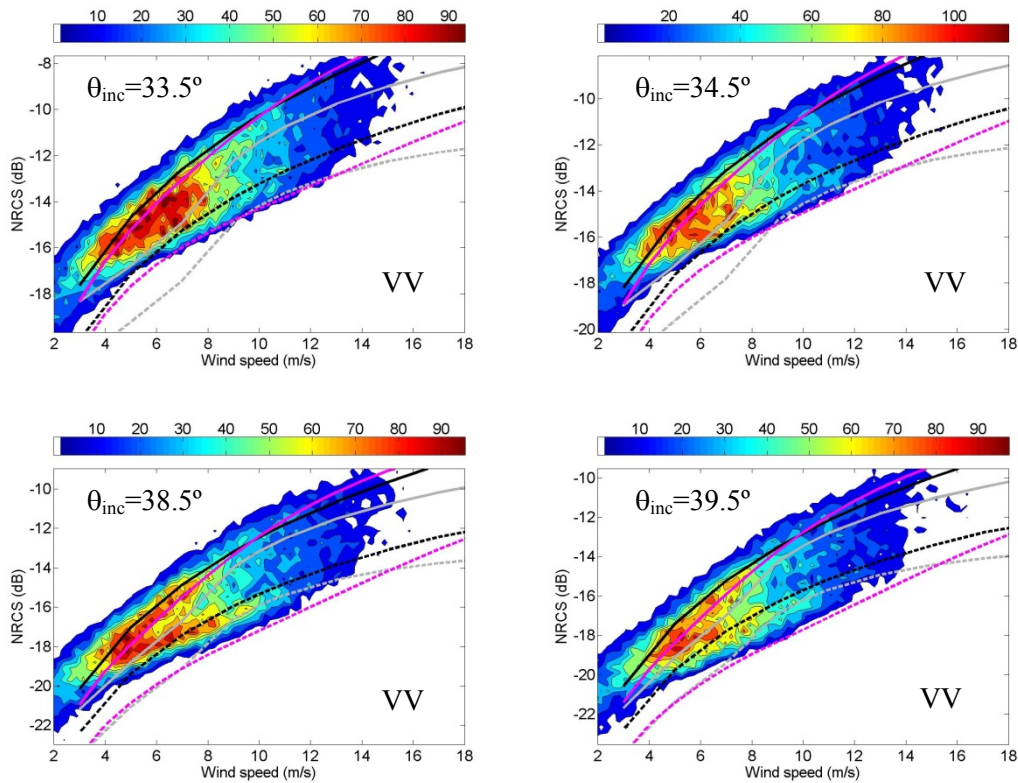


Fig. 2.11 Two-dimensional histogram of the NRCS in VV polarization versus wind speed for different incidence angles (33.5° , 34.5° , 38.5° , 39.5°). Black curves correspond to numerical calculations performed with SSA2 and Hwang spectrum. Grey curves correspond to SSA2 and Elfouhaily spectrum. Magenta curves correspond to CMOD5n geophysical model function. In particular solid lines depict up-wind cases whereas dashed lines depict cross-wind cases.

The Hwang spectrum shows a better match with the measurements than both Elfouhaily spectrum and the empirical model function. This is particularly evident in cross-wind and high incidence angles.

Figure 2.14 shows the clouds of VV-polar measurements by ASAR collected, as function of the wind direction, within different incidence angle ranges ($30^\circ\div 32^\circ$, $33^\circ\div 35^\circ$, $36^\circ\div 38^\circ$, $39^\circ\div 41^\circ$) and corresponding to wind speeds between 5 and 10 m/s. Overlaid are the simulated NRCS obtained by using the SSA2 model with the Hwang wave height spectrum. Solid and dashed lines refer to 10 and 5 m/s wind respectively. For each wind speed two curves are plotted, corresponding one to the minimum and the other to the maximum angle within the observed range. As depicted in Fig. 2.14, the modulation of the measured VV-NRCS with the wind direction is well predicted by the SSA2 model. Some discrepancies are found in HH-polarization (see Fig. 2.15) for low wind speeds. The dashed curves under-estimate HH-NRCS at 5 m/s wind and the prediction errors increase with the incidence angle.

Differences between up-wind and down-wind scattering are clearly visible above 38° in VV-polarization and above 28° in HH-polarization. As discussed in section 2.2.3, one of the reasons of such difference is represented by the strong non-linear coupling among long and short waves. The non-linear description of the sea surface is not captured by SSA2 neither by any of the models presented in this chapter. The inclusion of a non-linear representation of the sea surface into the scattering model will be addressed in chapter 4. Wind retrieval from both VV and HH ocean scatterometry experiences saturation at high wind speeds. Recently Zadelhoff *et al.*, [2013, 2014], Hwang *et al.* [2013,2014] have investigated the suitability of C-band cross-polarized ocean backscattering to retrieve very high winds. They have compared VV and VH polarized signals from RADARSAT-2, acquired during severe hurricane events, to collocated ECMWF winds and SFMR wind measurements by NOAA's Hurricane-Hunter aircraft. From this data set a Geophysical Model Function (GMF) valid for strong-to-extreme/severe wind speeds (i.e. $20 \text{ m/s} \leq U_{10} \leq 45 \text{ m/s}$) has been derived:

$$\begin{aligned} \sigma_{VH}^0 \Big|_{dB} &= 0.580 \cdot U_{10} [m/s] - 35.652, & U_{10} [m/s] &\leq 18.1823 \text{ m/s} \\ \sigma_{VH}^0 \Big|_{dB} &= 0.218 \cdot U_{10} [m/s] - 29.07, & 18.1823 \text{ m/s} &\leq U_{10} [m/s] \leq 45 \text{ m/s} \end{aligned} \quad (2.40)$$

This GMF is incidence angle independent and is made of two parts: one, valid from low to high wind-speeds (known as *Vachon* and *Wolfe* formula), the other applicable from high to extreme wind. In this chapter we only focus on low to high wind speeds, whereas the discussion on high to extreme winds is postponed to chapter 3. Figure 2.16 shows the cloud of Sentinel-1 measurements in HV-polarization versus ECMWF forecasted wind for different incidence angle ranges (20° - 23° , 24° - 28° , 29° - 33.5° , 34.5° - 38.5° , 39.5° - 43° , 43.75° - 46°). The colours represent the frequency of observations. The black solid and dashed lines show the *Vachon et al* [2011] and the *Zhang et al* [2014] empirical model functions. The magenta lines depict the SSA2 model computation, with Hwang spectrum, at the extreme angles of the observed areas: in particular solid magenta lines refer to up-wind cases at the lowest incidence angles whereas dashed magenta lines correspond to cross-wind cases at the highest incidence angles. The grey lines, instead, depict the SSA2 model computation, with Elfouhaily spectrum, at the extreme angles of the observed areas. Green and red dots show the RADARSAT-2 measurements in Quad-Pol mode with and without noise correction: these dots are used as a reference.

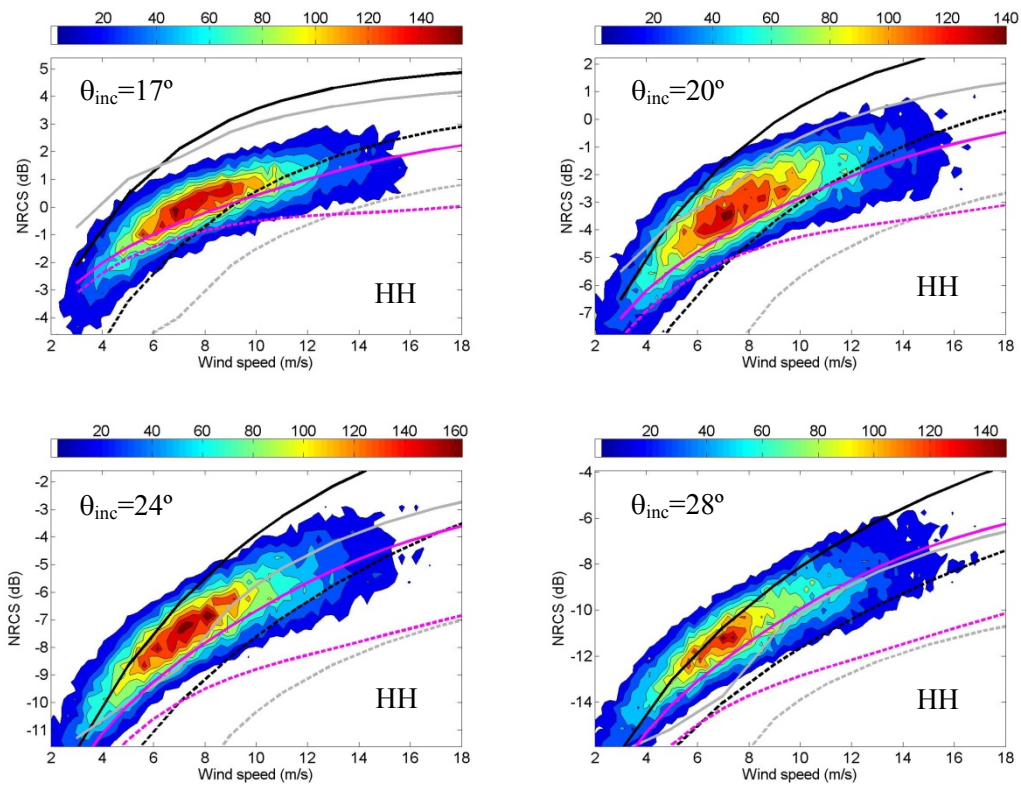


Fig. 2.12 Same as Fig. 2.11 but for HH polarization.

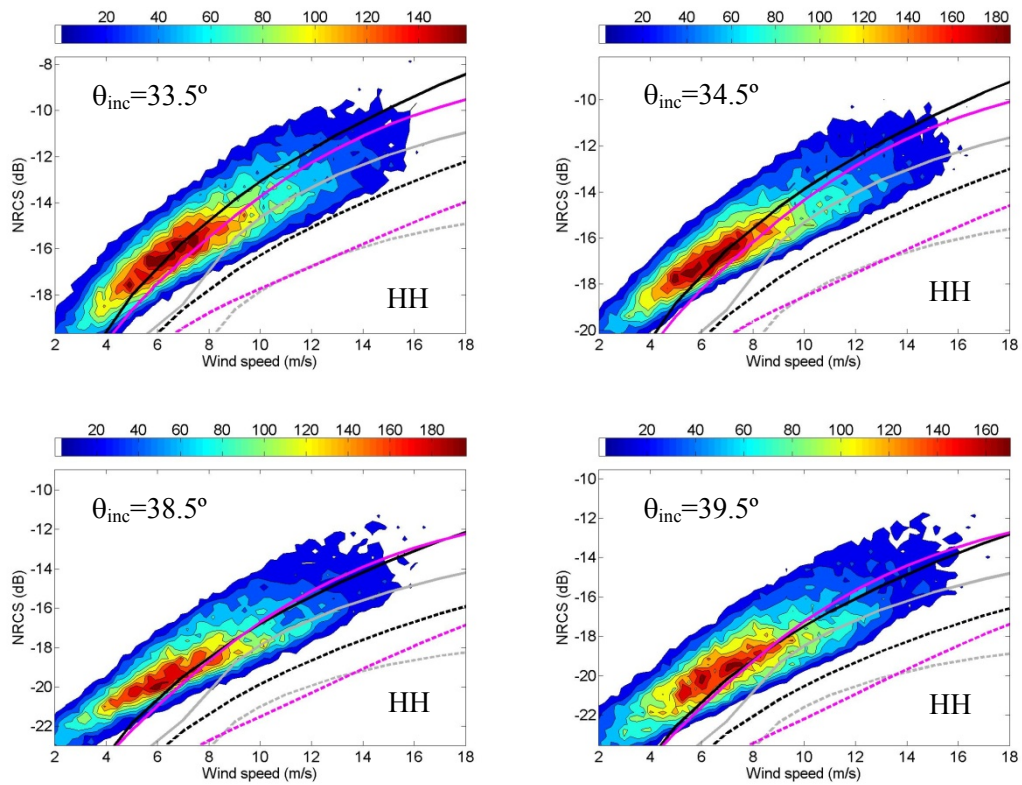


Fig. 2.13 Same as Fig. 2.12 but for HH polarization.

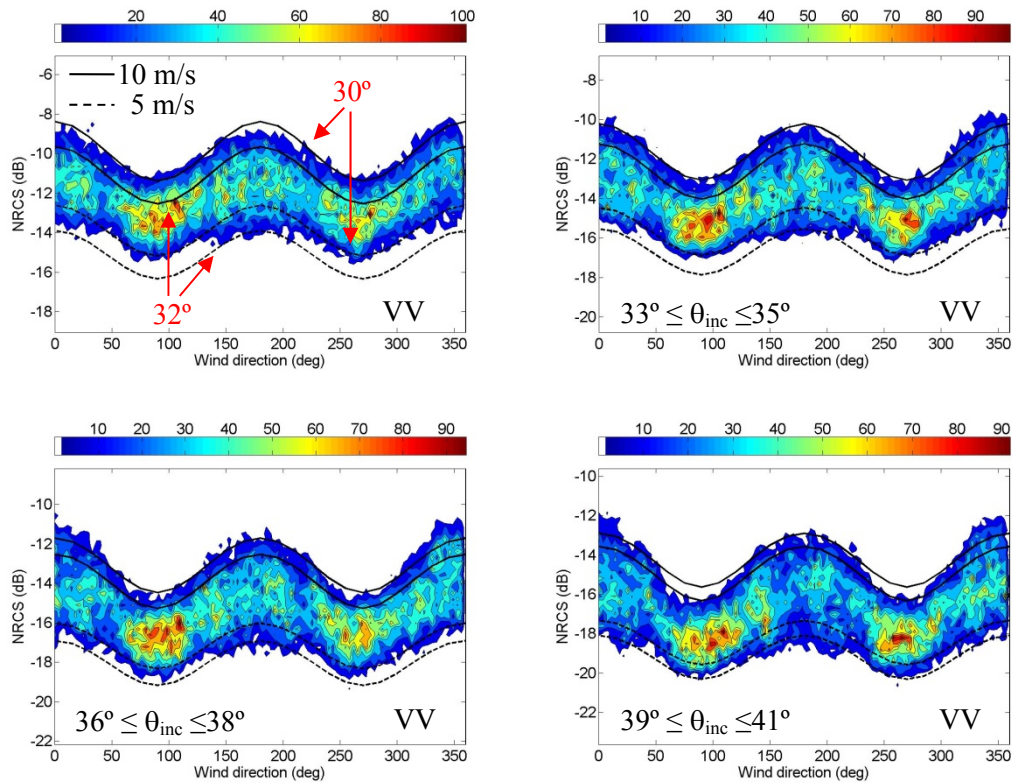


Fig. 2.14 Clouds of ASAR measurements collected in VV-polarization at different incidence angle ranges ($30^\circ \div 32^\circ$, $33^\circ \div 35^\circ$, $36^\circ \div 38^\circ$, $39^\circ \div 41^\circ$) and corresponding to wind speeds between 5 and 10 m/s. Overlaid are the SSA2 simulated NRCS: Solid lines refer to 10 m/s wind (at minimum and maximum incidence angles within the observed range), whereas dashed lines refer to 5 m/s (at minimum and maximum incidence angles).

Only Sentinel-1 data with adequate signal-to-noise ratios have been considered: they correspond to the centre of the EW swaths where the expected NESZ values are between -28 and -34 dB (see table 2.2). Within the wind speed range $5 \div 15$ m/s, the agreement between SSA2 model and measurements is better than 2 dB. Numerical computations of the SSA2 model with Elfouhaily and Hwang spectrum show some systematic difference:

- Within the wind speed range $5 \div 8$ m/s the Elfouhaily spectrum slightly underestimates VH-NRCS;
- Below 5 m/s the cross-polar scattering estimates associated with the two spectra are comparable;
- Above 10 m/s and up to 25 m/s the Hwang spectrum shows a better match with the measurements than the Elfouhaily one. Differences between the two spectra can reach up to 2.5 dB;
- Above 10 m/s, the rates of increase of NRCS versus the wind speed in up-wind and cross-wind cases are slightly different for the Hwang spectrum, whereas they are about the same for the Elfouhaily spectrum.

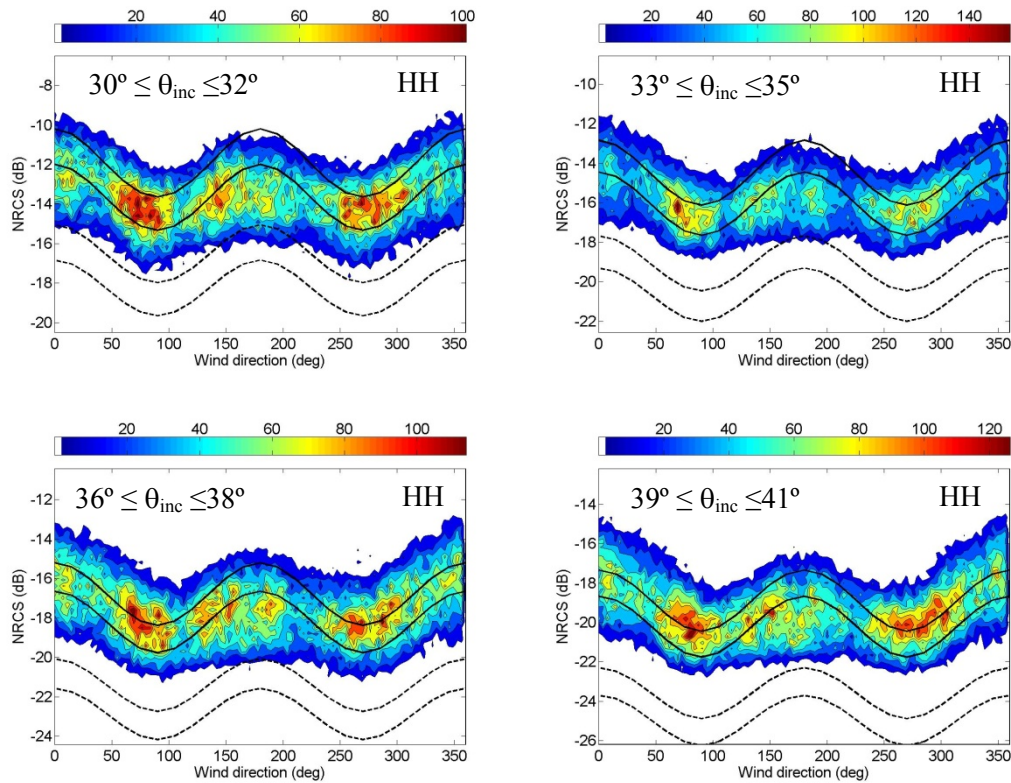


Fig. 2.15 Same as Fig. 2.14 for HH-polarization.

A clear mismatch is visible between Sentinel-1 and RADARSAT-2 noise corrected data at 20° and 24° incidence: the cross-polar backscattering coefficient for RADARSAT 2 is, in fact, systematically lower than for Sentinel-1. This effect is more evident at low wind speed and almost disappears above 29° , where the RADARSAT 2 measurements are found more consistent with Sentinel-1 data.

2.6 Conclusions

In this chapter, we provided a review of approximate scattering wave theories from random sea surfaces in a unified notation. Particular emphasis was put on the functional form of the scattering amplitude. We classified the models in three families: the high-frequency approximation (Kirchhoff and GO), the low-frequency models (SPM), and the so-called unified methods, which replace the description of the two-scale scattering mechanism with a single expression of the scattering amplitude. This expression is not only valid at the two extreme regimes, namely GO and SPM, but it is also valid between them. We tried to outline the main principles of the methods and, following the example of Elfouhaily & Guerin [2004], we attempted to evaluate the different methods according to some fundamental criteria, which are synthesized in Table 2.1.

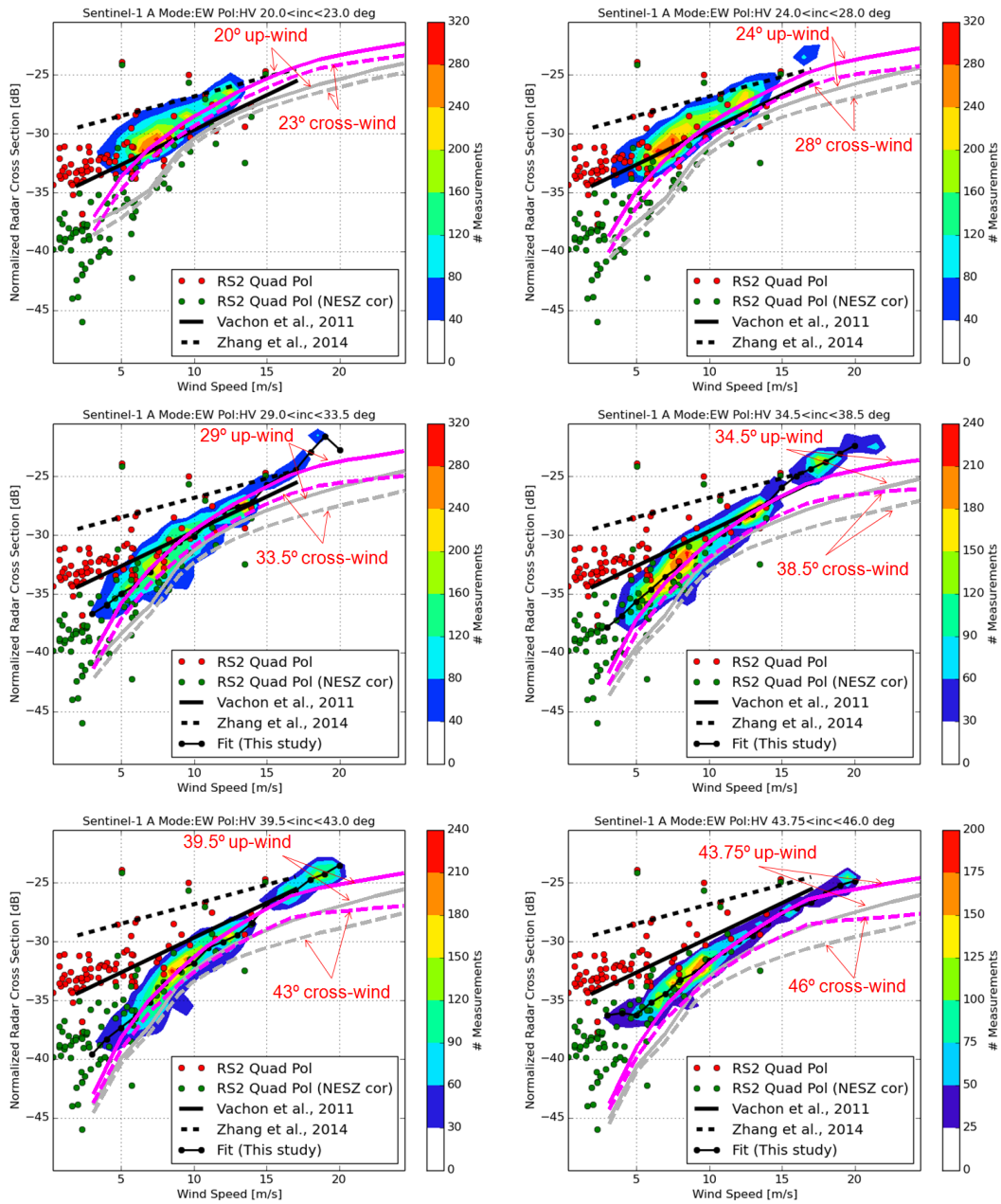


Fig. 2.16 Cloud of Sentinel-1 measurements in HV-pol versus ECMWF wind for different incidence angle ranges (20°-23°, 24°-28°, 29°-33.5°, 34.5°-38.5°, 39.5°-43°, 43.75°-46°). The colours represent the frequency of observations. Magenta and grey lines correspond to SSA2 model combined with Hwang and Elfouhaily spectrum respectively.

In addition, we made in depth comparisons between the proposed methods and empirical geophysical model functions at C, X and Ku- band. From these comparisons, it appears that only the Weighted Curvature Approximation (WCA) and the 2nd-order Small Slope Approximation (SSA2) methods satisfy the accuracy requirement and, among them, only the SSA2 provides a full polarimetric scattering matrix. We investigated the effect of different directional wave height spectra on the backscattering computation and we identified two alternative methodologies to further improve the accuracy of the

scattering computation: the first based on the inclusion of steep breaking waves in the scattering models (either WCA or SSA2), the second based on an optimization of the wave spectrum to better match well-known empirical model functions at different frequencies. We used both Envisat-ASAR and Sentinel-1 data sets, collocated with ASCAT and ECMWF winds, to verify the performance of the SSA2 model against real measurements for different wind fields, polarizations (VV, HH and VH) and incidence angles. The overall agreement between theoretical calculations and measured data is remarkable. There is still room for improvement in the development of the scattering model: among others, inclusion of foam and non linear hydrodynamic coupling between long and short waves will be discussed in the following chapters.

3 On the Use of Cross-Polar Scattering to Observe Very High Winds

This chapter investigates the potential of cross-polarization (VH) to extend the upper dynamic range of the wind measurements from ocean scatterometry. An analytical model for the VH-polar scattering of the microwave radiation from ocean is proposed. The model combines the 2nd order Small Slope Approximation Theory with the Vector Radiative Transfer Theory to obtain a statistical expression of the ocean scattering in presence of foam. Cross-polarized backscatter signals from RADARSAT-2 C-band SAR imagery, acquired during severe weather events, and collocated/time-coincident SFMR (Stepped-Frequency Microwave Radiometer) wind measurements by NOAA's hurricane-hunter aircraft are used to verify the model. The validity of the model has also been proven against ECMWF (European Centre for Medium-range Forecasts) forecasted winds. The results suggest that the present scattering model can be a valuable tool for understanding VH at very high wind speeds and for interpreting the data collected by the future dual polarimetric windscatterometer (SCA) which will be flown on the Second Generation Meteorological Operational satellite programme (MetOp-SG) [Loiselet *et al.*, 2013; Fois *et al.*, 2012] as an evolution of the ASCAT instrument on board MetOp [Edwards *et al.*, 2000; Figa-Saldaña *et al.*, 2002].

This chapter is based on the results published by the authors in [Fois *et al.*, 2014b, 2015b].

3.1 Introduction

Nowadays, coastal areas around the globe are more vulnerable to hurricanes and destructive tropical storms than ever before. This is due to the significant growth in coastal population and infrastructures. Fully formed, hurricanes may stretch over 800 km in diameter and reach a height of 15 km. Most of these storms spin out over the open sea, nevertheless, about five to ten hurricanes per year strike land, producing, very often, catastrophic damages. Most dangerous is the storm surge, a wall of water that sweeps across the coastline where the hurricane makes landfall. Only Cyclone Bhopal killed more than 300,000 people in 1970 and is among one of the deadliest natural disasters in history [Neil & Husain, 1971]. Hurricanes are also costly: in 2005, hurricane Katrina was

the most expensive natural disaster in U.S. history, causing more than hundred billion dollars worth of damages. In recent years, significant improvements in hurricane prediction have been made thanks to the use of coastal radars and instrumented aircraft. U.S. Air Force and NOAA hurricane hunter aircraft fly through the eye of the storm and drop sensors to measure wind speed, temperature and air pressure, providing vital information on hurricane structure. The planes are equipped with Stepped-Frequency Microwave Radiometers (SFMR) [Uhlhorn & Black, 2003] providing wind speeds with an accuracy of about 4 m/s across a range of measured wind speeds from 10 m/s to 70 m/s. Although SFMR is calibrated against GPS dropsondes and provides reliable estimates of sea surface winds, it has limited coverage capability, being able to take measurements only along the flight paths. On the contrary, spaceborne scatterometers measure wind fields over the worldwide oceans on a daily basis to improve weather forecasts. Current operating scatterometers use only co-polar scattering to retrieve wind speeds and directions. The main reason behind this design choice is associated with the fact that the Signal-to-Noise Ratio (SNR) in co-polarization is expected to be higher than in cross-polarization for most winds. However, airborne measurements over hurricanes, performed at C-band and Ku-band [Fernandez *et al.*, 2006], have confirmed that co-polar scattering suffers from problems of incidence- and azimuth angle-dependent signal saturation and dampening, which make it only weakly sensitive to wind speed variations above 25 m/s. This shortcoming impairs the ability to provide accurate hurricane warnings. Errors in wind sometimes prevent communities from correctly identifying the most vulnerable regions where emergency preparations are needed. Given the expense of hurricane evacuations and emergency preparations and the undermining effect of false alarms on population response, unnecessary hurricane warnings should be avoided. Recently, the analysis of RADARSAT-2 C-band SAR data and collocated wind measurements by the NOAA hurricane hunter aircraft [Van Zadelhoff *et al.*, 2014; Zhang & Perrie, 2012; Hwang *et al.*, 2010a; 2010b; 2014] have revealed that cross-polar scattering does not show any evident loss of sensitivity as the wind speed increases above 25 m/s, thus allowing accurate retrieval of strong-to-severe wind speeds. As a consequence, the use of cross-polarization in addition to the most common VV or HH polarization becomes imperative for proper hurricane forecasting with space-borne ocean scatterometers. Adequate modelling of the cross-polar scattering mechanisms from the ocean is at the basis of understanding the hurricane-force wind relationship. By comparing 19 RADARSAT-2 hurricane-images, with collocated SFMR, European Centre for Medium-range Forecasts (ECMWF) winds and in situ buoy measurements, Zadelhoff *et al.* [2014] derived a Geophysical Model Function (VH GMF). This GMF, found as

being insensitive to the wind direction and the radar incidence angle, is made of two parts (see equation 2.40): one, valid from low to high wind-speeds (up to about 18 m/s), known as Vachon and Wolfe formula [Vachon & Wolfe, 2011], the other applicable from high to extreme wind (from 18 m/s up to about 45 m/s). Theoretical derivations by Hwang *et al.* [2010b] and Voronovich *et al.* [2011], show that the cross polar signals depict an incidence angle dependence. Although, the small-slope-approximation theory (SSA2) can recover some trends of the cross-polarized backscattering, it underestimates the magnitude at very high winds. The big difference, in [Voronovich *et al.*, 2011, Fig.2], between measured and theoretical backscattering value at low wind speeds (<7 m/s) could be explained either by the limited cross-polar isolation capability of the RADARSAT-2 SAR antenna ($X_{pol} > -34$ dB) or by the low signal-to-noise ratio (SNR) in the data.

The SSA2 model does not account for foam and whitecaps generated by breaking waves, thus it is not adequate for backscattering computations at very strong winds. In fact, above 20 m/s, generated foam and spume droplets transform the near surface layer into a two-phase “liquid”, which properties (density, dielectric constant etc.) may significantly differ from the air. The aim of this chapter is to establish a physically-based model for the description of the sea-surface cross-polar scattering with potential for high wind applications. In the present work, the relative contributions of foam and surface roughness on VH-NRCS (Normalized Radar Cross Section) are analyzed over a wide range of wind speeds and directions. In section 3.2, the influence of wind on sea surface roughness and whitecap coverage is described together with the dielectric properties of foam, foam thickness, air void fraction and bubble sizes. In Section 3.3, a mathematical formulation of the scattering model is presented. In Section 3.4 numerical results are compared with real data from RADARSAT-2, Sentinel-1 and with the VH GMF. A parametric analysis of the model is performed together with an assessment of the saturation and damping of both co-polar and cross-polar signals. Section 3.5 addresses some further improvements of the model which will be considered more in depth in future works on the subject.

3.2 Properties of the Ocean Sea Surface

3.2.1 Properties of the rough ocean surface

In this chapter we use the Elfouhaily unified spectrum [Elfouhaily *et al.*, 1997], discussed in chapter 2, to describe the 2-dimensional properties of the rough ocean surface.

3.2.2 Properties of the sea foam

The sea-foam definition includes, in a broad sense, both whitecaps on the sea surface and bubble plumes under the surface. Anguelova gave a detailed definition of sea-foam in [Anguelova & Gaiser, 2013]. The foam is described as a vertical structure comprising: large thin-walled bubbles with high air content (dry-foam), close to the air-foam interface, and smaller thick-walled bubbles with high water content (wet-foam), close to the sea-water boundary. The key parameters describing the sea foam are: the air void fraction f_a (defined as the fraction of a unit volume of seawater that is occupied by air), the foam layer thickness δ , the bubble radius r_s , and the number of bubbles per unit volume N . Sea foam layer thicknesses vary from a few centimetres up to a few meters in active whitecaps, and from decimetres down to a few centimetres when the whitecaps decay. Our model refers to [Reul & Chapron, 2003] to compute the foam-layer dynamics. For the computation of the dielectric constant of sea foam, ε_f , at microwave frequencies we refer to the *Polder-van Santen* formulation [Anguelova, 2008]:

$$\varepsilon_f = \varepsilon_e + 3f_v \varepsilon_e \frac{\varepsilon_i - \varepsilon_e}{\varepsilon_i + 2\varepsilon_e - f_v(\varepsilon_i - \varepsilon_e)}. \quad (3.1)$$

Here, ε_e and ε_i are environment and inclusions permittivities, whereas f_v is the inclusion volume fraction. Breaking ocean waves entrain air bubbles that contribute to the volume scattering mechanism. The size distribution of the entrained bubbles is an important factor in controlling the foam scattering process, but little is known about bubble properties and formation mechanisms inside whitecaps. On the basis of recent laboratory and field measurements, we consider bubbles with radii r_s , from 0.05 mm to 10 mm [Militskii *et al.*, 1977; Guo *et al.*, 2001; Deane and Stokes, 2002; Anguelova and Gaiser, 2012], with a broad peak around radii of 0.05 mm and 2 mm.

We model the foam scatterers as spherical Rayleigh bubbles with a radius r_s , a dielectric constant $\varepsilon_i = \varepsilon_{ir} - j \varepsilon_{ii}$, and volume fraction f_v , embedded in a medium with a dielectric constant $\varepsilon_e = \varepsilon_{er} - j \varepsilon_{ei}$. The foam layer can be characterized by an absorption coefficient κ_a , and a volume scattering coefficient κ_s , given by the following expressions [Fung & Chen, 2010]:

$$\kappa_a = 2k_{ei}(1 - f_v) + f_v k_{er} \frac{\varepsilon_{ii}}{\varepsilon_{er}} \left| \frac{3\varepsilon_e}{\varepsilon_i + 2\varepsilon_e} \right|^2, \quad (3.2)$$

where k_{er} and k_{ei} are the real and imaginary parts of the host medium wave number, $k(\varepsilon_e)^{0.5}$, and k is the wave number in free space;

$$\kappa_s = \frac{8\pi}{3} N k_{er}^4 r_s^6 \left| \frac{\varepsilon_i - \varepsilon_e}{\varepsilon_i + 2\varepsilon_e} \right|^2, \quad (3.3)$$

where N is the number of bubbles per unit volume, that is related to the volume fraction, f_v , by: $N = 3 f_v / (4\pi r_s^3)$. For sea foam, we assign seawater as environment and air bubbles as inclusions thus, $\varepsilon_e = \varepsilon$ (sea water permittivity), $f_v = f_a$ and $\varepsilon_i = \varepsilon_0 = 1$. Assuming a monotonic change in void fraction with depth, as presented by Angeluova *et al.* [2013], we choose to use an exponential void fraction profile:

$$f_a(z) = a_v - m \cdot e^{b_v \cdot z}, \quad (3.4)$$

with

$$\begin{cases} a_v = v_{af} + m \\ b_v = \frac{1}{d} \cdot \ln\left(\frac{a_v - v_{fw}}{m}\right) \end{cases}. \quad (3.5)$$

Here, m is a parameter that controls the shape of the profile, d is the foam thickness. Coefficients a_v and b_v are determined from the following boundary conditions: $f_a(0) = a_v$ and $f_a(d) = b_v$, where v_{af} and v_{fw} are the void fractions at the air–foam and foam–water boundaries. Figure 3.1a depicts the variation of air content in depth of 10 cm foam layer for an exponential profile ($m=1$). Figure 3.1b shows the real and imaginary part of the foam dielectric constant as function of the air content, at C-band (5.4 GHz) for seawater at 20°C and 34 psu salinity. Figure 3.1c displays how the volume scattering (solid-blue), the absorption (dashed-red) and extinction coefficients vary with f_a . Using well known relationships from electromagnetic theories, the foam penetration depth, d_{fp} , can be derived from the following integral equation [Anguelova & Gaiser, 2011]:

$$\int_0^{d_{fp}} \kappa_e(z) dz = 1, \quad (3.6)$$

where $\kappa_e = \kappa_s + \kappa_a$ is the power extinction coefficient. In the simple case of κ_e constant with z , one gets:

$$d_{fp} = 1/\kappa_e . \quad (3.7)$$

As discussed in [Anguelova and Gaiser, 2011; 2012], the limited foam skin depth and penetration depth at microwave frequencies, narrows our interest to only floating foam layers, excluding deeper bubble plumes. As described in section 3.3, for an adequate representation of the scattering mechanism from foam, we will consider an electromagnetic wave incident on a slab of random scatterers overlying a homogeneous half-space with a randomly rough surface (i.e. the rough sea surface).

There are several empirical models which express the percentage of whitecap coverage as function of the wind speed, among them we recall the model proposed by Reul and Chapron in [2003], expressing the sea foam coverage as function of the wind speed at the reference height 10 m:

$$F(U_{10}) = \left[\int_{c_{min}}^{c_p} \tau \cdot c \Lambda(c, U_{10}) dc \right] \times e^{(\alpha \Delta T - \beta)} . \quad (3.8)$$

where c is the velocity of the waves carrying a whitecap. The distribution function Λc represents the average length per unit surface area of breaking fronts moving with velocities in the range c to $c + dc$; $\tau = 2\pi a c / g$ is the persistence time of foam layers at the surface, where a is a constant of proportionality and g the acceleration due to gravity. When the foam layer persistence time is shorter than the duration of active breaking event, i.e. $a \leq 0.8$, only crest-foam contributes to the computation of the whitecap coverage; if, instead, $a > 0.8$, only static foam type is considered in the coverage model. ΔT is the difference between the sea temperature and the air temperature in °C, whereas α and β are constants, which values are different for crest (0.198, 0.91) and static (0.0861, 0.38) type of foam. The exponential term in equation (3.8) is an empirical correction factor for atmospheric stability impact. The integral in (3.8) is restricted to waves faster than $c_{min} = (g \lambda_{min} / 2\pi)^{0.5}$ and slower than the phase speed at the peak of the wave spectrum, c_p . In the present work, we refer to the unified Elfouhaily wave spectrum [Elfouhaily *et al.*, 1997], whose development was based on available field and wave-tank measurements along with physical arguments. In our simulation we only consider waves longer than 15 cm. Depending on the choice of the function Λ , Reul and Chapron [2003] assessed the capability of equation (3.8) to accurately forecast the whitecap coverage as function of wind speed. In particular, Reul and Chapron [2003] showed that the Melville and Matusov model performs well for both “*dynamic foam*” (or “*crest foam*”) coverage

corresponding to breaking wave crests, and the “static foam” coverage corresponding to older foam that remains in the wake of a breaker.

An important parameter which is directly related to the overall impact of the foam thickness on microwave backscattering as function of wind speed is the foam-layer thickness ($\bar{\delta}_\tau$) weighted by the corresponding surface foam coverage and averaged over all breaking wave scales for a given wind:

$$\hat{\delta}_\tau(U_{10}) = \int_{\delta_{\min}}^{\delta_p} \bar{\delta}_\tau \cdot dF(\bar{\delta}_\tau, U_{10}). \quad (3.9)$$

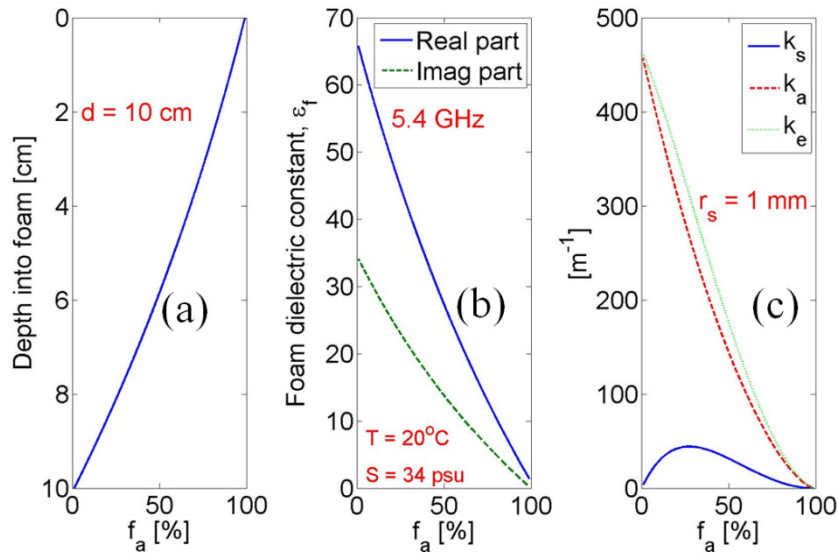


Fig.3.1. a) Air void fraction profile versus depth into the foam; b) foam dielectric constant versus air void fraction; c) volume-scattering, absorption and extinction coefficients versus air void fraction.

3.3 Description of the Scattering Model

3.3.1 Scattering from a Rough Ocean Surface

We base the computation of the microwave scattering from a rough ocean surface, on the 2nd order Small Slope Approximation (SSA2) theory [Voronovich, 1994], which has been deeply discussed in section 2.3.6. At the top of Fig. 3.2, from the left to the right side, we report the SSA2-Normalized Radar Cross Section at C-band (5.4 GHz) versus the incidence angle for three different wind speeds 5, 10 and 15 m/s (up-wind cases). At the bottom of the same figure, we show the behaviour of the NRCS versus the wind direction at 37.5° incidence and wind speeds of 5, 15 and 25 m/s.

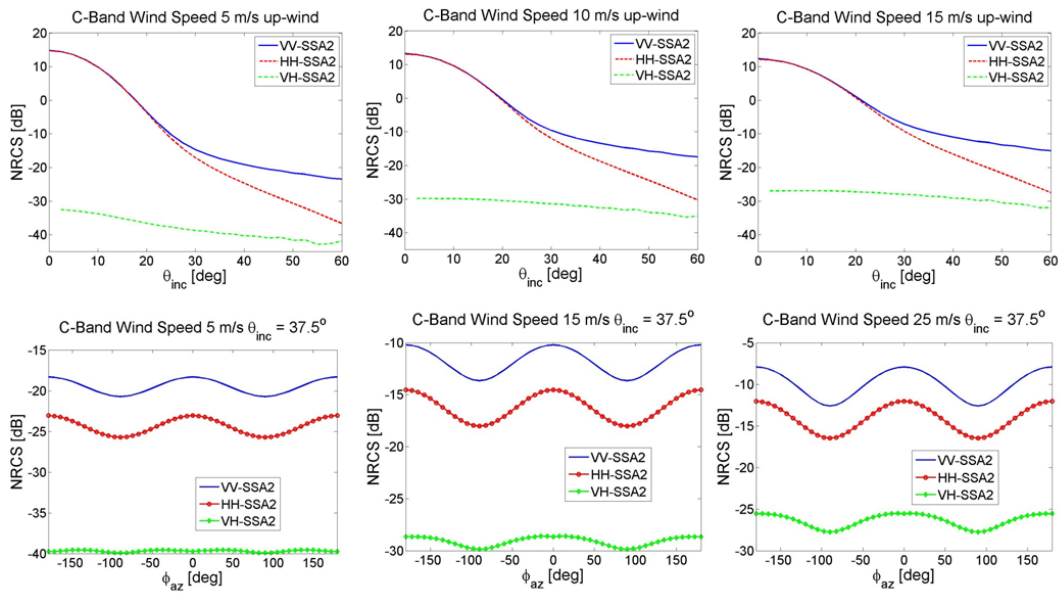


Fig.3.2. SSA2 Normalized Radar Cross section at C-band (5.4 GHz). The top figures, from the left to the right side, depict the NRCS behaviour versus the incidence angle for 5, 15 and 25 m/s up-winds respectively; whereas the bottom figures depict the NRCS behaviour versus the wind direction at 37.5° incidence for wind speeds of 5, 15 and 25 m/s.

One can see that the cross-polar scattering is less sensitive to the incidence angle than the co-polar scattering. For instance, in the case of 10 m/s up-wind, the NRCS in VH-polarization shows only 5 dB dynamic range for incidence angles varying from 0° up to 60° : this is a quite small number when compared to the 30-40 dB dynamic range of VV and HH-polarization. The cross-polar scattering does not show any clear specular contribution. The behaviour of the cross-polar scattering with the wind direction looks different from the co-polar one. Co-polar signals experience stronger modulation with the wind direction than the cross-polar signals: this is particularly evident at low incidence angles and low wind speeds. The directional variation of VH NRCS is wind speed dependent and incidence angle dependent. For a wind speed of 5 m/s, the peak-to-peak scattering modulation of VH-polarization, induced by the wind direction, is only 0.1 dB at 22.5° and 0.4 dB at 37.5° (see Fig. 3.2): these are relatively small numbers when compared to the peak-to-peak modulation of VV and HH polarizations (in the order of 3-5 dB). For a wind speed of 25 m/s, instead, the peak-to-peak scattering modulation of VH-polarization is about 1 dB at 22.5° and 2 dB at 37.5° . In summary:

- the higher the wind speed the higher the directional variation of VH NRCS;
- the higher the incidence angle the higher the directional variation of VH NRCS.

3.3.2 Scattering from Sea Foam

At high wind speed conditions, generated foam and whitecaps associated with intensive breaking of waves become a dominant surface feature, which is not taken into account in the SSA2 model. In this section, we discuss the scattering from a layer of Rayleigh scatterers sitting above the rough sea surface and representing the foam. The geometry of the problem is shown in Fig.3.3.

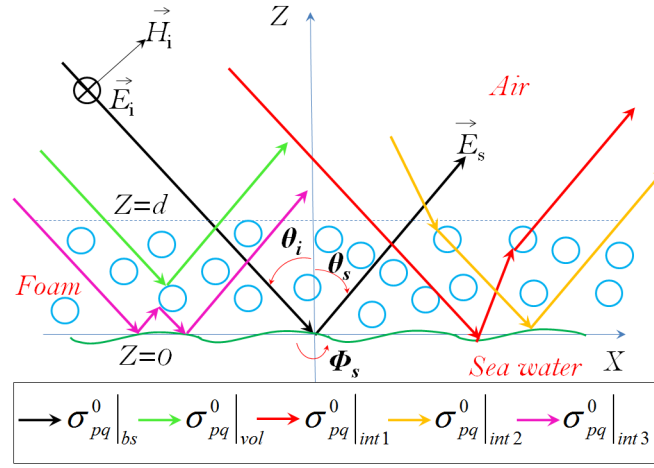


Fig.3.3. Geometry of the foam scattering problem.

According to [Huang & Jin, 1995], we identify five major contributing terms to the total scattering from a Rayleigh layer. The first term represents scattering from the bottom surface. It is indicated as $\sigma_{pq}^0|_{bs}$, where p and q denote vertical or horizontal polarization, respectively. It represents the following processes: the incident intensity passes through the foam and is attenuated by the layer before reaching the bottom boundary, where it is scattered and goes through layer attenuation again before it goes ahead into the observed direction. The expression of $\sigma_{pq}^0|_{bs}$ is:

$$\sigma_{pq}^0(\mathbf{k}_s, \mathbf{k}_i)|_{bs} = \sigma_{pq}^0(\mathbf{k}_s, \mathbf{k}_i)|_{SSA2} \exp[-\kappa_e d(\sec\theta_i + \sec\theta_s)] \quad (3.10)$$

The second term, $\sigma_{pq}^0|_{vol}$, is due to volume scattering from the layer:

$$\begin{aligned}
\sigma_{pq}^0(\mathbf{k}_s, \mathbf{k}_i) \Big|_{vol} = & \\
\frac{4\pi \cos \theta_s}{\kappa_e \cos \theta_i} \exp[-\kappa_e d(\sec \theta_i + \sec \theta_s)] & \\
\times P_{pq}(\theta_s, \phi_s; \pi - \theta_i, \phi_i) \{ \exp[-\kappa_e d(\sec \theta_i + \sec \theta_s)] - 1 \} & \quad (3.11)
\end{aligned}$$

We have modeled the foam scatterers as spherical Rayleigh particles with phase functions, P_{pq} , given in [Tsang *et al.*, 1985; section 3.2 pag.132]. The third term, $\sigma_{pq}^0|_{int-1}$, represents volume-surface interaction when the bottom surface has a significant reflectivity. The incident intensity goes through volume scattering, attenuation by the foam layer, reflection by the bottom rough sea surface, attenuation by the layer again, and transmission into the direction of observation. The expression of the third term is:

$$\begin{aligned}
\sigma_{pq}^0(\mathbf{k}_s, \mathbf{k}_i) \Big|_{int-1} = & \\
\frac{4\pi \cos \theta_s}{\kappa_e \cos \theta_i} \exp[-\kappa_e d(\sec \theta_i + \sec \theta_s)] & \\
\times \int_0^{\pi/2} d\theta' \sin \theta' \int_0^{2\pi} d\phi' \sum_{t=v,h} P_{pt}(\theta_s, \phi_s; \theta', \phi') R_{iq}(\theta', \phi'; \theta_i, \phi_i) & \quad (3.12) \\
\times \frac{\sec \theta_s}{\sec \theta' - \sec \theta_s} \{ 1 - \exp[-\kappa_e d(\sec \theta' - \sec \theta_s)] \} &
\end{aligned}$$

The order of reflection and volume scattering can be reversed leading to the fourth contributing term, $\sigma_{pq}^0|_{int-2}$:

$$\begin{aligned}
\sigma_{pq}^0(\mathbf{k}_s, \mathbf{k}_i) \Big|_{int-2} = & \\
\frac{4\pi \cos \theta_s}{\kappa_e \cos \theta_i} \exp[-\kappa_e d(\sec \theta_i + \sec \theta_s)] \times & \\
\int_0^{\pi/2} d\theta' \sin \theta' \int_0^{2\pi} d\phi \sum_{t=v,h} R_{pt}(\theta_s, \phi_s; \pi - \theta', \phi') P_{iq}(\pi - \theta', \phi'; \pi - \theta_i, \phi_i) & \quad (3.13) \\
\times \frac{\sec \theta'}{\sec \theta' - \sec \theta_i} \{ 1 - \exp[-\kappa_e d(\sec \theta' - \sec \theta_i)] \} &
\end{aligned}$$

The last scattering term, $\sigma_{pq}^0|_{int-3}$, is generated by the following mechanism: the incident intensity is attenuated by the foam layer before reaching the bottom boundary. Here it is first scattered, then volume scattered before reflection by the bottom rough surface, attenuation by the layer and transmission into the direction of observation:

$$\begin{aligned}
\sigma_{pq}^0(\mathbf{k}_s, \mathbf{k}_i) \Big|_{\text{int-3}} = & \\
\frac{4\pi \cos \theta_s}{\kappa_e \cos \theta_i} \exp[-\kappa_e d (\sec \theta_i + \sec \theta_s)] \times & \\
\int_0^{\pi/2} d\theta' \sin \theta' \int_0^{2\pi} d\phi' \sum_{l=v,h} R_{pl}(\theta_s, \phi_s; \pi - \theta', \phi') \int_0^{\pi/2} d\theta'' \sin \theta'' \cdot & \quad (3.14) \\
\int_0^{2\pi} d\phi'' \sum_{l=v,h} P_{il}(\pi - \theta', \phi'; \theta'', \phi'') R_{lq}(\theta'', \phi''; \theta_i, \phi_i) & \\
\times \frac{\sec \theta'}{\sec \theta' + \sec \theta''} \{1 - \exp[-\kappa_e d (\sec \theta' + \sec \theta'')]\} &
\end{aligned}$$

In equations (3.10)-(3.14) the elements R_{pq} can be expressed as a function of the bistatic scattering coefficient:

$$R_{pq}(\theta, \phi; \theta', \phi') = \frac{1}{4\pi} \sigma_{pq}^0(\theta, \phi; \theta', \phi') \Big|_{SSA2} \frac{\cos \theta'}{\cos \theta}. \quad (3.15)$$

With reference to Fig. 3.3, we will focus on the backscattering case that is identified by the following relationships: $\theta_s = \theta_i$, $\phi_s = 180^\circ$ and $\phi_i = 0^\circ$.

3.3.3 Complete Scattering Model

For a sea surface with static-foam coverage F_S and crest-foam coverage F_C , the total scattering coefficient is given by:

$$\begin{aligned}
\sigma_{pq}^0 \Big|_{\text{Total}} = (1 - F_S - F_C) \sigma_{pq}^0 \Big|_{SSA2} + & \\
F_S \sigma_{pq}^0 \Big|_{\text{static-foam}} + F_C \sigma_{pq}^0 \Big|_{\text{crest-foam}} & \quad (3.16)
\end{aligned}$$

where $\sigma_{pq}^0 \Big|_{\text{static-foam}}$ and $\sigma_{pq}^0 \Big|_{\text{crest-foam}}$ are both sum of five scattering contributions as described in section-3.3.2. Figure 3.4a shows both static and dynamic foam coverage as function of the wind speed for two different values of ΔT ; the corresponding average weighted thicknesses are depicted in Fig. 3.4b.

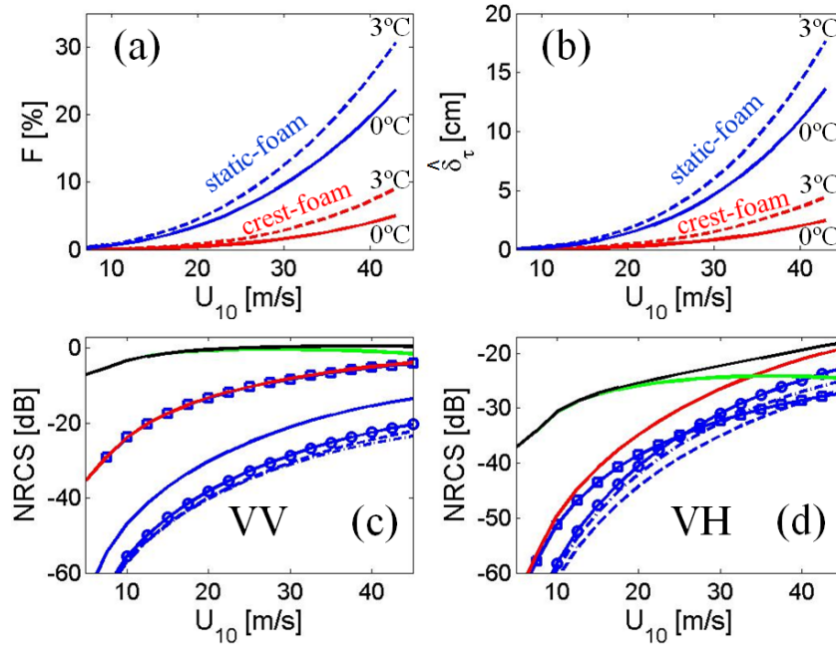


Fig. 3.4. a) Static (blue) and crest (red) foam coverage for $\Delta T=3^{\circ}\text{C}$ (dashed lines) and $\Delta T=0^{\circ}\text{C}$ (solid lines); b) weighted average thickness of static and crest-foam; c) and d) Scattering contributions in VV-and VH polarizations versus wind speed at 22.5° incidence, up-wind direction: $F_c\sigma^{\circ}|_{bs-crest}+F_s\sigma^{\circ}|_{bs-static}$ (blue-lines with squares), $F_c\sigma^{\circ}|_{vol-crest}+F_s\sigma^{\circ}|_{vol-static}$ (solid blue-lines), $F_c\sigma^{\circ}|_{int1-crest}+F_s\sigma^{\circ}|_{int1-static}$ (blue-dashed lines), $F_c\sigma^{\circ}|_{int2-crest}+F_s\sigma^{\circ}|_{int2-static}$ (blue-lines with circles), $F_c\sigma^{\circ}|_{int3-crest}+F_s\sigma^{\circ}|_{int3-static}$ (blue-dashed dotted lines), $(1-F_c-F_s)\sigma^{\circ}|_{SSA-2}$ (green lines), foam total scattering (red lines), foam+surface total scattering (black-lines).

Although crest-foam is thicker than the static-foam, the corresponding $\hat{\delta}_t$ is smaller than for static foam because of the smaller coverage. Figure 3.4c and 3.4d show the different C-band scattering contributions in VV and VH polarization versus the wind speed (upwind) in the case of $\theta_{inc}=22.5^{\circ}$, $\Delta T=3^{\circ}\text{C}$, $r_s=2\text{mm}$ and $f_a=0.98$ (dry-foam). These two figures show that:

- In VV-polarization, the scattering from the bottom surface (blue-line with squares) is the most dominant foam scattering contributor. The difference between bottom surface scattering and volume scattering (blue curve) is higher than 20 dB at low wind speeds. This difference decreases (down to about 10 dB) as the wind speed increases.
- In VV-polarization, the volume scattering from the spherical bubbles is about 5÷10 dB higher than the scattering generated by volume-surface interactions ($\sigma_{pq}^{\circ}|_{int-1}$, $\sigma_{pq}^{\circ}|_{int-2}$, and $\sigma_{pq}^{\circ}|_{int-3}$).
- In VH-polarization, the scattering from the bottom surface is the dominant foam scattering contributor at low wind speeds and the weakest contributor at very strong wind speeds.

- d) In VH-polarization, the blue line corresponding to volume scattering is very small and thus out of the plotting range. This does not surprise, as the spherical scatterers give small cross polarization in the plane of incidence.
- e) In VH-polarization, the surface scattering $(1-F_c-F_s) \sigma^{\circ}|_{SSA-2}$ saturates above 30 m/s, whereas the foam scattering term steadily increases, thus becoming the dominant scattering process above 33 m/s. By adding the foam scattering to the surface scattering, the resulting NRCS does not show any loss of sensitivity to the wind above 30 m/s (black line in the plot).
- f) The effect of foam on VV NRCS is less evident than for VH NRCS because of two main reasons. The first reason is that the foam scattering process is largely dominated by the bottom surface scattering, that is less sensitive to wind than the other foam scattering mechanisms (i.e. volume and volume-surface scattering). The second reason, is that the surface scattering is always higher than the foam scattering.

3.4 Observing Systems and Measurement Campaigns

3.4.1 RADARSAT-2 Hurricane Campaigns

Recently, a number of papers [Zhang *et al.*, 2011; Zhang & Perrie, 2011; Hwang *et al.*, 2010; Vachon and Wolfe, 2011; van Zadelhoff *et al.*, 2013, 2014] have been published on the use of cross-polar (VH or HV) scattering to observe and retrieve high winds. These papers are based on data acquired by the RADARSAT-2 satellite. RADARSAT-2 was launched in December 2007 by the Canadian Space Agency. The satellite deploys a C-band multi-polarimetric SAR [Slade, 2009]. A fully polarimetric mode of acquisition, called Fine Quad Pol Mode, is available. In this mode, the radar alternates Tx-pulses in horizontal and vertical polarizations, and receives simultaneously echoes from each pulse in both polarizations. A swath width of 25 km can be accessed within the incidence angle range $18^{\circ} \div 49^{\circ}$. The ground resolution of the fine-quad pol products is $16.5 \div 6.8 \times 7.6 \text{ m}^2$ (i.e. across-track \times along-track resolution), the Noise Equivalent Sigma Zero (NESZ) ranges between -39 dB (at 18° incidence) and -31 dB (at 49° incidence), whereas the cross-talk is lower than -32 dB.

The ScanSAR beam modes of RADARSAT-2 provide images of large areas mainly for monitoring applications. In the ScanSAR modes a number of antenna beams (two, three or four) are used in combination. The wide swath of the ScanSAR modes is paid by a coarser spatial resolution.

The widest ScanSAR swath has a nominal width of 500 km, an imaging resolution of $163 \div 73 \times 100 \text{ m}^2$ with 4×2 looks. In ScanSAR modes, only a single polarization is transmitted whereas two polarizations are simultaneously received (VV and VH, or HH and HV). The associated noise floor is significantly higher ($-30 \text{ dB} < \text{NESZ} < -25 \text{ dB}$) than the one of the fine-quad polarization mode. In order to verify the scattering model described in section 3.3, Fine Quad Pol data and ScanSAR wide swath data, acquired over several Hurricanes, are used in combination with collocated wind velocity measurements from various sources such as: SFMR [van Zadelhoff *et al.*, 2013, 2014] and ECMWF simulations [van Zadelhoff *et al.*, 2013, 2014].

3.5 Numerical Results and Comparison with Measurements

3.5.1 Wind Speed Dependence

Results of numerical simulations for the co-polarized and cross-polarized NRCS, as function of the wind speed, are depicted in Fig. 3.5a and 3.5b for two different wind directions, corresponding to up-wind (solid-lines) and cross-wind (dashed-lines) cases. The void fraction, f_a , is 0.98, the foam bubble radius, r_s , is 2 mm and $\Delta T=3^\circ\text{C}$. Four incidence angles are analyzed: 22.5° (blue), 27.5° (green), 32.5° (red) and 37.5° (cyan). These angles are consistent with the mean incidence angles analyzed in [van Zadelhoff *et al.*, 2014; Hwang *et al.*, 2014a, 2015] where RADARSAT-2 data (covering the range $20^\circ\div 40^\circ$) were sorted into incidence angle bins, with 5° bin width. Figure 3.5c compares the modelled cross-polar NRCS with (SSA2+Radiative Transfer Theory) and without (SSA2 alone) the inclusion of foam. It can be seen that scattering from foam is significant, especially above 25 m/s wind speed, becoming the dominant scattering mechanism above 33 m/s, as shown in Fig. 3.4d (red curve). Figure 3.5d shows the effect of changes in ΔT (red lines) and r_s (blue lines) on VH σ° . Here, ΔT is increased from 0°C to 9°C with 3°C step, and r_s is increased from 0.5 mm to 2 mm with 0.5 mm step. The slope of VH σ° versus U_{10} (wind speed at 10 m height) becomes steeper as ΔT or r_s increases. It is worth noting that surface layer conditions are generally well mixed in hurricanes and vertical temperature gradients are unlikely.

Fig. 3.6 provides the distribution of all retrieved SFMR wind speeds versus collocated VH RADARSAT-2 measurement points from 9 hurricanes listed in [van Zadelhoff *et al.*, 2014; Table-I]. The different colours in the plot refer to different median incidence angles. Overlaid are our simulated cross-polar VH-NRCS, obtained (for the 4 median incidence angles) in both up-wind and cross-wind configurations, and VH-GMF (in red).

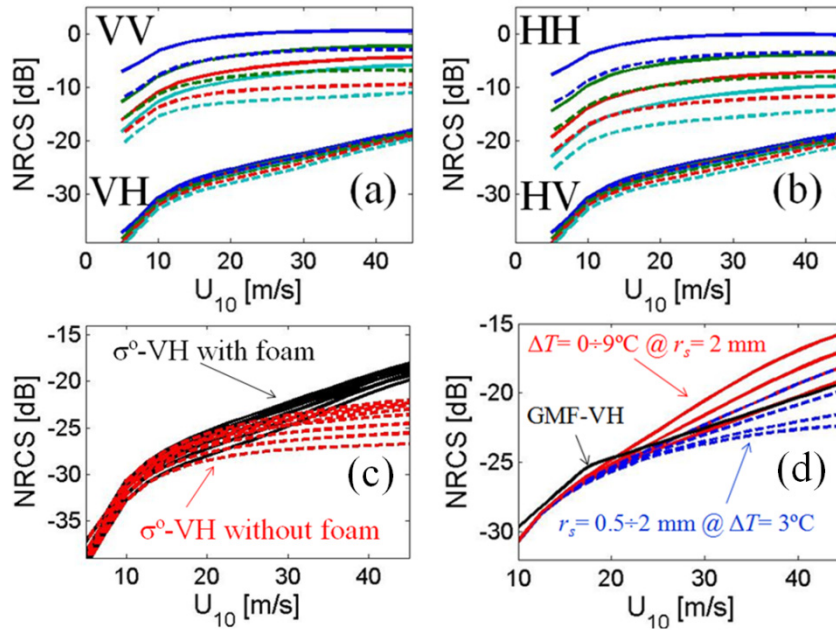


Fig. 3.5. a) and b) Normalized radar cross-section in VV, VH, HH and HV pol from the numerical scattering model with $\Delta T=3^\circ\text{C}$, $r_s=2\text{mm}$ and $f_o=0.98$. Solid and dashed lines refer to upwind and crosswind cases respectively. Four different incidence angles are investigated: 22.5° , 27.5° , 32.5° and 37.5° . c) Comparison of the modelled cross-polar NRCS with and without foam for the case $\Delta T=3^\circ\text{C}$, $r_s=2\text{mm}$ and $f_o=0.98$. d) Effect of ΔT variations (red lines) and r_s variations (blue dashed lines) on σ^o -VH and comparison with GMF-VH (in black).

In a similar way, Fig. 3.7 depicts the VH measurements collected by RADARSAT-2 over 19 hurricanes versus forecasted ECMWF wind speeds. This figure shows a clear incidence angle relationship with the highest incidence angles at lowest backscatter values. The agreement between real measurements and simulated results, obtained with the total scattering model reported in equation (3.15), is very promising and demonstrates the importance of the effect of scattering from dry foam in the computation of the cross-polar NRCS.

3.5.2 Wind Direction Dependence

The modulation of the VH NRCS with wind direction has been a point of interesting discussions in [van Zadelhoff *et al.*, 2013, 2014; Hwang *et al.*, 2014, 2015; Hwang, 2013; Horstmann *et al.*, 2014]. In [van Zadelhoff *et al.*, 2014], the wind direction dependence is performed by comparing the VH measurements to the NWP (Numerical Weather Prediction) model calculations and wind retrievals from the VV GMF. These comparisons present both positive and negative associated aspects. The VV wind retrievals are perfectly collocated to the VH observations but have wind speed sensitivity issues beyond 25 m/s.

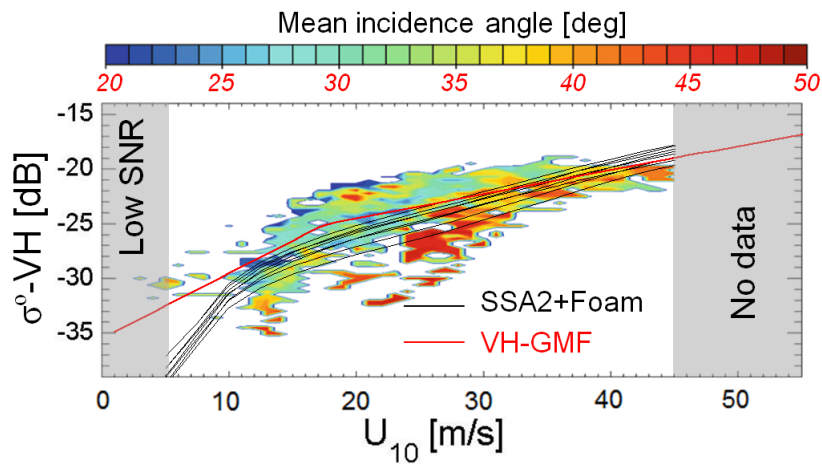


Fig. 3.6. Distribution of all retrieved SFMR wind speeds versus collocated VH measurement points from 9 RADARSAT-2 hurricane images [van Zadelhoff *et al.*, 2014]. The red line shows the VH-GMF. Overlaid are the simulated cross-polar NRCS (in black) obtained in both up-wind and cross wind for four median incidence angles: 22.5°, 27.5°, 32.5° and 37.5°.

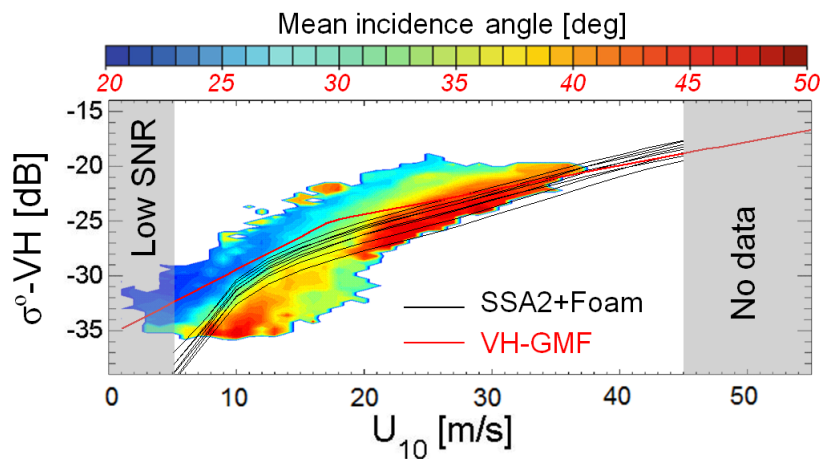


Fig. 3.7. Distribution of all forecasted ECMWF wind speeds versus collocated VH measurements from 19 hurricane RADARSAT-2 images [van Zadelhoff *et al.*, 2014]. The red line shows the VH-GMF. Overlaid are the simulated cross-polar NRCS (in black) obtained in both up-wind and cross-wind for four median incidence angles: 22.5°, 27.5°, 32.5° and 37.5°.

On the contrary, a global NWP model (in this case the ECMWF model) has a resolution coarser than RADARSAT-2 and needs correction for space/time collocation differences with RADARSAT-2.

As a result of an in-depth trade-off analysis, Zadelhoff *et al.* conclude on the basis of the ECMWF model and VV retrieved winds that there is no or very weak wind direction dependence in the VH backscattered signals. In fact, the ECMWF data reproduce the wind direction dependency of VV, whereas, for the same data sample, no VH wind direction dependency is found.

On the basis of collocated buoy and RADARSAT-2 measurements, instead, Hwang *et al.* [2014] found that the directional signature of cross-polar scattering was as strong as (or even stronger than) that of the co-polar scattering. To better understand the physics

behind this controversial discussion, we refer to the clouds of RADARSAT-2 measurements collected in VV and VH polarizations between 30° and 35° incidence and corresponding to wind speeds within the range $10 \div 15$ m/s. In Fig. 3.8 the data are depicted with respect to the ECMWF wind direction. The two solid lines and the two dashed lines shown in the same figure are the simulated VH NRCSs for 15 m/s (solid lines) and 10 m/s (dashed lines) wind speeds at the incidence angles of 30° and 35° . The agreement between real data and simulations is remarkable. Our scattering model confirms that the wind direction dependence of the VH NRCS is much weaker than the one of VV NRCS. It is also clear that the big spread in VH backscattering is mostly associated with changes in wind speed. For this specific study case, in fact, a jump of 5 m/s in wind speed implies a jump of about 4 dB in NRCS.

Changes in wind direction, instead, generates only a weak modulation of the NRCS, which is estimated to be less than 1 dB.

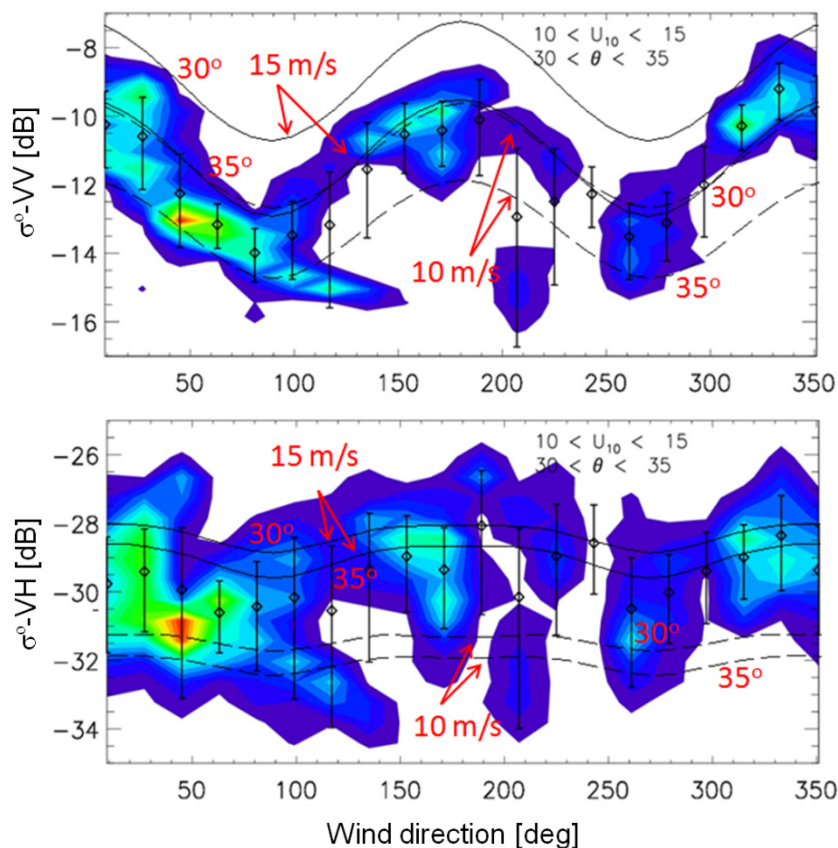


Fig. 3.8. Clouds of RADARSAT-2 measurements collected in VV and VH-polarizations between 30° and 35° incidence and corresponding to wind speeds within the range $10 \div 15$ m/s. Overlaid are the simulated NRCS: solid lines refer to 15 m/s wind (at 30° and 35° incidence), whereas dashed lines refer to 10 m/s (at 30° and 35° incidence).

3.5.3 The Importance of 2nd Order Bragg Effects

It is not yet clear why the cross-polar scattering is less sensitive to the wind direction than the co-polar scattering. To this aim, we have made some investigation on the Small Slope Approximation theory. The SSA2 always accounts for Bragg scattering of the second order. As explained in [Voronovich & Zavorotny, 2011], it is possible to identify the 2nd order Bragg terms that are responsible for a departure of the SSA2 from the Composite Bragg (CB) theory. By quitting these terms one may obtain the SSA2-0 model that is an approximation of the CB model. As depicted in Fig. 3.9 for the case of 5 m/s wind and 22.5° incidence, the wind direction dependence of SSA2-0 and SSA2 is very different. The SSA2-0 shows a much stronger modulation of the NRCS with the wind direction and weaker backscattering in comparison with the SSA2 model. This demonstrates how important is the inclusion of second-order Bragg scattering for a proper description of the cross-polar NRCS.

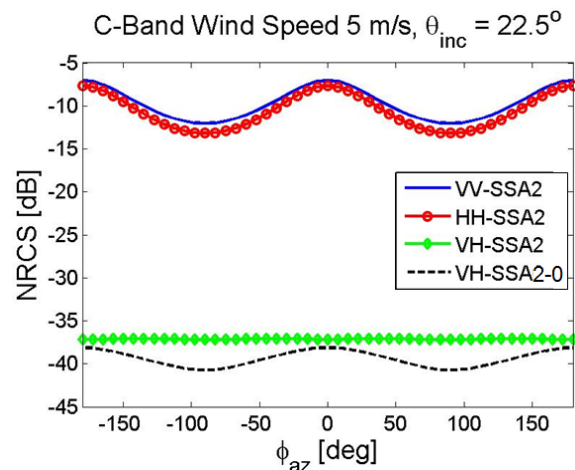


Fig. 3.9 Dependence of NRCS on wind direction in C-band for 5 m/s wind and 22.5° incidence.

3.5.4 Full-polarimetric Signal Saturation

The effect of foam on co-polar and cross-polar C-band signal saturation above 25 m/s has been assessed for four different foam coverage models [Monahan & Woolf, 1989; Monahan & O’Muircheartaigh, 1980; Bondur & Sharkov 1982; Melville & Matusov, 2002]. Figure 3.10 is just an extract of our analysis: here, we depict the difference $\sigma^\circ(U10) - \sigma^\circ(25\text{m/s})$ (in dB) versus the wind speed (in logarithmic scale), for four incidence angles (in blue 29°, in green 34°, in red 40° and in cyan 50°) and polarizations (VV, HH, VH and HV). Solid lines correspond to up-wind cases whereas dashed lines

correspond to cross-wind cases. The wind speed has been increased from 25 m/s up to 70 m/s. These plots show that:

- a) For the co-polar cases the wind speed sensitivity increases with the incidence angle. This particular feature is more evident in HH-pol than in VV-pol.
- b) Below 40° incidence VV and HH polarizations behave in a similar way.
- c) Beyond 40° incidence, significant differences between VV and HH-pol occur, with HH-pol being more sensitive to wind-speed increase than VV-pol.
- d) In agreement with the results reported by Fernandez *et al.* in [2006], the saturation and damping of the simulated co-polar signals occurs at wind speeds above 50 m/s in up-wind cases, and above 60 m/s in cross-wind cases.
- e) High wind speed sensitivity in cross-polarization is higher than in co-polarization, with cross-wind cases being more sensitive than up-wind cases. Hence, more accurate wind speed estimations may be expected from VH-pol.
- f) VH and HV polarizations behave in the same way in agreement with the reciprocity theorem.
- g) The effect of the incidence angle on NRCS saturation is much weaker in cross-polarization than in co-polarization.
- h) The saturation and damping of the simulated cross-polar signals occur at wind speeds above 60 m/s for all the incidence angles analyzed.
- i) The deviations associated with the use of different foam coverage models are modest and do not change the overall conclusions.

3.5.5 Future Improvements of the Model

Effects associated with rain

The eye of a hurricane acts as a partial vacuum, causing inward spiraling winds at the sea surface. These spiraling winds evaporate moisture from the warm ocean surface and eventually veer upward producing clouds and rain. Falling rain cools the air, causing downbursts of wind at the surface. The rain effect on NRCS is not considered in the present model. Rain mainly introduces wind variations (downbursts) as seen in wind fields retrieved by C-band scatterometers and SARs [Portabella *et al.*, 2012]. Ku-band scatterometers are also strongly affected by rain droplet scattering and attenuation. The winds will be underestimated if the NRCS in rainy areas is not properly corrected. In order to account for the rain effect on the radar signals, one could think to modify the sea surface spectrum as proposed by Zhang *et al.* in [2014], where the short wave part of the

spectrum is represented as the sum of three terms: the wind-driven spectrum in the gravity region (dampened by the raindrops), the spectrum in the gravity-capillary region and the rain-generated ring wave spectra. The analysis of the rain effects on the simulated radar backscattering from ocean is left to future dedicated papers.

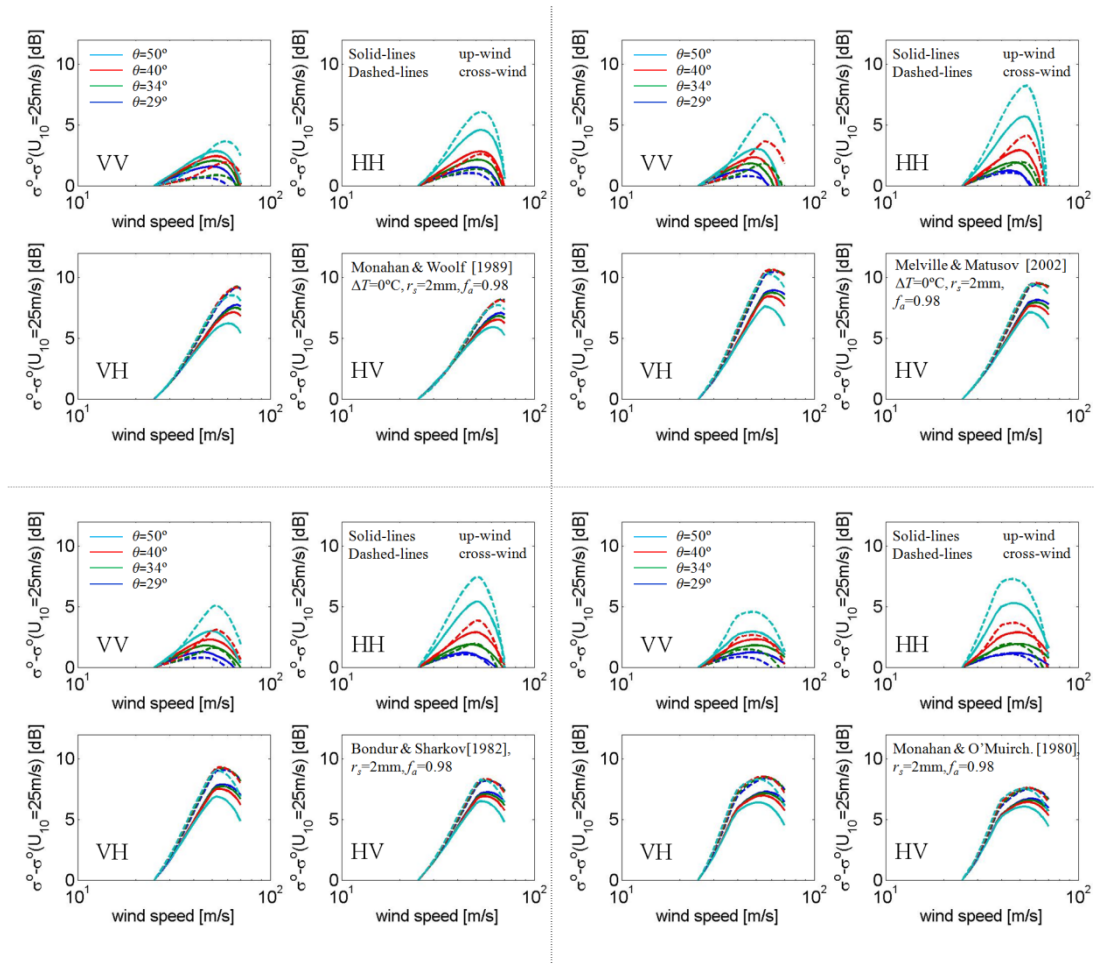


Fig. 3.10. Windspeed dependence of C-band radar backscatter above 25m/s for various incidence angles (29°, 34°, 40° and 50°) and two wind directions (up-wind and cross-wind). Four different foam coverage models are used: Monahan & Woolf [1989], Monahan & O’Muircheartaigh [1980], Bondur & Sharkov [1982] and Melville & Matusov [2002].

Bubble Size

Among the few reports documenting the bubble size distributions within the foam one should mention Militskii et al. [1977], where the authors stated that the diameters of the bubbles within the foam layer span between 0.2 mm and 2 mm. Through the analysis of a sequence of foam images, Guo *et al.* [2001] estimate an average bubble size of 0.5 mm “in the bottom half of the foam layer”. The size of the bubbles depends on the environmental conditions, such as wind fields [Anguelova & Gaiser, 2012] and ocean

salinity scenarios [Wu, 2000]. On the basis of recent laboratory and field measurements [Deane & Stokes, 2002; Leifer *et al.*, 2006], we consider bubbles, close to the surface, with radii from 0.05 mm to 10 mm, with most likely radii from 0.05 mm to 2 mm. Within this range, different bubble sizes were analyzed in section 3.4 in order to describe the corresponding effects on both co-polar and cross-polar NRCS. Further measurements are definitely needed to understand and derive physical relationships between bubble size, wind fields, depth into the foam and ocean salinity. The inclusion of these relationships into our analytical model can further improve the physical description of foam backscattering.

3.6 Conclusions

In this chapter, a new analytical model for the full polarimetric scattering of microwave radiation from the ocean has been investigated. The model combines the 2nd order Small Slope Approximation Theory with the Vector Radiative Transfer Theory to obtain a statistical expression for the ocean full-polarimetric scattering matrix (in presence of foam) as function of wind speed and direction. A set of nineteen Hurricane images by RADARSAT-2 C-band SAR in VV and VH, collocated in time and space with ECMWF model winds and, when available, SFMR wind measurements by NOAA's hurricane-hunter aircraft, have been used to verify the model. A good agreement is found between scattering simulations and real measurements. Both measured and simulated cross-polarized data show no distinguishable loss of sensitivity to the wind speed up to 60 m/s, thus proving the big potential of cross-polarized scattering for the retrieval of severe wind speeds from ocean scatterometry. Moreover, our simulations confirm that the cross-polar scattering is less sensitive to incidence angle and wind direction than the co-polar scattering.

Future missions with advanced microwave sensors are planned for launch in the near future; they ask not only for better spatial resolution, radiometric resolution and stability but also for wider swaths and multi-polarization observation capabilities. This is the case for the satellites in the Second Generation Meteorological Operational satellite programme (MetOp-SG), which will replace the current MetOp system in the 2020+ time frame. Among other instruments, MetOp-SG will deploy a C-band scatterometer, named SCA [Fois *et al.*, 2014], similar to ASCAT on MetOp [Gelsthorpe *et al.*, 2000], but with an additional polarization (VH added to the standard VV), higher spatial resolution, increased coverage and stability. The higher spatial resolution will better describe the spatial variations in hurricanes and coastal wind fields, whereas, wider swaths will

provide more complete coverage. Wider swaths imply wider ranges of incidence angles to be explored, and thus new challenges in the modelling of the interaction of the electromagnetic and oceanic waves. Therefore, in future prospective, the proposed radar backscatter model, being based on a description of the underlying physical phenomenon, has the big potential of providing a better comprehension of the relationship between measured microwave backscatter and surface wind field beyond the well established empirical models (which are basically free of explicit physical assumptions). In addition, the proposed model captures some of the most desirable features: it is applicable over a wide range of wind speeds, radar frequencies, incidence angles, polarizations and arbitrary radar look direction with respect to the wind direction. Other factors, such as long wave spectrum, viscosity, sea water temperature, and surface tension, are also taken into account. Further improvements might arise from the inclusion of rain effects into the full-polarimetric scattering computation and from a better description of the bubble size versus wind fields, depth into the foam and ocean salinity: we leave such improvements to future dedicated works.

4 The Sea Surface Doppler Signature

This chapter describes an innovative analytical model of the full-polarimetric sea surface scattering and Doppler signature. The model combines the Small-Slope-Approximation theory (at the 2nd order) with a weak non-linear sea surface representation. Such a model is used to examine the variation of the Doppler central frequency/bandwidth and of the Normalized Radar Cross-section as function of wind-speed and direction. The results suggest that the model can be a valuable tool for the accurate observation of sea surface currents.

This chapter is based on the results published by the author in [Fois *et al.*, 2015a].

4.1 Need for Ocean Motion Data

Accurate knowledge of spatial and temporal surface current behaviour in the open ocean and coastal waters is essential for a variety of applications, such as the monitoring of changes in coastal regions, risk management for coastal and off-shore structures, and ship operations. Currents are generated from the forces acting upon the water mass including the rotation of the Earth, winds, temperature and salinity differences and tidal forces. Additionally, depth contours and the shoreline influence the currents' direction and strength. Use of SAR-derived Doppler observation to estimate surface current in some selected areas of strong persistent current, such as Gulf stream and Agulhas current, has emerged recently [Chapron *et al.*, 2003, 2005; Johannessen *et al.*, 2008], even if the validation was based on the few opportunities offered by Lagrangian surface drifters of the world ocean drifter program.

Surface currents moreover emerge when long-term differences are taken between scatterometer winds and Numerical Weather Prediction (NWP) model winds. Satellite scatterometer winds are, in fact, derived from ocean roughness, which depends on the relative motion difference between air and sea, whereas NWP model winds are provided with respect to a fixed Earth reference. These differences have also been favourably compared to SAR Doppler measurements. Although scatterometer winds are used beneficially for NWP model initialization [Stoffelen *et al.*, 2013], it may be clear that for the more successful use of scatterometer winds in NWP analyses, the ocean currents and motion need to be known and taken into account.

The measurement of ocean currents from a satellite in low Earth orbit is difficult due to

the very high satellite velocity (approximately 7 km/s) with respect to that of the ocean current to be measured (from a few cm/s to some m/s). As a consequence, accurate knowledge of the satellite radar beam pointing would be required. An alternative approach for removing the satellite and Earth-rotation components of the observed Doppler velocity would be to make use of some reference surface currents known a priori by independent means such as drifting buoys, current meters and coastal Doppler radars as well as the land masses whose earth-relative velocity is zero by definition.

Even if promising methodologies have been developed, some intrinsic limitations on the use of SAR Doppler shift for surface current mapping remains, such as the need to rely on a model quantifying the wind contribution to the total Doppler shift.

In fact, one major challenge is that Doppler shift is not only sensitive to the underlying ocean surface current and to satellite orbital position/attitude knowledge errors, but it is also strongly dependent on wind speed and direction. Depending on the wind speed, the Doppler shift induced by the wind (wind drift) could be much higher than the one induced by the current. Improved understanding and modelling of the microwave sea surface Doppler signature thus becomes imperative for accurate determination of ocean currents. The modelling of the Doppler spectrum of a time-varying ocean surface has gained considerable attention in the last decade. Knowledge of how the evolution of the ocean surface wave spectrum affects the scattered electromagnetic waves is essential for a quantitative understanding of the properties of the measured microwave Doppler spectra. Such an understanding is complex because of the complicated hydrodynamics influencing the motion of the ocean surface waves. Non-linear hydrodynamics couple the motion of the large and small waves and, in turn, change the shapes and the statistical characteristics of the surface wave components and thus its interaction with the winds. These hydrodynamic surface interactions are not represented in the simplest linear sea-surface models, which assume that each surface harmonic propagates according to the dispersion relation of water waves. Among the first meaningful papers, one should mention the early works of Bass [1968] and Barrick [1977], who used a surface perturbation theory to predict the Doppler spectra; Valenzuela and Laing [1970], instead, obtained similar results by using a composite surface model. Later, Doppler spectra were studied by Thompson and Romeiser [1989]-[2000], who computed the spectra using a time-dependent composite model. This model reduces to *specular* and *small perturbation* limits for VV and HH-polarizations and its time dependence is based on the use of a linear modulation transfer function. Zavorotny and Voronovich [1998] made use of an approximate “two-scale” surface model based on a directional wave spectrum, which takes into account the wave age. In Creamer *et al.* [1989], the authors proposed a non-

linear model for the description of hydrodynamic surface interactions which was eventually used by Rino *et al.* [1991] to simulate the Doppler spectra from dynamically evolving surface realizations. However, the simulations were performed with a rather large electromagnetic wavelength (7.5 m) and were restricted to only 70 degrees incidence angle. Later, Toporkov *et al.* [2000, 2007], Soriano *et al.* [2006], Li and Xu [2011], Johnson *et al.* [2001], Hayslip *et al.* [2003] made significant steps forward in modelling L-band and X-band non-linear surface scattering properties at low wind speeds. In these works, since no statistical formulation was available, Doppler spectra were generated by averaging the backscattered field from a large number of sampled time-evolving surfaces; a procedure which is very time consuming. A further difficulty arises from the fact that the Creamer technique is computationally demanding and actually dissuasive for two-dimensional surface simulations. Therefore most of the studies have been limited to one-dimensional surfaces.

An alternative numerical method for studying the evolution of free and bound waves on the non-linear ocean surface was proposed by West *et al.* in [1987]. Although this method is more efficient than the Creamer technique [Johnson *et al.*, 2001], it is susceptible to instability problems and breaks down when steep features in the surface are formed.

Recently, the use of the Choppy Wave Model (CWM) in combination with the Weighted Curvature Approximation [Nouguier *et al.*, 2009, 2010, 2011] in the context of sea Doppler spectrum calculation has shown significant advantages in terms of analytical simplicity and numerical efficiency. However, the Weighted Curvature Approximation (WCA) does not provide a full-polarimetric description of the sea surface Doppler signature. In addition, most of the numerical results reported by Nouguier *et al.* in [2011] refer only to one-dimensional representations of the sea surface. Although in the last 10 years the modelling of sea surface Doppler signature has made significant progress, an efficient analytical model of the full polarimetric sea surface Doppler spectrum is still missing. Additionally, not many comparisons with real measurements have been published: among the few attempts one should mention the works by Plant and Alpers [1994] and Mouche *et al.* [2008].

In this chapter, we present an analytical physical model for accurate estimation of full-polarimetric microwave sea-surface scattering and Doppler signatures. This model combines an adequate sea surface description, based on the CWM, with 2nd order Small-Slope-Approximation (SSA) wave scattering theory to simulate both scattering and Doppler spectra over a wide range of wind speeds, radar frequencies, incidence angles, different polarizations and arbitrary radar look direction with respect to the wind direction. In Section 4.2, the properties of the ocean sea surface are discussed and

differences between linear and non-linear sea surface representations are presented. Statistical properties of the CWM are also discussed. The section ends with the description of an efficient procedure to undress the sea surface spectrum. Section 4.3 is dedicated to the description of the scattering model, whereas Section 4.4 highlights the links between the present general analytical model and simplified scattering theories. In Section 4.5, the results are first compared with other scattering theories and then (in Section 4.6) with real measurements from Envisat-ASAR (C-band radar), the well-established Empirical Geophysical Model Function CDOP [Mouche *et al.*, 2012], and data collected at Ku band during the SAXON-FPN campaign [Plant and Alpers, 1994; Plant *et al.*, 1994].

Being capable of estimating full-polarimetric Doppler spectra of microwave backscatter from ocean surface, this model could be used to explore ocean surface motion retrievals, thus potentially supporting the definition of future scatterometers capable of simultaneous measurement of Ocean Vector Wind (OVW) and Ocean Vector Motion (OVM) on a global scale.

4.2 Properties of the Sea Surface Doppler Spectra

In this section, we focus our attention on the properties of the surface wave spectrum and how they depend on environmental parameters such as the local wind vector. As discussed in chapter 2, one of the most well known and accepted spectral models is the Elfouhaily unified spectrum [Elfouhaily, 1997]. The development of this spectrum was based on available field and wave-tank measurements along with physical considerations. The ocean surface wave spectrum by Kudryavtsev *et al.*, [1999], also discussed in chapter 2, has improved the modelling of short-gravity and capillary waves. The spectral shape results from the solution of the energy spectral density balance equation. Across this chapter, also other well known ocean surface wave vector spectra will be analyzed and their effect on both NRCS and Doppler shift will be addressed; among them, the Apel composite wide band spectrum [Apel, 1994], the Pierson-Moskowitz Spectrum [Pierson & Moskowitz, 1964] and the advanced roughness spectrum by Hwang *et al.* [2011, 2013]. Very often, the ocean sea surface is represented by a Gaussian wave height distribution: this is also called linear sea-surface model, which assumes that each surface harmonic propagates according to the dispersion relation typical of water waves. However, non-linear surface waves can have an important impact on the interpretation of scattering data and cannot be ignored for a correct estimation of the sea surface Doppler shift. Non-linear hydrodynamic modulation of short waves by large waves changes the

statistics of the sea surface waves and it is one of the reasons for the observed upwind/downwind asymmetry of the measured NRCS. The deviation from the Gaussian law of the sea surface slope distribution has been well documented since the pioneering work by Cox and Munk [1954]. One should also mention the early works of Hasselmann [1962] and Longuet-Higgins [1963]; however, these theories are only applicable to long gravity waves. For short waves, instead, non-linear wave-wave interactions become important and must be accounted for: a way of doing this is to use the non-linear model for surface waves by Creamer *et al.* [1989]. This theory captures the lowest-order non-linear behaviour of surface waves, but lacks a statistical formulation and the numerical implementation of this theory is highly time-consuming. A numerically efficient weakly non-linear model, called ‘‘Choppy Wave Model’’ (CWM) has been recently developed to overcome these main limitations [Nouguier *et al.*, 2009]. The CWM is based on a non-linear transformation of the linear surface and it allows a statistical formulation of the surface height/ slopes and higher-order moments. The CWM is limited to the lowest order non-linearity. Its main strength is to provide a good compromise between simplicity, stability and accuracy. Because of these desirable features, the Choppy Wave Model will be adopted in this chapter.

4.2.1 Linear Sea Surface Representation

Without loss of generality we can express the linear sea surface in time as:

$$h(\mathbf{r}, t) = \int d\mathbf{k} [\hat{h}(\mathbf{k}) \exp(-i\omega_{\mathbf{k}} t) + \hat{h}^*(-\mathbf{k}) \exp(i\omega_{\mathbf{k}} t)] e^{i\mathbf{k} \cdot \mathbf{r}} . \quad (4.1)$$

where $\hat{h}(\mathbf{k})$ is the complex amplitude of the wave, $\mathbf{r} = (x, y)$ is the horizontal coordinate, \mathbf{k} is the corresponding wave number of polar coordinates (k, ϕ) , and $\omega_{\mathbf{k}}$ is the gravity-capillary dispersion relationship for infinite-depth sea:

$$\omega_{\mathbf{k}} = \sqrt{g|\mathbf{k}| \left[1 + \left(\frac{|\mathbf{k}|}{k_M} \right)^2 \right]} . \quad (4.2)$$

with $k_M = 363.2$ rad/m being the wave number with minimum phase speed and $g = 9.81$ m/s² the gravity acceleration constant. Denoting with $C(\mathbf{r}, t) = \langle h(\mathbf{r}, t)h(\mathbf{0}, 0) \rangle$ the spatiotemporal covariance function of the surface, that is:

$$C(\mathbf{r}, t) = \int d\mathbf{k} [S_a(\mathbf{k}) \exp(-i\omega_{\mathbf{k}} t) + S_a(-\mathbf{k}) \exp(i\omega_{\mathbf{k}} t)] e^{i\mathbf{k} \cdot \mathbf{r}}. \quad (4.3)$$

where

$$\begin{cases} S_a(\mathbf{k}) = S(\mathbf{k}) \cos^2\left(\frac{\phi - \phi_w}{2}\right) \\ S_a(-\mathbf{k}) = S(\mathbf{k}) \sin^2\left(\frac{\phi - \phi_w}{2}\right) \end{cases}. \quad (4.4)$$

In (4.4), $S(\mathbf{k})$ is the centrosymmetric wave spectrum and the angle ϕ_w is the wind direction.

4.2.2 Non-Linear Sea Surface Representation

As a non-linear representation of the sea surface, we will use the CWM, that is based on a Lagrangian approach and takes into account the horizontal displacement of particles. Practically, the non-linear surface can be expressed as a horizontal deformation of the linear surface as follows:

$$(\mathbf{r}, h(\mathbf{r}, t)) \rightarrow (\tilde{\mathbf{r}}, \tilde{h}(\tilde{\mathbf{r}}, t)). \quad (4.5)$$

where

$$\begin{cases} \tilde{\mathbf{r}} = \mathbf{r} + \mathbf{D}(\mathbf{r}, t) \\ \tilde{h}(\tilde{\mathbf{r}}, t) = h(\mathbf{r}, t) \end{cases}. \quad (4.6)$$

The displacement \mathbf{D} is the so called Riesz Transform of the function h :

$$\mathbf{D}(\mathbf{r}, t) = \int d\mathbf{k} i \frac{\mathbf{k}}{k} e^{i\mathbf{k} \cdot \mathbf{r}} \hat{h}(\mathbf{k}, t). \quad (4.7)$$

and

$$\hat{h}(\mathbf{k}, t) = \frac{1}{(2\pi)^2} \int d\mathbf{r} e^{-i\mathbf{k}\cdot\mathbf{r}} h(\mathbf{r}, t) \quad (4.8)$$

is the two-dimensional spatial transform of the linear surface. The transformation (4.6) defines a modified process $\tilde{h}(\tilde{\mathbf{r}}, t)$ which has been shown to possess non-Gaussian height and slope distributions, as well as a modified spectrum [Nouguier *et al.*, 2009].

4.2.3 Statistical Properties of the Sea Surface

Following the example of Nouguier *et al.* in [2009], this section shortly recalls the spatial statistical properties of the non-linear sea surface, \tilde{h} , at a given time $t=0$. Let us introduce the partial and total absolute moments of the spectrum:

$$\sigma_{\alpha\beta\gamma}^2 = \int \frac{k_x^\alpha k_y^\beta}{|\mathbf{k}|^\gamma} S(\mathbf{k}) d\mathbf{k}, \quad \sigma_n^2 = \int |\mathbf{k}|^n S(\mathbf{k}) d\mathbf{k}. \quad (4.9)$$

Where k_x and k_y are the components of \mathbf{k} along the x and y axis. Using the same notation as in [Nouguier *et al.*, 2009], the characteristic function of the non-linear surface is given by:

$$\Phi(\nu) = \langle e^{i\nu\tilde{h}} \rangle = (1 - i\nu\sigma_1^2 + \nu^2\Sigma_1) \exp\left(-\frac{1}{2}\nu^2\sigma_0^2\right), \quad (4.10)$$

with $\Sigma_1 = \sigma_{111}^4 - \sigma_{201}^2\sigma_{021}^2$. A Fourier inversion of (4.10) provides the probability distribution function (pdf) of elevations:

$$\tilde{P}_0(z) = P_0(z) \left(1 + \frac{\Sigma_1}{\sigma_0^2} - \frac{\sigma_1^2}{\sigma_0^2} z - \frac{\Sigma_1}{\sigma_0^4} z^2\right), \quad (4.11)$$

being $P_0(z)$ a Gaussian distribution of elevations with standard deviation σ_n and zero mean value. Starting with a zero mean linear surface, the resulting non-linear surface becomes a non-zero mean random non-Gaussian process. An expression of the slopes of the non-linear surface can be obtained by differentiating equation (4.6). An integral formula providing the pdf of slopes has been provided in [Nouguier *et al.*, 2009] (Eq. 47).

Figure 4.1 shows the pdf of elevations (left) and the pdf of slopes (right) of a linear and CWM surfaces for wind speed of 10 m/s (Elfouhaily spectrum). The skewness of the CWM surface is slightly negative and the mean square height (msh) is slightly decreased. There is no significant creation of kurtosis with respect to the Gaussian case. The tail of the slope distribution of the CWM surface shows a slower decrease than the one of the linear surface. Statistics of the linear and nonlinear sea surface are summarized in Table 4.1: this table highlights a magnification of the rms slopes induced by the non-linear CWM transformation of the sea surface. This magnification may generate small errors in the estimation of the radar cross section. A way to correct this artefact is to undress the non-linear sea surface spectrum.

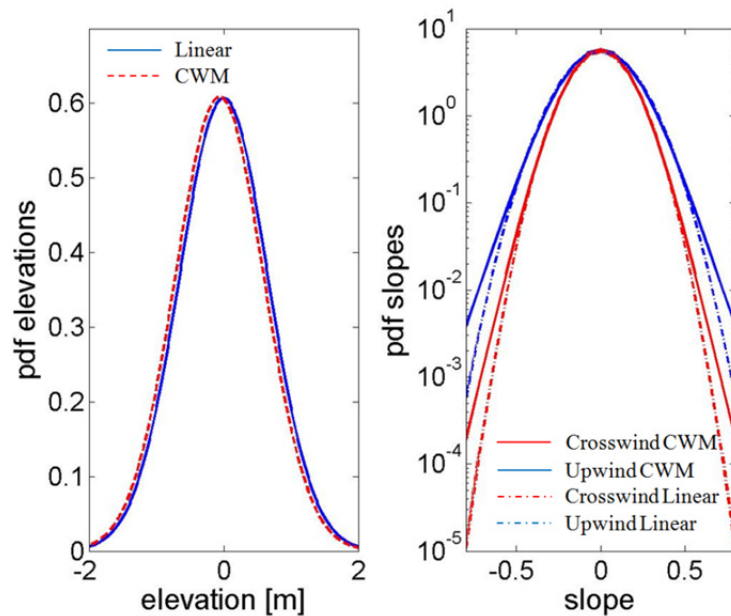


Fig. 4.1. Distribution of elevations (left) and distribution of slopes (right) for linear and CWM surfaces at wind speed of 10 m/s.

Tab. 4.1 Statistics of linear & CWM surfaces				
Wind Speed (m/s)	Surface	Root mean square		
		Height (m)	Slope upwind	Slope crosswind
5	linear	0.1625	0.1369	0.1120
5	CWM	0.1628	0.1382	0.1129
7	linear	0.3195	0.1516	0.1255
7	CWM	0.3201	0.1533	0.1266
10	linear	0.6573	0.1870	0.1562
10	CWM	0.6586	0.1902	0.1585
12	linear	0.9481	0.2035	0.1693
12	CWM	0.9498	0.2076	0.1723

4.2.4 Spectral Undressing

With reference to Figure 4.2a, we consider the Elfouhaily spectrum as the reference measured sea surface wave height spectrum, $S_{ref}(\mathbf{k})$. Being the result of a measurement, this spectrum already includes non-linear features. By applying the non-linear sea surface transformation (4.6), $S_{ref}(\mathbf{k})$ is changed in $\tilde{S}(\mathbf{k})$, named “dressed” spectrum, which statistical properties are different from the ones of $S_{ref}(\mathbf{k})$. In particular, the dressed spectrum shows an enhanced curvature that needs to be corrected: a way to do this is by “undressing” $\tilde{S}(\mathbf{k})$. We call the “undressed” spectrum, $S(\mathbf{k})$, the spectrum that after CWM transformation provides the same root mean square height and slope as the reference spectrum $S_{ref}(\mathbf{k})$. Soriano *et al.* in [2006] proposed a simple undressing method based on an optimization of the high frequency part of the spectrum. Nouguier *et al.* [2009, 2010] used the iterative procedure proposed by Elfouhaily *et al.* [1999] to perform the undressing. However, not many details on the practical implementation were provided in the above-mentioned papers.

In this work, we propose an alternative technique that is based on the use of a parametric representation of the directional sea surface spectrum. The parameters are then optimized through an iterative procedure to make both mss (mean square slope) and msh (mean square height) of the parametric spectrum consistent with the mss and msh of the measured spectrum. For each wind-speed, we first represent the sea spectrum as linear combination of seven different directional spectra: Elfouhaily *et al.* [1997], Kudryavstev *et al.* [1999], Apel [1994], Pierson and Moskowitz [1964], Hwang *et al.* [2011], Fung and Lee [1982], and Donelan-Plant [2002]. The 14 coefficients of the linear combination (7 coefficients for the curvature spectrum and 7 for the spreading function) are optimized, for different values of the wind speed, to match as close as possible the root mss and the root msh of the Elfouhaily spectrum. Practically, the calculation of the parameters is performed with the help of the Matlab routine `lsqnonlin` [Coleman & Li, 1996]. A similar optimization procedure has been used efficiently in [Fois *et al.*, 2014a] to match Ku and C-band experimental Normalized Radar Cross-sections.

The advantage of combining existing sea surface spectra is that the solution of the optimization has always a physical meaning. Other approaches based on parametric fitting of the sea surface spectra, instead, very often bring to non-physical solutions. As a starting point of the optimization, we consider a spectrum identical to the Elfouhaily one; the coefficients of the linear combination are eventually changed to solve a non-linear least-squares problem, so that the non-linear surfaces possess the same height and slopes

root mean squares as the linear Elfouhaily surface. In Table 4.2, both root mss and root msh of the linear and undressed non-linear sea surface are compared for different wind speeds. Figure 4.2b shows the undressed spectrum against the Elfouhaily spectrum for 12 m/s wind speed: both curvature spectra and spreading functions are plotted. For the spreading function, we have limited our study to spectra with second harmonic. From our analysis, the undressing procedure was found to have very little impact on the Doppler signature. Therefore, for the specific purpose of Doppler analysis, such a complicated spectral correction can be avoided.

Tab. 4.2 Root Mean Square of The Undressed Spectrum

Wind Speed (m/s)	Surface	Root mean square		
		Height (m)	Slope upwind	Slope crosswind
5	linear	0.1625	0.1369	0.1120
5	undr.+CWM	0.1625	0.1370	0.1120
7	linear	0.3195	0.1516	0.1255
7	undr.+CWM	0.3196	0.1516	0.1254
10	linear	0.6573	0.1870	0.1562
10	undr.+CWM	0.6579	0.1874	0.1562
12	linear	0.9481	0.2035	0.1693
12	undr.+CWM	0.9490	0.2036	0.1691

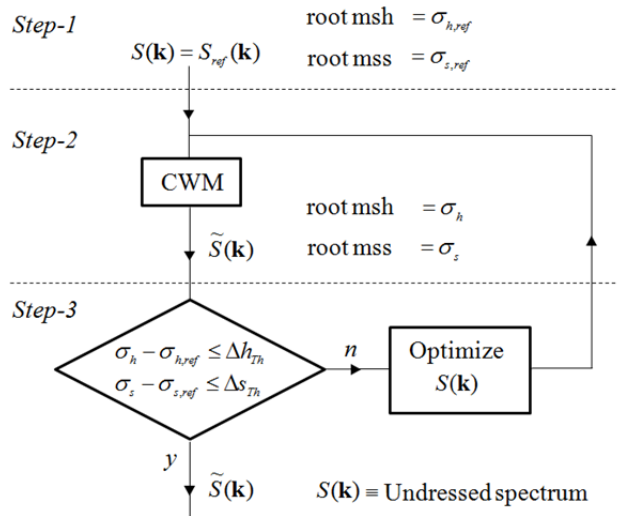


Fig. 4.2a. Schematic of the undressing procedure.

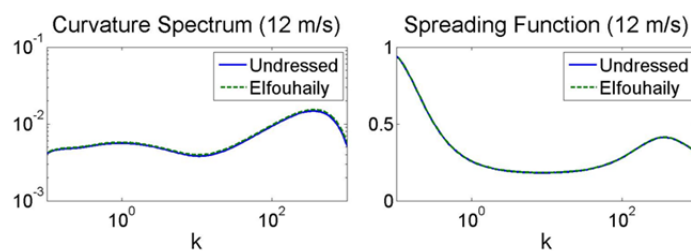


Fig. 4.2b. Comparison between the Elfouhaily and the undressed curvature spectrum (left) and the spreading function (right) for 12 m/s wind speed.

4.3 The microwave full polarimetric sea surface Doppler signature

As anticipated in chapter 2, an example of an advanced backscattering model for the ocean surface is the *Kirchhoff Approximation* model (KA) [Beckmann & Spizzichino, 1987], which can only be applied to surfaces with horizontal roughness scale and average radius of curvature (r_c) larger than the electromagnetic wavelength (see Eq. 2.9). The Kirchhoff approximation correctly models quasi-specular scattering, but disregards polarization. The KA model is exact when the signal wavelength tends to zero (*geometrical optics* limit, GO), if multiple reflections/shadowing can be neglected. When both the standard deviation and correlation length of surface heights are smaller than the wavelength, a different method must be used. The *Small Slope Approximation* (SSA) [Voronovich, 1994], in principle, can be applied to any wavelength, provided that the tangent of grazing angles of incident/scattered radiation sufficiently exceeds the rms slope of roughness. For a sea surface, the slopes are generally small except for steep breaking waves, which represent a relatively small percentage and occur only at strong and very strong wind speeds. The Small Slope Approximation is the result of a Taylor expansion with respect to the powers of surface slopes. It is common practice to call SSA1 and SSA2 the expansions performed at the first and second order respectively, the second being able to estimate the cross-polarized component of scattering in the plane of incidence. In this chapter, we will refer to the second-order Small-Slope Approximation model, SSA2, being the only model able to provide accurate full polarimetric sea-surface scattering signatures [Fois *et al.* 2014b, 2015b].

4.3.1 Second Order SSA for the Linear Sea Surface

In this chapter we refer to the scattering geometry, notations and definitions provided in section 2.3. In the follow, we shortly recall the expression of the scattering amplitude of SSA2 for a linear sea surface:

$$\mathbf{S}_{\alpha_s, \alpha_i}^{SSA-2}(\mathbf{k}_s, \mathbf{k}_i, t) \Big|_{Lin.} = \frac{1}{Q_z} \int \frac{d\mathbf{r}}{(2\pi)^2} \exp[-i\mathbf{Q}_H \cdot \mathbf{r} + iQ_z h(\mathbf{r}, t)] \times \left[\mathbf{B}_{\alpha_s, \alpha_i}(\mathbf{k}_s, \mathbf{k}_i) - \frac{i}{4} \int M_{\alpha_s, \alpha_i}(\mathbf{k}_s, \mathbf{k}_i, \xi) \hat{h}(\xi, t) e^{i\xi \cdot \mathbf{r}} d\xi \right]^2, \quad (4.12)$$

Values M , B_2 and B are 2×2 matrices; their expressions are given in appendix-B. The second term in the squared parenthesis of equation (4.12) represents the second-order

correction to the SSA1 model. We also recall the expression of the spatiotemporal covariance function:

$$\begin{aligned} \text{Cov}(\mathbf{k}_s, \mathbf{k}_i; t) \Big|_{Lin.} = \\ \frac{4\pi}{Q_z^2} \int \frac{d\mathbf{r}}{(2\pi)^2} R_{\alpha_s \alpha_i}(\mathbf{k}_s, \mathbf{k}_i; \mathbf{r}, t) \exp[-i\mathbf{Q}_H \cdot \mathbf{r}] \end{aligned} \quad (4.13)$$

where R is given by equations (2.28)-(2.30). Note that the spatiotemporal covariance function computed at the time $t=0$ provides the Normalized Radar Cross Section (NRCS). With reference to equation (2.30), we express the spectrum of roughness in the form: $S(\xi, t) = S_a(\xi) \exp(-i\omega_\xi t) + S_a(-\xi) \exp(i\omega_\xi t)$. The Doppler spectrum is the Fourier transform of the spatiotemporal covariance function:

$$S_{Dop}(\omega) \Big|_{Lin.} = \int dt e^{-i\omega t} \text{Cov}(\mathbf{k}_s, \mathbf{k}_i; t) \Big|_{Lin.} \quad (4.14)$$

and $f = \omega/2\pi$ is the Doppler frequency shift.

4.3.2 Second Order SSA for the Non-Linear Sea Surface

We use the Choppy Wave Model described in section 4.2.2 as non-linear sea surface representation. In this case, the SSA2 presents the following expression for the scattering amplitude at the time t :

$$\begin{aligned} \mathbf{S}_{\alpha_s \alpha_i}^{SSA-2}(\mathbf{k}_s, \mathbf{k}_i, t) \Big|_{Non-Lin.} = \tilde{\mathbf{S}}_{\alpha_s \alpha_i}^{SSA-2}(\mathbf{k}_s, \mathbf{k}_i, t) = \\ = \frac{1}{Q_z} \int \frac{d\mathbf{r}}{(2\pi)^2} J(\mathbf{r}, t) \exp[-i\mathbf{Q}_H \cdot (\mathbf{r} + \mathbf{D}(\mathbf{r}, t)) + iQ_z h(\mathbf{r}, t)] \cdot \\ \times \left[\mathbf{B}_{\alpha_s \alpha_i}(\mathbf{k}_s, \mathbf{k}_i) - \frac{i}{4} \int M_{\alpha_s \alpha_i}(\mathbf{k}_s, \mathbf{k}_i, \xi) \hat{h}(\xi, t) e^{i\xi \cdot \mathbf{r}} d\xi \right] \end{aligned} \quad (4.15)$$

where $J(\mathbf{r}, t)$ is the Jacobian of the transformation $\mathbf{r} \rightarrow \mathbf{r} + \mathbf{D}(\mathbf{r}, t)$:

$$\begin{aligned} J(\mathbf{r}, t) = 1 + \nabla \cdot \mathbf{D}(\mathbf{r}, t) + \\ \partial_x D_x(\mathbf{r}, t) \partial_y D_y(\mathbf{r}, t) - \partial_x D_y(\mathbf{r}, t) \partial_y D_x(\mathbf{r}, t) \end{aligned} \quad (4.16)$$

By neglecting the quadratic terms in D_x and D_y we may approximate:

$$J(\mathbf{r}, t) \approx 1 + \nabla \cdot \mathbf{D}(\mathbf{r}, t). \quad (4.17)$$

The spatiotemporal covariance function can be written as:

$$\begin{aligned} \text{Cov}(\mathbf{k}_s, \mathbf{k}_i; t) \Big|_{\text{Non-Lin.}} = \\ \frac{4\pi}{Q_z^2} \int \frac{d\mathbf{r}}{(2\pi)^2} \tilde{R}_{\alpha_s \alpha_i}(\mathbf{k}_s, \mathbf{k}_i; \mathbf{r}, t) \exp[-i\mathbf{Q}_H \cdot \mathbf{r}] \end{aligned} \quad (4.18)$$

where

$$\begin{aligned} \tilde{R}_{\alpha_s \alpha_i}(\mathbf{k}_s, \mathbf{k}_i; \mathbf{r}, t) = & -\left| \chi_{\alpha_s \alpha_i}(\mathbf{k}_s, \mathbf{k}_i; t) \right|^2 + \\ & \sum_{n=1}^4 \sum_{m=1}^4 \Psi_{\alpha_s \alpha_i}^{(m,n)}(\mathbf{k}_s, \mathbf{k}_i; \mathbf{r}, t) \end{aligned} \quad (4.19)$$

The expression of the terms $\Psi_{\alpha_s \alpha_i}^{(m,n)}(\mathbf{k}_s, \mathbf{k}_i; \mathbf{r}, t)$ and $\chi_{\alpha_s \alpha_i}(\mathbf{k}_s, \mathbf{k}_i; t)$ are reported in appendix-C.

4.3.3 Doppler Central Frequency and Doppler Spread

The Doppler central frequency f_D and the Doppler bandwidth B_D can be obtained through the first two moments of the Doppler spectrum:

$$f_D = \frac{1}{2\pi} \frac{\int \omega \cdot S_{Dop}(\omega) d\omega}{\int S_{Dop}(\omega) d\omega}. \quad (4.20)$$

and

$$B_D = \sqrt{\frac{1}{(2\pi)^2} \frac{\int \omega^2 \cdot S_{Dop}(\omega) d\omega}{\int S_{Dop}(\omega) d\omega} - (f_D)^2}. \quad (4.21)$$

These quantities can be quickly computed by the model since they do not depend on time. To better clarify, there are two alternative ways to compute f_D and B_D . The first requires the evaluation of the scattering amplitude as function of time: its Fourier transform will then provide the Doppler Spectrum and from this, by using equations (4.20) and (4.21), f_D and B_D can be derived. The second approach consists in using the following relationships between Doppler spectrum and the spatiotemporal covariance function:

$$\int \omega \cdot S_{Dop}(\omega) d\omega = -i \left. \frac{\partial Cov}{\partial t} \right|_{t=0} . \quad (4.22)$$

and

$$\int \omega^2 \cdot S_{Dop}(\omega) d\omega = - \left. \frac{\partial^2 Cov}{\partial t^2} \right|_{t=0} . \quad (4.23)$$

The second approach represents a more direct derivation of the Doppler central frequency and the Doppler spread which does not require the computation of the Doppler spectrum, $S_{Dop}(\omega)$. This computation could be quite time consuming, particularly at high frequencies (X, Ku, Ka-bands) where a smaller time step is required to avoid aliasing effects. Through the use of equations (4.22) and (4.23), both central Doppler frequency and Doppler spread can be calculated at the same cost as the NRCS.

4.3.4 Derivation of Special Scattering Cases

The Kirchhoff Approximation

Equation (4.18) provides the complete expression of the spatiotemporal covariance function of the analytical model. From this equation, special scattering cases can be easily derived. For instance, if only the terms $\Psi_{\alpha_s, \alpha_i}^{(m,n)}$, with $m=1,2,3,4$ and $n=1$, are considered, we obtain exactly the Kirchhoff Approximation combined with the Choppy Wave Model (KA-CWM); a model that has been widely investigated by Nouguier *et al.* [2009, 2010, 2011]. Thanks to its simplicity, KA-CWM can be used to quickly check the effect of different input wave height spectra on both Doppler shift and Doppler spread. Figure 4.3 shows f_D and B_D in V-polarization versus incidence angle at X-band at 5, 7 and 9 m/s

wind speed (upwind) for linear and CWM surfaces. Because of the use of the Kirchhoff approximation, the results in V and H-polarization are identical. As expected, higher Doppler frequencies are observed when passing to non-linear surfaces, the increase being more pronounced at high winds. An even more visible impact is observed on the Doppler width, which is found much larger than in the linear case and quasi insensitive to the incidence angles above 40 degrees, while the linear counterpart falls off rapidly. Both Doppler shift and the Doppler spread change with the wave height spectrum. In Figure 4.3, four sea surface spectra are analyzed [Elfouhaily *et al.*, 1997; Apel, 1994; Pierson & Moskowitz, 1964; Hwang *et al.*, 2011].

The highest Doppler shift and Doppler spread is found when the Elfouhaily unified sea surface spectrum is used. It is also interesting to note that results obtained with the linear sea surface model are much more sensitive to spectral changes than the results obtained with the CWM non-linear sea surface. This particular behaviour, explains also why the Doppler signature after CWM transformation is weakly sensitive to the spectral undressing procedure discussed in section 4.2. In Figure 4.3, for the linear surface case, the maximum Doppler shift and, also, the maximum Doppler bandwidth occur at different incidence angles depending on the input spectrum. When, instead, the CWM is used, these maximum levels occur approximately at the same incidence angle, which is around 22° for the Doppler shift and around 28° for the Doppler bandwidth. With reference to the results reported by Nouguier *et al.* [2010], a not negligible difference is found on the Doppler bandwidth, at small incidence angles. This difference is related to the fact that Nouguier *et al.* assumed the waves to travel only toward (or away from) the radar. This means that in equation (4.3) $S_a(\mathbf{k})$ vanishes in the half-space of wave number pointing to the radar look direction (i.e. $S_a(\mathbf{k})$ is half sided). In our model, instead, we have made the assumption of a centro-symmetric wave spectrum, where the waves are supposed to move in all directions following the law reported in equation (4.4).

The High-Frequency Approximation of SSA2

We have already pointed out that the computation of SSA2 scattering amplitude is very complex as it requires the calculation of four-fold integrals with oscillating functions. To facilitate calculations, Voronovich and Zavorotny [2001] performed the following transformation:

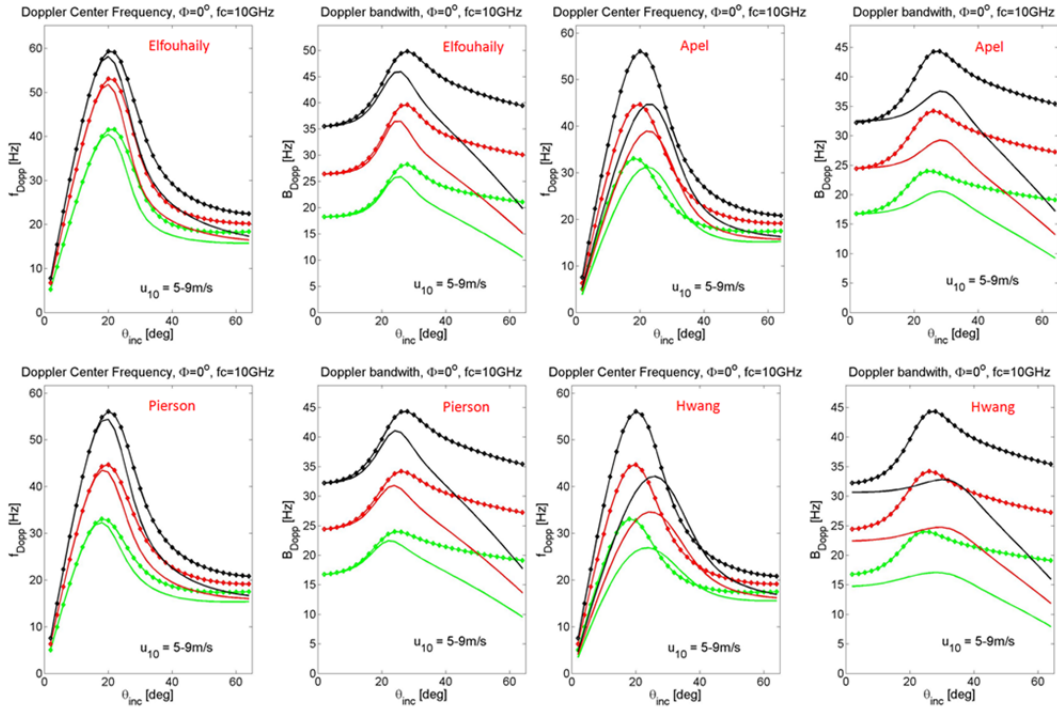


Fig.4.3. Comparison of KA (solid lines) and KA-CWM (solid lines with diamonds) Doppler shift and Doppler spread, at X-band (10 GHz) for 3 different wind speeds: 5 (green lines), 7 (read lines) and 9 (black lines) m/s, upwind. Four input sea surface wave height spectra are analyzed: [Elfouhaily et al.,1997; Apel, 1994; Pierson & Moskowitz, 1964; Hwang et al., 2011].

$$\begin{aligned}
 B_{\alpha_s \alpha_i}(\mathbf{k}_s, \mathbf{k}_i) - \frac{i}{4} \int M_{\alpha_s \alpha_i}(\mathbf{k}_s, \mathbf{k}_i, \xi) h(\xi, t) e^{i\xi \cdot \mathbf{r}} d\xi \approx \\
 B_{\alpha_s \alpha_i}(\mathbf{k}_s, \mathbf{k}_i) \cdot \text{Exp} \left[-\frac{i}{4B_{\alpha_s \alpha_i}(\mathbf{k}_s, \mathbf{k}_i)} \int M_{\alpha_s \alpha_i}(\mathbf{k}_s, \mathbf{k}_i, \xi) h(\xi, t) e^{i\xi \cdot \mathbf{r}} d\xi \right]. \quad (4.24)
 \end{aligned}$$

This simple model is often called High-Frequency Approximation of SSA2, or SSA2-HF. Our simulations confirm the adequacy of this approximation for the computation of the NRCS. As depicted in Figure 4.4, in fact, there is no significant difference in NRCS between SSA2 and SSA-HF. We cannot say the same for the Doppler shift, since the high-frequency approximation leads to an overestimation of the Doppler central frequency, particularly for HH polarization. This is clearly shown in Fig.4.4a, where the SSA2 model (for a linear surface) and the SSA2-HF model are compared at C-band for wind speed of 5 m/s (upwind). Although, the two models provide about the same Doppler bandwidth (Fig. 4.4b) and the same NRCS (Fig. 4.4c), the estimated Doppler shifts in HH-polarization look very different and this makes the equation (4.24) questionable when used to accurately estimate the Doppler signature of the sea surface.

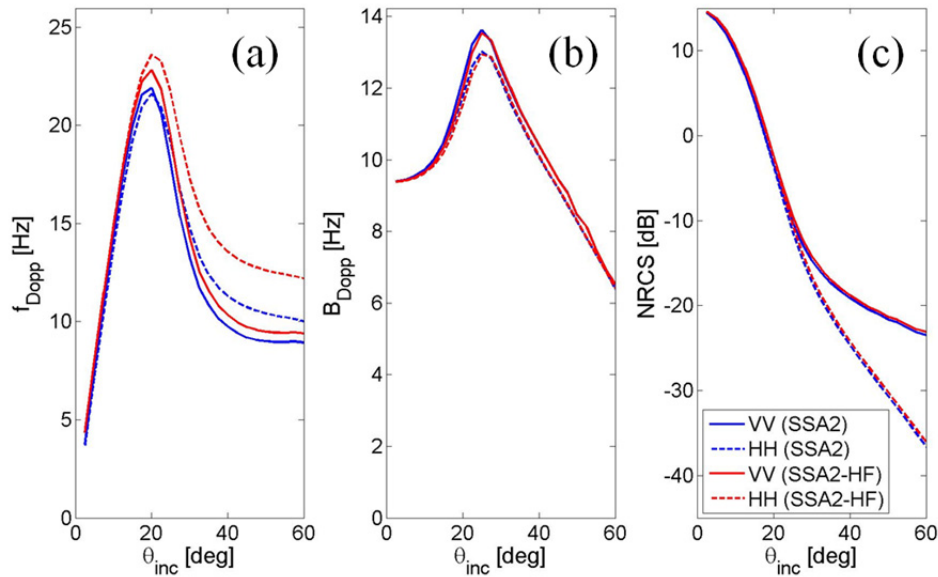


Fig. 4.4. Comparison between SSA2 (linear surface case) and its high frequency approximation at C-band (5.3 GHz) for 5 m/s upwind. The Elfouhaily spectrum has been used as input for the calculation.

An additional drawback of this simplified model is its inability to estimate cross-polarized scattering components in the plane of incidence.

4.4 Observing Systems and Measurement Campaigns

4.4.1 The SAXON-FPN Campaign

The Synthetic Aperture Radar and X Band Ocean Nonlinearities (SAXON)-Forschungsplattform Nordsee (FPN) program was a 3-year campaign with the main objective of the ocean microwave scattering. The program was a joint effort between Germany and the United States. The experiment was split into two phases. Phase I took place in the North sea on and around the German Forschungsplattform Nordsee (FPN) during November 1990. Phase II consisted of a smaller field experiment on the same platform in November 1991, and a series of four workshops.

In this study, we use the data collected between December 10 and 15, 1991, during phase II of the SAXON-FPN experiment [Plant & Alpers, 1994]. Two coherent, continuous wave (CW) microwave systems with pencil beam antennas were operated from the German research platform. These systems operated at Ku and Ka bands, 14 and 35 GHz, respectively. Each system used two antennas, one for transmitting and one for receiving. Both antennas were dual-polarized, and the two polarizations were separated upon reception by offsetting the transmitted frequencies by 60 MHz. Only like polarizations, HH and VV on transmission and reception, were recorded. One way, half-

power antenna beam widths at Ku band were 6.6° in the E -plane and 5.0° in the H -plane. The antennas were operated at a height of 26 m above mean low water level. The antenna foot-print on the surface varied from $3 \times 5 \text{ m}^2$ at 50° to $5 \times 10 \text{ m}^2$ at 80° incidence. The spot sizes were much smaller than the dominant wavelengths which ranged from about 60 to 150 m during the experiment. The presence of sea currents during the measurements is unknown, although one of the instruments deployed during the SAXON-FPN campaign was a current meter. Data were sampled at 3150 Hz per channel, separated into in-phase and quadrature channels for each polarization. Calibration constants were determined both before and after the experiment as described in [Plant *et al.*, 1994].

4.4.2 The ENVISAT-ASAR Data Sets

The Doppler shift measurements from ASAR Wave Mode (WM) and Wide Swath Mode (WSM) images represent a unique data set providing new insights on both kinematic and dynamic properties of the radar-detected moving ocean surface.

Data collected in Wide Swath Mode (i.e. ScanSAR mode) cover wide strip images, 405 km size, with 150 m-resolution, in HH or VV polarisation.

The Wave Mode of the instrument was originally used to record the changes in backscatter from the sea surface due to ocean wave action. Wave Mode data cover vignettes with a minimum size of 5 km x 5 km spaced 100 km along-track in HH or VV polarisation. The positions of the wave vignettes across-track correspond to two different incidence angles: 23° and 33.5° .

For each Level-1b product, Doppler shift anomalies are obtained by subtracting the predicted geometrical Doppler shift, corresponding to the relative motion between the satellite platform and the rotating Earth [Raney, 1986], from the measured Doppler centroids. The Doppler centroid is estimated using Madsen's method [Madsen, 1989] and further refined using the look-power-balancing algorithm [Jin, 1996]. The Doppler centroid determines the centre frequency of the azimuth matched filter in the SAR processor. An accurate estimation of this quantity is essential for the ground processor, as it affects not only the image focusing but also the noise and ambiguity levels of the processed image.

Grids of estimated Doppler centroids and anomalies are included in ASAR Level-1b products. The grid sampling is regular in slant range and corresponds, on ground, to about 9 km at near swath and 3.5 km at far swath. The along-track sampling is about 8 km. The Doppler anomalies represent the motions of the observed scenes relative to the fixed Earth. However, the Doppler anomalies cannot be linked to geophysical quantities unless

additional corrections are applied. Variations of backscattering in along track can generate a bias in the estimates of the Doppler centroid: such a bias need to be compensated for. A viable way to do this is by using Madsen's method [Madsen, 1989] and the look-power-balancing algorithm [Jin, 1996].

A second independent bias might arise when the antenna pattern model, used in the ground processor, does not accurately reproduce the shape of the actual antenna pattern. A third error is generated by existing inaccuracies in satellite orbit and attitude parameters. Together, these last two errors generate an offset which varies strongly with the elevation angle (e.g. off-nadir angle) and varies slowly with time. Such an offset can be considered constant along azimuth and can be corrected by subtracting the average Doppler Centroid value for the portion of each azimuth line which is over land (where the geophysical Doppler shift is assumed zero). The detailed description of the computation and calibration (i.e. correction) of the Doppler centroid anomaly is given in [Hansen *et al.*, 2011]. After correction, the resulting Doppler anomalies for WM Level-1b products are provided with about 5 Hz Root Mean Square (RMS) errors, corresponding to slant range velocity accuracies of 0.35 m/s at 23° incidence and 0.21 m/s at 33.5° incidence angle. Corrected Doppler anomalies from ASAR Wave Mode and Wide Swath Mode are used in the next section to validate the SSA2-CWM model. By collocating wind measurements from ASCAT scatterometer [Figa-Saldaña *et al.*, 2002] with calibrated Doppler centroid anomalies retrieved from Envisat ASAR, an empirical geophysical model function (CDOP) has been developed [Mouche *et al.*, 2012; Collard *et al.*, 2008]. This model predicts Doppler shifts at both VV and HH polarizations as function of incidence angle, wind speed and wind direction with respect to radar look direction. The CDOP model is the counterpart of the C-band MODel (CMOD) function [Stoffelen and Anderson, 1997], which relates NRCS to wind.

4.5 Numerical Results and Comparison with Measurements

4.5.1 Linear versus Nonlinear Sea Surface

In this section, we compare the Doppler spectra corresponding to dynamic non-linear choppy sea surfaces and to linear sea surfaces. The wind speeds used for the comparison are 5 m/s, 9 m/s and 13 m/s. Three incident wave frequencies are analyzed: 5.3 GHz (C-band), 10 GHz (X-band) and 14 GHz (Ku-band). Figure 4.5 shows Doppler shift, Doppler spread and Normalized Radar Cross-section. Three colours are used to represent the wind speed behaviour: the blue lines refer to 5 m/s, red lines to 9 m/s and finally green lines refer to 13 m/s. Solid lines are used for VV polarization, dashed lines for HH

polarization, whereas the lines with circles depict the VH polarization. As anticipated from the theory, we observe a polarization dependency. The predicted wind-induced Doppler shift is larger in HH than in VV polarization. This result is not surprising, because the radar signal is more sensitive to the smaller waves in VV polarization than in HH. On the contrary, the radar signal is more sensitive to larger propagating waves in HH polarization than in VV polarization. Shorter gravity ocean waves are slower, whereas larger propagating waves are faster. As compared to the co-polar signals, the cross-polarised backscatter experiences a much lower Doppler shift across the full range of incidence angle investigated, due to its different scattering properties. The Doppler shift of the cross-polarization looks less sensitive to wind speed variations than the co-polarization; in fact, the blue, red and green f_D curves almost overlap above 30° incidence angle. Another important difference is that the central Doppler frequency for the co-polar signal shows an evident peak around 22° incidence, whereas this peak is not visible in VH polarization. For the co-polar case, the Doppler width B_D , experiences a peak around 25° incidence, whereas for angles above 25° it decreases almost linearly. For the cross-polar case, instead, B_D , does not show any peak and, at low incidence angle ($\theta_{\text{inc}} < 20^\circ$), B_D is expected to be larger than its co-polar counterpart. An even more evident difference is observed on the NRCS, which is found weakly sensitive to the incidence angle in VH polarization (because of the absence of specular contribution in the scattering mechanism) and very sensitive to θ_{inc} in VV and HH polarizations.

Figure 4.6 provides the same information as Figure 4.5 but for a non-linear CWM sea surface. At small incidence angles, linear and non-linear Doppler spectra almost coincide, because the influence of the horizontal velocity component on the Doppler spectrum is small. As the incidence angle increases, non-linear sea surfaces show larger Doppler central frequency and Doppler spread than the corresponding linear sea surfaces. This happens because the Choppy Wave Model corrects the horizontal component of particle velocities by adding a displacement, related to the surface elevation, to the horizontal position of the particles. These considerations are also supported by the results found in [Toporkov and Brown, 2000; Li and Xu, 2011; Nie *et al.*, 2012].

In the linear case (see Fig. 4.5), VV and HH Doppler spectra almost overlap at low incidence angles: the relative shift between the two spectra increases with the angle of incidence in the range 20° - 50° (with the H-pol central Doppler frequency being larger than the V-pol one) and eventually decreases at very high incidence angles (i.e. above 50°). For non-linear surfaces, instead, the relative shift between the two co-polar spectra keep growing above 50° , with the horizontal polarization displaying increasingly larger values than the vertical polarization.

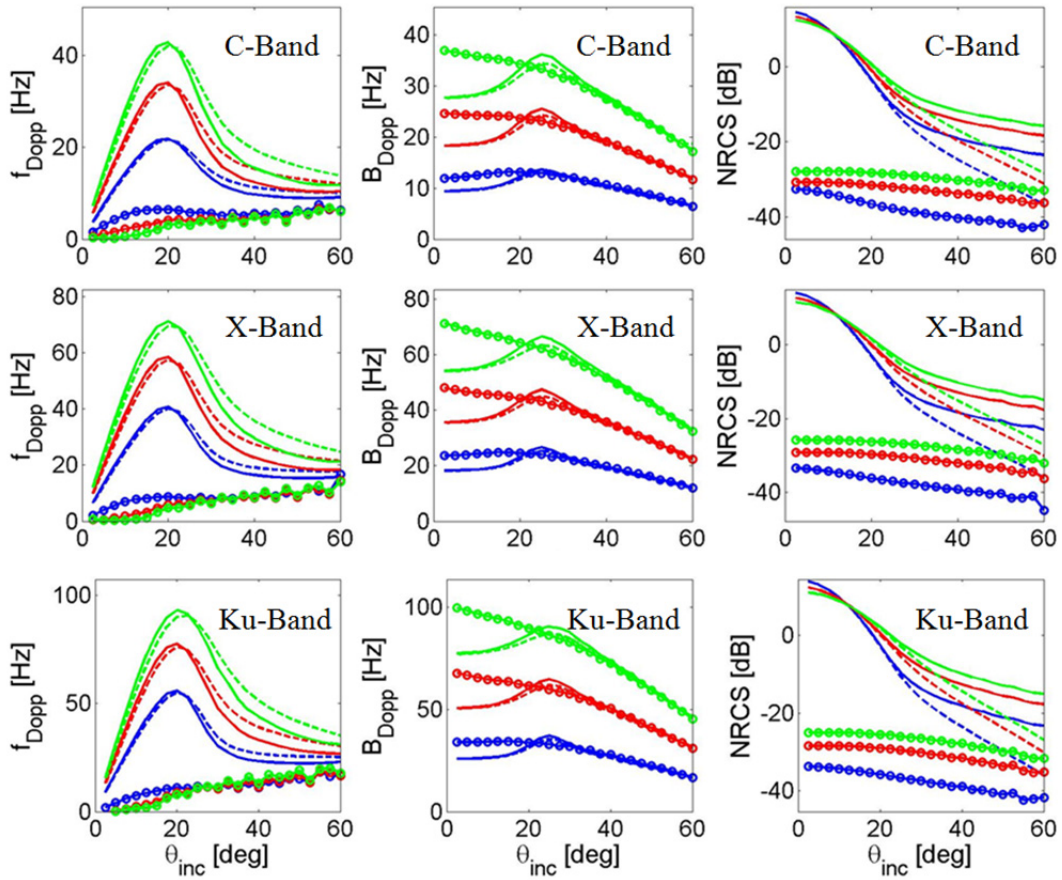


Fig. 4.5. Doppler shift, Doppler Bandwidth and NRCS computed by SSA2-LIN at three different bands: C-band (1st row), X-band (2nd row) and Ku-band (3rd-row). Green lines refer to 13 m/s wind speed (up-wind), whereas the red and blue lines refer to 9 and 5 m/s respectively. In the figures dashed lines are used for HH, solid lines for VV and circles for VH.

By comparing Figure 4.5 and 4.6, the dependence of the cross-polar Doppler signatures on the wind speed is about the same, with the exception of a small decrease in the cross-polar Doppler shift, as result of the CWM transformation.

As already pointed out for the simple KA model, also for SSA2 the Doppler width is found much larger than in the linear case above 30° incidence, where B_D falls off rapidly for linear surfaces. It is worth noting that the Doppler bandwidth in VV polarization is found larger than the one in HH polarization, particularly for higher incidences and speeds. The difference between B_D in VV and B_D in HH is almost negligible at small incidence angles and becomes visible above 30° . Compared to SSA2-CWM, the SSA2-LIN provides slightly different normalized cross-section with maximum differences occurring at high incidence angles, up to 1 dB at Ku-band, 1.5 dB at X-band and about 2 dB at C-band, for the wind speeds investigated.

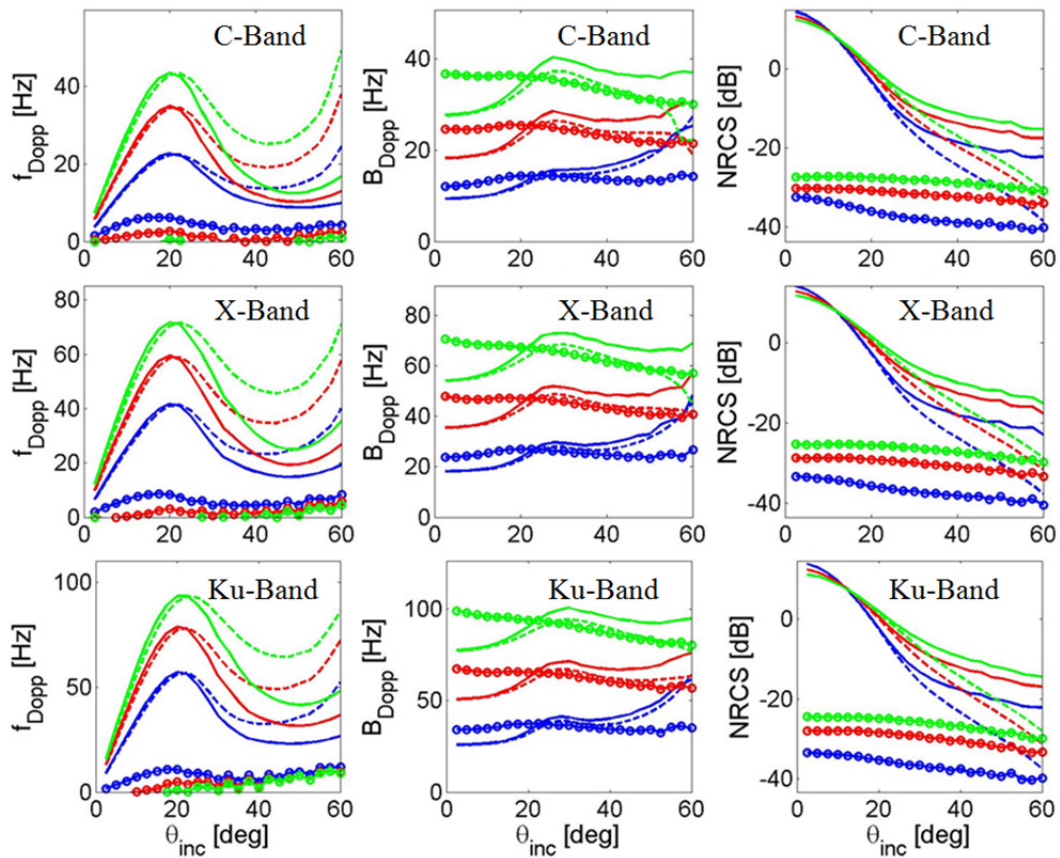


Fig. 4.6. Same as Fig.4.5 but for SSA2-CWM (see text).

4.5.2 Comparison with measurements and empirical GMFs

To validate the model, we use the WM (Wave Mode) data collected by the Advanced Synthetic Aperture Radar (ASAR), onboard the ENVISAT satellite. The C band (5.35 GHz) instrument was able, during ten years of mission, to obtain measurements of Doppler anomalies versus wind speeds as reported in [Mouche *et al.*, 2008; Chapron *et al.*, 2005]. Two incidence angles were investigated: 23° in VV polarization and 33.5° in VV and HH polarizations. In both cases, the Doppler shift was evaluated over a 10×10 km² area. In [Mouche *et al.*, 2008], the authors state that with such a resolution cell the effect of sea current on the measurements of central Doppler frequency was negligible. Collocated wind speed and direction measurements were used to find a relationship between the radial wind speed component and the induced Doppler shift.

In Figure 4.7, we present the results given by our analytical model, based on SSA2-CWM (and Elfouhaily wave height spectrum), considering only wind speeds in up-and down-wind direction. The white curves correspond to our model, whereas the dashed black curves refer to the CDOP [Mouche *et al.*, 2012] geophysical model function. The solid black line instead refers to the high frequency approximation of the scattering model, as

described in section 4.3.4 (for a more detailed description of this model, the reader may refer to [Mouche et al., 2008]). The simulated SSA2-CWM Doppler frequency shifts display a functional relationship versus wind speed in good agreement with the observations, up to a wind speed of ± 15 m/s. The consistency of SSA2-CWM with the data at 23° incidence in VV polarization is particularly remarkable. As shown in Fig.4.7a, the high-frequency approximation by Mouche et al. [2008] reproduces also rather well the ASAR data at 23° in VV-polarization, whereas at 33.5° incidence and low wind speeds it overestimates the Doppler shift for both polarizations. The joint distribution map of Fig. 4.7a looks approximately centrosymmetric: in fact, it shows about the same behaviour in up-wind and down-wind cases, except for the different sign of the Doppler shift. At 33.5° incidence, instead, the joint distribution maps (in VV and HH-polarizations) of observed Doppler anomaly and line-of-sight winds show some asymmetries between up-wind and down-wind. In particular, the absolute measured Doppler shift in up-wind is a few hertz larger than in down-wind (see Fig. 4.7b-c). The fact that SSA2-CWM was not able to reproduce such asymmetry does not surprise, as the Choppy Wave Model is a weak non-linear sea surface model. The measurements collected at 33.5° incidence, show that the scatterers in HH-polarization are faster than in VV-polarization: horizontally polarized Doppler spectra are, in fact, shifted toward higher frequencies than the corresponding vertically polarized spectra. This was also observed at X and Ku band both at sea and in tanks [Lee *et al.*, 1995, 1996; Plant *et al.*, 1997,1999] and more recently at L band [Forget *et al.*, 2006]. This phenomenon was interpreted as the manifestation of bound waves or non-Bragg mechanisms. Numerical computations conducted with SSA2-CWM (and reported in Fig. 4.7b-c) confirm the role of water waves non-linearities in the difference between the HH and VV Doppler spectra, by reproducing (both qualitatively and quantitatively) the main features of the observed wind-driven Doppler shift, as a function of incidence angle, wind speed and polarization of the electromagnetic waves. In Figure 4.8, we have further analyzed the difference between f_D in VV and HH polarization at 4 different incidence angles (30° , 35° , 40° and 45°). Comparisons with the CDOP relative Doppler shift between HH and VV polarization, show a good agreement. As additional verification, we use the data collected between December 10 and 15, 1991, during phase II of the SAXON-FPN experiment [Plant & Alpers, 1994]. Fig. 4.9 shows an analysis at Ku-band of the measured Doppler shifts and bandwidths in HH and VV polarizations as function of wind speed and direction (for 50° and 60° incidence).

The measurements are compared with the analytical SSA2-CWM model. This figure clearly shows the increase in the HH-VV difference with increasing incidence angle when looking upwind and also shows that this difference disappears when the antennas are

directed perpendicular to the wind direction. Furthermore, the data indicate a slight tendency for the offset difference to increase with increasing wind speed for the upwind case. It is worth noting that both VV and HH offsets are negative when the antenna look direction has a downwind component. The modulation of f_D with the wind direction predicted by the model looks overall in good agreement with the measurements taken at different wind speeds.

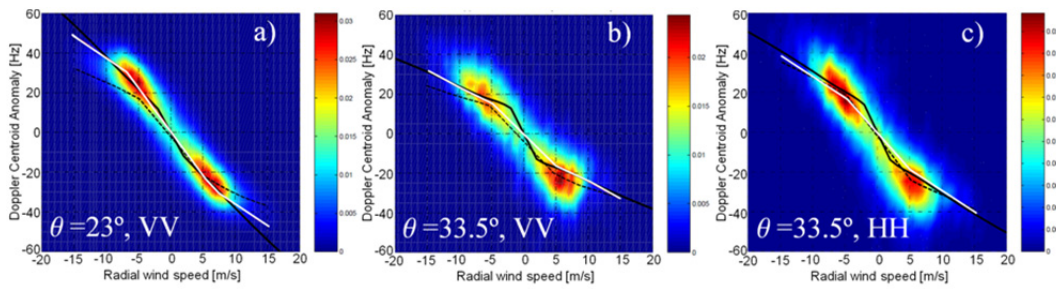


Fig. 4.7. Joint distribution maps of observed Doppler anomaly (at C-band) and line-of-sight winds versus predictions given by our analytical SSA2-CWM (white curves) model for up-wind (positive wind speed values) and down-wind cases (negative wind speed values). In dashed black the Doppler shifts provided by the CDOP empirical model and solid black the Doppler shifts as predicted by the High-frequency approximation of the scattering model, proposed by Mouche et al. in [2008]. (a) VV polarization and 23° incidence angle, (b) VV polarization and 33.5° incidence angle, (c) HH polarization and 33.5° incidence angle. The colours used in the Doppler maps represent the occurrence of the ASAR measurements.

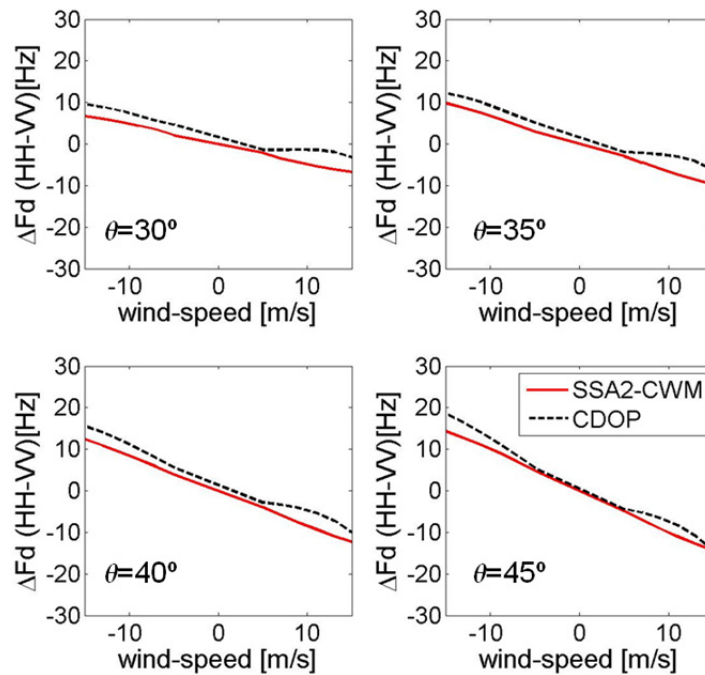


Fig. 4.8. Difference between the VV and HH central Doppler frequency as derived by our analytical SSA2-CWM model (in red) and as provided by the CDOP Geophysical Model Function (in black).

In Figure 4.9, the squares and the circles refer to VV and HH measurements respectively. Blue, red and green colours identify the measurements corresponding to wind speeds within the range 0-5 m/s, 5-10 m/s and 10-15 m/s respectively. Overlaid are the simulated results: in particular, solid lines represent VV simulated data and dashed lines HH simulated data.

The analysis is made at three wind speeds: 5 m/s (blue lines), 10 m/s (red lines) and 15 m/s (green lines). From our simulations, the Doppler bandwidth, B_D , is expected to show an almost flat behaviour versus the wind direction: this is found consistent with the measurements. As opposed to the real data, the simulations predict a slightly larger bandwidth in V-pol than in H-pol. We have limited our investigation up to 60° incidence, because above this limit the main hypothesis at the basis of the Small Slope Approximation Theory may be violated, as the tangent of grazing angles of incident/scattered radiation may not sufficiently exceed the rms slope of roughness for most winds.

4.6 Conclusions

The Doppler shift measured by a space-borne active microwave instrument over the ocean can be expressed as the sum of three main terms:

$$f_{D_Total} = f_{D_wind} + f_{D_current} + f_{D_geometry}$$

These terms represent the contributions to the central Doppler frequency associated with the wind, e.g. wind drift, (polarization dependent), the ocean current (polarization independent) and the geometry of observation (polarization independent). Nowadays, thanks to the very accurate knowledge of spacecraft attitude and motion, the last term can be easily estimated and removed to get a geophysical Doppler shift or velocity. A last geophysical processing step is then needed to estimate the radial surface current. This final step, is definitely the most complex one because it must rely on a Geophysical model function providing the wind driven Doppler shift associated with a specific wind speed and direction. With this picture in mind, the analytical model described in this chapter could be a valuable tool to retrieve ocean surface currents. The results reported in the previous sections show that the ocean Doppler spectrum at microwave frequencies can be different for different polarizations. Co-polar scattering experiences Doppler frequency shifts higher than the cross-polar scattering. The Doppler shift increases with the wind-speed. The rate of this increase depends on the wind directions (as we approach the cross-wind direction, the wind-speed sensitivity gets weaker).

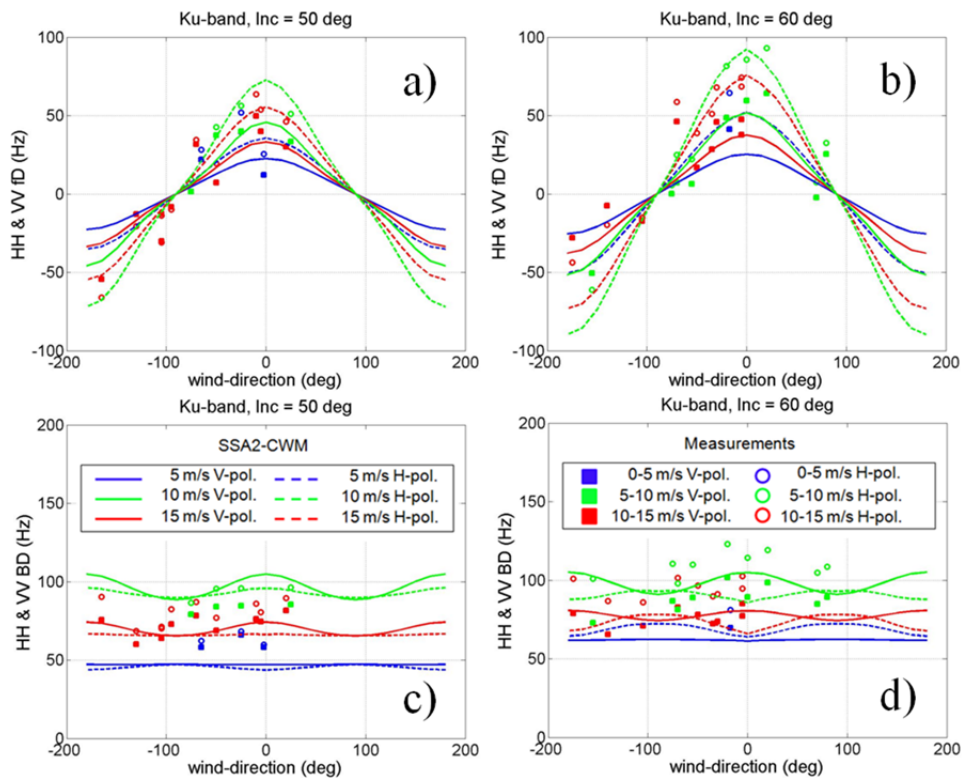


Fig. 4.9. Difference at Ku-band between HH and VV Doppler offsets and spread as function of the angle between the antenna look direction and the wind direction at two incidence angles: 50° (a)-(c) and 60° (b)-(d). Blue, red and green colours identify the measurements corresponding to wind speeds within the range 0-5 m/s, 5-10 m/s and 10-15 m/s respectively. Overlaid are the simulated results: in particular, solid lines represent VV simulated data and dashed lines HH simulated data. The analysis is made at three wind speeds: 5 m/s (blue lines), 10 m/s (red lines) and 15 m/s (green lines).

In principle, we could use the frequency shift between two polarizations (VV-HH, HH-VH or VV-VH) to identify the wind contribution to the sea surface velocity, thus allowing for the observation of ocean currents.

In this chapter, we have presented an innovative analytical model for the full-polarimetric sea surface scattering and Doppler signature based on the Small Slope Approximation Theory at the 2nd order combined with a weakly non-linear sea surface representation, named Choppy Wave Model. This would be the first full polarimetric physical based model describing both scattering and Doppler signature of non-linear sea surfaces. The analytical expression of the model avoids the use of highly demanding Monte-Carlo simulations which are required for more physically based models using exact numerical solution of Maxwell's equations. By using an Intel® Core™ i5-4590 Processor (Quad Core, 3.30GHz Turbo, 8GB DDR3 SDRAM at 1600MHz), no more than 4 hours are needed to generate NRCS, Doppler shift and Doppler spread versus incidence and direction angles at 5 different wind speeds, at 3 different frequencies bands. All the simulations have been performed considering a 2D sea surface representation, whereas most of the results in the literature refer to a 1D sea surface representation. To

our knowledge, only few attempts to describe the sea surface scattering and Doppler signature of a 2D sea surface have been made [Soriano *et al.*, 2006; Li & Xu, 2011]; but those attempts were always limited, due to computational constraints, to very low wind speeds ($< 5\text{m/s}$) and low frequencies (L-band).

Simplified scattering theories have been derived from the proposed SSA2-CWM model. Simulation results have been compared with real measurements from Envisat-ASAR and from the SAXON-FPN Ku-band campaign, showing remarkable agreement. The results are also consistent with the empirical Geophysical model function CDOP. In future prospective, this model could be used to resolve one of the biggest unknowns in ocean current retrieval: the determination of the wind-driven contribution to the total sea surface Doppler shift. The SSA2-CWM model may also support the definition and the exploitation of new observation principles, based on multi-polarimetric Doppler Scatterometry, such as the DopSCAT concept [Fabry *et al.* 2013], aiming to provide simultaneous measurements of the Ocean Vector Wind and the Ocean Vector Current on a global scale. The proposed Doppler model is also particularly suited to the interpretation of along-track interferometric synthetic aperture radar data, which include information on surface currents.

5 Toward the Definition of a Future Mission Concept

In the atmosphere, it is primarily heating that drives the global circulation and winds. The latter, in turn, determine the characteristics of the air-sea interaction and drive ocean surface currents together with the overturning circulation. Both the atmosphere and the ocean exhibit a complicated circulation pattern and their interaction determines much of the climate variability on time scales from several hours to seasons, years, decades and millennia. Understanding this variability is essential to detect and predict climate change arising from external sources, such as solar irradiance variations and human activities. Improved knowledge of the dynamics of the global ocean circulation thus becomes imperative for predicting climate change. An accurate prediction of climate conditions requires global measurements of the forcing of the ocean waters and of their motion. Ocean flows depend on aspects such as temperature and salt content, which together determine mass density and hence vertical movements. The ocean water flows include the major ocean currents which are continuous (with fluctuating velocity and position), medium and small scale circulation features (eddies), coastal and tidal currents as well as waves generated by wind. Satellite altimetry has led to significant improvements in the understanding of the large scale (> 200km) oceanic circulation [Fu *et al.*, 2010; Zhang *et al.*, 2007], providing unequalled views of the ocean eddy field and its kinetic energy on a global scale, and advance our understanding of ocean dynamics and its variability. Existing altimeters are capable of measuring large-scale changes in the ocean such as El Niño, La Niña and sea level variations. However, the wide spacing of several hundred kilometers between the satellite ground tracks severely limits the cross-track resolution. As a matter of fact, Sea Surface Height (SSH) products have spatial resolutions coarser than 100 km and temporal resolutions of about 10 days. Therefore, satellite altimetry cannot measure the small-scale (20- 100 km) ocean eddies, which contain most of the energy and empower the mixing and transport of water. These processes are important in determining how fast climate is changing. In the last years, new technologies have been developed in order to enhance future altimetric missions (namely SWOT [Durand *et al.*, 2007] and WaveMill [Gommenginger *et al.*, 2014] concepts) and virtual constellation possibilities have been studied (e.g. Jason [Bannoura *et al.*, 2005], CryoSat-2/SIRAL [Galín *et al.*, 2013], SARAL/AltiKa [Abdalla *et al.*, 2014], HY-2 [Wang *et al.*, 2013], Sentinel-3/SRAL [Le Roy *et al.*, 2009]). Ocean currents and eddies, at scales shorter than

100 kilometers, play a key role in the transport of heat, carbon and nutrients in the ocean. Short-scale currents and eddies affect global climate through modulation of sea surface temperature and heat flux, as well as in the oceanic uptake of carbon dioxide from the atmosphere. Large-scale (thousands of kilometers), long period (> 1 year) oceanic circulations are driven by small-scale, short-period atmospheric forces and oceanic processes [Freilich, 2002; Milliff *et al.*, 1999; Large *et al.*, 1991]. The wide range of important oceanic time and space scales, and their intrinsic coupling, represents the most challenging problem for the design of future ocean observing systems. Gaining knowledge on short-period, small-scale air-sea interaction processes and on the coupling among scales would lead to improvements in the ability of computer models to predict future climate changes. Consequently, future ocean observing missions shall require global measurements of the important small-scale forcing, with revisit times (dictated by selected orbit and measurement geometry) sufficiently short to guarantee an adequate sampling of the associated processes.

Eddies in the North Atlantic have typical radii of 20-30 km, amplitudes of 45 cm, and translational velocities of 2.5 km/day [Fabry *et al.*, 2013]. This would require daily measurements with spatial sampling of 10-20 km. Consequently, observation requirements in terms of spatial resolution will certainly go even below 25 km resolution. For coastal applications, the constraints in terms of spatial resolution and revisit time are even more stringent thus challenging the performance of future ocean observing systems.

Conventional interferometric techniques [Romeiser and Thompson, 2000] provide measurements of sea surface scatterer velocities by computing the phase difference among two return signals from the same point at two different times. It is also possible to measure sea surface velocities from estimates of the SAR Doppler anomalies [Chapron *et al.*, 2003, 2005]. Although both techniques provide velocity products at high spatial resolution (order of kilometers), they have several disadvantages: the lack of global coverage due to frequent mode-switching and duty-cycle limitation, the poor temporal coverage and the fact that only one component of the surface wave motion vector can be measured. In addition, the line-of-sight velocity depends on the wind field [Chapron *et al.*, 2005; Mouche *et al.*, 2008; Johannessen *et al.*, 2008], which influence has to be correctly removed before the strength of the range-directed surface current can be determined; for SARs, this correction is possible only if the ocean wind vector is accurately known by other means.

Scatterometers, on the other hand, with an antenna that provides multiple views, global ocean coverage and simultaneous wind vector estimation, appear, at first glance, to be ideal candidates for ocean surface current mapping using Doppler shift information.

Nowadays, radar scatterometers are primarily designed to measure wind speed and direction from ocean radar backscatter, with spatial resolutions of tens of kilometers and swath widths wider than thousand kilometers. As these instruments were not specifically designed for Doppler measurements, new observation principles and data processing techniques must first be developed and validated. The combined availability of Ocean Vector Winds (OVW) and Ocean Vector Motion (OVM) would further allow a better comparison of earth-fixed atmospheric model, or in situ observed winds, and the ocean-relative winds from the scatterometer. Ocean winds are affected by currents and also by the temperature variations across ocean eddies which cause variations in atmospheric stability. Collocated OVW and OVM measurements would potentially resolve these effects.

Starting from the principles of ocean Scatterometry, this chapter presents an innovative microwave mission concept, called DopSCAT (Doppler Scatterometer), capable of resolving small-scale features and their variations in time and space, with the objective of providing simultaneous worldwide measurements of OVW and OVM for operational use in weather and marine forecasting. Section 5.1 of this chapter identifies the background and scientific issues to be addressed by Ocean Doppler Scatterometry, considering the contribution of past and present activities in the field. It provides a scientific justification for the mission, summarizes the specific research objectives of Doppler Scatterometry and outlines the mission requirements, including required geophysical data products and observational parameters. Section 5.2 provides an overview of the system elements, including instrument design, principle of observation, data processing and calibration. Section 5.3 makes a comparison of expected versus required performance and ability to fulfill the research/observational objectives based upon the documented system concept. This chapter is based on results published by the authors in [Fois *et al.*, 2015c, 2015d].

5.1 User Requirements and Observing System Specifications

5.1.1 Background

In the following we give an overview of the main remote sensing techniques which are used to measure ocean currents.

Satellite altimetry provides estimates of surface ocean currents in geostrophic balance at a course resolution. In a geostrophic current, pressure gradient force and Coriolis force balance each other. The geostrophic balance holds only for currents having spatial scales larger than a few tens of kilometers and time scales longer than several days. In the tropics and elsewhere at the smaller spatial and temporal scales the ageostrophic

components of the currents become dominant, particularly in coastal areas where bathymetry and tidal flows play a major role in driving currents.

Satellite Synthetic Aperture Radars (SARs) provide accurate measurements of the surface current in line-of-sight [Chapron *et al.*, 2005]. One of the parameters required to perform the azimuth processing of a Synthetic Aperture Radar image is the Doppler shift (i.e. centroid) of the return echo signal. The Doppler shift is generated by the relative motion between satellite, rotating Earth and the dynamic sea surface. The Doppler centroid can be estimated from measurements of sensor trajectory and attitude or by analyzing the characteristics of the received data in the Doppler frequency domain [Madsen, 1989]. The first method can be used to compute the Doppler shift associated with the relative motion between the satellite platform and the rotating Earth. The second method, instead, computes the total Doppler shift, that includes not only the relative motion between satellite and rotating Earth but also possible motions of the observed targets. The difference between the two Doppler shifts has a geophysical meaning, as it “quantifies” the sea surface movement. However, a mandatory condition to give geophysical meaning to the measured Doppler centroid is that the attitude of the platform must be known with sufficient accuracy, so that its effect can be subtracted to derive the sea surface velocity information [Johannesen *et al.*, 2008]. This sea surface velocity has two main contributions: the wind-wave induced motion, and the background surface current. If the wind-wave induced ocean surface motion in the range direction can be estimated, then the remaining Doppler shift can be attributed to the surface current in the line-of-sight of the radar instrument. Although the Doppler anomaly derived from satellite SAR instruments provides high spatial resolution surface current estimates, the limited SAR data coverage and the fact that surface velocity can only be extracted in the radar line-of-sight hamper the capability of the technique in measuring ocean surface current vectors. Furthermore, the range Doppler ambiguity of the pulse compression waveform (often a linear FM up-chirp) limits the accuracy.

SAR Along Track Interferometry (ATI) provides measures of the Doppler shift of the backscattered signal by performing a difference in phase between two images of the same area of the ocean, collected with a time-lag sufficiently shorter than the decorrelation time of the ocean, which depends on environmental conditions (e.g. wind speed and direction). As for the SAR also for ATI only the line-of-sight of the velocity vector can be measured. Typically, along track interferometry requires the use of two satellites flying in formation and this makes the costs of the mission development and operations very high.

Thermal and Visible Imagery represents a viable way of estimating advective ocean surface currents from sequential infrared satellite imagery, by means of the Maximum

Cross-Correlation (MCC) technique [Emery *et al.*, 1986; Crocker *et al.*, 2007]. This technique has been proven to be useful in mapping the short space and time scale structures of the East Australian Current [Bowen *et al.*, 2002, 2005], the California Current [Tokmakian *et al.*, 1990], the Gulf Stream and the coastal waters off British Columbia [Emery *et al.*, 1986, 1992]. The capability of the MCC method is very limited in case of low surface gradients, cloud cover and isothermal flow. The technique fails over areas that do not show strong and coherent features over several days.

Sun glitter Mean Square Slope [Kudryavtsev *et al.*, 2012a; 2012b] is a method to retrieve and interpret fine spatial variations of the sea surface roughness in sun glitter optical imagery. The retrieval processing makes use of a transfer function relating the sun glitter brightness contrast to the mean square slope contrast. The results document significant benefit from the synergetic use of sun glitter and radar imagery for quantitative investigations of surface signatures of ocean phenomena, including internal waves and mesoscale ocean currents.

GOCE (Gravity and steady-state Ocean Circulation Explorer): A primary goal of the GOCE mission is the global determination of the ocean's geostrophic current systems. GOCE provides estimates of the shape of the marine geoid in radial direction with centimetric precision over spatial scales of 100-200 km. The difference between the mean ocean surface, as derived from satellite altimetry, and the marine geoid provides the ocean steady-state Mean Dynamic Topography (MDT) [Bingham *et al.*, 2011]. The dynamic ocean topography can be mapped into ocean surface circulation, as most of the long-term ocean currents are in geostrophic balance.

Scatterometry provides estimates of the surface wind speed over the ocean based on surface roughness measurements. Differences between the winds from Numerical Weather Prediction (NWP) model and from scatterometers are used to estimate time-varying ocean surface currents [Stoffelen and Vogelzang, 2011]. In fact, scatterometer winds depend on ocean roughness, which is linked to the relative motion between air and sea, whereas NWP model winds are computed with respect to an Earth-fixed frame.

Microwave Imager can be used to derive sea-ice motion by following the displacement of brightness temperature features in sequential images [Kimura and Wakatsuchi, 2000]. The procedure for the calculation of ice motion is based on the maximum cross-correlation method [Ninnis *et al.*, 1986; Emery *et al.*, 1991]. By using the Thorndike and Colony [1982] relationship between the ice motion and geostrophic wind, the mean ocean current can be derived. The sea-level pressure data produced by the European Centre for Medium-Range Weather Forecasts (ECMWF) is used for the calculation of the geostrophic wind. The effect of the geostrophic wind is subtracted from the ice motion to

generate ocean surface current maps.

Current Earth Observation (EO) measurement systems (e.g. GOCE, CryoSat, SMOS, Sentinel-1) and future EO missions (e.g. Sentinels and MetOp-SG) can, in principle, provide new information on ocean currents. However, these systems are not optimized to estimate ocean surface currents.

5.1.2 User Product Requirements

User requirements for ocean surface current measurements have been derived and presented in Table 5.1, based on outputs from an international User Consultation Meeting (UCM) by the ESA GlobalCurrent Project (GlobCurrent UCM, IFREMER, Brest, France, 7-9 March 2012) [Donlon, 2013]. The requirements are expressed as geophysical quantities with corresponding accuracy, spatial and temporal sampling, coverage and length of data records. The majority of users request higher resolution products closer to the coast (1-2 km), 1-10 km for inland seas and 10-25 km spatial resolution for global products. Based on these user needs, our study shall target global coverage with a spatial resolution of 10-25 km and higher resolution, where possible, at regional and local scales. Hourly products are required in tidal areas, if possible, and daily products as a minimum requirement for all areas. Table 5.1 reveals that a single year of data products is sufficient for demonstration purposes. A long-term archive of at least 10 years (preferably 20 years) is requested by users. The majority of users require near real-time delivery of the products. The accuracy of the products is typically less than 0.20 m/s and independent of current regimes.

Tab. 5.1 Accuracy and resolution needs for different applications [Donlon, 2013]

Application	Coverage	Accuracy [cm s ⁻¹]		Spatial Res [km]		Temporal Res. [hr]		Length of Record [years]
		Thr.	Obj.	Thr.	Obj.	Thr.	Obj.	
Weather Service	Global	20	10	25	12.5	24	6	10+
Ocean Service	Global	20	10	25	12.5	24	1	10
Search and Rescue	Regional	20	10	5	1	24	1	5
Scientific Research	Regional	20	10	25	1	24	6	10
Marine Renewable Energy	Local	20	10	5	0.1	24	1	10
Pollution	Local	20	10	10	0.1	24	1	5
Sailing	Global	20	10	10	--	24	--	--
Ship Routing	Global	10	5	20	1	24	1	5
Wave Forecasting	Global	20	10	25	2	24	0.5	1
Oil and Gas	Local-Reg.	20	10	5	1	24	1	1
Marine Offshore	Global	20	10	25	10	24	6	10
Fisheries Management	Local	20	10	25	1	24	6	10

5.1.3 Observing System Specifications

Addressing the user needs set out in the previous section, requires repeated measurements of ocean currents at temporal and spatial scales compatible with the remote

sensing mission. The envisaged remote sensing component is a C-band dual polarimetric Doppler Scatterometer mission, named DopSCAT. The DopSCAT instrument is a real-aperture fan-beam pulsed imaging radar operating at 5.4 GHz with 6 waveguide-array antennas configured in 3 antenna-pair assemblies similar to those of ESA's MetOp-ASCAT instrument [Gelsthorpe *et al.*, 2000]. Each of the DopSCAT beams acquires a continuous image of the backscattering coefficient of the ocean, called σ° , and a continuous image of the ocean's Doppler shift over the swath. Both sides of the satellite ground-track are illuminated, each with three azimuth views. This geometry of observation foresees a gap between right and left-side swaths. At each acquisition the radar will measure, simultaneously, the σ° and the ocean's Doppler shift. The measurements of the Doppler shift is possible by transmitting two chirps with opposite slopes (i.e. one up-chirp and one down-chirp) at the same time [Fabry *et al.*, 2013], instead of a single chirp, as most of the wind scatterometers do. The received echoes are then processed on ground with two different matched filters, one adapted to the up-chirp and the other to the down-chirp, to generate two different images. The cross-correlation between these images provides accurate estimates of the ocean's Doppler shift. From the three different azimuth views, the OVM can thus be retrieved. The OVW is estimated using the classical processing of wind scatterometers. For each azimuth view, independent looks are summed in range and azimuth, in order to achieve a good radiometric quality of the image on each Wind Vector Cell (WVC). The three σ° measurements of the same WVC (also called σ° triplet) can be related to the wind vector through a Geophysical Model Function (GMF) [Verhoef *et al.*, 2008; Portabella and Stoffelen, 2006]. The wind inversion is based on a search for minimum distance between the measured σ° triplet and simulated backscatter triplets lying on the GMF surface in the 3D measurement space (space of triplets), taking into account instrumental and geophysical noise sources [Portabella and Stoffelen, 2006]. Due to measurement noise and the double harmonic wind direction dependence, multiple solutions are usually found (wind ambiguities), which have to be filtered out using background wind and wind error covariance information provided by a NWP model (ambiguity removal). Accurate measurement of the wind vector is essential to retrieve oceanic surface currents. As a matter of fact, the OVM, related to the Doppler frequency shifts, measured by a space-borne active microwave instrument over the ocean, can be expressed as the sum of three main terms:

$$\mathbf{v}_O^{Tot} = \mathbf{v}_O^{wind} + \mathbf{v}_O^{curr} + \mathbf{v}_O^{sat-earth} . \quad (5.1)$$

These terms represent the contributions to the OVM associated with the surface wave motion induced by the wind, \mathbf{v}_O^{wind} , the ocean current, \mathbf{v}_O^{curr} and the relative motion between satellite and rotating Earth, $\mathbf{v}_O^{sat-earth}$. Nowadays, thanks to the very accurate knowledge of spacecraft attitude and motion, the total OVM or geophysical Doppler shift can be estimated and spacecraft and Earth contributions removed. A last geophysical processing step is then needed to estimate the radial surface current. This final step, is definitely the most complex one, because it must rely on a Geophysical Model Function providing the wind driven OVM associated with a specific wind speed and direction [Mouche *et al.*, 2012; Fois *et al.*, 2015a; Romeiser and Thompson, 2000]. Errors in wind vectors imply errors in the estimates of OVM. In the absence of OVM, measurements of ocean Doppler shift can also be used in combination with preliminary wind field estimates and Geophysical Model Functions (such as SSA2-CWM or CDOP) to improve the wind retrieval accuracy [Mouche *et al.*, 2012]. It is important to highlight that the measurement of \mathbf{v}_O^{Tot} is normally contaminated by radar ambiguities. These ambiguities are associated with the Pulse Repetition Frequency (PRF) of the radar. In order to avoid such ambiguities, the PRF shall be sufficiently high to properly sample the Doppler bandwidth of the radar echoes, with a consequent reduction of the radar swath. As described in section 5.2, the use of a dual chirp, that is a combination of one up-chirp and one down chirp, allows un-ambiguously to measure \mathbf{v}_O^{Tot} without increasing the PRF (thus avoid the reduction of the radar swath).

Selection of Frequency

Historically, European and American scatterometers work at different bands. The European Space Agency uses C-band (5.3 GHz) and the National Aeronautics and Space Administration (NASA) uses Ku-band (14 GHz). At higher frequencies, short ocean waves have stronger influence on backscatter, this explains the higher sensitivity of Ku-band to low-winds. On the other hand, Ku-band is more affected by atmospheric effects. Clouds and rain can significantly attenuate the Ku-band signals. In addition, rain droplets distort the gravity-capillary waves and this can complicate the wind vector retrieval. All these effects become smaller at lower frequencies. We note that the main ocean currents are associated with large SST gradients and therefore, often, with adverse weather. Considering the high technology readiness level of the main radar subsystems (e.g. antenna, travelling wave tube, radar electronics) and the extensive heritage in retrieving wind fields through the use of consolidated Geophysical Model Functions, both frequencies could in principle be suitable to DopSCAT. Although no technology nor

performance limitations have been identified for the two frequencies, the C-band frequency has been retained for this study.

Polarization

Current operating scatterometers use only co-polar scattering to retrieve wind speeds and directions. The main reason behind this design choice is associated with the fact that the Signal-to-Noise Ratio (SNR) in co-polarization is expected to be higher than in cross-polarization for most winds. However, airborne measurements over hurricanes, performed at C-band and Ku-band [Fernandez *et al.*, 2006], have confirmed that co-polar scattering suffers from problems of incidence- and azimuth angle-dependent signal saturation and dampening, which make it only weakly sensitive to wind speed variations above 25 m/s. This shortcoming impairs the ability to provide accurate hurricane warnings. Recently, the analysis of RADARSAT-2 C-band multi-polarization SAR data and collocated wind measurements by the NOAA Hurricane Hunter aircraft [Fois *et al.*, 2014b, 2015b; Van Zadelhoff *et al.*, 2013; Hwang *et al.*, 2010a, 2010b, 2014] have revealed that cross-polar scattering does not show any evident loss of sensitivity for wind speed well above 25 m/s, thus allowing accurate retrieval of strong-to-severe wind speeds. As a consequence, the use of cross-polarization in addition to the most common VV polarization becomes imperative for proper hurricane forecasting with space-borne ocean scatterometers. The results reported in the previous chapter and in [Fois *et al.*, 2015a] show that the ocean Doppler spectrum at microwave frequencies can be different for different polarizations. Co-polar scattering experiences Doppler frequency shifts higher than the cross-polar scattering. The Doppler shift increases with the wind-speed. The rate of this increase depends on the wind directions: as we approach the cross-wind direction, the wind speed sensitivity gets weaker. Geophysical Model Functions such as SSA2-CWM and CDOP can be used to identify the wind contribution to the sea surface velocity (see equation 5.1), thus making the observation of ocean currents possible. The preferred polarization for measuring ocean currents is VV, because of the highest signal-to-noise ratio, which has a direct impact on the accuracy of the ocean motion vector retrieval.

Incidence angle

The incidence angle of the instrument affects both electromagnetic scattering and Doppler signature from the ocean. Typical incidence angles for ocean application range between 20° and 65°. Below 20° the wind directional sensitivity is very poor, whereas above 65° the link-budget performance of the radar are strongly degraded, because of the

very long slant range distances involved and the low values of the normalized radar cross section, which decreases with the incidence angle. On the other hand, in order to obtain clear measurements of surface current it is desirable to observe the ocean at high incidence angles. In fact, high incidence angles reduce the relative contribution of vertical components of wave motions to the Doppler signature of the ocean.

Revisit requirements

As outlined in section 5.1.2, most of the applications require global coverage in 24 hours. This imposes constraints on the swath width and correspondingly on the antenna design, the level of transmit power and the radar instrument timing. With the incidence angle range adopted for DopSCAT (from 20° to 65°), 99% of the Earth is covered within 48 hours, whereas 87% of the Earth is covered within 24 hours.

Doppler measurement capability

The DopSCAT system has to perform Doppler measurements in addition to backscattering measurements. This requirement imposes constraints on the type of waveform to be transmitted, on the instrument timing and on the data processing.

Spatial Resolution and Sampling

In technical terms, the single-look resolution of a scatterometer is limited by the bandwidth of the transmit signal and by the antenna length. Although, single-look data have high resolution, they are impractical to work with, as they are characterized by a large speckle noise. Speckle arises from interference between the different scatterers within a single resolution cell. To reduce this uncertainty, radar intensity images are typically incoherently averaged. The number of independent samples in the average is known as the equivalent number of looks. In section 5.1.2, we have pointed out that the resolution required to meet the DopSCAT mission objectives is between 10 and 25 km on global scale. Accordingly, two types of products can be defined: a nominal product with spatial resolution of $25 \times 25 \text{ km}^2$ and spatial sampling of 12.5 km, along with a high-resolution product with spatial resolution $< 12.5 \times 25 \text{ km}^2$ (across-track \times along-track) and spatial sampling of 6.25 km.

Radiometric Resolution (k_p)

In scatterometry, it has become customary to define the measurement error in terms of the so called k_p parameter, which is the normalized standard deviation of the

measurement error or percentage error. A goal of scatterometer design is the minimization of k_p . The k_p requirement drives the antenna elevation pattern shape, the average transmitted power and the modulation parameters of the transmit signal. For a homogeneous scene, the radiometric resolution can be expressed as:

$$k_p = \sqrt{\frac{1}{N_A N_R} \left(1 + \frac{1}{\left(\frac{S}{N}\right)^2} \right) + \frac{1}{N_N} \left(\frac{1}{\left(\frac{S}{N}\right)^2} \right)}. \quad (5.2)$$

where N_A and N_R are the number of independent along-track and across-track looks, whereas N_N is the number of independent noise looks. The quantity S/N is the Signal-to-Noise Ratio (SNR). The radiometric resolution for the nominal products in VV and VH-polarization shall be compliant with the requirements specified in Table 5.2, corresponding to different wind scenarios. The analytical full-polarimetric scattering model SSA2-CWM [Fois *et al.*, 2014b, 2015a] together with the empirical models CMOD5n [Verhoef, 2008] and VH-GMF [Zadelhoff *et al.*, 2014] will be used in this chapter as geophysical model functions for the transfer between vector wind and backscattering coefficient of the ocean. Portabella and Stoffelen [2006] discussed inhomogeneous scenes, but this is not elaborated here.

Tab. 5.2 Radiometric resolution requirements for different polarizations and wind scenarios

Polarization	Wind Speed [m/s]	Wind Direction	Radiometric Resolution [%]	
			$\theta_i \leq 25^\circ$	$\theta_i > 25^\circ$
VV	4	Up-wind	≤ 3	$\leq (0.175 \theta_i - 1.375)$
VV	25	Cross-wind	≤ 3	≤ 3
VH	15	Up-wind	≤ 15	≤ 15
VH	40	Cross-wind	≤ 5	≤ 5

θ_i is the incidence angle in degrees

Radiometric bias and stability

Two main radiometric parameters are defined for the DopSCAT mission: the *Radiometric Bias* (RB) and the *Radiometric Stability* (RS). The combination of these two quantities provides the *Radiometric Accuracy* (RA), describing the total error in the measurement of σ° . The *Radiometric Bias* is defined as the bias in the measured radar cross-section of a calibration target over the mission lifetime. Correction for this bias (absolute calibration) is unlikely to be critical, as it can be compensated for in the retrieval of geophysical quantities. It becomes relevant principally when comparing data from different reference targets or when DopSCAT’s data are compared with data from other C-band instruments.

A threshold of 0.4 dB (at 1-sigma) is considered adequate, since such constant offsets can be dealt with by cross-calibration. The *Radiometric Stability* is defined as the standard deviation of measurements of the radar cross-section of an unsaturated invariant target, taken at different times. This is critical for a wind scatterometer as the wind vector retrieval relies on the stability of the relationship between backscatter and wind field. A radiometric stability of 0.1 dB at 1-sigma) is considered for DopSCAT.

Radar Ambiguities

Radar ambiguities are important design parameters as they influence technical choices, such as the antenna dimensions, the antenna pattern shape (e.g. side lobe levels) and the instrument timing, e.g. Pulse Repetition Frequency (PRF) and duration of the transmit pulses. Radar ambiguities are typically specified by the Total Ambiguity Ratio (TAR), which is given by the ratio of powers from distributed targets in the ambiguous and unambiguous zones. The TAR computation is performed with reference to a specific test scenario, named “well”. The ambiguity at the centre of a well of 100 km × 100 km located anywhere within the observed swath shall be < 1 % at the near swath point and < 3 % at the far swath point, with the requirement value linearly interpolated between those extremes inside the swath. The σ° inside the well is uniform and corresponds to ocean backscattering at the noise level (i.e., corresponding to 4 m/s crosswind for VV polarization and 15 m/s crosswind for VH polarization). The σ° outside the well (background reflectivity) corresponds to typical C-band backscattering from land, that is:

$$\sigma^{\circ}(\theta_i) = 10 \text{ Log}(\cos \theta_i) \quad [\text{dB}], \text{ for VV and HH polarizations;}$$

$$\sigma^{\circ}(\theta_i) = 10 \text{ Log}(\cos \theta_i) - 5 \quad [\text{dB}], \text{ for VH and HV polarizations.}$$

The consequences of this requirement on the instrument design, and specifically on the instrument cross-talk, are addressed in appendix-E.

5.2 Measurement System Concept

This section provides the technical description of the DopSCAT mission. It shows how the implementation concept can respond to the scientific mission requirements defined in section 5.1. After an overview of the proposed orbit, the observation principle is described in detail, followed by the instrument concept and its subsystems, the on-ground processing and calibration concept.

5.2.1 Orbit Selection and Geometry of Observation

The same sun-synchronous orbit of the MetOp satellites has been chosen for the DopSCAT mission. The osculating Kepler elements of the reference orbit are:

Semi-major axis,	$a_e = 7195.605$ km (corresponding to a 29 day repeat cycle)
Eccentricity,	$e_e = 0.001165$;
Inclination,	$\psi = 98.701^\circ$;
RAAN,	$\Omega = 62.4731 + 0.98564735 \times N_d$;
Arg. of Perigee,	$\omega = 90.00^\circ$;

N_d being the number of Julian days from 1 Jan 2000 00:00, corresponding to a descending node, Mean Local Solar Time 09:30. A yaw steering law is applied to compensate the drift of the satellite ground-track due to Earth rotation: this law maximizes the overlap between fore, mid and aft beams. The Geometry of observation of DopSCAT is depicted in Figure 5.1. Six swaths are alternatively illuminated on ground by six fixed fan beam-antennas, with a time sampling dictated by the PRF of the radar. The swaths are oriented at 45° (Fore-left), 90° (Mid-left), 135° (Aft-left), 225° (Aft-right), 270° (Mid-right) and 315° (Fore-right) with respect to the satellite ground track. Mid swaths extend from 20° incidence up to 53.75° , whereas side swaths extend from 27.42° incidence up to 65° . This corresponds to an overall performance swath of 660 km on both sides of the sub-satellite ground-track, with a gap of 525 km in between. Such a swath ensures a 99% global coverage in 48 hours. The antenna mechanical pointing, which is the angle between the nadir direction and the antenna bore-sight, is 34° for the mid antennas and 43° for the side antennas.

5.2.2 Observation Principle

The DopSCAT mission concept consists of a single satellite carrying a C-band (5.4 GHz, i.e. ~ 5.7 cm wavelength) Doppler scatterometer. The satellite configuration is constrained by the accommodation of the 6 slotted waveguide antennas configured on three roof top shaped antenna assemblies. The 6 antennas are activated in sequence, with only one antenna transmitting and receiving. The switching between the antennas is performed on a pulse to pulse basis. Each antenna transmits V-polarized signals and receives simultaneously both V and H-polarized echoes from the ocean. Linearly frequency-modulated pulsed signals (chirps) are commonly used by radar systems, as they have significant advantages with respect to CW pulsed signals.

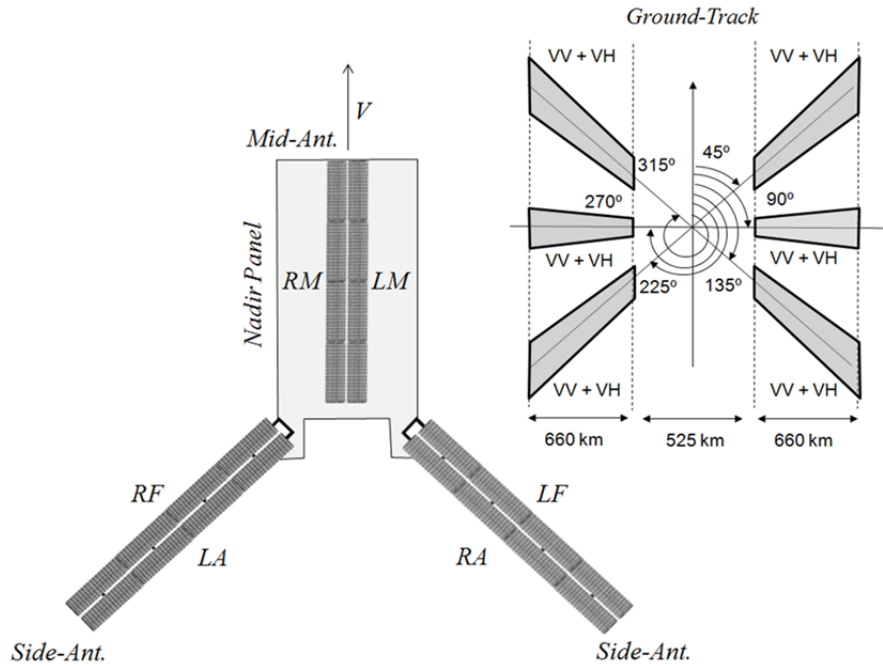


Fig. 5.1 Geometry of observation. Six waveguide array antennas are used to observe 6 swaths on ground (3 on each side of the sub-satellite ground track). The terms RF, LA, RA, LF, MR and ML stand for Right-Fore, Left-Aft, Right-Aft, Left-Fore, Mid-Right and Mid-Left antennas respectively.

The range resolution of a CW-radar system depends on the pulse duration: the shorter the transmit pulse the better the resolution, with a corresponding limitation in average radiated power and sensitivity. For chirp signals, however, the range resolution depends on the bandwidth of the transmit waveform: the larger the bandwidth the higher the resolution, without any relation to the pulse length or average radiated power. For DopSCAT, the transmitted signal is a dual-chirp, a combination of two linear frequency modulated pulses: one with increasing frequency in time, i.e. up-chirp, and the other with decreasing frequency, i.e. down-chirp. Up and down-chirps are transmitted at the same time and have the same bandwidth (B) and pulse duration (τ):

$$s(t) = s_u(t) + s_d(t) = \left\{ A \exp \left[j2\pi \left(f_c t + \frac{1}{2} \frac{B}{\tau} t^2 \right) \right] + A \exp \left[j2\pi \left(f_c t - \frac{1}{2} \frac{B}{\tau} t^2 \right) \right] \right\} \text{rect}_\tau(t) \quad (5.3)$$

In equation (5.3), the sub-indexes u and d stand for “up-chirp” and “down-chirp” respectively, f_c is the carrier frequency and A is an arbitrary amplitude factor, rect_τ is a rectangular function of duration τ . The use of dual-chirps allows estimating not only the backscattering coefficient of the wind-driven ocean surface but also the Doppler shift associated with the moving ocean. The demonstration of this capability can be based on

the radar ambiguity function. In a radar system, the choice of a radar waveform plays an important role in enabling the system to separate two closely located targets, in either range or speed. Therefore, it is often necessary to examine a waveform and understand its resolution and ambiguity in both range and speed domains. In radars, the range is measured using the delay and the speed is measured using the Doppler shift. Thus, the range and the speed are used interchangeably with the delay and the Doppler. To improve the signal to noise ratio (SNR), modern radar systems often employ a matched filter in the data processing. The ambiguity function of a waveform $s(t)$ is defined as:

$$\chi(\tau_s, f_D) = \int_{-\infty}^{\infty} s(t) \cdot s^*(t - \tau_s) \cdot e^{j2\pi f_D t} dt \quad (5.4)$$

where * denotes the complex conjugate, τ_s the time delay and j is the imaginary unit. Note that for zero Doppler shift ($f_D=0$) this reduces to the autocorrelation of $s(t)$. This exact representation makes the ambiguity function a popular tool for designing and analyzing waveforms. This approach provides the insight of the resolution capability in both delay and Doppler domains for a given waveform. Based on this analysis, one can then determine whether a waveform is suitable for a particular application. A constant envelope Linear Frequency-Modulated (LFM) pulse has an ambiguity function skewed in the delay-Doppler plane. In the matched filter output, slight Doppler mismatches for the LFM pulse do not change the general shape of the pulse and reduce the amplitude very little, but they do appear to shift the pulse in time. Therefore, an uncompensated Doppler shift changes the target apparent range: this phenomenon is called range-Doppler coupling. Figure 5.2 uses the ambiguity function to explore the range-Doppler relationship for a Linear Frequency-Modulated Pulse. In particular, Figure 5.2a depicts the up-chirp (positive chirp rate) case and Figure 5.2b the down-chirp (negative chirp rate) case. The ambiguity functions of LFM pulses with opposite chirp rates are skewed in opposite direction, meaning that the introduced delay has an opposite sign. While one return is delayed the other one is anticipated of the same quantity. The delay is proportional to the Doppler shift and inversely proportional to the chirp rate:

$$\tau_s = f_D \cdot \left(\frac{\tau}{B} \right) \quad (5.5)$$

Figure 5.2c shows the relative apparent time delay between two LFM pulses with opposite rates subjected to a common Doppler shift. By estimating the delay and

inverting equation (5.5), it is possible to retrieve the Doppler shift affecting the received data. An accurate way to retrieve the Doppler shift is by computing the cross-correlation between the data processed with a matched filter having positive rate and the same data processed with a matched filter having negative rate. The displacement of the peak of the cross correlation function from half of the horizontal axis gives a measurement of the time delay between the up and down- chirps. This concept is depicted in Figure 5.2d, where a shift of N samples (corresponding to a generic time delay) between the two LFM signals is reflected in a shift of N samples of the peak of the cross-correlation function. More details on the processing steps required to generate Doppler shift and backscattering products are given in section 5.2.5.

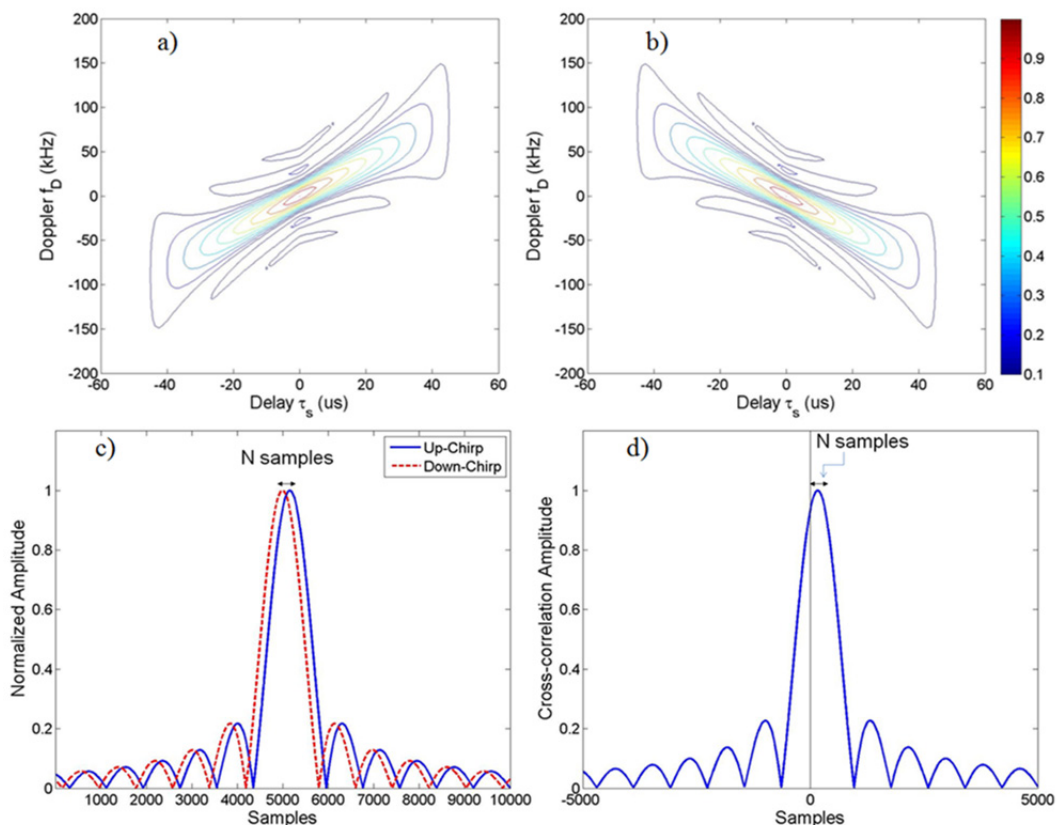


Fig. 5.2 The ambiguity function of a) an up-chirp and b) a down-chirp LFM pulse; c) relative time delay between two LFM pulses with opposite rates subjected to a common Doppler shift; d) result of the cross-correlation.

5.2.3 Instrument Concept

Figure 5.3 shows the DopSCAT instrument block diagram. The instrument comprises: antenna subsystem (composed of 6 dual-polarization waveguide antennas), switch matrix, transmit unit, receive unit, central electronic unit, instrument control unit, instrument power unit. The antennas consist of slotted waveguide arrays, connected through bareline

feed networks to the beam-switching matrix. Side antenna assemblies require rotating RF-joints for deployment. The DopSCAT antennas are considered a key component of the instrument, as they have direct impact on performance figures like e.g. radiometric stability. Their stability is therefore considered of utmost importance. The design of the DopSCAT antennas is based on a aluminium support structure and RF elements are also made of aluminium. Two single-sideband transmit LFM pulses are generated, one with positive rate (up-chirp) and the other with negative rate (down-chirp). These pulses are up-converted to the carrier frequency by quadrature mixers and then amplified by two distinct High Power Amplifiers (HPAs). The use of two amplifiers instead of one avoids the generation of intermodulation products that might occur when the input to a non-linear device, such as the HPA, is composed of two frequencies. To better explain the meaning of this sentence, we refer to equation (5.5). The transmit signal $s(t)$ is the sum of two chirps with opposite rates (see Figure 5.4a) and this implies that at each time instant (t_0), during the pulse duration (τ), two distinct frequencies, f_1 and f_2 , are simultaneously transmitted. When a signal containing these frequency components passes through a High Power Amplifier, the input signal undergoes a non-linear transformation and the output waveform will not only contain the two fundamental frequencies f_1 and f_2 but also a number of linear combinations of f_1 and f_2 . These combinations of the fundamental frequencies are the intermodulation products. As illustrated in Figure 5.4a, for the case of a double-chirp, the following relation holds: $f_1 = -f_2$. Figure 5.4b provides an example of power spectral density at the output of a HPA when the input waveform is the sum of two CW (Continuous Wave) signals with $f_1 = -f_2 = 5$ kHz, and the non linear transfer function of the HPA is $y = 0.5e-3x^3 + 1e-7x^2 + 0.1x + 3e-3$. By using two HPAs, one for the amplification of the up-chirp and the other for the amplification of the down-chirp the intermodulation products $k_1f_1 + k_2f_2$ disappear. After the amplification stage, modulated up-chirp and down-chirp transmit pulses are combined, routed to the switch matrix and radiated through the antennas. In reception, the echo signals (V and H) are routed through the switch matrix unit to the receive unit, where they are filtered and amplified. They are then routed to the central electronic unit for further processing including analogue-to-digital/ down-conversion, data compression and packetisation. The instrument control unit receives commands and information from the onboard computer. It sets up the instrument operation parameters, controls image acquisitions, relays telemetry information and manages fault/limit checking and takes action when appropriate. It also maintains the instrument time reference, synchronized to an onboard Global Positioning System (GPS) receiver. The instrument power unit convert the Direct Current (DC) unregulated power supply from the platform to appropriately conditioned DC power for

all the electronics units as well as provides the heater power for the thermal control. As alternative to the option of having two distinct TWTs dedicated to the amplification of up and down-chirps, we could also think to use only one TWT and transmit the up and down chirps one after the other: this method is called *time separation* approach. This means that the pulse duration shall be doubled. The main problem of this approach is that the two chirps would see the ocean surface at two different times.

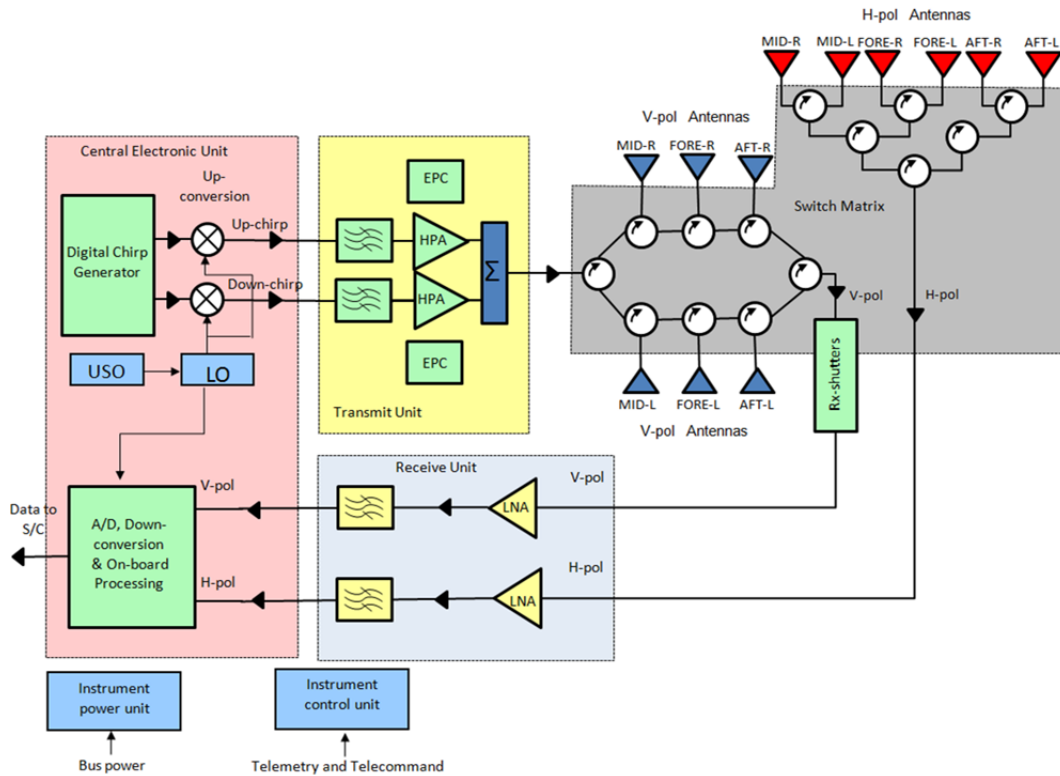


Fig. 5.3 DopSCAT instrument block diagram.

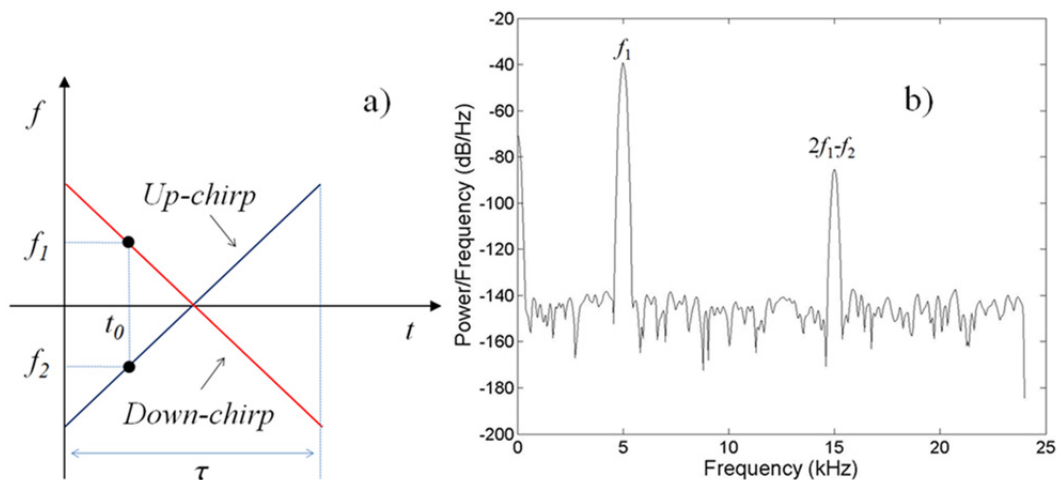


Fig. 5.4 a) Representation of the transmit double-chirp signal; b) example of power spectral density at the output of a HPA when the input waveform is the sum of two CW signals having frequencies $f_1=f_2=5$ kHz. The non linear transfer function of the HPA is $y=0.5e-3x^3+1e-7x^2+0.1x+3e-3$.

Observing the ocean at different time generates a decorrelation effect among the two processed images, thereby the accuracy of the cross-correlation technique is affected. The *time separation* approach has additional drawbacks, which will be discussed in section 5.2.5.

5.2.4 Instrument Subsystems

Antenna Subsystem

The antenna subsystem consists of three assemblies: one MID antenna assembly and two SIDE antenna assemblies. Each assembly includes the support structure, the thermal hardware and the array antennas, one at each side of a roof-like structure, as depicted in Figure 5.1a. Both MID and SIDE array antennas comprise four electrical / mechanical panels, each made of 8 radiating waveguides for each of the two linear polarizations (V and H). The radiating waveguides are fed by a bareline network [Magnusson *et al.*, 2013], which ensures high thermal stability performance and improved amplitude and phase excitation flexibility when compared with classical coupling waveguides. The MID antenna aperture is $2.85 \text{ m} \times 0.3 \text{ m}$, whereas the SIDE antenna aperture is $3.19 \text{ m} \times 0.3 \text{ m}$. The antenna structural and mechanical design makes use of technological heritage from MetOp. Hold Down and Release Mechanisms (HDRMs) are used to hold the SIDE antenna assemblies during launch. Deployment and Latch Mechanism (DLM) are in charge of the deployment of the two SIDE antenna assemblies arms after release of the HDRMs. A baseplate panel structure is used to support the Deployment and Latch Mechanisms and the MID antenna assembly.

Radio Frequency and Digital Electronics

The radio frequency (RF) and digital electronics of the DopSCAT instrument use well-established technologies thanks to the long European heritage in developing C-band radar instruments (e.g. Envisat ASAR, Sentinel-1, MetOp ASCAT). Nevertheless, the use of C-band signals and high peak RF power increases the risk of multipaction. A number of specific risk-retirement activities were undertaken in the frame of MetOp-SG and special measures were implemented in the design of the radar switch matrix for mitigating possible risks.

The transmit unit comprises two High Power Amplifiers (HPA): each consisting of a Vacuum Tube Amplifier (Travelling Wave Tube or Klystron) and the Electronic Power

Conditioner (EPC). The single Vacuum Tube Amplifier amplifies the RF transmit chirp pulses to a high power level of about 1.1 kilowatts. The EPC converts the main bus voltage to the secondary high voltage levels as required to operate the Vacuum Tube Amplifier. To avoid generation of inter-modulation products, one of the two HPAs is devoted to the amplification of up-chirp pulses, whereas the second HPA is devoted to the amplification of down-chirp pulses. Up-chirps and down-chirps are summed through a power combiner. Because of the concentration of power after the power combiner, multipaction must be avoided by an appropriate design of the radar front-end.

The Switch Matrix (SM) distributes the amplified transmit pulses via a high power ferrite switch matrix to the individual antennas according to a timing scheme provided by the Instrument Control Unit (ICU). The received radar returns are pre-amplified by a Low Noise Amplifier (LNA) before they are fed into the Central Electronic Unit (CEU). Being a key part of the DopSCAT internal calibration scheme, the SM includes further calibration couplers, as well as detectors for the transmitted and the reflected RF power.

The Central Electronic Unit comprises the direct digital pulse synthesis and up-conversion to the radar frequency in transmit, and the down-conversion, analogue-to-digital conversion and data compression/conditioning in reception. The CEU also generates pulses which are injected into the transmit path within the switch matrix. The master oscillator, which is used for instrument timing and synchronization, is also located within the CEU.

5.2.5 Level-1 Data Processing

In this section an overview of the processing steps going from the Level-0 products to the Level-1 products is given. The whole processing flow is depicted in Figure 5.5 and consists of two main chains for the generation of σ^0 images (Fig. 5.5a) and Doppler shift measurements (Fig. 5.5b). The generation of σ^0 measurements foresees the following basic processing steps.

Level-0 injection: this processing block loads the data and the related annotations from the Level-0 formatted files. Some fundamental checks on the data are made, such as: the identification and removal of saturated samples, duplicated data, and spurious signals. The following data corrections are also implemented: remove constant biases from the I (in-phase) and Q (in-quadrature) channels, correct for gain imbalance in the I and Q channels, correct for non-orthogonality between the I and Q channels, compensate for variations in relative gain of each polarization combination (VV and VH).

Doppler Centroid compensation (DC): this block performs the Doppler Centroid compensation starting from motion and geometric information provided by the platform Attitude and Orbit Control Systems (AOCS) and then compensated across the image. After this processing step, the Doppler spectrum is sitting in baseband. The predicted geometrical Doppler shift is given by the relative velocity of the satellite and the rotating Earth according to a general formula demonstrated by Raney [1986]. The DC estimate will be further refined by measuring the Doppler shift over land areas (see appendix-F).

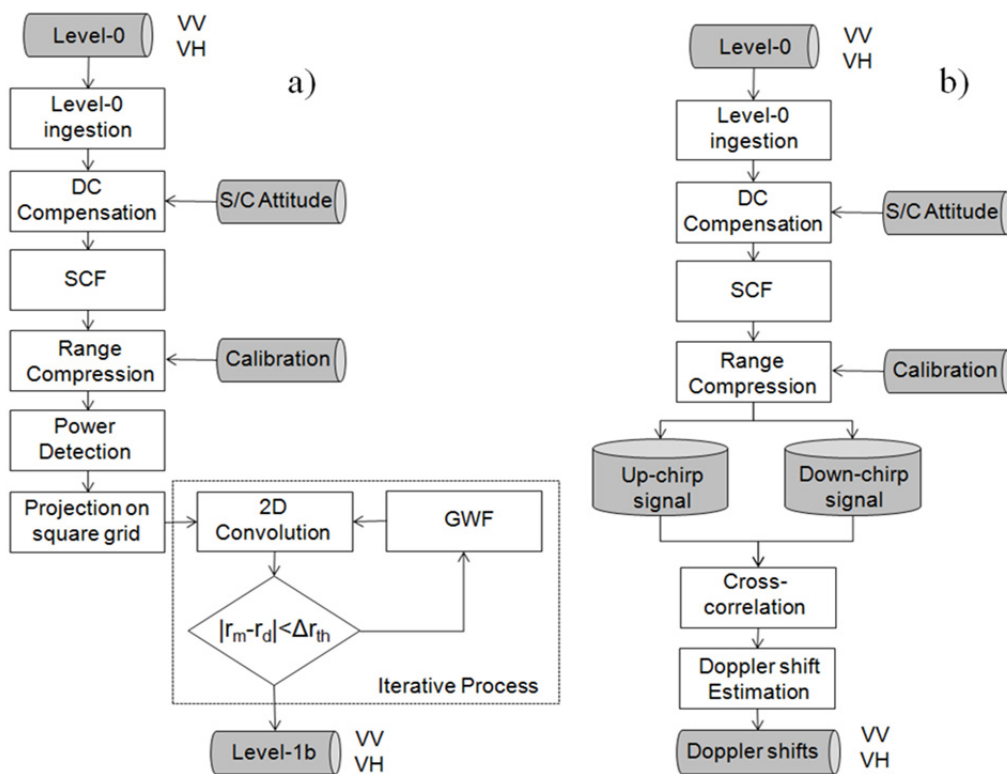


Fig. 5.5 Level-1 data processing flow for the generation of Normalized Radar Cross section images (left) and for the estimation ocean's Doppler shifts (right).

Separation Compression Filter (SCF): this block is used to separate the dual chirp echo signal into an up-chirp component and a down-chirp component, thus avoiding undesired interferences from down-chirps to up-chirps and vice versa [Tagawa *et al.*, 2004]. In order to explain the SCF procedure, we recall equation (5.3) and its frequency representation:

$$S(\omega) = S_u(\omega) + S_d(\omega) \equiv S_u(\omega)[1 + G_u(\omega)], \text{ with } G_u(\omega) = \frac{S_d(\omega)}{S_u(\omega)} \quad (5.6)$$

Where $S_u(\omega)$ and $S_d(\omega)$ are Fourier transforms of $s_u(t)$ and $s_d(t)$ respectively. The echo signal corresponding to N scatterers illuminated by a dual-chirp $s(t)$ can be formulated as:

$$r(t) = \sum_{i=1}^N r_u^i(t) + \sum_{i=1}^N r_d^i(t) \equiv r_u(t) + r_d(t) \quad (5.7)$$

The frequency representation of (5.7) is:

$$R(\omega) = R_u(\omega) + R_d(\omega) \equiv R_u(\omega)[1 + G_u(\omega)], \text{ with } \frac{R_d(\omega)}{R_u(\omega)} = G_u(\omega) \quad (5.8)$$

where $G_u(\omega)$, defined by equation (5.6), is known a priori. Therefore $R_u(\omega)$ can be easily extracted from $R(\omega)$ as it follows:

$$R_u(\omega) = \frac{R(\omega)}{[1 + G_u(\omega)]} \quad (5.9)$$

and similarly

$$R_d(\omega) = \frac{R(\omega)}{[1 + G_d(\omega)]} \equiv \frac{R(\omega)}{[1 + \frac{S_u(\omega)}{S_d(\omega)}]} \quad (5.10)$$

By applying the inverse Fourier transforms of (5.9) and (5.10) we finally obtain $r_u(t)$ and $r_d(t)$. In the most general case, the $G_u(\omega)$ function in (5.8) is different from the one used in (5.6), because it is affected by delay and Doppler shifts. Therefore, it is advisable to use the SCF procedure after the following steps have been performed:

- geometrical DC compensation (by apriori geometrical and pointing knowledge);
- geophysical Doppler shift estimation (by cross-correlation of up and down chirps echoes);
- geophysical Doppler shift compensation (i.e. the estimated Geophysical Doppler shift is used in building up the separation compression filter).

A more detailed discussion on SCF procedure is given in Appendix-G. The Separation Compression Filter is more effective when the up and down chirps are simultaneously transmitted and is definitely less effective when the time separation approach (up and down chirp consecutively transmitted) is used. In the last case, in fact, both undesired distortion effects on the system impulse response function and degradations of radar ambiguities occur. To overcome this issue one could think to adopt alternative techniques, such as the Mismatched Filter Optimization by Rabasty and Savy [2014], to improve both IRF and ambiguity performance.

Range Compression: this block performs a convolution along the range direction between the raw data and the chirp replica. The convolution is efficiently performed in the Fourier domain. A range-dependent gain correction is also implemented. This correction includes elevation antenna pattern correction and range spreading loss correction. The chirp replica could be either up-chirp or down-chirp depending on whether we process up-chirp or down-chirp echoes.

Projection on a Square Grid: this step consists of a projection of the range compressed data on a regular grid of Wind Vector Cells (WVC). A WVC is a box on the reference Earth surface where the corresponding Level 1 product measurements are attributed. The spacing of the measurement WVCs in along- and across-track directions represents the spatial sampling of the product (i.e. 12.5 km for the nominal product and 6.25 km for the high resolution product).

Convolution with Ground Weighting Function: after power detection and slant-to-ground projection of the image, we perform an aggregation of the detected compressed signals in a box centred in the WVC for each beam and polarization [Verhoef *et al.*, 2012]:

$$GWF(x, y) = w\left(\frac{x}{L_x}, \frac{y}{L_y}\right) \quad (5.11)$$

with L_x , L_y being respectively the across- and along-track dimensions of the Ground Weighting Function (GWF). This convolution is performed at each WVC and operates a spatial aggregation, per beam, in along and across-track directions. The main objective of this averaging is to obtain a set of σ^0 measurements (one per beam) for each WVC in each swath at the desired spatial resolution and radiometric resolution. Moreover, box car filters are proven to be effective to allow both open ocean and coastal processing [Verhoef *et al.*, 2012]. The two-dimensional w window is centred at the WVC and its widths determine the spatial resolution of the averaged σ^0 values, which are obtained by

convolving w with the contributing Impulse Response Functions. The results of these convolutions are called Spatial Response Functions (SRFs). The accuracy of the OVW and OVM retrievals depends on the closeness of overlap of the contributing SRFs. The two parameters L_x and L_y can be optimized, by beam and polarization, in order to generate averaged σ^0 values at the required spatial resolution ($25 \times 25 \text{ km}^2$ for the nominal product and less than $12 \times 25 \text{ km}^2$ for the high-resolution product).

As depicted in Fig. 5.5b, the first processing steps are the same as those required for the generation of NRCS images. The Doppler shift products require the range-compression with both up and down-chirp reference functions. In this way, two different range-compressed images are obtained. A cross-correlation of the two images is then performed. The Doppler shift is given by the location of the maximum of the cross-correlation function. The measurements of the Doppler shift allows for determination of the Line-of-Sight (LOS) velocity for each WVC. The effect of pointing errors on the determination of the Line-of-Sight velocity is discussed in appendix-F. The accuracy of the time shift (t_s) estimates is given by the Cramèr-Rao lower bound [Quazi, 1981]:

$$\sigma_{t_s}^2 \geq \left\{ 2T \int_{f_1}^{f_2} (2\pi f)^2 \frac{|\gamma(f)|^2}{1-|\gamma(f)|^2} df \right\}^{-1}, \quad (5.12)$$

where $\gamma(f)$ is the coherence function, T is the observation time and $B = f_2 - f_1$ is the bandwidth. More specifically, $\gamma(f)$ depends on the signal autospectrum, $S(f)$, and the noise autospectrum, $N(f)$:

$$|\gamma(f)|^2 = \frac{S(f)^2}{[S(f) + N(f)]^2}, \quad (5.13)$$

Assuming $S(f)$ and $N(f)$ are constant over the band extending from f_1 to f_2 , the calculation of the Cramèr-Rao lower bound variance of the time delay t_s can be simplified [Quazi, 1981]. The observation time T depends on the resolution of the Doppler products and can be written as:

$$T = \frac{2r \sin \theta_i}{c}, \quad (5.14)$$

where r is the desired resolution and θ_i the incidence angle. The accuracy of the Doppler shift estimates, corresponding to t_s , can be obtained as:

$$\sigma_{f_D} = \sigma_{t_s} \left(\frac{B}{\tau} \right), \quad (5.15)$$

In the same Wind Vector Cell (WVC) we might be able to collect several (N_{obs}) Doppler measurements (one per Tx-pulse). The higher the Pulse Repetition Frequency of the DopSCAT instrument, the higher N_{obs} . We can use these N_{obs} measurements to improve the accuracy of the Doppler estimates as it follows:

$$\sigma_{f_D} \Big|_{N_{obs}} = \frac{\sigma_{f_D}}{\sqrt{N_{obs}}}, \text{ with } N_{obs} = \frac{r_{Along-Track}}{V_{beam} \left(\frac{1}{PRF_{eff}} \right)}, \quad (5.16)$$

being $r_{Along-Track}$ the along-track resolution, V_{beam} the beam velocity and PRF_{eff} the effective PRF (i.e. the instrument PRF divided by the number of antennas). We note that geophysical variability at the ocean surface may enhance the noise in the OVM, similar to the concept of geophysical noise in OVW [Portabella & Stoffelen, 2006]. As explained in Appendix-F, Doppler shift measurements performed over land areas (where the shifts are expected to be equal to 0 Hz) allow correcting residual pointing errors caused by: errors in satellite orbit and attitude parameters, thermoelastic distortions and electronic mispointing of the antenna subsystem. The residual pointing error after correction over land is estimated as being less than a few hertz, which corresponds to a small bias (< 0.2 m/s) in OVM retrieval.

5.2.6 Scientific Data Processing

The ocean winds processing takes the radiometrically calibrated backscatter product to derive winds near the ocean surface (at a nominal height of 10 m). Near-surface ocean wind fields are retrieved from DopSCAT Level 1b data, by means of a Geophysical Model Function (GMF), relating backscattering values to wind vectors. The wind retrieval is an inversion problem that has to be solved on each WVC. The three σ° values, collected by the Fore, Aft and Mid antennas over the same WVC are inputs to the problem. A set of ambiguous wind vectors is derived from a Bayesian optimization

[Stoffelen & Portabella, 2006]. These 2-4 vectors have the highest probability of representing the true wind. Usually, two wind vectors are obtained as the most likely solutions, with directions separated by 180°.

Two GMFs are used in this work: the CMOD5n [Verhoef *et al.*, 2008] and SSA2-CWM [Fois *et al.*, 2015a]. A wind direction ambiguity removal step is further applied, based on a variational meteorological analysis and relying on prior numerical weather prediction (NWP) model wind and error information [Vogelzang *et al.*, 2009]. The OVM retrieval is performed by searching for minimum distances between the Doppler measurements and the Doppler frequency corresponding to a certain OVM. To this aim it is important to recall the relation between OVM and Doppler frequency, that is:

$$f_{D,i}^{OVM} = 2 \frac{v_{OVM}}{\lambda} \sin(\theta_{inc}) \cos(\varphi_{AZ}^i), \quad (5.17)$$

where v_{OVM} is the OVM amplitude, θ_{inc} is the incidence angle and φ_{AZ}^i , $i \in (1,6)$, is the difference between the OVM direction and azimuth angle (i.e., 45°, 90°, 135° for Fore-Right, Mid-Right and Aft-Right antennas respectively).

Note that the total sensitivity to OVM is somewhat dependent on incidence angle and azimuth with maximum OVM amplitude sensitivity in the outer swath for $\varphi_{AZ}^{i=2,5} = 0^\circ \wedge 180^\circ$ and maximum OVM direction sensitivity for $\varphi_{AZ}^{i=2,5} = 90^\circ \wedge 270^\circ$, resulting in a weakly non-linear OVM retrieval. Maximum sensitivity corresponds to minimum error. Subsequently, in a second step, ocean current retrieval makes use of Geophysical Model Functions such as SSA2-CWM [Fois *et al.*, 2015a] and CDOP [Mouche *et al.*, 2012] to remove the Doppler contribution associated with surface wave motion.

5.2.7 End-to-End System Calibration and Characterization

The achievement of radiometric performance requirements is ensured by the on-ground payload characterization and by the in-orbit calibration (i.e. internal and external calibration). The complete transmission and receive chains are characterized prior to launch over the temperature range predicted in orbit. These measurements also include characterization of the complete internal calibration subsystems, which will monitor any transfer function variations in the radar electronics in orbit. An exception is made for the antenna subsystem, for which a combination of measurements at panel level and theoretical prediction of the radiation patterns is used. The in-orbit verification of the

antenna pattern will be performed using transponder measurements (external calibration). The instrument/system parameters, as determined on ground, are stored and used as initial setting for error corrections and data processing. The internal calibration subsystem permanently monitors the transfer function variations of the complete radar electronics with high temporal resolution (every pulse repetition interval) through the measurements of:

- The TWTs output RF power levels by using attenuators and a power detectors;
- The transmit pulse waveform through a calibration loop;
- The receive chain transfer function;
- The system noise in absence of transmit pulse.

It, however, excludes the antenna subsystem, which is covered by the external calibration. Power and gain variations of the radar electronics due to temperature excursions along the orbit and changing solar illumination over the seasons, and due to aging are determined. The system noise measurement is used for the noise subtraction (part of the ground processing) in order to remove any biases in the σ^0 estimates. Considerable heritage exists in Europe for achieving high calibration accuracy for spaceborne scatterometers (e.g. MetOp ASCAT [Wilson *et al.*, 2010; Gelsthorpe *et al.*, 2000; Figa-Saldaña *et al.*, 2002], MetOp-SG SCA [Fois *et al.*, 2012]). This heritage is applied for the design of the instrument internal calibration subsystem. The external calibration complements the system calibration through an end-to-end characterization of the complete radar measurement chain using external targets. Its purposes are to verify and characterize: the two-dimensional antenna gain (for both VV and VH polarizations), the beam pointing of the satellite, the channel imbalance, the cross-polar radiation level, the system IRF, the ambiguity performance. Two types of targets are used for external calibration: point targets with known radar cross-section such as active transponders and corner reflectors, distributed natural targets with well-characterized radar cross-section such as stable ice sheets and well-developed forests. Specific requirements are required for the active transponders. They have to acquire the DopSCAT signals and transmit them back with a time delay to avoid coupling between the receive and transmit chains and to minimize clutter contamination. Dual-polarization channels with high isolation are required to calibrate the dual polarimetric system. Satellite tracking in elevation and azimuth is also needed to maintain high polarization isolation and sensitivity. An important aim of the external calibration using transponders is the measurement of the antenna pattern, which cannot be characterized adequately on-ground. The complete two-dimensional pattern

characterization is possible with measurements performed over several orbit repeat cycles [Wilson *et al.*, 2010].

5.3 Performance Estimation

In this chapter, the performance of the proposed DopSCAT mission concept is assessed against the mission requirements presented in section 5.2. In sections 5.3.2 and 5.3.3 the performance of Level-1 and Level-2 products, as defined in sections 5.2.5 and 5.2.6, are presented. For Level-1 products, the performance is expressed against the radiometric and geometric requirements of the DopSCAT image, whereas for Level-2 they are expressed against the geophysical requirements of the scientific data. Finally, the end-to-end ability to produce simulated geophysical results from a synthetic scene is demonstrated to validate the overall data product concept and assess the expected performance of the mission.

5.3.1 End-to-End Simulator

The DopSCAT end-to-end simulator is a tool to simulate and analyze the performance of the mission, i.e. from the observed scene to the retrieved Level-2 geophysical parameters. The architecture of the end-to-end simulator is schematically shown in Fig.5.6 and comprises different modules.

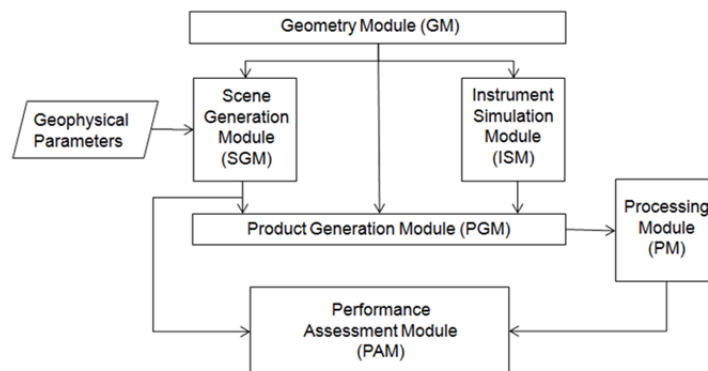


Fig. 5.6 High-level block diagram of the DopSCAT End-to-End simulator.

Geophysical Parameters

The retrieval of OVWs is a non-linear problem and the accuracy of the estimated winds depends on the wind input state. An average over different wind conditions is made to mitigate and possibly eliminate this dependence. The wind speed distribution is often

represented by a Weibull distribution, with a maximum around 8 m/s, that is [Lin *et al.*, 2012]:

$$f(v) = \frac{p2}{p1} \left(\frac{v}{p1} \right)^{p2-1} e^{-\left(\frac{v}{p1} \right)^{p2}}, \quad (5.18)$$

where $p1 = 10$ m/s and $p2 = 2.2$ m/s. The wind direction distribution is, instead, well represented by a uniform distribution [Lin *et al.*, 2012].

Scene Generation Module

The GMFs are empirically derived functions that relate backscatter or wave motion measurements to surface wind vectors and viewing geometries (incidence angle, azimuth angle, wind vector). For C-band VV simulations, we use the CMOD5n or SSA2-CWM model for ocean backscatter and the SSA2-CWM or CDOP model for the wave motion.

Geometric Module

The correct determination of the ocean wind vector signature and the ocean vector motion, requires that every wind vector cell (WVC) on the surface be visited by three different views, corresponding to the views of the Fore, Mid and Aft antennas. The observation geometry is calculated for every WVC in the swath using a simplified orbital model together with specific satellite pointing information.

Instrument Simulation Module

The backscatter variance depends on the instrument, as clearly stated in equation (5.2), but also on the variability of the ocean surface (sub-WVC variability). For winds below 4 m/s this variability is substantial. Moreover, the sub-WVC variability is sampled differently by the three beams, which have different SRFs, and this represents the largest contribution to the geophysical noise. The geophysical noise model is empirically modelled as a function of wind speed as: $k_g(v) = 0.12 \exp(-v/12)$ [Portabella & Stoffelen, 2006]. The instrumental and geophysical noise contributions are assumed Gaussian and uncorrelated.

Product Generation Module

The product generation module models the total scattering coefficient as:

$$\sigma^o = \sigma_{GMF}^o (1 + \sqrt{k_p^2 + k_g^2} \cdot N[0,1]) , \quad (5.19)$$

This module models also the total Doppler shift as:

$$f_D = (f_D^{GMF} + f_D^{Curr}) \cdot (1 + \sqrt{(\sigma_{f_D}^g)^2 + (\sigma_{f_D}^{X-corr})^2} \cdot N[0,1]) , \quad (5.20)$$

where $N[0,1]$ is a Gaussian PDF with zero mean and unit standard deviation, $\sigma_{f_D}^{X-corr}$ is the uncertainty related to the cross-correlation operation and $\sigma_{f_D}^g$ is the uncertainty in Doppler related to the geophysical noise. The modelling of the geophysical error is very complicated. In principle, such a model should take into account for all those effects and dependences that are not considered in the GMF. As an example, imperfections of the geophysical model function, rain, atmospheric and wave-field variability can affect the accuracy of both backscatter and Doppler measurements. However, thanks to the coarse spatial resolution of the scatterometer, these effects have a very little impact on the accuracy of wind vector retrieval with some exceptions represented by confused sea state, high wind variability and intense rain. These special cases occur less than 5% of time in a year. In these cases, the quality of the retrieved winds and Doppler shift is seriously compromised.

Processing Module

The retrieval of wind vectors from ocean scatterometry is based on the use of geophysical model functions, which relate the wind fields to backscatter measurements. The Bayesian wind inversion process searches for minimum distances between backscatter measurements and backscatter model solutions lying on the empirical GMF surface [Stoffelen & Portabella, 2006]. The normalized square distance $MLE(\mathbf{v}|z)$ from backscatter measurements, $z = (\sigma^o)^{0.625}$, to backscatter wind solutions, $z_{GMF,i}(\mathbf{v})$, lying on the surface of the GMF, can be expressed as:

$$MLE(\bar{\mathbf{v}} | z) = \frac{1}{\langle MLE \rangle} \sum_{i=1 \dots N} |z_i - z_{GMF,i}(\bar{\mathbf{v}})|^2 , \quad (5.21)$$

where N is the dimension of the backscatter vector (i.e. the number of views per WVC), and $\langle \text{MLE} \rangle$ is an empirical normalization factor that accounts for the instrumental noise variance, $\text{var}\{\sigma^o\}$, and deviations from the ocean wind GMF due to geophysical noise. Once the wind retrieval has been completed, the OVM retrieval step is started:

$$MLE(\vec{v}_{OVM} | f_D) = \sum_{i=1 \dots N} |f_{D,i} - \hat{f}_{D,i}(\vec{v}_{OVM})|^2, \quad (5.22)$$

The OVM is retrieved by searching for minimum distances between the Doppler measurements and the Doppler frequency corresponding to a certain OVM, finally resulting in a OVM vector. Subsequently, the SSA2-CWM (or CDOP) GMF is used to estimate the local wind-induced (due to Stokes' drift) OVM contribution. The residual OVM is associated with possible ocean currents.

5.3.2 Level-1 Performance

Table 5.3 provides a complete list of DopSCAT parameters and information used for the assessment of its Level-1 performance. The instrument concept is based on the use of low PRF (32 Hz), high peak power (2.2 Kw, i.e. 1.1 Kw per up and down transmitted chirp) and short pulse duration (< 2ms). This design choice has several advantages:

Tab. 5.3 DopSCAT Parameters

Parameters	UoM	Value	Parameters	UoM	Value
Peak Power	[W]	2200	MID-ANT Height	[m]	0,32
Carrier Frequency	[GHz]	5,4	SIDE-ANT Length	[m]	3,21
Pulse Duration	[ms]	2	SIDE-ANT Height	[m]	0.32
Tx signal	[#]	Double-chirp	Spatial Res.	[km×km]	25×25
ChirpRate [MID]	[kHz/ms]	417,5	Spatial Sampling	[km×km]	12,5×12,5
ChirpRate [SIDE]	[kHz/ms]	205	Number of Ant.	[#]	6
PRF	[Hz]	32	Pol. [MID-ANT]	[#]	VV and VH
Tx+Rx Losses	[dB]	3,4	Pol. [SIDE-ANT]	[#]	VV and VH
Noise Figure	[dB]	1,4	Swath Size	[km]	2×660
MID-ANT Length	[m]	2,87	Min. Inc. Angle	[°]	20

- It is well suited for Traveling Wave Tube (TWT) transmitter technology based on RADARSAT heritage;
- It offers the advantage of having noise measurement windows completely free from ground echo signal (instead of relying on suppression of echoes by the antenna directivity);
- It offers a simple way to implement external calibration without interfering with the nominal operation (the transponders inject their response signal into the noise measurement window, as explained in [Fois *et al.*, 2012]);

- It is ideally suited for raw data sampling and therefore minimal on board processing, as the duty cycle of the receiver (fraction of time where data are acquired) is minimized.

The radiometric performance achieved by the DopSCAT instrument is largely a function of the radiation pattern generated by the antenna subsystem. The azimuth and elevation cuts of the antenna patterns in V-polarization are given in Fig.5.7a. Both side and mid antenna patterns are optimized for a performance swath limited by a minimum incidence angle (of 20° for the mid antennas and 27° for the side antennas) and a maximum incidence angle (of 53° for the mid antennas and 65° for the side antennas). More specifically, the elevation pattern needs to fit into a certain mask that is characterized by the swath (gain increasing toward far swath), a nadir suppression region and the wrong side swath (mirrored around nadir, particularly important when assessing the radar ambiguity ratio). The azimuth side lobes for any elevation angle shall be smaller than -25 dB, in order to meet the requirement on the total ambiguity ratio as specified in section 5.1.3. As a result of a performance optimization, the antenna tilt angles (off-nadir) shall be 43° for the side beams and 34° for the mid beams.

The variations in the radiometric resolution and total ambiguity ratio as a function of the incidence angle are shown in Fig. 5.7b-d. The VH-polarization represents the worst-case scenario for kp . This depends entirely on the ocean backscattering, which is lower in VH than in VV polarization [Fois *et al.*, 2015b; Van Zadelhoff *et al.*, 2013]. The curves correspond to the lowest altitude (823 km) over the orbit, however no significant differences are found at the highest altitude (849 km).

Radiometric resolution and ambiguity error show both sufficient margins with respect to the requirements reported in section 5.1.3. These margins can be used to mitigate the risks associated with the development of the most critical instrument items (antenna and TWT). Figures 5.7e-f provide the accuracy in the estimation of the Doppler shift for VV and VH-polarization respectively, as per equations (5.12)-(5.16). Fig. 5.8 shows the near swath spatial response functions with and without Separation Compression Filter (SCF) for the side antenna case. The use of the SCF allows filtering the disturbance generated when down-chirp echoes are convolved with an up-chirp reference signal (or alternatively when up-chirp echoes are convolved with a down-chirp reference signal). The SRF, as observed in the output radar imagery, is characterized by a main lobe, where most of the energy is concentrated, and by side-lobes of varying energy and spatial distribution. The spatial resolution, measured as the half-power width of the SRF is $25 \text{ km} \times 25 \text{ km}$ for the nominal product and less than $12.5 \text{ km} \times 25 \text{ km}$ for the high resolution product. Two

main radiometric parameters are defined for the DopSCAT mission: the radiometric stability and the absolute radiometric bias. The combination of these two quantities provides the radiometric accuracy, describing the absolute error in the measurement of σ^0 . Tables 5.4-5.5 show the overall radiometric budgets. For radiometric stability, harmonic and drift errors are considered, while for absolute radiometric bias, only bias errors are taken into account. The random errors are already included in the evaluation of the instrument IRF and in the computation of the noise equivalent sigma zero, so they are not part of the following budgets. The error types are classified according to their time dependence. The bias errors are residual fixed offsets, which are stable over the entire lifetime of the mission. They are assumed to have a uniform distribution within a certain interval around the nominal value. Drift errors are variations due to ageing effects, which appear as slow variations in time from zero to a peak value D .

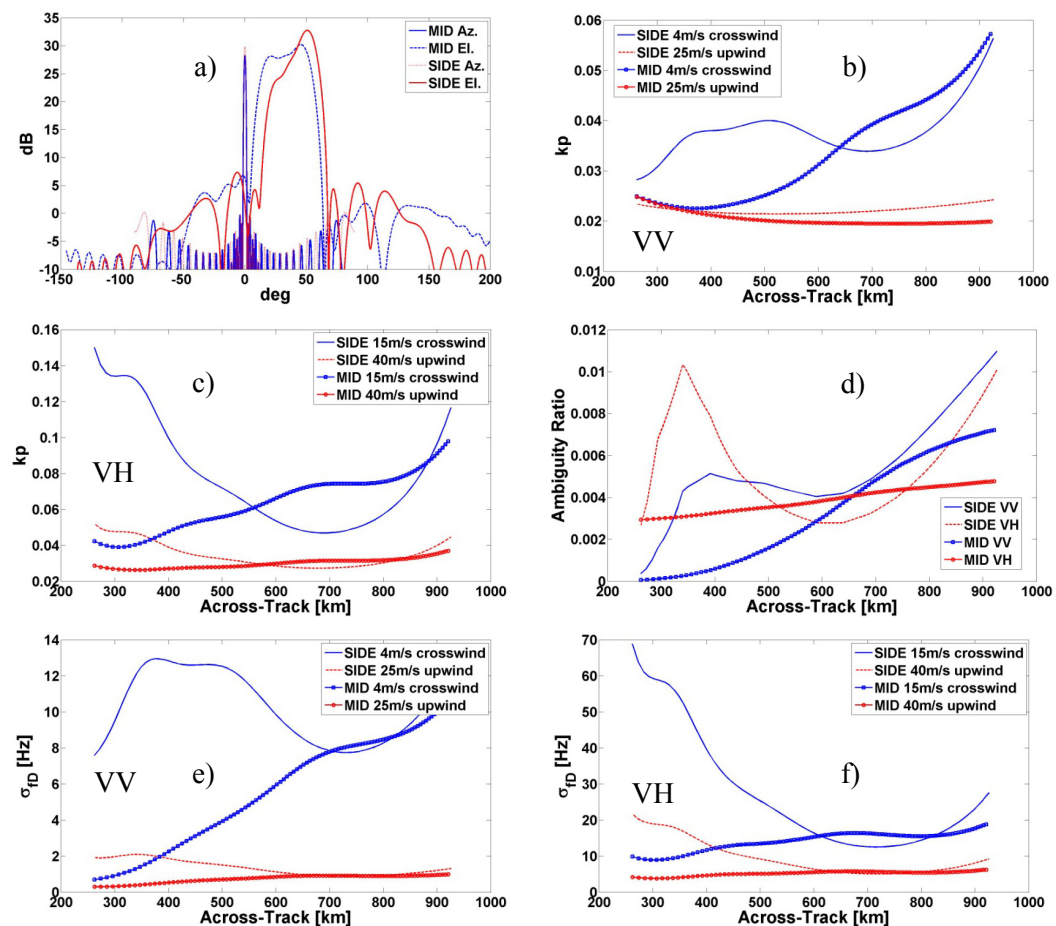


Fig. 5.7 a) Mid and Side antenna azimuth and elevation cuts for VV-polarization; b) radiometric resolution in VV-polarization versus across-track position for both mid and side swaths in the two extreme wind cases, i.e. 4 m/s cross-wind and 25 m/s up-wind; c) radiometric resolution in VH-polarization versus across-track position for both mid and side swaths in the two extreme wind cases, i.e. 15 m/s cross-wind and 40 m/s up-wind; d) Total ambiguity ratio over mid and side swaths in VV and VH-pol.; e) and f) accuracy in the estimation of the Doppler shift for VV and VH-polarizations.

Within the interval D the drift errors are assumed to have a uniform distribution. Harmonic errors have a periodic behaviour along the orbit, with mean value zero (thus they do not contribute to the bias error) and peak value H . The harmonic errors can also be quadratically summed up, as long as they have different period T or their relative phasing is not zero. The random errors are all those unpredictable variations quicker than the real aperture time of the scatterometer. Bias and drift errors are quadratically summed to achieve the total bias error and the total drift error respectively. The radiometric stability is defined as the standard deviation of the measurements taken at different times of the radar cross section of a reference target, of such magnitude that receiver noise is insignificant, with the system operating within its dynamic range. Perturbations due to the propagation path of the electromagnetic signal are neglected.

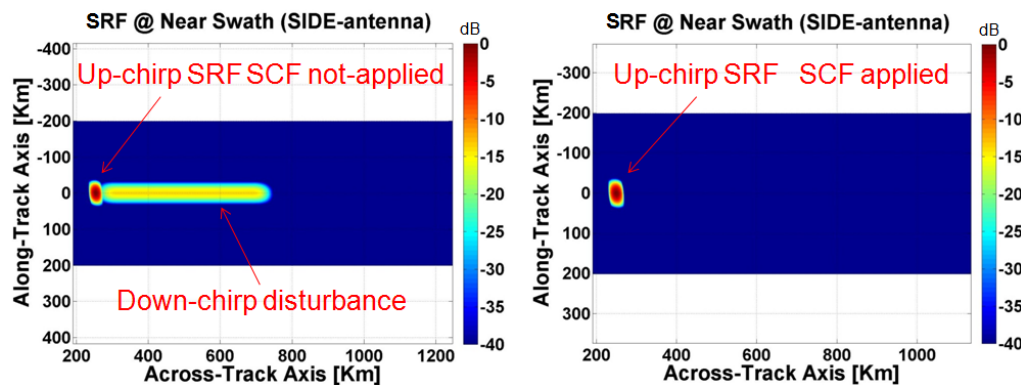


Fig.5.8 Spatial Response Function computed at near side swath without SCF (left) and with SCF (right).

Tab. 5.4 Radiometric Stability Preliminary Allocation

Error sources	Sensitivity	Origin	Error (1σ)	dB RMS
Knowledge errors				
AOCS error (AKE)	1.11 dB/°	MetOp-SG	0.014°	0.015
Harmonic errors				
S/C thermo-elastic pointing stability	1.11 dB/°	MetOp-SG	0.002°	0.002
Antenna thermo-elastic pointing stability	1.11 dB/°	[Magnusson et al., 2013]	0.045°	0.05
Antenna electrical pointing stability	1.11 dB/°	[Magnusson et al., 2013]	0.019°	0.021
Antenna gain thermal variations	1	[Magnusson et al., 2013]	0.06 dB	0.06
Total harmonic errors				0.082
Drift errors				
External calibration (ageing)	1	[Wilson et al., 2010]	0.04 dB	0.04
Internal calibration error (ageing)	1	[Wilson et al., 2010]	0.02 dB	0.02
Total drift errors				0.044
Radiometric stability				0.093

The absolute radiometric bias, on the other hand, is defined as the bias in radar cross-section within the scene and over time and includes errors from processing and calibration. Table 5.5 provides the overall bias budget and values for the main contributors; amongst them, the external calibration error deserves special attention. The external calibration is based on the use of active transponders, which simulate a point

target with calibrated cross-section. The transponders produce time-delayed echoes so that the received signal is less affected by ground clutter contamination. Measurements of the antenna pattern are taken at several elevation angles. The combination of these measurements with those performed over uniform distributed targets (such as tropical forests) allows the 2-dimensional antenna pattern to be retrieved. This calibration procedure is subject to the following errors:

- Transponder calibration errors;
- Processing and interpolation errors (including noise-subtraction errors);
- Bias errors that reflect the thermal state at a specific orbit location.

The budget in Table 5.5 does not include the bias errors that are known, and can thus be compensated in the ground processor. The numbers provided in Table 5.4-5.5 are based on ASCAT heritage [Wilson *et al.*, 2010] and on recent ESA predevelopment activities on critical instrument subsystems of the MetOp-SG wind scatterometer [Magnusson *et al.*, 2013; Ayllon *et al.*, 2014].

Tab. 5.5 Absolute Radiometric Bias Preliminary Allocation

Absolute Radiometric bias	Origin	dB RMS
Bias errors (thermal state at a specific location)	[Wilson <i>et al.</i> , 2010]	0.15
Processing errors	[Wilson <i>et al.</i> , 2010]	0.15
External calibration errors	[Wilson <i>et al.</i> , 2010]	0.25
Radiometric bias		0.32

5.3.3 Level-2 Performance

The estimation of the performance of Level-2 product retrievals has been performed on the basis of simulated and real data from ASCAT [Gelsthorpe *et al.*, 2000] wind fields and from OSCAR [Johnson *et al.*, 2007] ocean current fields. The wind vector data by ASCAT together with the observation geometry are used as input to the geophysical model functions (e.g. SSA2-CWM, CMOD5n, CDOP) to generate backscatter maps and wind-driven Doppler-frequency maps. Ocean current vector measured by OSCAR are, instead, used together with the geometry of observation to compute equation (5.15), that is the Doppler shift associated to the current. All these operations are performed by the scene generation module (SGM). The instrument generation module, instead, computes the Signal-to-Noise Ratio (SNR) and the Radiometric Resolution (k_p) starting from geometrical information and σ^0 maps (please refer to equation (5.2)). The product generation module PGM, corrupts the σ^0 and the Doppler frequency simulated data by adding instrumental, geophysical and processing errors, as per equations (5.17) and

(5.18). The Level-2 processor takes the corrupted data of the PGM as inputs and, by applying equation (5.19), it first derives the wind vector and then uses the wind vector to compute the wind-driven frequency shift. This quantity together with the one associated with relative motion between satellite and rotating Earth are subtracted from the total Doppler shift (computed via cross-correlation between up and down chirp) to obtain the Doppler contribution of potential sea surface currents. Equation (5.20) is finally used to retrieve the sea surface currents from the associated Doppler shift.

Simulations with DopSCAT end-to-end simulator indicate that the accuracy objectives of 0.1 m/s specified for the current product are close to being achieved over a wide range of wind speed and directions. Performance analysis of Level-2 data product has been carried out considering all possible system sources of errors (e.g., instrument and geophysical noise). Fig. 5.9a-b show an example of ASCAT wind field used in the simulation: both wind speeds and directions are depicted (only the right swath is shown). Horizontal and vertical axis show the geographic longitude and the latitude of the observed area. In the same figures, three different polygons are illustrated: they correspond to the swaths illuminated by the three right antennas of DopSCAT. In particular, the green polygon refers to the fore antenna, the red to the aft antenna, and the blue one to the mid antenna. Only the data within the common area are used in the Level-2 processing. Fig. 5.9a-b show the result of the wind retrieval by using equation (5.21) on VV-pol data. Figure 5.10 shows the two-dimensional histograms of the retrieved wind solution versus the real wind for wind speed (Fig. 5.10a) and wind direction (Fig. 5.10b). The accuracy in wind speed is better than 0.7 m/s, whereas the accuracy in wind direction is better than 7 degrees.

Note that the right plot is computed for winds larger than 4 m/s. This is done to avoid the noise produced by the weak wind direction sensitivity at low winds (i.e. the wind direction error increases with decreasing wind speed). With reference to the same Figure 5.10, we indicate with N the number of data. The quantities m_x and m_y provide the mean values along the horizontal and vertical axis, respectively, whereas $m(y-x)$ and $s(y-x)$ are the bias and the standard deviation of the displayed data with respect to the diagonal. The parameter cor_xy gives the correlation between the distributions of data over horizontal- and vertical-axis. The contour lines are in logarithmic scale: ten contour levels are plotted. By using equations (5.17) and (5.21) we can derive the OVM. The retrieved wind vectors are then used to remove the wind contribution (\mathbf{v}_O^{wind}) from the total OVM, \mathbf{v}_O^{Tot} , in equation (5.1). The remaining \mathbf{v}_O^{curr} can then be related to potential currents. Results of the retrieval are shown in Fig. 5.9c-d for both horizontal components of the ocean current.

Figure 5.10c-d provide the two-dimensional histograms of the retrieved components of current versus the real components of current. The figures show almost no bias in current speed and very small standard deviations (i.e. 0.14 m/s and 0.19 m/s for the meridional and zonal component respectively). Extensive Monte-Carlo simulations over several possible wind and current scenarios have demonstrated the capability of the present DopSCAT concept in estimating ocean currents with accuracy below 0.2 m/s, at a spatial resolution of 25 km (i.e. spatial sampling of 12.5 km) and a temporal resolution of 24 hrs. With reference to the user requirements listed in Table 5.1, a spatial resolution of 25 km is not sufficient to cover coastal applications (such as search and rescue, marine renewable energy, oil and gas) but it would be more than adequate for most of the applications. The higher resolution product can, on one hand, extend the use of DopSCAT to coastal areas but, on the other hand, the accuracy of the estimated currents would be degraded. In fact, the accuracy depends on the radiometric resolution, which in turn depends on the number of looks and thus on the spatial resolution of the product.

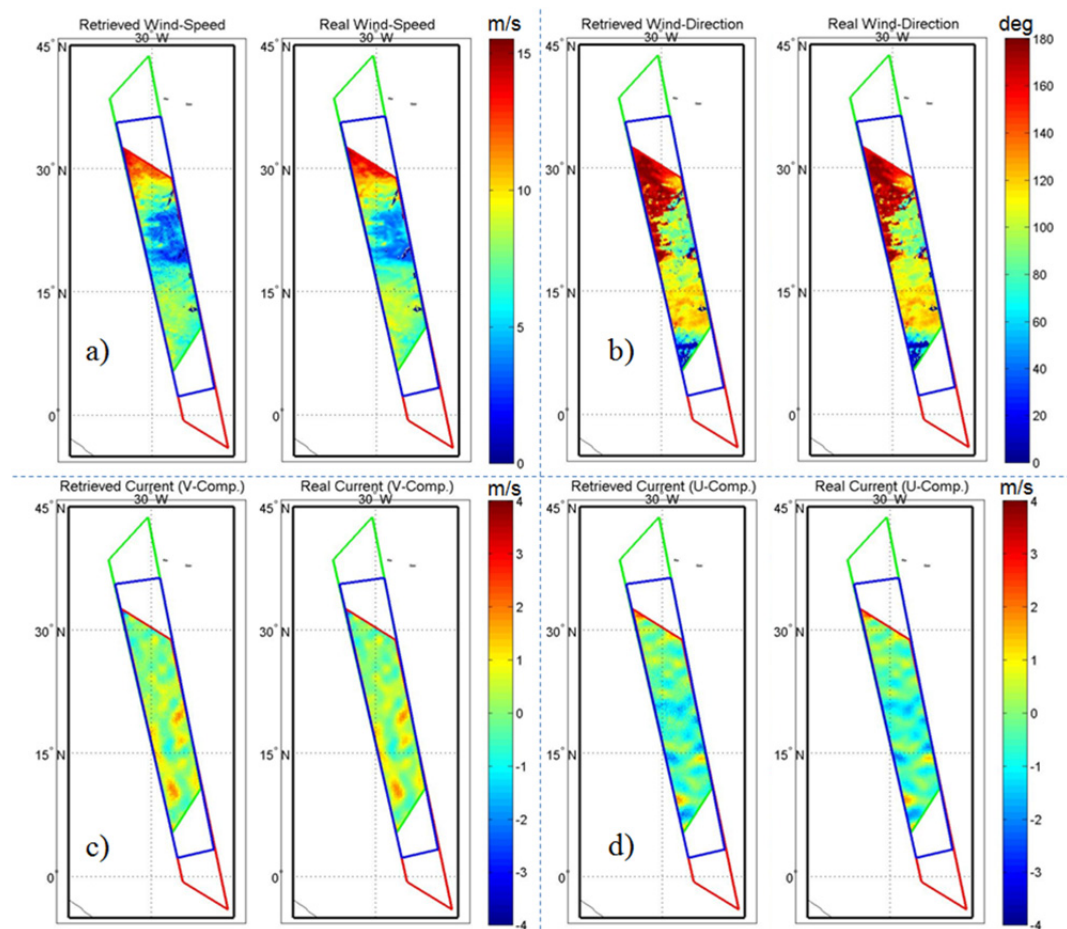


Fig. 5.9 a)-b) Comparison between real and retrieved wind vectors (VV-pol case); c)-d) Comparison between real and retrieved sea surface current vectors. Green , blue and red polygons represent the fore, mid and aft swaths. The interception between the three areas identifies those data where the retrieval can be applied.

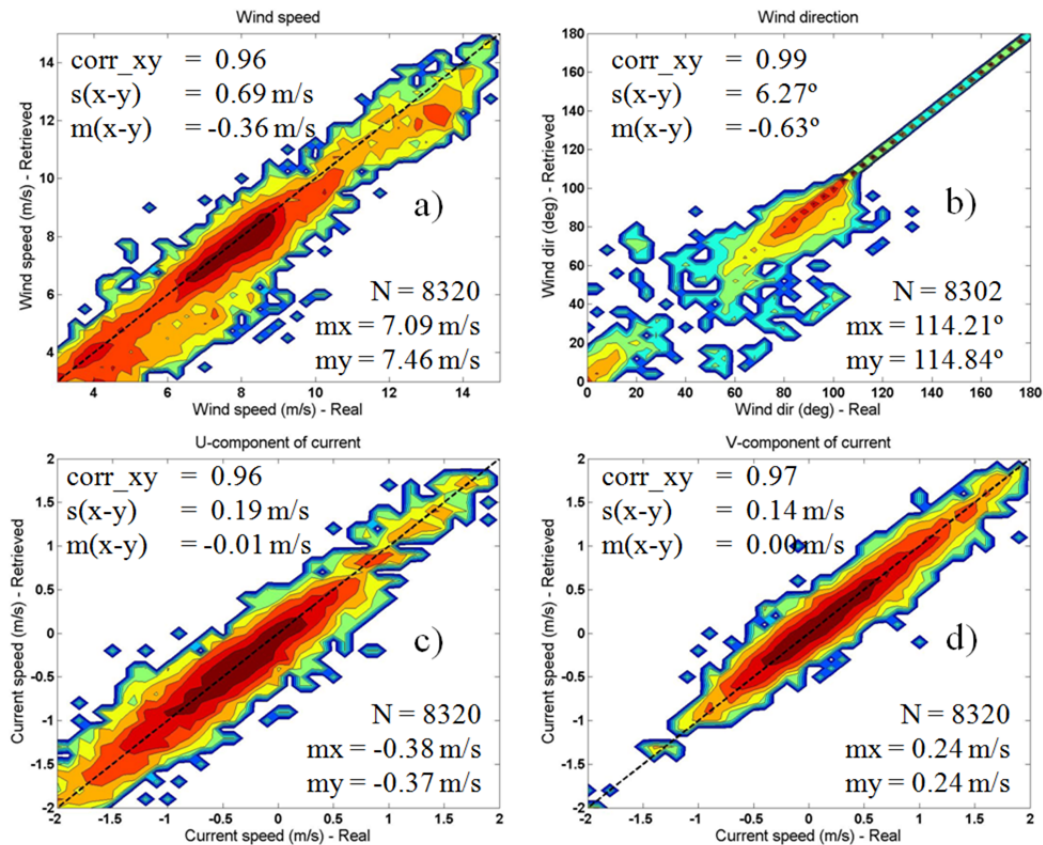


Fig. 5.10 a) Two-dimensional histogram of the retrieved wind speed versus the real wind speed; b) two-dimensional histogram of the retrieved wind direction versus the real wind direction (only winds above 4 m/s are used in the wind direction plot); c) two-dimensional histogram of the retrieved zonal component of the ocean current vector versus the real zonal component of the ocean current vector; d) same as figure c) but for the meridional component of the ocean current vector.

For high-resolution products, we expect an accuracy worse than 1 m/s in the ocean current estimates, which is only sufficient to meet the users' needs on a monthly time scale by performing temporal averages.

5.4 Conclusions

A number of scientific and operational applications require the measurement of ocean surface currents. Ocean surface current is a necessary input for ship routing, marine search and rescue, wave forecasting, seismic survey, maritime security, marine accidents and emergency response, anthropogenic and natural pollution, offshore operations, aquaculture, offshore renewable energy, amongst others [Donlon, 2013]. Ocean surface currents are complex and in coastal regions highly dynamic, and therefore need to be monitored with short time sampling (on a daily basis) on a global scale. To this aim, pros and cons of different satellite remote sensing techniques are discussed. Ocean Doppler scatterometry can provide simultaneous and accurate measurements of wind fields and

ocean motion vectors that can be used to generate global surface ocean current maps at a spatial resolution of 25 km (i.e. 12.5 km spatial sampling) on a daily basis (thanks to the very large swath). These maps will allow gaining some insights on the upper ocean mesoscale dynamics. From the user product requirements and observing system requirements, an innovative instrument concept, named DopSCAT, is derived. Special focus is given to the observation principle, the instrument architecture and the on-ground data processing. An end-to-end performance estimation of the DopSCAT mission is carried out using simulated input datasets that are generated either from ASCAT and OSCAR data or from the end-to-end simulator using values inferred from real data. The Level-1 performance, described in section 5.3.2, is compliant with the specifications given in section 5.1.3. In particular, the very good radiometric resolution in VV polarization would enable precise estimation of the wind vector: this is a necessary condition for an accurate estimation of the ocean motion. The use of double chirps instead of classical single up or down chirps enables Doppler shift to be estimated. Disturbances caused by the range processing of double chirps can be filtered by using Separation Compression Filters. Doppler frequency shifts associated with the geometry of observation and the relative movement between the radar and the rotating earth can be corrected thanks to the precise knowledge of the satellite attitude and motion. Residual Doppler shifts after corrections quantify the ocean motion.

Results of nominal Level 2 products simulations indicate that the threshold requirement of 0.2 m/s accuracy in sea surface current will be met for a wide range of conditions.

It is particularly important to note that the goal requirement of 0.1 m/s is very close to being met apart for cases of low wind speeds (<5 m/s) at far swath locations. The analysis of high-resolution products indicates a higher RMSE (>1 m/s), which is currently not compliant with the 0.2 m/s threshold requirement. Nevertheless, the resolution of the nominal product would allow covering most of the users' applications listed in Table 5.1.

The DopSCAT concept represents a major improvement with respect to current and future planned wind-scatterometers, as it provides the unique capability of simultaneous measurements of Ocean Vector Wind and Ocean Vector Motion on a global scale together with the capability of measuring very strong wind speeds (up to 60 m/s) through the use of cross-polarization. At instrument level, no critical elements have been identified for the DopSCAT development. The DopSCAT subsystems are, in fact, entirely based on heritage from past and current C-band radar missions (e.g., MetOp's ASCAT, MetOp-SG's SCA, Sentinel-1, RADARSAT-2).

6 Conclusions and Recommendations

In the past four years, the authors have studied and further developed the full-polarimetric modelling of ocean backscatter (with the extension to high wind speed cases) and Doppler signature. These improved models have led to the insight that it would be possible with a coherent scatterometer to measure both Ocean Vector Wind and Ocean Vector Motion. The authors have also developed a signal processing method and made a system design for this new advanced scatterometer application. The results are laid down in this thesis and in several journal publications. This chapter concludes the thesis and it gives recommendations for practical applications and usage in the fields of interest.

6.1 Conclusions

In chapter 2, a review of approximate scattering wave theories from random sea surfaces is provided. The main principles of the different theories are discussed and in depth comparisons between the proposed methods and empirical geophysical model functions at C, X and Ku- band are made. From these comparisons we can conclude that:

- Only the Weighted Curvature Approximation (WCA) and the 2nd-order Small Slope Approximation (SSA2) methods satisfy the accuracy requirement and, among them, only the SSA2 provide a full polarimetric scattering description.
- Theoretical calculations for co-polar signals in C-band and Ku-band are in good overall agreement with the experimental data represented by the empirical models, CMOD5 and NSCAT, with the exception of HH-polarization at high incidence angles (above 40°). The discrepancy between the measured and the simulated HH normalized radar cross-sections, is in part due to the inefficiency of the ocean wave spectrum and in part due to scattering contribution from breaking waves, not taken into account by the most common analytical scattering theories.
- To further improve the accuracy of the scattering computation two alternative methodologies can be followed. The first based on the inclusion of steep breaking waves in the scattering models, the second based on an optimization of the wave spectrum to better match well known empirical model functions at different frequencies.
- The use of SSA2 in combination with an optimized wave height spectrum shows a remarkable agreement with both Envisat-ASAR and Sentinel-1 data sets, collocated with ASCAT and ECMWF winds.

In chapter 3, the analytical model for the full polarimetric scattering of microwave radiation from the ocean is extended to the case of very high winds, where current empirical geophysical model functions are not accurate and fail in predicting both wind speeds and directions. The proposed model combines the 2nd order Small Slope Approximation Theory with the Vector Radiative Transfer Theory to obtain a statistical expression for the ocean full-polarimetric scattering matrix (in presence of foam) as function of wind speed and direction. Numerical results are compared with hurricane images by RADARSAT-2 C-band SAR in VV and VH, collocated in time and space with ECMWF model winds and, when available, SFMR wind measurements by NOAA's hurricane-hunter aircraft. From our analysis we can conclude that:

- In VH-polarization, the surface scattering saturates above 30 m/s, whereas the foam scattering term steadily increases, thus becoming the dominant scattering process above 33 m/s. By adding the foam scattering to the surface scattering, the resulting NRCS does not show any loss of sensitivity to the wind above 30 m/s.
- The effect of foam on VV NRCS is less evident than for VH NRCS because of two main reasons. The first reason is that the foam scattering process is largely dominated by the bottom surface scattering, which is less sensitive to wind than the other foam scattering mechanisms (i.e. volume and volume-surface scattering). The second reason, is that the surface scattering is always higher than the foam scattering.
- For the co-polar cases the wind speed sensitivity increases with the incidence angle: this particular feature is more evident in HH-pol than in VV-pol.
- Below 40° incidence VV and HH polarizations behave in a similar way. Beyond 40° incidence, instead, significant differences between VV and HH-pol occur, with HH-pol being more sensitive to wind-speed increase than VV-pol.
- The saturation and damping of the simulated co-polar signals occurs at wind speeds above 50 m/s in up-wind cases, and above 60 m/s in cross-wind cases.
- High wind speed sensitivity in cross-polarization is higher than in co-polarization, with cross-wind cases being more sensitive than up-wind cases. Hence, more accurate wind speed estimations may be expected from VH-pol.
- The effect of the incidence angle on NRCS saturation is much weaker in cross-polarization than in co-polarization.
- The deviations associated with the use of different foam coverage models are modest and do not change the overall conclusions.

Chapter 4 focuses on the Doppler signature of the ocean. The Doppler shift measured by a space-borne active microwave instrument over the ocean is expressed as the sum of

three main terms, representing the contributions to the central Doppler frequency associated with the wind (polarization dependent), the ocean current and the geometry of observation (both polarization independent). Chapter 4 presents an analytical model for the full-polarimetric sea surface scattering and Doppler signature, based on the Small Slope Approximation Theory at the 2nd order combined with both a linear and a weakly non-linear sea surface representation, namely SSA2-LIN and SSA2-CWM. The results obtained at different frequencies (C, X and Ku-bands) show that:

- The predicted wind-induced Doppler shift is larger in HH than in VV polarization. The radar signal is, in fact, more sensitive to the smaller waves in VV polarization than in HH. On the contrary, the radar signal is more sensitive to larger propagating waves in HH polarization than in VV polarization. Shorter gravity ocean waves are slower, whereas larger propagating waves are faster.
- As compared to the co-polar signals, the cross-polarised backscatter experiences a much lower Doppler shift across the full range of incidence angle investigated, due to its different scattering properties. The Doppler shift of the cross-polarization looks less sensitive to wind speed variations than the co-polarization.
- The central Doppler frequency for the co-polar signal shows an evident peak around 22° incidence, whereas this peak is not visible in VH polarization.
- At small incidence angles, linear and non-linear Doppler spectra almost coincide, because the influence of the horizontal velocity component on the Doppler spectrum is small. As the incidence angle increases, non-linear sea surfaces show larger Doppler central frequency and Doppler spread than the corresponding linear sea surfaces. This happens because the Choppy Wave Model corrects the horizontal component of particle velocities by adding a displacement, related to the surface elevation, to the horizontal position of the particles.
- Compared to SSA2-CWM, the SSA2-LIN provides slightly different normalized cross-section with maximum differences occurring at high incidence angles, up to 1 dB in Ku-band, 1.5 dB in X-band and about 2 dB in C-band, for the wind speeds investigated.
- Numerical results obtained by using the SSA2-CWM model are in good agreement with real measurements from Envisat-ASAR and SAXON-FPN Ku-band campaign. The results are also consistent with the empirical Geophysical model function CDOP.

Chapter 5 proposes an innovative mission concept for a C-band fan-beam wind scatterometer (DopSCAT) with both ocean vector wind and ocean motion vector measurement capability. The mission design is based on the novel coherent scattering

model derived in chapter 4. An End-to-End simulator of the DopSCAT mission concept is developed and extensive Monte-Carlo simulations over several possible wind and current scenarios are performed. The main conclusions of chapter 5 are summarized in the following sentences:

- The use of double chirps instead of classical up or down chirps enables Doppler shift to be estimated. Disturbances caused by the range processing of double chirps can be filtered by using Separation Compression Filters.
- Doppler frequency shifts associated with the geometry of observation and the relative movement between the radar and the rotating Earth can be corrected thanks to the precise knowledge of the satellite attitude and motion and the use of land areas, where the Doppler frequency shift must be zero by definition. Residual Doppler shifts after corrections quantify the ocean motion.
- The proposed mission design allows very good radiometric resolution in VV polarization. This enables precise estimation of the wind vector, that is a necessary condition for an accurate estimation of the ocean motion.
- Ocean Doppler scatterometry provides simultaneous and accurate measurements of wind fields and ocean motion vectors, which can be used to generate global surface ocean current maps at a spatial resolution of 25 km (i.e. 12.5 km spatial sampling) on a daily basis. These maps will allow gaining some insights on the upper ocean dynamics at mesoscale.
- Results of Level 2 nominal products simulations indicate that the threshold requirement of 0.2 m/s accuracy in sea surface current will be met for a wide range of conditions. The goal requirement of 0.1 m/s is very close to being met apart for cases of low wind speeds (<5 m/s) at far swath locations.
- The analysis of high-resolution products (12.5 km) indicates a higher RMSE (>1 m/s), which is currently not compliant with the 0.2 m/s threshold requirement. Nevertheless, the resolution of the nominal product would allow covering most of the users' applications listed in chapter 5.
- At instrument level, no critical elements have been identified for the DopSCAT development. The DopSCAT subsystems are, in fact, entirely based on heritage from past and current C-band radar missions (e.g. MetOp's ASCAT, MetOp-SG's SCA, Sentinel-1, RADARSAT-2).

6.2 Recommendations

In this section recommendations for the improvement of the physical scattering models described in the thesis are given. In addition important advises are given to define and design future families of ocean scatterometers.

- A necessary condition to improve the agreement between physical based scattering models and real measurements is to enhance the description of the directional sea surface wave spectrum. To this aim, dedicated instrumentations and measurement campaigns are needed to properly observe the wide range of ocean wavelengths (from millimeters to hundred meters) as a function of wind speed and direction.

Future improvements of the proposed scattering models might arise from:

- The inclusion of the rain effects on the radar signals by including dampening effects in the gravity part of the sea surface spectrum and rain-generated ring wave spectra in the gravity-capillary region.
- The inclusion of scattering from steep breaking waves. Steep frontal slopes of breaking waves generate specular reflections which contribute to the co-polar scattering but do not contribute to the cross-polar scattering, because specular reflections do not depolarize the scattered waves.
- For the case of extreme wind speeds, the inclusions of more consolidated physical relationships between bubble size, wind fields, depth into the foam and ocean salinity.

In the definition and design of future ocean scatterometers it is advisable to:

- Have cross-polar measurements in addition to the classical co-polar measurements. VH-pol is, in fact, best suited to retrieve very high-winds.
- Have Doppler measurement capability in addition to the classical wind vector measurement capability. This can be done, without any technology challenge, by transmitting a double chirp instead of a single chirp and then relying on an innovative coherent processing approach involving both up-chirp and down-chirp data streams.

Acronyms

AKE	Attitude Knowledge Error
AMI	Advanced Microwave Instrument
AOCS	Attitude and Orbital Control System
ASAR	Advanced Synthetic Aperture Radar
ASCAT	Advanced Scatterometer
CEU	Central Electronic Unit
CW	Continuous Wave
CWM	Choppy Wave Model
DC	Direct Current or Doppler Centroid
DLM	Deployment and Latch Mechanism
DOPSCAT	Doppler Scatterometer
ECMWF	European Centre for Medium-Range Weather Forecasts
ENVISAT	Environmental Satellite
EPC	Electronic Power Conditioner
ERS	European Remote-Sensing Satellite
FFT	Fast Fourier Transform
GMF	Geophysical Model Function
GO	Geometrical Optics
GPS	Global Positioning System
GWF	Ground Weighting Function
HDRM	Hold Down and Release Mechanism
HPA	High Power Amplifier
ICU	Instrument Control Unit
KA	Kirchhoff Approximation
LFM	Linear Frequency Modulation
LNA	Low Noise Amplifier
METOP	Meteorological Operational Satellite
NRCS	Normalized Radar Cross Section
NSCAT	NASA Scatterometer
NWP	Numerical Weather Prediction
OVM	Ocean Vector Motion
OVW	Ocean Vector Wind
PRF	Pulse Repetition Frequency
QuickSCAT	Quick Scatterometer
RF	Radio Frequency
SA	Scattering Amplitude
SASS	SeaSat-A Scatterometer System
S/C	Spacecraft
SFMR	Stepped-Frequency Microwave Radiometer
SM	Switch Matrix
SNR	Signal-to-Noise Ratio
SSA1	1 st -order Small Slope Approximation
SSA2	2 nd -order Small Slope Approximation
SPM	Small Perturbation Method
SPM	2 nd -order Small Perturbation Method
TSM	Two Scale Model
TWT	Travelling Wave Tube
WCA	Weighted Curvature Approximation
WVC	Wind Vector Cell
Xtalk	Cross-Polar Isolation or Cross-talk

Appendix

A. Kirchhoff Kernels

The general expression for the Kirchhoff Kernel writes:

$$\mathbf{K}_{11}(\mathbf{k}_s, \mathbf{k}_i) = R_{11}[(K_1^2 + q_{ks}q_{ki})\hat{\mathbf{k}}_s \cdot \hat{\mathbf{k}}_i - k_s k_i], \quad (\text{A.1})$$

$$\mathbf{K}_{12}(\mathbf{k}_s, \mathbf{k}_i) = R_{12}[K_1(q_{ks} + q_{ki})(\hat{\mathbf{k}}_s \times \hat{\mathbf{k}}_i) \cdot \hat{\mathbf{z}}], \quad (\text{A.2})$$

$$\mathbf{K}_{21}(\mathbf{k}_s, \mathbf{k}_i) = -R_{21}[K_1(q_{ks} + q_{ki})(\hat{\mathbf{k}}_s \times \hat{\mathbf{k}}_i) \cdot \hat{\mathbf{z}}], \quad (\text{A.3})$$

$$\mathbf{K}_{22}(\mathbf{k}_s, \mathbf{k}_i) = -R_{22}[(K_1^2 + q_{ks}q_{ki})\hat{\mathbf{k}}_s \cdot \hat{\mathbf{k}}_i - k_s k_i], \quad (\text{A.4})$$

Here, $R_{\alpha_s \alpha_i}$ are Fresnel coefficients:

$$R_{11} = \frac{\varepsilon_2 \frac{Q}{2} - \sqrt{\varepsilon_2 K_1^2 - (K_1^2 - \frac{Q^2}{4})}}{\varepsilon_2 \frac{Q}{2} + \sqrt{\varepsilon_2 K_1^2 - (K_1^2 - \frac{Q^2}{4})}}, \quad (\text{A.5})$$

$$R_{22} = \frac{\frac{Q}{2} - \sqrt{\varepsilon_2 K_1^2 - (K_1^2 - \frac{Q^2}{4})}}{\frac{Q}{2} + \sqrt{\varepsilon_2 K_1^2 - (K_1^2 - \frac{Q^2}{4})}}, \quad (\text{A.6})$$

$$R_{12} = R_{21} = \frac{R_{11} + R_{22}}{2}, \quad (\text{A.7})$$

with $Q = |\mathbf{K}_s - \mathbf{K}_i|$.

B. The Bragg and WCA Kernels

As clearly discussed in [Voronovich & Zavorotny, 2001], the general expression for the 1st order Bragg kernel writes:

$$B_{11}(\mathbf{k}_s, \mathbf{k}_i) = 2q_{ks}q_{ki} \frac{(\varepsilon_2 - 1)(q_{ks}^{(2)}q_{ki}^{(2)}\hat{\mathbf{k}}_s \cdot \hat{\mathbf{k}}_i - \varepsilon_2 k_s k_i)}{(\varepsilon_2 q_{ks}^{(1)} + q_{ks}^{(2)})(\varepsilon_2 q_{ki}^{(1)} + q_{ki}^{(2)})}, \quad (\text{B.1})$$

$$B_{12}(\mathbf{k}_s, \mathbf{k}_i) = 2q_{ks}q_{ki} \frac{(\varepsilon_2 - 1)K_1 q_{ks}^{(2)}(\hat{\mathbf{k}}_s \times \hat{\mathbf{k}}_i) \cdot \hat{\mathbf{z}}}{(\varepsilon_2 q_{ks}^{(1)} + q_{ks}^{(2)})(q_{ki}^{(1)} + q_{ki}^{(2)})}, \quad (\text{B.2})$$

$$B_{21}(\mathbf{k}_s, \mathbf{k}_i) = 2q_{ks}q_{ki} \frac{(\varepsilon_2 - 1)K_1 q_{ki}^{(2)}(\hat{\mathbf{k}}_s \times \hat{\mathbf{k}}_i) \cdot \hat{\mathbf{z}}}{(q_{ks}^{(1)} + q_{ks}^{(2)})(\varepsilon_2 q_{ki}^{(1)} + q_{ki}^{(2)})}, \quad (\text{B.3})$$

$$B_{22}(\mathbf{k}_s, \mathbf{k}_i) = -2q_{ks}q_{ki} \frac{(\varepsilon_2 - 1)K_1^2 q_{ks}^{(2)}(\hat{\mathbf{k}}_s \cdot \hat{\mathbf{k}}_i)}{(q_{ks}^{(1)} + q_{ks}^{(2)})(q_{ki}^{(1)} + q_{ki}^{(2)})}. \quad (\text{B.4})$$

The vertical components of the appropriate wave-vectors in the first (air) and the second (dielectric) medium are:

$$q_{ks}^{(1)} = \sqrt{K_1^2 - k_s^2} \quad q_{ks}^{(2)} = \sqrt{\varepsilon_2 K_1^2 - k_s^2}$$

$$\text{Im} q_{ks}^{(1,2)} \geq 0$$

$$q_{ki}^{(1)} = \sqrt{K_1^2 - k_i^2} \quad q_{ki}^{(2)} = \sqrt{\varepsilon_2 K_1^2 - k_i^2}$$

$$\text{Im} q_{ki}^{(1,2)} \geq 0$$

The second order Bragg terms write:

$$\begin{aligned}
(\mathbf{B}_2)_{11}(\mathbf{k}_s, \mathbf{k}_i; \xi) = & \\
& \frac{2q_{ks}q_{ki}(\varepsilon_2 - 1)}{(\varepsilon_2q_{ks}^{(1)} + q_{ks}^{(2)})(\varepsilon_2q_{ki}^{(1)} + q_{ki}^{(2)})} \left[-2 \frac{\varepsilon_2 - 1}{\varepsilon_2q_\xi^{(1)} + q_\xi^{(2)}} \right. \\
& (q_{ks}^{(2)}q_{ki}^{(2)}(\hat{\mathbf{k}}_s \cdot \xi)(\hat{\mathbf{k}}_i \cdot \xi) + \varepsilon_2k_s k_i \xi^2) \\
& - (\varepsilon_2K_1^2(q_{ks}^{(2)} + q_{ki}^{(2)}) + 2q_{ks}^{(2)}q_{ki}^{(2)}(q_\xi^{(1)} - q_\xi^{(2)}))(\hat{\mathbf{k}}_s \cdot \hat{\mathbf{k}}_i) \\
& \left. + 2\varepsilon_2 \frac{q_\xi^{(1)} + q_\xi^{(2)}}{\varepsilon_2q_\xi^{(1)} + q_\xi^{(2)}} (k_i q_{ks}^{(2)}(\hat{\mathbf{k}}_s \cdot \xi) + k_s q_{ki}^{(2)}(\hat{\mathbf{k}}_i \cdot \xi)) \right] , \tag{B.5}
\end{aligned}$$

$$\begin{aligned}
(\mathbf{B}_2)_{12}(\mathbf{k}_s, \mathbf{k}_i; \xi) = & \\
& \frac{2q_{ks}q_{ki}(\varepsilon_2 - 1)K_1}{(\varepsilon_2q_{ks}^{(1)} + q_{ks}^{(2)})(q_{ki}^{(1)} + q_{ki}^{(2)})} \left[-2 \frac{\varepsilon_2 - 1}{\varepsilon_2q_\xi^{(1)} + q_\xi^{(2)}} \right. \\
& (q_{ks}^{(2)}(\hat{\mathbf{k}}_s \cdot \xi)((\xi \times \hat{\mathbf{k}}_i) \cdot \hat{\mathbf{z}})) \\
& - (\varepsilon_2K_1^2 + q_{ks}^{(2)}q_{ki}^{(2)} + 2q_{ks}^{(2)}(q_\xi^{(1)} - q_\xi^{(2)}))((\hat{\mathbf{k}}_s \times \hat{\mathbf{k}}_i) \cdot \hat{\mathbf{z}}) \\
& \left. + 2\varepsilon_2 \frac{q_\xi^{(1)} + q_\xi^{(2)}}{\varepsilon_2q_\xi^{(1)} + q_\xi^{(2)}} k_s ((\xi \times \hat{\mathbf{k}}_i) \cdot \hat{\mathbf{z}}) \right] , \tag{B.6}
\end{aligned}$$

$$\begin{aligned}
(\mathbf{B}_2)_{21}(\mathbf{k}_s, \mathbf{k}_i; \xi) = & \\
& \frac{2q_{ks}q_{ki}(\varepsilon_2 - 1)K_1}{(q_{ks}^{(1)} + q_{ks}^{(2)})(\varepsilon_2q_{ki}^{(1)} + q_{ki}^{(2)})} \left[2 \frac{\varepsilon_2 - 1}{\varepsilon_2q_\xi^{(1)} + q_\xi^{(2)}} \right. \\
& (q_{ki}^{(2)}(\hat{\mathbf{k}}_i \cdot \xi)((\xi \times \hat{\mathbf{k}}_s) \cdot \hat{\mathbf{z}})) \\
& - (\varepsilon_2K_1^2 + q_{ks}^{(2)}q_{ki}^{(2)} + 2q_{ki}^{(2)}(q_\xi^{(1)} - q_\xi^{(2)}))((\hat{\mathbf{k}}_s \times \hat{\mathbf{k}}_i) \cdot \hat{\mathbf{z}}) \\
& \left. - 2\varepsilon_2 \frac{q_\xi^{(1)} + q_\xi^{(2)}}{\varepsilon_2q_\xi^{(1)} + q_\xi^{(2)}} k_i ((\xi \times \hat{\mathbf{k}}_s) \cdot \hat{\mathbf{z}}) \right] , \tag{B.7}
\end{aligned}$$

$$\begin{aligned}
(\mathbf{B}_2)_{22}(\mathbf{k}_s, \mathbf{k}_i; \xi) = & \\
& \frac{2q_{ks}q_{ki}(\varepsilon_2 - 1)K_1^2}{(q_{ks}^{(1)} + q_{ks}^{(2)})(q_{ki}^{(1)} + q_{ki}^{(2)})} \left[-2 \frac{\varepsilon_2 - 1}{\varepsilon_2q_\xi^{(1)} + q_\xi^{(2)}} \right. \\
& ((\hat{\mathbf{k}}_s \cdot \xi)(\hat{\mathbf{k}}_i \cdot \xi) - \xi^2 \hat{\mathbf{k}}_s \cdot \hat{\mathbf{k}}_i) \\
& \left. - (q_{ks}^{(2)} + q_{ki}^{(2)} + 2(q_\xi^{(1)} - q_\xi^{(2)}))(\hat{\mathbf{k}}_s \cdot \hat{\mathbf{k}}_i) \right] . \tag{B.8}
\end{aligned}$$

With reference to equation (2.22) the kernels used for the Weighted Curvature Approximation (WCA) are:

$$A(\mathbf{r}) = (iQ_z A_1(\mathbf{r}))^2 - A_2(0), \tag{B.9}$$

$$W(\mathbf{r}) = 2A_2(\mathbf{r})[A_2(\mathbf{r}) - 2(iQ_z A_1(\mathbf{r}))^2], \tag{B.10}$$

where

$$A_1(\mathbf{r}) = \int d\xi \zeta S(\xi) \frac{\mathbf{Q}_H \cdot \hat{\xi}}{Q_H} e^{i\xi \cdot \mathbf{r}}, \quad A_2(\mathbf{r}) = \int d\xi \zeta^2 S(\xi) \left(\frac{\mathbf{Q}_H \cdot \hat{\xi}}{Q_H} \right)^2 e^{i\xi \cdot \mathbf{r}}. \quad (\text{B.11})$$

C. Spatiotemporal covariance function determination for non-linear sea surfaces

The spatiotemporal covariance function of the backscattered field is the limit of the statistical average for infinity illumination area A :

$$\begin{aligned} \text{Cov}(\mathbf{k}_s, \mathbf{k}_i; t) \Big|_{\text{Non-Lin.}} = \\ \lim_{A \rightarrow \infty} \frac{4\pi \left\langle \left| \tilde{\mathbf{S}}_{\alpha_s \alpha_i}^{\text{SSA-2}}(\mathbf{k}_s, \mathbf{k}_i, t) - \left\langle \tilde{\mathbf{S}}_{\alpha_s \alpha_i}^{\text{SSA-2}}(\mathbf{k}_s, \mathbf{k}_i, t) \right\rangle \right|^2 \right\rangle}{A} = \\ \lim_{A \rightarrow \infty} \frac{4\pi \left(\left\langle \tilde{\mathbf{S}}_{\alpha_s \alpha_i}^{\text{SSA-2}}(\mathbf{k}_s, \mathbf{k}_i, t) \tilde{\mathbf{S}}_{\alpha_s \alpha_i}^{\text{SSA-2}*}(\mathbf{k}_s, \mathbf{k}_i, t) \right\rangle - \left| \left\langle \tilde{\mathbf{S}}_{\alpha_s \alpha_i}^{\text{SSA-2}}(\mathbf{k}_s, \mathbf{k}_i, t) \right\rangle \right|^2 \right)}{A} \end{aligned} \quad (\text{C.1})$$

with

$$\begin{aligned} & \langle \tilde{\mathbf{S}}_{\alpha_s \alpha_i}^{\text{SSA-2}}(\mathbf{k}_s, \mathbf{k}_i, t) \tilde{\mathbf{S}}_{\alpha_s \alpha_i}^{\text{SSA-2}*}(\mathbf{k}_s, \mathbf{k}_i, t) \rangle = \\ & \frac{1}{Q_z^2} \iint \frac{d\mathbf{r}_1}{(2\pi)^2} \frac{d\mathbf{r}_2}{(2\pi)^2} e^{-i\mathbf{Q}_H \cdot (\mathbf{r}_1 - \mathbf{r}_2)} \\ & \langle e^{iQ_z (h(\mathbf{r}_1, t) - h(\mathbf{r}_2, t))} e^{-i\mathbf{Q}_H \cdot (\mathbf{D}(\mathbf{r}_1, t) - \mathbf{D}(\mathbf{r}_2, t))} \\ & \left\{ 1 + \nabla \cdot \mathbf{D}(\mathbf{r}_1, t) + \nabla \cdot \mathbf{D}(\mathbf{r}_2, t) + (\nabla \cdot \mathbf{D}(\mathbf{r}_1, t))(\nabla \cdot \mathbf{D}(\mathbf{r}_2, t)) \right\} \\ & \times \left\{ \left| \mathbf{B}_{\alpha_s \alpha_i}(\mathbf{k}_s, \mathbf{k}_i) \right|^2 + \right. \\ & \frac{i}{4} \mathbf{B}_{\alpha_s \alpha_i}(\mathbf{k}_s, \mathbf{k}_i) \int M_{\alpha_s \alpha_i}^*(\mathbf{k}_s, \mathbf{k}_i, \xi_2) h^*(\xi_2, t) e^{-i\xi_2 \cdot \mathbf{r}_2} d\xi_2 \\ & - \frac{i}{4} \mathbf{B}_{\alpha_s \alpha_i}^*(\mathbf{k}_s, \mathbf{k}_i) \int M_{\alpha_s \alpha_i}(\mathbf{k}_s, \mathbf{k}_i, \xi_1) h(\xi_1, t) e^{i\xi_1 \cdot \mathbf{r}_1} d\xi_1 + \\ & \left. \frac{1}{16} \iint d\xi_1 d\xi_2 M_{\alpha_s \alpha_i}(\mathbf{k}_s, \mathbf{k}_i, \xi_1) M_{\alpha_s \alpha_i}^*(\mathbf{k}_s, \mathbf{k}_i, \xi_2) \cdot \right. \\ & \left. h(\xi_1, t) h^*(\xi_2, t) e^{i(\xi_1 \cdot \mathbf{r}_1 - \xi_2 \cdot \mathbf{r}_2)} \right\} \end{aligned} \quad (\text{C.2})$$

and

$$\begin{aligned}
\langle \tilde{\mathbf{S}}_{\alpha_s \alpha_i}^{SSA-2}(\mathbf{k}_s, \mathbf{k}_i, t) \rangle &= \\
&= \frac{1}{Q_z} \int \frac{d\mathbf{r}}{(2\pi)^2} J(\mathbf{r}, t) \exp[-i\mathbf{Q}_H \cdot \mathbf{r}] \\
&\langle \exp[-i\mathbf{Q}_H \cdot D(\mathbf{r}, t) + iQ_z h(\mathbf{r}, t)] \\
&\times \left[B_{\alpha_s \alpha_i}(\mathbf{k}_s, \mathbf{k}_i) - \frac{i}{4} \int M_{\alpha_s \alpha_i}(\mathbf{k}_s, \mathbf{k}_i, \xi) h(\xi, t) e^{i\xi \cdot \mathbf{r}} d\xi \right] \rangle
\end{aligned} \tag{C.3}$$

Using standard properties of Gaussian processes [Papoulis, 1965], we have

$$\begin{aligned}
Cov(\mathbf{k}_s, \mathbf{k}_i; t) \Big|_{Non-Lin.} &= \\
&\frac{1}{Q_z^2} \int \frac{d\mathbf{r}}{(2\pi)^2} \tilde{R}_{\alpha_s \alpha_i}(\mathbf{k}_s, \mathbf{k}_i; \mathbf{r}, t) \exp[-i\mathbf{Q}_H \cdot \mathbf{r}]
\end{aligned} \tag{C.4}$$

with

$$\begin{aligned}
\tilde{R}_{\alpha_s \alpha_i}(\mathbf{k}_s, \mathbf{k}_i; \mathbf{r}, t) &= \left| \chi_{\alpha_s \alpha_i}(\mathbf{k}_s, \mathbf{k}_i; t) \right|^2 + \\
&\sum_{n=1}^4 \sum_{m=1}^4 \Psi_{\alpha_s \alpha_i}^{(m,n)}(\mathbf{k}_s, \mathbf{k}_i; \mathbf{r}, t)
\end{aligned} \tag{C.5}$$

The expressions of the different components of $\tilde{R}_{\alpha_s \alpha_i}(\mathbf{k}_s, \mathbf{k}_i; \mathbf{r}, t)$ are provided here below.

Expression of $\chi_{\alpha_s \alpha_i}$

The term $\chi_{\alpha_s \alpha_i}(\mathbf{k}_s, \mathbf{k}_i; t) = \langle \tilde{\mathbf{S}}_{\alpha_s \alpha_i}^{SSA-2}(\mathbf{k}_s, \mathbf{k}_i, t) \rangle$ represents the coherent scattered amplitude and it can be expressed as:

$$\begin{aligned}
\chi_{\alpha_s \alpha_i}(\mathbf{k}_s, \mathbf{k}_i; t) &= \\
&\text{Exp} \left[\frac{-Q_z^2 \sigma_0^2 - Q_H^2 \sigma_{\hat{\mathbf{Q}}_H}^2}{2} \right] \left\{ (1 - iQ_z \sigma_1^2) B_{\alpha_s \alpha_i}(\mathbf{k}_s, \mathbf{k}_i) \right. \\
&- \frac{i}{4} \int d\xi e^{i\xi \cdot \mathbf{r}} M_{\alpha_s \alpha_i}(\mathbf{k}_s, \mathbf{k}_i, \xi) \cdot \\
&\left. [(1 - iQ_z \sigma_1^2)(iQ_z S(\xi, t) - \mathbf{Q}_H \cdot \hat{\xi} S(\xi, t)) - |\xi| S^*(\xi, t)] \right\}
\end{aligned} \tag{C.6}$$

with

$$\begin{cases} \sigma_0^2 = C(\mathbf{0},0) = \int d\xi S(\xi,0) \\ \sigma_1^2 = C_1(\mathbf{0},0) = \int d\xi |\xi| S(\xi,0) \\ \sigma_n^2 = C_n(\mathbf{0},0) = \int d\xi |\xi|^n S(\xi,0) \\ \sigma_{\hat{\mathbf{Q}}_H}^2 = C_{\hat{\mathbf{Q}}_H}(\mathbf{0},0) = \int d\xi (\hat{\mathbf{Q}}_H \cdot \hat{\xi})^2 S(\xi,0) \end{cases} \quad (C.7)$$

Expression of $\Psi_{\alpha_s, \alpha_i}^{(1,1)}$

The term $\Psi_{\alpha_s, \alpha_i}^{(1,1)}$ in equation (C.5) is simply given by:

$$\begin{aligned} \Psi_{\alpha_s, \alpha_i}^{(1,1)}(\mathbf{k}_s, \mathbf{k}_i; \mathbf{r}, t) &= \\ &= \left| B_{\alpha_s, \alpha_i}(\mathbf{k}_s, \mathbf{k}_i) \right|^2 \text{Exp}\left[\frac{-Q_z^2 S_0(\mathbf{r}, t) - Q_H^2 S_{\hat{\mathbf{Q}}_H}(\mathbf{r}, t)}{2} \right], \\ &= \left| B_{\alpha_s, \alpha_i}(\mathbf{k}_s, \mathbf{k}_i) \right|^2 E(\mathbf{r}, t) \end{aligned} \quad (C.8)$$

with

$$\begin{cases} S_0(\mathbf{r}, t) = 2[\sigma_0^2 - C(\mathbf{r}, t)] \\ S_{\hat{\mathbf{Q}}_H}(\mathbf{r}, t) = 2[\sigma_{\hat{\mathbf{Q}}_H}^2 - C_{\hat{\mathbf{Q}}_H}(\mathbf{r}, t)] \\ C_{\hat{\mathbf{Q}}_H}(\mathbf{r}, t) = \int d\xi (\hat{\mathbf{Q}}_H \cdot \hat{\xi})^2 S(\xi, t) e^{i\mathbf{r} \cdot \xi} \end{cases} \quad (C.9)$$

and

$$E(\mathbf{r}, t) = \text{Exp}\left[\frac{-Q_z^2 S_0(\mathbf{r}, t) - Q_H^2 S_{\hat{\mathbf{Q}}_H}(\mathbf{r}, t)}{2} \right]. \quad (C.10)$$

Expression of $\Psi_{\alpha_s, \alpha_i}^{(1,2)}$

The term $\Psi_{\alpha_s, \alpha_i}^{(1,2)}$ in equation (C.5) has the following form:

$$\begin{aligned} \Psi_{\alpha_s \alpha_i}^{(1,2)}(\mathbf{k}_s, \mathbf{k}_i; \mathbf{r}, t) = \\ \frac{i}{4} \mathbf{B}_{\alpha_s \alpha_i}(\mathbf{k}_s, \mathbf{k}_i) \text{Exp}\left[\frac{-Q_z^2 S_0(\mathbf{r}, t) - Q_H^2 S_{\hat{\mathbf{Q}}_H}(\mathbf{r}, t)}{2}\right] \times \\ \int d\xi M_{\alpha_s \alpha_i}^*(\mathbf{k}_s, \mathbf{k}_i; \xi) S^*(\xi, t) \left\{ (e^{i\mathbf{r}\cdot\xi} - 1)[iQ_z - \mathbf{Q}_H \cdot \hat{\xi}] \right\} \end{aligned} \quad (\text{C.11})$$

or equivalently:

$$\begin{aligned} \Psi_{\alpha_s \alpha_i}^{(1,2)}(\mathbf{k}_s, \mathbf{k}_i; \mathbf{r}, t) = \frac{i}{4} \mathbf{B}_{\alpha_s \alpha_i}(\mathbf{k}_s, \mathbf{k}_i) E(\mathbf{r}, t) \times \\ \int d\xi M_{\alpha_s \alpha_i}^*(\mathbf{k}_s, \mathbf{k}_i; \xi) Z_2(\xi, t) = \\ = \frac{i}{4} \mathbf{B}_{\alpha_s \alpha_i}(\mathbf{k}_s, \mathbf{k}_i) E(\mathbf{r}, t) \cdot mzd(\mathbf{k}_s, \mathbf{k}_i; \mathbf{r}, t) \end{aligned} \quad (\text{C.12})$$

being

$$\begin{cases} Z_2(\xi, t) = S^*(\xi, t) \left\{ (e^{i\mathbf{r}\cdot\xi} - 1)[iQ_z - \mathbf{Q}_H \cdot \hat{\xi}] \right\} \\ mzd(\mathbf{k}_s, \mathbf{k}_i; \mathbf{r}, t) = \int d\xi M_{\alpha_s \alpha_i}^*(\mathbf{k}_s, \mathbf{k}_i; \xi) Z_2(\xi, t) \end{cases} \quad (\text{C.13})$$

In order to simplify the notation, the dependence of mzd on α_s, α_i will be intentionally omitted.

Expression of $\Psi_{\alpha_s \alpha_i}^{(1,3)}$

Similarly to $\Psi_{\alpha_s \alpha_i}^{(1,2)}$, the term $\Psi_{\alpha_s \alpha_i}^{(1,3)}$ can be written as:

$$\begin{aligned} \Psi_{\alpha_s \alpha_i}^{(1,3)}(\mathbf{k}_s, \mathbf{k}_i; \mathbf{r}, t) = \\ -\frac{i}{4} \mathbf{B}_{\alpha_s \alpha_i}^*(\mathbf{k}_s, \mathbf{k}_i) \text{Exp}\left[\frac{-Q_z^2 S_0(\mathbf{r}, t) - Q_H^2 S_{\hat{\mathbf{Q}}_H}(\mathbf{r}, t)}{2}\right] \times \\ \int d\xi M_{\alpha_s \alpha_i}(\mathbf{k}_s, \mathbf{k}_i; \xi) S(\xi, t) \left\{ (1 - e^{i\mathbf{r}\cdot\xi})[iQ_z + \mathbf{Q}_H \cdot \hat{\xi}] \right\} \end{aligned} \quad (\text{C.14})$$

We also define:

$$\begin{cases} Z_1(\xi, t) = S(\xi, t) \left\{ (1 - e^{i\mathbf{r}\cdot\xi}) [iQ_Z + \mathbf{Q}_H \cdot \hat{\xi}] \right\} \\ mzu(\mathbf{k}_s, \mathbf{k}_i; \mathbf{r}, t) = \int d\xi M_{\alpha_s, \alpha_i}(\mathbf{k}_s, \mathbf{k}_i; \xi) Z_1(\xi, t) \end{cases}, \quad (\text{C.15})$$

thus

$$\begin{aligned} \Psi_{\alpha_s, \alpha_i}^{(1,3)}(\mathbf{k}_s, \mathbf{k}_i; \mathbf{r}, t) = \\ -\frac{i}{4} \mathbf{B}_{\alpha_s, \alpha_i}^*(\mathbf{k}_s, \mathbf{k}_i) E(\mathbf{r}, t) \times mzu(\mathbf{k}_s, \mathbf{k}_i; \mathbf{r}, t) \end{aligned} \quad (\text{C.16})$$

In order to simplify the notation, the dependence of mzu on α_s, α_i will be intentionally omitted.

Expression of $\Psi_{\alpha_s, \alpha_i}^{(1,4)}$

The term $\Psi_{\alpha_s, \alpha_i}^{(1,4)}$ is the result of two double integrals, one over the wave number vector ξ_1 and the other over the wave number vector ξ_2 :

$$\begin{aligned} \Psi_{\alpha_s, \alpha_i}^{(1,4)}(\mathbf{k}_s, \mathbf{k}_i; \mathbf{r}, t) = \\ \frac{1}{16} \text{Exp}\left[\frac{-Q_z^2 S_0(\mathbf{r}, t) - Q_H^2 S_{\hat{\mathbf{Q}}_H}(\mathbf{r}, t)}{2}\right] \times \\ \int \int d\xi_1 d\xi_2 M_{\alpha_s, \alpha_i}(\mathbf{k}_s, \mathbf{k}_i; \xi_1) \cdot \\ M_{\alpha_s, \alpha_i}^*(\mathbf{k}_s, \mathbf{k}_i; \xi_2) \left\{ S(\xi_1, t) e^{i\mathbf{r}\cdot\xi_2} \delta(\xi_1 - \xi_2) \cdot \right. \\ \left. + \left[S(\xi_1, t) (1 - e^{i\mathbf{r}\cdot\xi_1}) [iQ_Z + \mathbf{Q}_H \cdot \hat{\xi}_1] \right] \times \right. \\ \left. \left[S^*(\xi_2, t) (e^{i\mathbf{r}\cdot\xi_2} - 1) [iQ_Z - \mathbf{Q}_H \cdot \hat{\xi}_2] \right] \right\} \end{aligned} \quad (\text{C.17})$$

and it can be also expressed as

$$\begin{aligned}
\Psi_{\alpha_s, \alpha_i}^{(1,4)}(\mathbf{k}_s, \mathbf{k}_i; \mathbf{r}, t) = & \\
\frac{1}{16} \text{Exp} \left[\frac{-Q_z^2 S_0(\mathbf{r}, t) - Q_H^2 S_{\hat{Q}_H}(\mathbf{r}, t)}{2} \right] \times & \\
\left\{ \int d\xi \left| M_{\alpha_s, \alpha_i}(\mathbf{k}_s, \mathbf{k}_i; \xi) \right|^2 S(\xi, t) e^{i\mathbf{r} \cdot \xi} + \right. & \\
\int d\xi_1 M_{\alpha_s, \alpha_i}(\mathbf{k}_s, \mathbf{k}_i; \xi_1) S(\xi_1, t) \times & \\
\left[(1 - e^{i\mathbf{r} \cdot \xi_1}) [iQ_z + \mathbf{Q}_H \cdot \hat{\xi}_1] \right] \times & \\
\int d\xi_2 M_{\alpha_s, \alpha_i}^*(\mathbf{k}_s, \mathbf{k}_i; \xi_2) S^*(\xi_2, t) \times & \\
\left. \left[(e^{i\mathbf{r} \cdot \xi_2} - 1) [iQ_z - \mathbf{Q}_H \cdot \hat{\xi}_2] \right] \right\} & \quad . \quad (C.18)
\end{aligned}$$

and by using a more compact notation:

$$\begin{aligned}
\Psi_{\alpha_s, \alpha_i}^{(1,4)}(\mathbf{k}_s, \mathbf{k}_i; \mathbf{r}, t) = & \\
\frac{1}{16} E(\mathbf{r}, t) \times \left\{ mzq(\mathbf{k}_s, \mathbf{k}_i; \mathbf{r}, t) + \right. & \\
\left. mzu(\mathbf{k}_s, \mathbf{k}_i; \mathbf{r}, t) \cdot mzd(\mathbf{k}_s, \mathbf{k}_i; \mathbf{r}, t) \right\} & \quad . \quad (C.19)
\end{aligned}$$

where

$$mzq(\mathbf{k}_s, \mathbf{k}_i; \mathbf{r}, t) = \int d\xi \left| M_{\alpha_s, \alpha_i}(\mathbf{k}_s, \mathbf{k}_i; \xi) \right|^2 S(\xi, t) e^{i\mathbf{r} \cdot \xi}. \quad (C.20)$$

The dependence of mzq on α_s, α_i has been intentionally omitted in order to simplify the notation.

Expression of $\Psi_{\alpha_s, \alpha_i}^{(2,1)}$

The term $\Psi_{\alpha_s, \alpha_i}^{(2,1)}$ can be calculated as a product of three terms:

$$\begin{aligned} \Psi_{\alpha_s \alpha_i}^{(2,1)}(\mathbf{k}_s, \mathbf{k}_i; \mathbf{r}, t) = \\ \left| \mathbf{B}_{\alpha_s \alpha_i}(\mathbf{k}_s, \mathbf{k}_i) \right|^2 \text{Exp} \left[\frac{-Q_z^2 S_0(\mathbf{r}, t) - Q_H^2 S_{\hat{\mathbf{Q}}_H}(\mathbf{r}, t)}{2} \right] \times \\ i \left[-\frac{Q_z S_1(\mathbf{r}, t)}{2} + \mathbf{Q}_H \cdot \nabla C(\mathbf{r}, t) \right] \end{aligned} \quad (\text{C.21})$$

or, equivalently:

$$\Psi_{\alpha_s \alpha_i}^{(2,1)}(\mathbf{k}_s, \mathbf{k}_i; \mathbf{r}, t) = \left| \mathbf{B}_{\alpha_s \alpha_i}(\mathbf{k}_s, \mathbf{k}_i) \right|^2 E(\mathbf{r}, t) \times i R_1(\mathbf{k}_s, \mathbf{k}_i; \mathbf{r}, t),$$

where

$$\begin{cases} S_1(\mathbf{r}, t) = 2[\sigma_1^2 - C_1(\mathbf{r}, t)] = 2 \int d\xi |\xi| [S(\xi, 0) - S(\xi, t) e^{i\xi \cdot \mathbf{r}}] \\ \hat{\mathbf{Q}}_H \cdot \nabla C(\mathbf{r}, t) = i \int d\xi (\hat{\mathbf{Q}}_H \cdot \xi) S(\xi, t) e^{i\mathbf{r} \cdot \xi} \end{cases} \quad (\text{C.22})$$

and

$$R_1(\mathbf{k}_s, \mathbf{k}_i; \mathbf{r}, t) = -\frac{Q_z S_1(\mathbf{r}, t)}{2} + \mathbf{Q}_H \cdot \nabla C(\mathbf{r}, t)$$

Expression of $\Psi_{\alpha_s \alpha_i}^{(2,2)}$

The term $\Psi_{\alpha_s \alpha_i}^{(2,2)}$ in equation (C.5) has the following form:

$$\begin{aligned} \Psi_{\alpha_s \alpha_i}^{(2,2)}(\mathbf{k}_s, \mathbf{k}_i; \mathbf{r}, t) = \frac{i}{4} \mathbf{B}_{\alpha_s \alpha_i}(\mathbf{k}_s, \mathbf{k}_i) E(\mathbf{r}, t) \times \\ \left\{ msd_{\mathbf{r}}(\mathbf{k}_s, \mathbf{k}_i; \mathbf{r}, t) + i \cdot mzd(\mathbf{k}_s, \mathbf{k}_i; \mathbf{r}, t) \cdot R_1(\mathbf{r}, t) \right\}. \end{aligned} \quad (\text{C.23})$$

where

$$\begin{cases} msd_{\mathbf{r}}(\mathbf{k}_s, \mathbf{k}_i; \mathbf{r}, t) = \int d\xi M_{\alpha_s \alpha_i}^*(\mathbf{k}_s, \mathbf{k}_i; \xi) \chi_2(\xi, t) e^{i\mathbf{r} \cdot \xi} \\ \chi_2(\xi, t) = |\xi| S(\xi, t) \end{cases} \quad (C.24)$$

omitting the dependence of $msd_{\mathbf{r}}$ on the polarization.

Expression of $\Psi_{\alpha_s \alpha_i}^{(2,3)}$

As for $\Psi_{\alpha_s \alpha_i}^{(2,2)}$, the term $\Psi_{\alpha_s \alpha_i}^{(2,3)}$ can be computed as:

$$\begin{aligned} \Psi_{\alpha_s \alpha_i}^{(2,3)}(\mathbf{k}_s, \mathbf{k}_i; \mathbf{r}, t) = & -\frac{i}{4} \mathbf{B}_{\alpha_s \alpha_i}^*(\mathbf{k}_s, \mathbf{k}_i) E(\mathbf{r}, t) \times \\ & \left\{ msu_0(\mathbf{k}_s, \mathbf{k}_i; 0, t) + \right. \\ & \left. i \cdot mzu(\mathbf{k}_s, \mathbf{k}_i; \mathbf{r}, t) \cdot R_1(\mathbf{k}_s, \mathbf{k}_i; \mathbf{r}, t) \right\} \end{aligned} \quad (C.25)$$

where

$$\begin{cases} msu_0(\mathbf{k}_s, \mathbf{k}_i; 0, t) = \int d\xi M(\mathbf{k}_s, \mathbf{k}_i; \xi) \chi_1(\xi, t) \\ \chi_1(\xi, t) = |\xi| S^*(\xi, t) \end{cases} \quad (C.26)$$

For the sake of notation simplicity, the dependence of msu_0 on the polarization has been intentionally omitted.

Expression of $\Psi_{\alpha_s \alpha_i}^{(2,4)}$

The compact form of $\Psi_{\alpha_s \alpha_i}^{(2,4)}$ is:

$$\begin{aligned} \Psi_{\alpha_s \alpha_i}^{(2,4)}(\mathbf{k}_s, \mathbf{k}_i; \mathbf{r}, t) = & \frac{1}{16} E(\mathbf{r}, t) \times \\ & \left\{ msu_0 \cdot mzd + i \cdot mzq \cdot R_1 + \right. \\ & \left. mzu \cdot msd_{\mathbf{r}} + i \cdot mzu \cdot mzd \cdot R_1 \right\} \end{aligned} \quad (C.27)$$

where the dependence of the different functions on $\mathbf{k}_s, \mathbf{k}_i; \mathbf{r}, t$ has been intentionally omitted to simplify the notation.

Expression of $\Psi_{\alpha_s \alpha_i}^{(3,1)}$

This term can be expressed as:

$$\begin{aligned} \Psi_{\alpha_s \alpha_i}^{(3,1)}(\mathbf{k}_s, \mathbf{k}_i; \mathbf{r}, t) &= \\ & \left| \mathbf{B}_{\alpha_s \alpha_i}(\mathbf{k}_s, \mathbf{k}_i) \right|^2 \text{Exp} \left[\frac{-Q_z^2 S_0(\mathbf{r}, t) - Q_H^2 S_{\hat{\mathbf{Q}}_H}(\mathbf{r}, t)}{2} \right] \times \\ & \quad i \left[\frac{Q_z S_1(\mathbf{r}, t)}{2} - \mathbf{Q}_H \cdot \nabla C(\mathbf{r}, t) \right] \\ & = \left| \mathbf{B}_{\alpha_s \alpha_i}(\mathbf{k}_s, \mathbf{k}_i) \right|^2 E(\mathbf{r}, t) \times i R_2(\mathbf{k}_s, \mathbf{k}_i; \mathbf{r}, t) \end{aligned} \quad (\text{C.28})$$

with

$$R_2(\mathbf{k}_s, \mathbf{k}_i; \mathbf{r}, t) = \frac{Q_z S_1(\mathbf{r}, t)}{2} + \mathbf{Q}_H \cdot \nabla C(\mathbf{r}, t).$$

Expression of $\Psi_{\alpha_s \alpha_i}^{(3,2)}$

The expression of $\Psi_{\alpha_s \alpha_i}^{(3,2)}$ is similar to the one of $\Psi_{\alpha_s \alpha_i}^{(2,2)}$

$$\begin{aligned} \Psi_{\alpha_s \alpha_i}^{(3,2)}(\mathbf{k}_s, \mathbf{k}_i; \mathbf{r}, t) &= \frac{i}{4} \mathbf{B}_{\alpha_s \alpha_i}(\mathbf{k}_s, \mathbf{k}_i) E(\mathbf{r}, t) \times \\ & \quad \left\{ msd_0 + i \cdot mzd \cdot R_2 \right\} \end{aligned} \quad (\text{C.29})$$

with

$$msd_0(\mathbf{k}_s, \mathbf{k}_i; 0, t) = \int d\xi M_{\alpha_s \alpha_i}^*(\mathbf{k}_s, \mathbf{k}_i; \xi) \chi_2(\xi, t). \quad (\text{C.30})$$

For simplicity, we have omitted from the notation the dependence of msd_0 on the polarization.

Expression of $\Psi_{\alpha_s \alpha_i}^{(3,3)}$

As for $\Psi_{\alpha_s \alpha_i}^{(3,2)}$, the term $\Psi_{\alpha_s \alpha_i}^{(3,3)}$ can be expressed as:

$$\Psi_{\alpha_s \alpha_i}^{(3,3)}(\mathbf{k}_s, \mathbf{k}_i; \mathbf{r}, t) = -\frac{i}{4} B_{\alpha_s \alpha_i}^*(\mathbf{k}_s, \mathbf{k}_i) E(\mathbf{r}, t) \times \left\{ msu_{\mathbf{r}} + i \cdot mzu \cdot R_2 \right\}. \quad (C.31)$$

with

$$msu_{\mathbf{r}}(\mathbf{k}_s, \mathbf{k}_i; \mathbf{r}, t) = \int d\xi M_{\alpha_s \alpha_i}(\mathbf{k}_s, \mathbf{k}_i; \xi) \chi_1(\xi, t) e^{i\mathbf{r} \cdot \xi}. \quad (C.32)$$

Expression of $\Psi_{\alpha_s \alpha_i}^{(3,4)}$

The term $\Psi_{\alpha_s \alpha_i}^{(3,4)}$ can be expressed as sum of 4 main elements:

$$\Psi_{\alpha_s \alpha_i}^{(3,4)}(\mathbf{k}_s, \mathbf{k}_i; \mathbf{r}, t) = \frac{1}{16} E(\mathbf{r}, t) \times \left\{ msu_{\mathbf{r}} \cdot mzd + i \cdot mzq \cdot R_2 + mzu \cdot msd_0 + i \cdot mzu \cdot mzd \cdot R_2 \right\}. \quad (C.33)$$

Expression of $\Psi_{\alpha_s \alpha_i}^{(4,1)}$

After simple manipulations, this term can be written as:

$$\Psi_{\alpha_s \alpha_i}^{(4,1)}(\mathbf{k}_s, \mathbf{k}_i; \mathbf{r}, t) = \left| B_{\alpha_s \alpha_i}(\mathbf{k}_s, \mathbf{k}_i) \right|^2 E(\mathbf{r}, t) \times \left\{ -\Delta C(\mathbf{r}, t) - R_1 \cdot R_2 \right\}. \quad (C.34)$$

where $\Delta C(\mathbf{r}, t)$ is the Laplacian operator, that is:

$$\Delta C(\mathbf{r}, t) = \nabla \cdot \nabla C(\mathbf{r}, t) = - \int d\xi |\xi|^2 S(\xi, t) e^{i\mathbf{r} \cdot \xi} . \quad (\text{C.35})$$

Expression of $\Psi_{\alpha_s \alpha_i}^{(4,2)}$

$$\Psi_{\alpha_s \alpha_i}^{(4,2)}(\mathbf{k}_s, \mathbf{k}_i; \mathbf{r}, t) = \frac{i}{4} B_{\alpha_s \alpha_i}(\mathbf{k}_s, \mathbf{k}_i) E(\mathbf{r}, t) \times \left\{ i \cdot msd_0 \cdot R_1 + i \cdot msd_r \cdot R_2 + mzd \cdot [-\Delta C - R_1 R_2] \right\} . \quad (\text{C.36})$$

Expression of $\Psi_{\alpha_s \alpha_i}^{(4,3)}$

$$\Psi_{\alpha_s \alpha_i}^{(4,3)}(\mathbf{k}_s, \mathbf{k}_i; \mathbf{r}, t) = -\frac{i}{4} B_{\alpha_s \alpha_i}^*(\mathbf{k}_s, \mathbf{k}_i) E(\mathbf{r}, t) \times \left\{ i \cdot msu_r \cdot R_1 + i \cdot msu_0 \cdot R_2 + mzu \cdot [-\Delta C - R_1 R_2] \right\} . \quad (\text{C.37})$$

Expression of $\Psi_{\alpha_s \alpha_i}^{(4,4)}$

The last term of the summation in equation (C.5) is:

$$\Psi_{\alpha_s \alpha_i}^{(4,4)}(\mathbf{k}_s, \mathbf{k}_i; \mathbf{r}, t) = \frac{1}{16} E(\mathbf{r}, t) \times \left\{ \begin{aligned} &msu_0 \cdot msd_0 + msu_r \cdot msd_r + i \cdot msu_r \cdot mzd \cdot R_1 \\ &+ i \cdot msu_0 \cdot mzd \cdot R_2 + i \cdot msd_r \cdot mzu \cdot R_2 \\ &+ i \cdot msd_0 \cdot mzu \cdot R_1 + mzd \cdot [-\Delta C - R_1 R_2] + \\ &+ mzu \cdot mzd \cdot [-\Delta C - R_1 R_2] \end{aligned} \right\} . \quad (\text{C.38})$$

D. Some Important Analytical Expressions

In the case of sea surface spectra with two azimuthal harmonics, the correlation functions and related Kirchhoff integrals can be efficiently computed with the help of the Bessel functions. The two dimensional sea spectrum can be expressed as:

$$S(\xi, t) = S_a(\xi) \exp(-i\omega_\xi t) + S_a(-\xi) \exp(i\omega_\xi t) \quad (D.1)$$

where

$$\begin{cases} S_a(\xi) = S(\xi) \cos^2\left(\frac{\phi - \phi_w}{2}\right) = S(\xi) \cos^2\left(\frac{\Theta}{2}\right) \\ S_a(-\xi) = S(\xi) \sin^2\left(\frac{\phi - \phi_w}{2}\right) = S(\xi) \sin^2\left(\frac{\Theta}{2}\right) \end{cases} \quad (D.2)$$

being Θ the angle with respect to the wind direction. The centrosymmetric spectrum $S(\xi)$ is equal to:

$$S(\xi) = M(\xi)(1 + \Delta(\xi) \cos(2\Theta)). \quad (D.3)$$

The function $M(\xi)$ represents the isotropic part of the spectrum modulated by $1 + \Delta(\xi) \cos(2\Theta)$, corresponding to the angular function. With the previous assumptions, the correlation function can be written as:

$$\begin{aligned} C(\mathbf{r}, t) &= \int d\xi S(\xi, t) \exp(i\xi \cdot \mathbf{r}) = \\ &= \int_0^\infty \int_0^{2\pi} d\xi d\Theta \xi [S_a(\xi) \exp(-i\omega_\xi t) + S_a(-\xi) \exp(i\omega_\xi t)] \times \\ &\quad \exp[ir\xi \cos(\Theta - \varphi_r)] = \\ &= \int_0^\infty d\xi \left[\sum_{n=-\infty}^\infty \frac{(i)^n e^{in\varphi_r}}{2\pi} J_n(r\xi) \left\{ \exp(-i\omega_\xi t) \times \right. \right. \\ &\quad \left. \int_0^{2\pi} d\Theta \xi M(\xi)(1 + \Delta(\xi) \cos(2\Theta)) \cos^2\left(\frac{\Theta}{2}\right) e^{in\Theta} + \right. \\ &\quad \left. \left. \exp(i\omega_\xi t) \int_0^{2\pi} d\Theta \xi M(\xi)(1 + \Delta(\xi) \cos(2\Theta)) \sin^2\left(\frac{\Theta}{2}\right) e^{in\Theta} \right\} \right] \end{aligned} \quad (D.4)$$

where $J_n(r\xi)$ is the Bessel function of order n . After some straightforward calculation, we obtain:

$$\begin{aligned}
C(\mathbf{r}, t) = & \\
& \int_0^\infty d\xi \xi \{ \cos(\omega_\xi t) M(\xi) \times \\
& [J_0(r\xi) - J_2(r\xi) \Delta(\xi) \cos(2\varphi_r)] + \\
& \frac{1}{2} \sin(\omega_\xi t) M(\xi) \times \\
& [(2 + \Delta(\xi)) J_1(r\xi) \cos(\varphi_r) - \Delta(\xi) J_3(r\xi) \cos(3\varphi_r)] \}
\end{aligned} \tag{D.5}$$

Similarly for $\Delta C(\mathbf{r}, t)$ and $C_1(\mathbf{r}, t)$ we get:

$$\begin{aligned}
\Delta C(\mathbf{r}, t) = & \\
& - \int_0^\infty d\xi \xi \{ \cos(\omega_\xi t) \xi^2 M(\xi) \times \\
& [J_0(r\xi) - J_2(r\xi) \Delta(\xi) \cos(2\varphi_r)] + \\
& \frac{1}{2} \sin(\omega_\xi t) \xi^2 M(\xi) \times \\
& [(2 + \Delta(\xi)) J_1(r\xi) \cos(\varphi_r) - \Delta(\xi) J_3(r\xi) \cos(3\varphi_r)] \}
\end{aligned} \tag{D.6}$$

and

$$\begin{aligned}
C_1(\mathbf{r}, t) = & \int_0^\infty d\xi \xi \{ \cos(\omega_\xi t) \xi M(\xi) \times \\
& [J_0(r\xi) - J_2(r\xi) \Delta(\xi) \cos(2\varphi_r)] + \\
& \frac{1}{2} \sin(\omega_\xi t) \xi M(\xi) \times \\
& [(2 + \Delta(\xi)) J_1(r\xi) \cos(\varphi_r) - \Delta(\xi) J_3(r\xi) \cos(3\varphi_r)] \}
\end{aligned} \tag{D.7}$$

With some algebra we obtain also:

$$\begin{aligned}
\hat{\mathbf{Q}}_{\text{H}} \cdot \nabla C(\mathbf{r}, t) &= \int_0^{\infty} d\xi \xi \cos(\omega_{\xi} t) \\
&\{-J_1(r\xi) \xi M(\xi) \cos(\varphi_r - \varphi_{\hat{\mathbf{Q}}_{\text{H}}}) - \\
&\frac{1}{2}[(J_1(r\xi) - J_3(r\xi)) \xi M(\xi) \Delta(\xi) \cos(\varphi_r - \varphi_{\hat{\mathbf{Q}}_{\text{H}}}) \cos(2\varphi_r) + \\
&(J_1(r\xi) + J_3(r\xi)) \xi M(\xi) \Delta(\xi) \sin(\varphi_r - \varphi_{\hat{\mathbf{Q}}_{\text{H}}}) \sin(2\varphi_r)]\} + \\
&\int_0^{\infty} d\xi \xi \sin(\omega_{\xi} t) \left\{ \frac{J_0(r\xi) \xi M(\xi)}{2} \left(1 + \frac{\Delta(\xi)}{2}\right) \cos(\varphi_{\hat{\mathbf{Q}}_{\text{H}}}) \right. \\
&+ \frac{J_4(r\xi) \xi M(\xi) \Delta(\xi)}{4} \cos(\varphi_{\hat{\mathbf{Q}}_{\text{H}}} - 4\varphi_r) \\
&- \frac{J_2(r\xi) \xi M(\xi)}{2} \left(1 + \frac{\Delta(\xi)}{2}\right) \cos(\varphi_{\hat{\mathbf{Q}}_{\text{H}}} - 2\varphi_r) \\
&\left. - \frac{J_2(r\xi) \xi M(\xi) \Delta(\xi)}{4} \cos(\varphi_{\hat{\mathbf{Q}}_{\text{H}}} + 2\varphi_r) \right\} \quad . \quad (D.8)
\end{aligned}$$

and

$$\begin{aligned}
C_{\hat{\mathbf{Q}}_{\text{H}}}(\mathbf{r}, t) &= \int_0^{\infty} d\xi \xi \sin(\omega_{\xi} t) \\
&\left\{ \frac{J_5(r\xi) M(\xi) \Delta(\xi)}{8} \cos(2\varphi_{\hat{\mathbf{Q}}_{\text{H}}} - 5\varphi_r) - \right. \\
&\frac{J_3(r\xi) M(\xi) (1 - 0.5\Delta(\xi))}{4} \cos(2\varphi_{\hat{\mathbf{Q}}_{\text{H}}} - 3\varphi_r) + \\
&\frac{J_1(r\xi) M(\xi) (1 + 0.5\Delta(\xi))}{4} \cos(\varphi_r) + \\
&\frac{J_1(r\xi) M(\xi) (1 + \Delta(\xi))}{4} \cos(2\varphi_{\hat{\mathbf{Q}}_{\text{H}}}) \cos(\varphi_r) - \\
&\frac{J_3(r\xi) M(\xi) \Delta(\xi)}{4} \cos(3\varphi_r) + \\
&\left. \frac{J_1(r\xi) M(\xi)}{4} \sin(2\varphi_{\hat{\mathbf{Q}}_{\text{H}}}) \sin(\varphi_r) \right\} \quad . \quad (D.9)
\end{aligned}$$

E. From Radar Ambiguity to Cross-Talk requirement

The requirement on radar ambiguity, presented in chapter 5, has an important implication on the cross-polar isolation (also called cross-talk or Xtalk) of the measurement system. In fact, the predicted VH-NRCS can be more than 25 dB lower than VV-NRCS at 15 m/s wind speed and 20° incidence angle. This is also supported by Fig.

2.10 and 2.16. Because of the significant difference in backscattering, VH-pol measurements will be contaminated by VV-pol echoes unless stringent constraints on the instrument cross-talk are imposed. To better explain the concept, it will be helpful recalling the expression of the VH-measured scattering:

$$M_{VH} = GTx_{VV} \cdot S_{VH} \cdot GRx_{HH} + GTx_{VH} \cdot S_{HH} \cdot GRx_{HH} + GTx_{VV} \cdot S_{VV} \cdot GRx_{VH} + GTx_{VH} \cdot S_{HV} \cdot GRx_{VH} \quad (E.1)$$

where

M_{VH}	Measured scattering in VH-polarization
GTx_{VV}	Tx Antenna Gain in V-polarization
GTx_{VH}	Leakage in transmission (from V to H)
GRx_{HH}	Rx Antenna Gain in H-polarization
GRx_{VH}	Leakage in receive (from V to H)
S_{VH}	Surface scattering in VH-polarization
S_{VV}	Surface scattering in VV-polarization
S_{HH}	Surface scattering in HH-polarization
S_{HV}	Surface scattering in HV-polarization

The first term in equation (E.1) is the useful signal (i.e. the one we want to measure), all the other terms are results of contaminations and, as such, shall be carefully monitored in order to meet the ambiguity requirement. If we consider the case of 20° incidence and 15 m/s wind speed, the second and the third term of equation (E.1) are of comparable magnitude. In fact, the Kirchhoff approximation of the scattering field holds well for small angles of incidence and thus $S_{VV} \approx S_{HH}$. In addition, we can also assume $GTx_{VH} \approx GRx_{VH}$ and $GTx_{VV} \approx GRx_{HH}$. The fourth term can be neglected as it is the product of two small leakages and a low backscattering value (S_{HV}).

The requirement asks for 1% ambiguity error at near swath (i.e. at 20°) with a wind speed within the well of 15 m/s. To simplify the problem and make it intuitive, let's focus only on what happens within the well and forget for a moment the ambiguous contributions arising from outside the well. To meet the 1% requirement, we need to impose:

$$\frac{GTx_{VH} \cdot S_{HH} \cdot GRx_{HH} + GTx_{VV} \cdot S_{VV} \cdot GRx_{VH}}{GTx_{VV} \cdot S_{VH} \cdot GRx_{HH}} \leq 0.01 \quad (E.2)$$

or equivalently,

$$\left(\frac{GTx_{VH}}{GTx_{VV}} \right) \left(\frac{S_{HH}}{S_{VH}} \right) + \left(\frac{S_{VV}}{S_{VH}} \right) \left(\frac{GRx_{VH}}{GRx_{HH}} \right) \leq 0.01 \quad (E.3)$$

and by using the assumptions discussed above

$$2 \left(\frac{GRx_{VH}}{GRx_{HH}} \right) \left(\frac{S_{VV}}{S_{VH}} \right) \leq 0.01 \quad (E.4)$$

The first ratio in brackets is a cross-talk term which is a measure of polarization contamination. The second term is the ratio between scattering in HH and VH which has been quantified as being about 25 dB, thus:

$$\left[2 \left(\frac{GRx_{VH}}{GRx_{HH}} \right) \left(\frac{S_{VV}}{S_{VH}} \right) \right]_{dB} \approx 3dB + Xtalk_{dB} + 25dB \leq -20dB \quad (E.5)$$

Equation (E.5) imposes a stringent constraint on the cross-talk:

$$Xtalk_{dB} \leq -48dB \quad (E.6)$$

The last constrain does not consider the contamination from region outside the well, so sufficient margins shall be put on (E.6) to guarantee compliance against the ambiguity requirement.

F. Compensation of the Geometrical Doppler Shift

The predicted geometrical Doppler shift is given by [Raney, 1986]:

$$f_{Dp} = \frac{2V_s}{\lambda} \sin \gamma \cos \alpha \left[1 - \frac{\omega_e}{\omega_s} (\varepsilon \cos \beta \sin \psi \tan \alpha - \cos \psi) \right] \quad (F.1)$$

Where

- V_s is the magnitude of the spacecraft velocity along its orbital path;
- λ is the radar wavelength;
- γ is the off-nadir angle or elevation angle of the radar beam;
- α is the angle between the range elevation plane and the spacecraft orbital plane;
- β is the argument of latitude;
- ψ is the inclination of the spacecraft orbital plane;
- ω_s is the angular rate of the spacecraft on its orbit;
- ω_e is the angular rate of the Earth's rotation;
- ε is equal to +1 or -1 for right and left looking observations, respectively.

In our simulations, we have made the assumption that the satellite adopts the same yaw steering law (along the orbit) of MetOp satellite. A yaw steering law is implemented to compensate the rotation of the Earth. In particular, the use of this steering law allows maximizing the overlap between fore, mid and aft beams. The reference frame selected for DopSCAT has positive Y-axis pointing towards the flight direction, positive Z-axis pointing towards outer space and the X-axis completing the right handed Cartesian reference system. The three satellite steering angles are:

$$\eta = C_X \sin(2 \cdot \text{PSO})$$

$$\xi = C_Y \sin(\text{PSO})$$

(F.2)

$$\zeta = C_Z \cos(\text{PSO}) \cdot \left[1 - \frac{(1 - C_Z \cos(\text{PSO}))^2}{3} \right]$$

Where (η, ζ, ξ) represent Pitch, Roll and Yaw angles respectively. The quantity PSO is the "Position sur l'Orbite", in radians. The angular coefficients C_X , C_Y and C_Z are:

$$\begin{aligned}
C_X &= -e_e^2 \left(\frac{a_e}{a} \right) \frac{\sin^2(i)}{2} \\
C_Y &= -e_e^2 \left(\frac{a_e}{a} \right) \sin(i) \cdot \cos(i) \\
C_Z &= \frac{k \cdot \cos(i - \pi/2)}{1 + k \cdot \sin(i - \pi/2)}
\end{aligned} \tag{F.3}$$

In equation (F.3), a_e is the semi-major axis of the Earth reference ellipsoid, $k = (\omega_e/\omega_s)$. A numerical computation of the geometrical Doppler shift for the Mid, Fore and Aft DopSCAT antennas is presented in Fig.F.1. Both Fore and Aft antennas show a significant Doppler shift up to about 150 KHz magnitude. In ERS-1/2 as well as in ASCAT-A/B an on-board demodulation was performed to compensate the Doppler shift, thus avoiding receiving data outside the filters bandwidth. Thanks to the advance in digital processing, data rate and data volume capability, it is possible for DopSCAT to sample the echoes signal with a frequency high enough to avoid spectral aliasing. Considering that the chirp bandwidth is about 1 MHz and that the geometrical Doppler shift is about 150 KHz, using a sampling frequency of 6 MHz would allow an adequate sampling of the total signal bandwidth. A similar approach has been also selected for MetOp-SG scatterometer and it has the big advantage of avoiding any processing on-board. Basically, for DopSCAT the demodulation of the received signals will be performed by the on-ground processor as depicted in Fig.5.5. The Doppler shift measurements as well as the NRCS measurements can be affected by pointing errors caused by:

- errors in satellite orbit and attitude parameters;
- thermoelastic distortions of the antenna subsystem;
- electronic mispointing of the antenna subsystem.

The error in Doppler measurement can be expressed in the following form:

$$f_{Derr} = f_D - f_{Dp} = f_{Dpe} + f_{D\sigma^0} + f_{D\Delta} \tag{F.4}$$

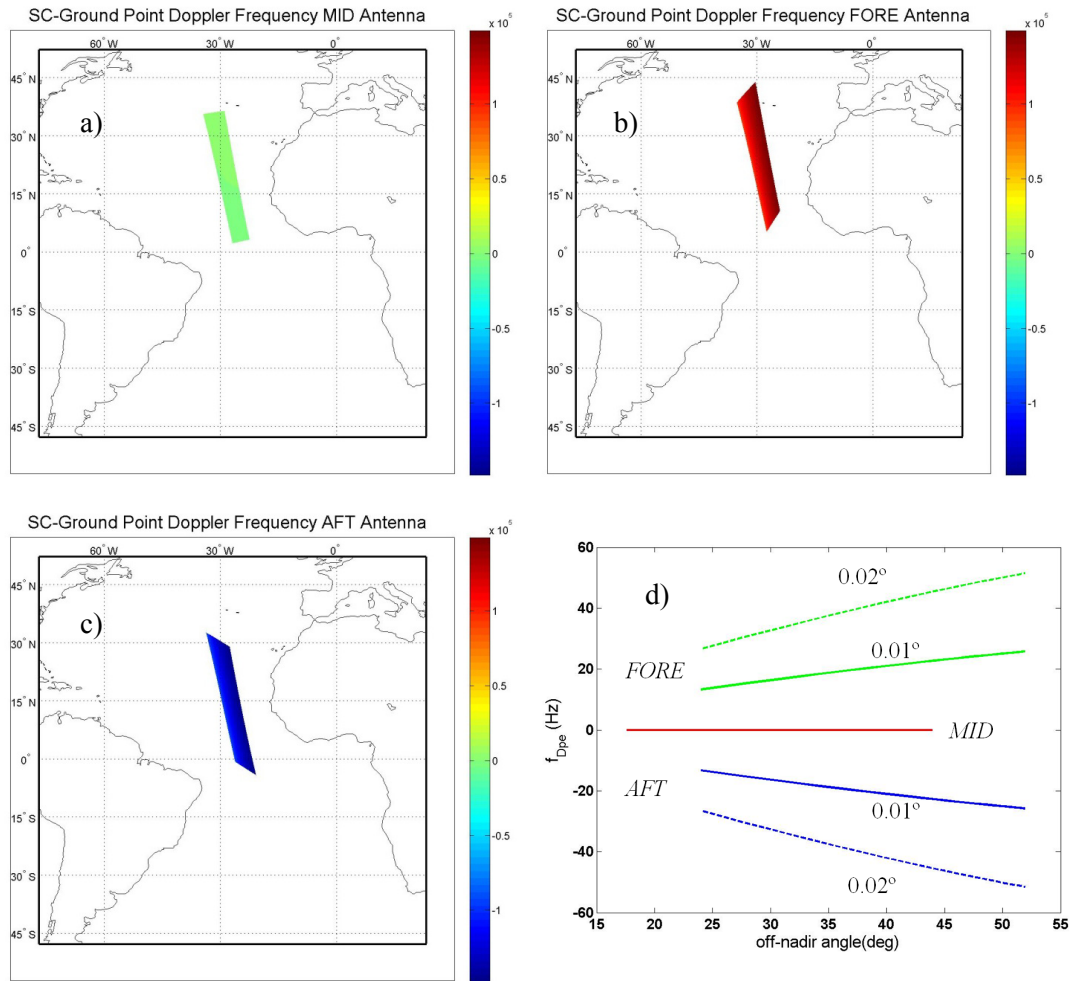


Fig. F.1 a), b) and c) Doppler shift corresponding to the geometry of observation of three (right-looking) antennas of DopSCAT. Both Fore and Aft antennas experience significant Doppler shifts. These shifts are positive for the Fore antenna and negative for the Aft antenna, and their absolute values can reach up to 150KHz magnitude. The on-board sampling frequency of DopSCAT shall be capable of sampling without aliasing a total band which is a combination of transmitted chirp band (about 1MHz) and predicted geometrical Doppler shift. In this way the compensation of the Geometrical Doppler shift can be performed directly on-ground; d) Doppler shift corresponding to pointing errors.

where $f_{D\sigma^0}$ is a Doppler shift caused by the uncertainty in the wind vector corresponding to the wrong pointing of the antennas, f_{Dpe} is an error in the prediction of the Doppler shift caused by a mispointing of the antenna beam, and $f_{D\Delta}$ is the residual error which includes all the other sources of errors not related to pointing. In the follow, we will only focus on the pointing related errors (i.e. $f_{D\sigma^0}$ and f_{Dpe}). The overall pointing errors for MetOp second generation are expected to be in the range 0.01° - 0.02° . The effect on wind retrieval of 0.01° - 0.02° uncompensated pointing errors is negligible and the corresponding Doppler shift errors $f_{D\sigma^0}$ (as computed by SSA2-CWM or CDOP geophysical model functions) are found less than 1 Hz. Figure F.2 shows f_{Dpe} as function

of the incidence angles for three DopSCAT antennas (Fore, Mid and Aft) and two different pointing errors (i.e. 0.01° and 0.02°). With reference to equation (F.4), f_{Dpe} is the biggest contributor, that is:

$$f_{Derr} = f_D - f_{Dp} \approx f_{Dpe} \quad (\text{F.5})$$

It is possible, till a certain extent, to correct these errors by measuring the Doppler shifts over land areas, where the shifts are expected to be equal to 0 Hz. The residual error after correction over land areas is estimated being less than a few hertz corresponding to a small bias (< 0.2 m/s) in OVM retrieval.

G. Performance of the SCF in presence of Doppler shift

As outlined in section 5.2.5, the Separation Compression Filter is used to separate the dual chirp echo signal into an up-chirp component and a down-chirp component, thus avoiding undesired interferences from down-chirps to up-chirps and vice versa. In the most general case, the $G_u(\omega)$ function in (5.8) is different from the one used in (5.6), because it is affected by delay and Doppler shifts. Therefore, if we directly apply the SCF without any compensation of the Doppler shift, the quality of the Impulse Response Function (IRF) will be degraded (e.g. the sidelobes of the IRF will increase, the peak of the IRF will decrease). In order to avoid such undesired effects, the Separation Compression Filter has to be performed after the following sequential steps:

- geometrical DC compensation (by a priori geometrical and pointing knowledge);
- geophysical Doppler shift estimation (by cross-correlation of up and down chirps echoes);
- geophysical Doppler shift compensation (i.e. the estimated geophysical Doppler shift is used in building up the separation compression filter).

We now refer to the set of instrument parameters listed in Table 5.3. For the MID antenna case, the chirp rate ($\mu=B/\tau$) is 417.5 KHz/ms and the pulse duration (τ) is 2 ms. Let assume that a double chirp, having the expression given in (5.3), is transmitted and an echo from a point scatterer, moving with a specific Doppler frequencies is received. Six cases are investigated, which correspond to different Doppler shifts of the point scatterer, i.e. $f_D = 0, 10, 30, 70, 80, 100$ Hz. The received echoes are processed in the two different ways:

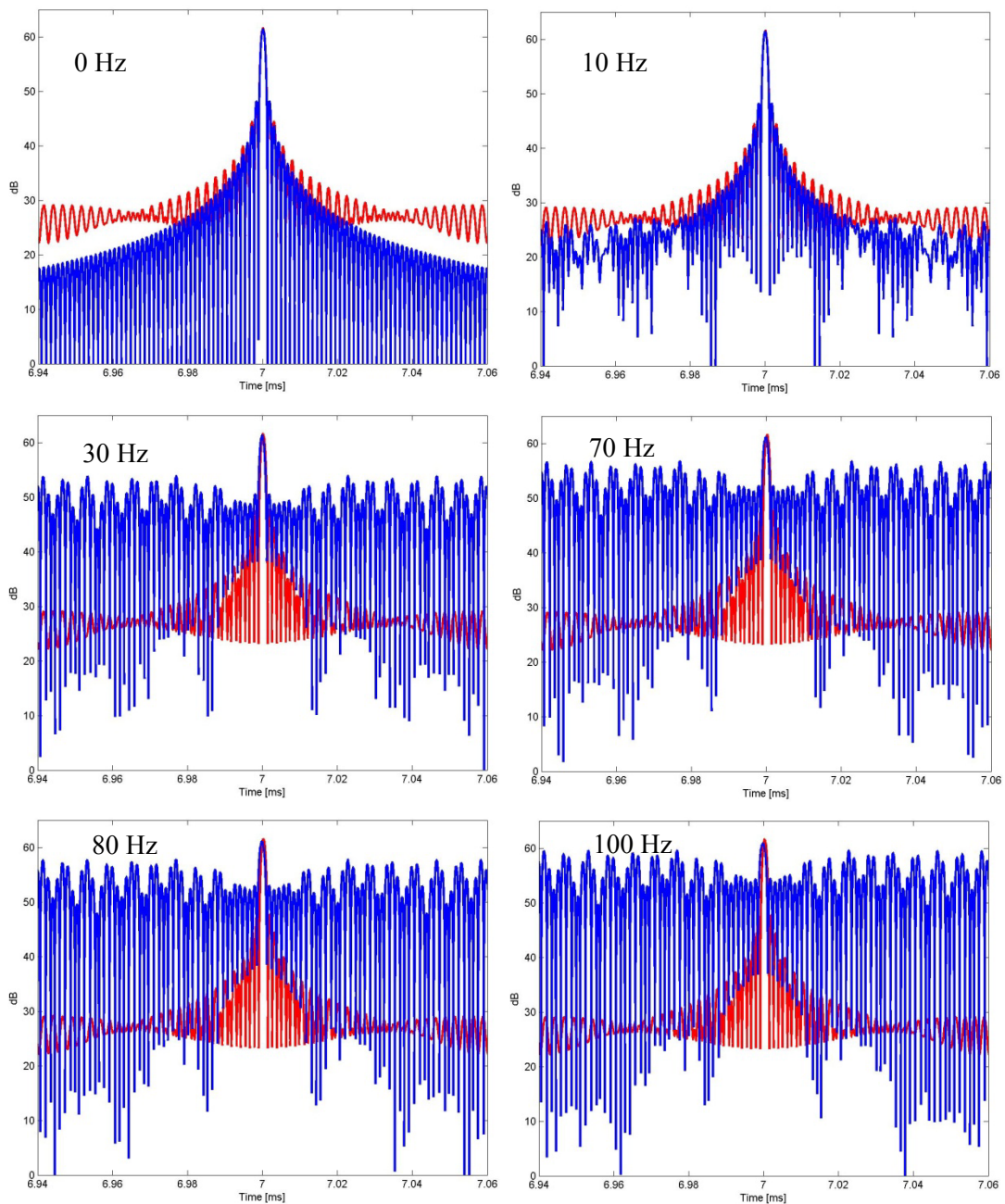


Fig. G.1 DopSCAT IRFs obtained under case study a) for different i.e. $f_D = 0, 10, 30, 70, 80, 100$ Hz. The red curves represent the IRFs without SCF.

- a) The geometrical DC is first compensated. A Separation Compression Filter, without geophysical Doppler compensation, is then applied. The output of the SCF finally goes through up-chirp matched filtering and detection stage. The resulting IRFs for the different f_D values are shown in Fig. G.1 (see blue curves).
- b) The geometrical DC is first compensated. A Separation Compression Filter, with geophysical Doppler compensation, is then applied. The output of the SCF finally

goes through up-chirp matched filtering and detection stage. The resulting IRFs for the different f_D values are shown in Fig. G.2 (see blue curves).

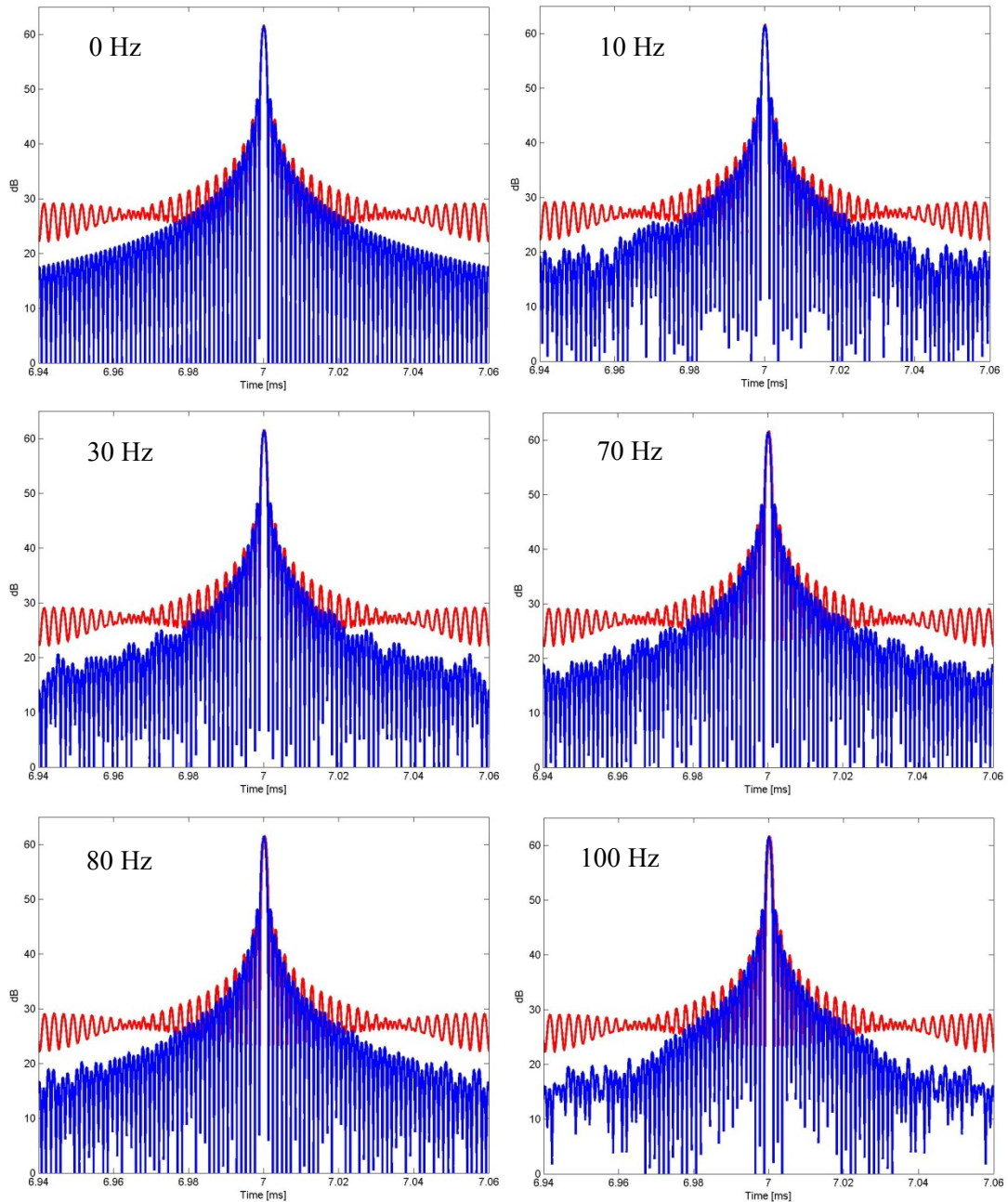


Fig. G.2 DopSCAT IRFs obtained under case study b) for different i.e. $f_D = 0, 10, 30, 70, 80, 100$ Hz. The red curves represent the IRFs without SCF.

The red curves in both Fig. G.1 and G.2 represent the IRFs without SCF. With reference to Fig.G.1, it is clear that, if the SCF does not make use of the estimated geophysical Doppler shift, the level of IRF sidelobes increase with f_D . With the current system parameters, a geophysical Doppler shift of a few tens of Hz is sufficient to corrupt the

resulting IRF. The results look very different if the SCF makes use of the estimated geophysical Doppler shift to refine the separation between up and down chirps (see Fig. G2). In this case, the IRFs are not corrupted by the separation process and the SCF improves the level of the IRF sidelobes, with respect to the case of no SCF (red curves in Fig. G2), for all the studied values of f_D . However, the above described performance depend also on the accuracy of the Doppler measurements. This accuracy is, among others, a function of the SNR (not considered in the previous simulations), the transmit bandwidth, the pulse duration, etc. A detailed expression of σ_{f_D} is given in section 5.2.5 [see equations (5.12)-(5.16)]. For the proposed system concept, σ_{f_D} is expected to be lower than 10 Hz (see Fig. 5.7e), in VV polarization and for most winds (between 4 m/s cross-wind and 25 m/s up-wind). An accuracy of 10 Hz has only a marginal impact on the IRF performance as it is significantly lower than the Doppler resolution (1 over the pulse duration, i.e. $1/\tau_s = 500$ Hz). This result is also confirmed by Fig. G1 (see the case $f_D=10$ Hz). In conclusion, it is only worth using the SCF procedure when the accuracy of the Doppler estimate is better than a few tens of hertz.

Acknowledgments

This work would not have been possible without the support and encouragements of my lovely wife Beatrice. She motivated me in this long adventure and made it possible for me to spend nights on my PhD after full days of work at the European Space Agency. All this effort has been rewarded by the birth of my little girl Martina...the most beautiful miracle in my life. I am mostly indebted with my promoter Prof.ir. Peter Hoogeboom and my supervisors Dr. Ad Stoffelen and Prof.dr.ir. François Le Chevalier for their guidance and invaluable technical help. I appreciated your encouragement, infinite patience and continuous support during our meetings. I am very grateful to Dr. Chung-Chi Lin, who first introduced me to ocean scatterometry and supported me with useful advices throughout the entire course of my PhD study. The time I spent between TUDelft and ESA, was a unique and enriching experience from the scientific and personal point of view. I am thankful to all my ESA colleagues I have been working with in the frame of MetOp 2nd Generation, especially Klaus Scipal and Nicolas Floury. Many thanks also to Gerd-Jan van Zadelhoff, for the valuable support in the analysis of the RADARSAT-2, SFMR and ECMWF data used in Chapter 3. Alexis Mouche deserves a special thank for the provision of the empirical Geophysical model function CDOP, and the provision of ASAR and sentinel-1 data used in Chapter 2 and 4. I would like to single out the long-term fruitful collaboration with Dr. Paul Hwang, to whom I'm very grateful for the interesting discussions on sea surface scattering and wave spectra, which have been captured in Chapter 2. The same special gratitude needs to be recognized to Bertran Chapron who really challenged my work with intriguing questions and stimulating discussions on Electromagnetic Scattering theories. I also wish to thank Alexander Voronovich, for the useful feedback on the SSA2 implementation, and Prof. William J. Plant for guiding me in the analysis of the SAXON-FPN data. Thanks go to Craig Donlon, for the support in the definition of the DopSCAT objectives and user requirements. All the conferences attended during my PhD were financially supported by Rhea System S.A; to this aim, I would like to acknowledge Nicola Mann, Ellemiek Westhoek and André Sincennes, for their unconditioned interest in my research. I do not know how to express my gratitude to Dr. Paul Sneoij, one of the most expert people in the field of Scatterometry: his help in properly translating the summary of the thesis from English to Dutch was unique. Thanks are expressed to my friends Marco Fornari and Riccardo Mecozzi for creating a supportive environment for my research, for the enjoyable time during lunch, coffee break, trips, etc. In conclusion, I wish to express my deep gratitude to Tania Casal and Gernot Plank for the constant encouragement during the work on the thesis and during these years of invaluable friendship.

Curriculum Vitae

Franco Fois received the Master degree (with distinction) in electronics engineering from the University of Rome La Sapienza in 2003. From 2003 to 2008, he worked in Alenia Spazio (now Thales Alenia Space) as a microwave instrument engineer with focus on radar sounders and synthetic aperture radars. Since April 2008, he has been working for Rhea Systems S.A. as a contractor for the European Space Agency (Directorate of Earth Observation Programmes) in the Microwave Instrument Pre-Development Section. He has been involved, as a performance engineer, in the preparation of several Earth Observation Missions such as MetOp-SG, Biomass, CoreH2O, Saocom-CS and Sentinel1-CS. From 2012, he is a PhD student at Delft University of Technology at the chair of Atmospheric Remote Sensing, with interest in Ocean Scatterometry and sea surface scattering theories.

List of Publications

This thesis is based on the following publications:

Fois, F., P. Hoozeboom, F.L. Chevalier, A. Stoffelen and A. Mouche (2015), DopSCAT: a Mission Concept for Simultaneous Measurements of Marine Winds and Surface Currents, *J. Geophys. Res. Oceans*, 2015JC011011R, (under review).

Fois, F.; Hoozeboom, P.; Le Chevalier, F.; Stoffelen, A., Future Ocean Scatterometry (2015), On the Use of Cross-Polar Scattering to Observe Very High Winds, *Geoscience and Remote Sensing, IEEE Transactions on*, vol.PP, no.99, pp.1,12, doi: 10.1109/TGRS.2015.2416203.

Fois, F., P. Hoozeboom, F.L. Chevalier, and A. Stoffelen (2015), An analytical model for the description of the full-polarimetric sea surface Doppler signature, *J. Geophys. Res. Oceans*, 120, 988–1015, doi:10.1002/2014JC010589.

Hwang, P. A., and F. Foies (2015), Surface roughness and breaking wave properties retrieved from polarimetric microwave radar backscattering, *J. Geophys. Res. Oceans*, 120, doi:10.1002/2015JC010782.

F. Foies, P. Hoozeboom, F. Le Chevalier, A. Stoffelen (2015), DopSCAT: a mission concept for a doppler wind-scatterometer, *Geoscience and Remote Sensing Symposium (IGARSS)*, IEEE International.

Hwang, P. A., and F. Foies (2015), Inferring Surface Roughness And Breaking Wave Properties From Polarimetric Radar Backscattering, *Geoscience and Remote Sensing Symposium (IGARSS)*, IEEE International.

F. Foies, P. Hoozeboom, F. Le Chevalier, A. Stoffelen, (2014), An Analytical Model for the Cross-Polar Scattering of Microwave Radiation from Ocean, *International Ocean Vector Wind Science Team Meeting*, 2-4 June 2014, Brest, France.

Fois, F.; Hoozeboom, P.; Le Chevalier, F.; Stoffelen, A., (2014), Future ocean scatterometry at very strong winds, *Geoscience and Remote Sensing Symposium (IGARSS)*, 2014 IEEE International, vol., no., pp.3886,3889, 13-18 July 2014, doi: 10.1109/IGARSS.2014.6947333.

Fois, F.; Hoozeboom, P.; Le Chevalier, F.; Stoffelen, A., (2014), An investigation on sea surface wave spectra and approximate scattering theories, *Geoscience and Remote Sensing Symposium (IGARSS)*, 2014 IEEE International, vol., no., pp.4366,4369, 13-18 July 2014, doi: 10.1109/IGARSS.2014.6947457.

F. Foies, P. Hoozeboom, F. Le Chevalier, A. Stoffelen, (2012), “Analysis and Modelling of Sea-Surface Doppler Spectra”, *American Geophysical Union, Fall Meeting 2012*, OS11C-1669.

References

- Abdalla, S. (2014), "Calibration of SARAL/AltiKa Wind Speed," *Geoscience and Remote Sensing Letters, IEEE*, vol.11, no.6, pp.1121,1123.
- Anguelova, M.D., (2008), "Complex dielectric constant of sea foam at microwave frequencies", *J. Geophys. Res.*, Vol. 113, C08001.
- Anguelova, M.D., and P.W. Gaiser, (2011), "Skin depth at microwave frequencies of sea foam layers with vertical profile of void fraction", *J. Geophys. Res.*, Vol. 116, C11002.
- Anguelova, M.D., and P.W. Gaiser, (2012), "Dielectric and radiative properties of sea foam at microwave frequencies: conceptual understanding of foam emissivity", *Remote Sensing*, pp. 1162-1189.
- Anguelova, M.D., and P.W. Gaiser, (2013), "Microwave emissivity of sea foam layers with vertically inhomogeneous dielectric properties", *Remote Sensing of Environment*, pp. 81-96.
- Anguelova, M.D. and F. Webster. Whitecap coverage from satellite measurements: first step toward modeling the variability of oceanic whitecaps. *J. Geophys. Res.*, 111(C3):C03017, 2006.
- Apel, J. R. (1994), "An improved model of the ocean surface wave vector spectrum and its effects on radar backscatter," *J. Geophys. Res.*, 99, 16,269-16,291.
- Aulard-Macler, M., (2011), "Sentinel-1 product definition", MDA Document, Num. SEN-RS-52-7440, ESA CDRL Num. PDL1-1, PDL2-1.
- Ayllon, N.; Aloisio, M.; Fois, F.; Lin, C.-C.; Loiselet, M.; Buck, C.; Piana, A.; Dionisio, R., (2014), "Suitability of an EIK and a TWT for a C-band high power amplifier for the Wind Scatterometer instrument of MetOp Second Generation," *Vacuum Electronics Conference, IEEE International*, vol., no., pp.471,472, 22-24, doi: 10.1109/IVEC.2014.6857694.
- Bannoura, W.J.; A. Wade; D.N. Srinivas (2005), "NOAA Ocean Surface Topography Mission Jason-2 project overview," *OCEANS, 2005. Proceedings of MTS/IEEE*, vol., no., pp.2155,2159 Vol. 3.
- Barrick, D. E. and B. L. Weber (1997), "On the nonlinear theory for gravity waves on the ocean's surface, Part II: Interpretation and applications," *J. Phys. Oceanogr.*, vol. 7, no. 1, pp. 11-21.
- Bass, F. G., I.M. Fuks, A. E. Kalmykov, I. E. Ostrovsky, A. D. Rosenberg (1968), "Very high frequency radiowave scattering by a disturbed sea surface Part I: Scattering from a slightly disturbed boundary," *IEEE Trans. Antennas Propagat.*, vol. 16, no. 5, pp. 554-559.
- Beckmann, P. and A. Spizzichino (1987). "The scattering of electromagnetic waves from rough surfaces". Artech House, Norwood.
- Bingham, R. J., P. Knudsen, O. Andersen, and R. Pail (2011), An initial estimate of the North Atlantic steady-state geostrophic circulation from GOCE, *Geophys. Res. Lett.*, 38, L01606, doi:10.1029/2010GL045633.
- Bondur, V. G. and E. A. Sharkov, (1982), "Statistical properties of whitecaps on a rough sea", *Oceanology*, 22, 274-279.
- Bentamy, A., P. Queffelec, Y. Quilfen and K. Katsaros (1999). Ocean surface wind fields estimated from satellite active and passive microwave instruments *IEEE Trans. Geosci. Remote Sens.* 37 2469-86.
- Bowen, M. M., W. J. Emery, J. Wilken, P. C. Tildesley, I. J. Barton, and R. Knewton, (2002), "Extracting multi-year surface currents from sequential thermal imagery using the maximum cross correlation technique," *J. Atmos. Ocean. Technol.*, vol. 19, no. 10, pp. 1665-1676.
- Bowen, M. M., J. L. Wilkin, and W. J. Emery, (2005), "Variability and forcing of the East Australian current," *J. Geophys. Res.*, vol. 110, no. C3, C03019.
- Brekhovskikh, L.M., (1952), "The diffraction of waves by a rough surface", *Zh. Eksper, i Teor. Fiz.*, 23, 275-289.
- Chapron, B., F. Collard and F. Ardhuin (2003), "Satellite SAR Sea Surface Doppler Measurements," *Proc. 2nd Workshop on Coastal and Marine Application of SAR*, 8-12, Svalbard, Norway, ESA Pub. ESA-SP565, pp. 133-139.

- Chapron, B., F. Collard and F. Ardhuin (2005), "Direct Measurements of Ocean Surface Velocity from Space: Interpretation and Validation," *J. Geophys. Res.*, 110, C07008.
- Chapron B, V. Kerbaol, D. Vandemark and T. Elfouhaily (2000). "Importance of peakedness in sea slope measurements and applications" *J. Geophys. Res.* 105 17 195–202.
- Chen, K.S., A.K. Fung, and D.E. Weissman, (1992). A backscattering model for ocean surfaces. *IEEE Trans. Geosci. and Remote Sens.*, 30(4):811-817.
- Coleman, T. F. and Y. Li (1996). "An interior trust region approach for nonlinear minimization subject to bounds. *SIAM J. OPT.*
- Collard, F., A. Mouche, B. Chapron, C. Danilo, and J. A. Johannessen, (2008), "Routine high resolution observation of selected major surface currents from space," in *Proc. SeaSAR, Frascati, Italy*.
- Cox, C. and W. Munk (1954). "Statistics from the sea surface derived from the sun glitter". *J. Marine Res.*, 13:198-227.
- Creamer, D. B., F. Henyey, R. Schult, and J. Wright (1989). "Improved linear representation of ocean surface waves". *J. Fluid Mech.*, 205:135-161.
- Crocker, R., D. K. Matthews, W. J. Emery, and D. G. Baldwin, "Computing Coastal Ocean Surface Currents From Infrared and Ocean Color Satellite Imagery," *IEEE Transactions on Geoscience and Remote Sensing*, Vol. 45, No. 2, 2007, pp. 435.
- Deane, G.B., (1997), "Sound generation and air entrainment by breaking waves in the surf zone", *J. Acoust. Soc. Am.* 102 (5), Pt. 1.
- Deane, G.B. and M.D. Stokes, (2002), "Scale dependence of bubble creation mechanisms in breaking waves", *Nature*, 418, 839-844.
- Desnos, Y-L., C. Buck, J. Guijarro, J-L. Suchail, R. Torres, E. Attema, (2000), "ASAR – Envisat's Advanced Synthetic Aperture Radar, Building on ERS Achievements towards Future Earth Watch Missions". *ESA Bulletin* 102, May 2000.
- De Zan, F., A.M. Guarnieri, (2006), "TOPSAR: Terrain Observation by Progressive Scans". *Geoscience and Remote Sensing, IEEE Transactions on*, 44(9), 2352-2360.
- Donelan, M. A., and W. J. P. Pierson (1987), "Radar scattering and equilibrium ranges in wind-generated waves with application to scatterometry," *J. Geophys. Res.*, 92, 4971-5029.
- Donlon, C., (2013), "ESA Data User Element (DUE) GlobCurrent User Requirement Document (URD)", *ESA report EOP-SM/2451/CD-cd*.
- Durand, M., Lee-Lueng Fu, D.P. Lettenmaier, D.E. Alsdorf, E. Rodriguez; D. Esteban-Fernandez, (2010), "The Surface Water and Ocean Topography Mission: Observing Terrestrial Surface Water and Oceanic Submesoscale Eddies," *Proceedings of the IEEE* , vol.98, no.5, pp.766,779.
- Edwards, P. G. and D. Pawlak, (2000), "MetOp: The Space Segment for EUMETSAT's Polar System," *ESA Bulletin*, No 102, May 2000, pp. 7-18, URL:
- Elfouhaily, T., C. Bourlier, and J.T. Johnson, (2004). Two families of non-local scattering models and the weighted curvature approximation. *Waves in random media*, 14(4):563-580.
- Elfouhaily, T., B. Chapron, K. Katsaros and D. Vandemark, (1997), "A Unified Directional Spectrum for Long and Short Wind-Driven Waves," *J. Geophys. Res.*, vol. 102, pp.15 781–15 796.
- Elfouhaily, T., and C.A. Guerin, (2004). A critical survey of approximate scattering wave theories from random rough surfaces. *Waves in Random and Complex Media*, 14(4):1-40.
- Elfouhaily T., S. Guignard, R. Awadallah, and D. R. Thompson, (2003), "Local and nonlocal curvature approximation: a new asymptotic theory for wave scattering". *Waves in Random Media*, 13(4):321-338.
- Elfouhaily, T., D. Thompson, D. Vandemark, and B. Chapron (1999), "Weakly nonlinear theory and sea state bias estimation", *J. Geophys. Res.*, 104(C4), 7641-7647.

- Emery, W. J., A. C. Thomas, M. J. Collins, W. R. Crawford, and D. L. Mackas (1986), An objective method for computing advective surface velocities from sequential infrared satellite images, *J. Geophys. Res.*, 91(C11), 12865–12878, doi:10.1029/JC091iC11p12865.
- Emery, W. J., C. W. Fowler, J. Hawkins, and R. H. Preller (1991), Fram Strait satellite image-derived ice motions, *J. Geophys. Res.*, 96(C3), 4751–4768, doi:10.1029/90JC02273.
- Emery, W. J., C. Fowler, and A. Clayson, (1992), "Satellite-image-derived Gulf Stream currents compared with numerical model results," *J. Atmos. Ocean. Technol.*, vol. 9, no. 3, pp. 286–304.
- Fabry, P., A. Recchia, J. de Kloe, A. Stoffelen, R. Husson, F. Collard, B. Chapron, A. Mouche, V. Enjolras, J. Johannessen, C. Lin and F. Fois (2013), "Feasibility study of sea surface currents measurements with doppler scatterometers", ESA Living Planet Programme, 16/9/2013-20/9/2013, Edinburgh, UK, ESA.
- Fernandez, D.E., J.R. Carswell, S. Frasier, P.S. Chang, P.G. Black and F.D. Marks (2006): "Dual-polarized C- and Ku-band ocean backscatter response to hurricane-force winds", *J. Geophys. Res.*, Vol. 111, Issue C8.
- Figa-Saldaña, J., J.J.W. Wilson, E. Attema, R. Gelsthorpe, M.R. Drinkwater, and A. Stoffelen, (2002), The advanced scatterometer (ASCAT) on the meteorological operational (MetOp) platform: A follow on for European wind scatterometers. *J. Remote Sensing*, Vol. 28, N. 3, pp. 404-412.
- Fois, F., C.C. Lin, H. Barré, M. Betto, M. Loiselet, G. Mason (2012). MetOp Second Generation Scatterometer Mission. Proc. EUMETSAT Meteorological Satellite Conference 2012, Sopot, Poland.
- Fois, F., P. Hoogeboom, F. Le Chevalier, A. Stoffelen (2014a) "An investigation on sea surface wave spectra and approximate scattering theories," *Geoscience and Remote Sensing Symposium (IGARSS)*, 2014 IEEE International , vol., no., pp.4366,4369, 13-18.
- Fois, F., P. Hoogeboom, F. Le Chevalier and A. Stoffelen (2014b), "Future ocean scatterometry at very strong winds", *Geoscience and Remote Sensing Symposium (IGARSS)*, 2014 IEEE International , vol., no., pp.3886,3889, 13-18.
- Fois, F., P. Hoogeboom, F.L. Chevalier, and A. Stoffelen (2015a), An analytical model for the description of the full-polarimetric sea surface Doppler signature, *J. Geophys. Res. Oceans*, 120, 988–1015, doi:10.1002/2014JC010589.
- Fois, F.; Hoogeboom, P.; Le Chevalier, F.; Stoffelen, A., (2015b), Future Ocean Scatterometry: On the Use of Cross-Polar Scattering to Observe Very High Winds, *Geoscience and Remote Sensing, IEEE Transactions on*, vol.PP, no.99, pp.1,12. 10.1109/TGRS.2015.2416203.
- Fois, F., P. Hoogeboom, F.L. Chevalier, A. Stoffelen, A. Mouche (2015c), DopSCAT: a Mission Concept for Simultaneous Measurements of Marine Winds and Surface Currents, *J. Geophys. Res. Oceans*, 2015JC011011R, under review.
- F. Fois, P. Hoogeboom, F. Le Chevalier, A. Stoffelen (2015d), DopSCAT: a mission concept for a doppler wind-scatterometer, *Geoscience and Remote Sensing Symposium (IGARSS)*, IEEE International.
- Forget, P., M. Saillard, and P. Broche (2006), "Observations of the sea surface by coherent L band radar at low grazing angles in a nearshore environment", *J. Geophys. Res.*, 111, C09015, doi:10.1029/2005JC002900.
- Freilich, M. H., (2002). *Satellite Observations of the Ocean: A View from the Research Community* College of Oceanic and Atmospheric Sciences Oregon State University.
- Fu, L.-L., D.B. Chelton, P.-Y. Le Traon, and R. Morrow. (2010). "Eddy dynamics from satellite altimetry". *Oceanography* 23(4):14–25, <http://dx.doi.org/10.5670/oceanog.2010.02>.
- Fung, A.K., and K.S. Chen, (2010), "Microwave Scattering and Emission Models for Users", Artech House.
- Fung, A. and K. Lee (1982), "A semi-empirical sea-spectrum model for scattering coefficient estimation," *Oceanic Engineering, IEEE Journal of*, vol.7, no.4, pp.166,176.

- Galim, N., D.J. Wingham, R. Cullen, M. Fornari, W.H.F. Smith, S. Abdalla (2013), "Calibration of the CryoSat-2 Interferometer and Measurement of Across-Track Ocean Slope," *Geoscience and Remote Sensing, IEEE Transactions on*, vol.51, no.1, pp.57,72.
- Gelsthorpe, R.V., E. Schied, J.J.W. Wilson, 2000. ASCAT-Metop's Advanced Scatterometer. ESA bulletin 102, May 2000.
- Gommenginger, C., B. Chapron, J. Marquez, B. Richards, M. Caparrini, G. Burbidge, D. Cotton, Adrien C.H. Martin (2014), "Wavemill: a new mission for high-resolution mapping of total ocean surface current vectors," *EUSAR 2014; 10th European Conference on Synthetic Aperture Radar; Proceedings of*, vol., no., pp.1,4.
- Guo, J.J., L. Tsang, W. Asher, K.H. Ding, C.T. Chen, (2001), "Applications of dense media radiative transfer theory for passive microwave remote sensing of foam covered ocean". *IEEE Trans. Geosci. Remote Sens.*, Vol. 1, pp. 570-572.
- Hansen, M.W.; Collard, F.; Dagestad, K.; Johannessen, J.A.; Fabry, P.; Chapron, B., (2011), "Retrieval of Sea Surface Range Velocities From Envisat ASAR Doppler Centroid Measurements," *Geoscience and Remote Sensing, IEEE Transactions on*, vol.49, no.10, pp.3582,3592.
- Hasselmann, K. (1962), "On the nonlinear energy transfer in a gravity-wave spectrum. Part 1. General theory". *J. Fluid Mech.*, 12:481-500.
- Hayslip, A. R., J.T. Johnson, and G. R. Baker (2003). "Further numerical studies of backscattering from time-evolving nonlinear sea surfaces". *Geoscience and Remote Sensing, IEEE Transactions on*, 41(10):2287-2293.
- Hersbach, H., (2010): Comparison of C-Band Scatterometer CMOD5.N Equivalent Neutral Winds with ECMWF. *J. Atmos. Oceanic Technol.*, 27, 721–736.
- Hesany, V., W. J. Plant, and W. C. Keller, (2000). The normalized radar cross section of the sea at 10 incidence, *IEEE Trans. Geosci. Remote Sens.*, 38, 64–72.
- Holliday, D., (1987). Resolution of a controversy surrounding the Kirchhoff approach and the small perturbation method in rough surface scattering theory, *IEEE Trans. Antennas Propag.*, AP-35, 120–122.
- Horstmann, J.; S. Falchetti, C. Wackerman, M. Caruso, H. Graber, (2014), "Wind retrieval at C-band cross polarization", *Geoscience and Remote Sensing Symposium, IGARSS-2014*.
- Huang, X.-Z., and Y.-Q. Jin, (1995), "Scattering and emission from two-scale randomly rough sea surface with foam scatterers", *IEE Proc.-Microw. Antennas Propag.*, Vol. 142, No. 2.
- Hwang, P.A., (2013), "Comment and discussion on Scatterometer Hurricane Wind Speed Retrievals using Cross 1 Polarization, by G-J van Zadelhoff et al."
- Hwang, P.A., D. M. Burrage, D. W. Wang, and J. C. Wesson, (2013): Ocean Surface Roughness Spectrum in High Wind Condition for Microwave Backscatter and Emission Computations*. *J. Atmos. Oceanic Technol.*, 30, 2168–2188.
- Hwang, P. A., W. Perrie, and B. Zhang, "Cross-polarization radar backscattering from the ocean surface and its dependence on wind velocity", *IEEE Geosci. Remote Sens. Lett.*, Vol. 11, No. 12, 2188-2192, Dec. 2014.
- Hwang, P. A., B. Zhang and W. Perrie (2010a), "Depolarized radar return for breaking wave measurements and hurricane wind retrieval", *Geophys. Res. Lett.*, 37, L01604.
- Hwang, P. A., B. Zhang, J. V. Toporkov, and W. Perrie (2010b), "Comparison of composite Bragg theory and quad-polarization radar backscatter from RADARSAT-2: With applications to wave breaking and high wind retrieval", *J. Geophys. Res.*, 115.
- Hwang, P. A., Derek M. Burrage, David W. Wang, and Joel C. Wesson (2011), "An advanced roughness spectrum for computing microwave I-band emissivity in sea surface salinity retrieval", *IEEE Trans. Geosci. Remote Sens.*, vol. 8, no. 3.
- Hwang, P. A. and F. Fois, (2015), "Surface roughness and breaking wave properties retrieved from

- polarimetric microwave radar backscattering", *J. Geophys. Res. Oceans*, 10.1002/2015JC010782.
- Hwang, P. A., A. Stoffelen, G.-J. van Zadelhoff, W. Perrie, B. Zhang, H. Li, and H. Shen (2015), Cross-polarization geophysical model function for C-band radar backscattering from the ocean surface and wind speed retrieval, *J. Geophys. Res. Oceans*, 120, 893–909.
- Jähne, B. and K. S. Riemer (1990), "Two-dimensional wave number spectra of small-scale water surface waves," *J. Geophys. Res.*, 95, 11,531-11,546.
- Jones, W. L., L. C. Schroeder, D. H. Boggs, E. M. Bracalente, R. A. Brown, G. J. Dome, W. J. Pierson and F. J. Wentz, 1982. The SEASAT-A satellite scatterometer: the geophysical evaluation of remotely sensed wind vectors over the ocean. *J. Geophys. Res.* 87 3297–317
- Jin, M.Y (1996). Optimal Range and Doppler Centroid Estimation for a ScanSAR System, *IEEE Transactions on Geoscience and Remote Sensing*. Volume 34, Issue 2, Page(s):479 – 488
- Johannessen, J. A., B. Chapron, F. Collard, V. Kudryavtsev, A. Mouche, D. Akimov and K.-F. Dagestad (2008), "Direct ocean surface velocity measurements from space: Improved quantitative interpretation of Envisat ASAR observations," *Geophysical Research Letters*, Vol. 35, L22608, doi:10.1029/2008GL035709.
- Johnson, E.S., F. Bonjean, G.S.E. Lagerloef, J.T. Gunn, and G.T. Mitchum, (2007): Validation and Error Analysis of OSCAR Sea Surface Currents. *J. Atmos. Oceanic Technol.*, 24, 688–701. doi: <http://dx.doi.org/10.1175/JTECH1971.1>
- Johnson, J. T., (1996). Application of numerical models for rough surface scattering. PhD thesis, Massachusetts Institute of Technology.
- Johnson, J. T., J. V. Toporkov, and G. S. Brown (2001). "A numerical study of backscattering from time-evolving sea surfaces: comparison of hydrodynamic models". *Geoscience and Remote Sensing, IEEE Transactions on*, 39(11):2411-2420.
- Kimura N., M. Wakatsuchi, (2000). Relationship between sea-ice motion and geostrophic wind in the northern hemisphere, *Geophysical Research Letters*, 27, no. 22, pp. 3735-3738.
- Kudryavtsev, V., D. Hauser, G. Caudal, and B. Chapron, (2003). A semiempirical model of the normalized radar cross-section of the sea surface, 1, Background model, *J. Geophys. Res.*, 108(C3), 8054.
- Kudryavtsev, V. N., V. K. Makin, (2007). "Aerodynamic roughness of the sea surface at high winds," *Atmospheric Boundary Layers*, 133-147.
- Kudryavtsev, V. N., V. K. Makin, and B. Chapron (1999). "Coupled sea surface-atmosphere model 2. spectrum of short wind waves," *J. Geophys. Res.*, 104(C4):7625-7639.
- Kudryavtsev V., A. Myasoedov, B. Chapron, J. A. Johannessen, F. Collard (2012a), Joint sun-glitter and radar imagery of surface slicks, *Remote Sensing of Environment*, Vol.120, pp.123-132 <http://dx.doi.org/10.1016/j.rse.2011.06.029>
- Kudryavtsev, V., A. Myasoedov, B. Chapron, J. A. Johannessen, and F. Collard (2012b), Imaging mesoscale upper ocean dynamics using synthetic aperture radar and optical data, *J. Geophys. Res.*, 117, C04029, doi:10.1029/2011JC007492.
- Kult, A., (2012), "ASAR products specifications", PO-RS-MDA-GS-2009, Issue 4, Rev. C, 01/20/2012.
- Large, W.G., W.R. Holland, and J.C. Evans (1991): "Quasi-geostrophic ocean response to real wind forcing: The effects of temporal smoothing". *J. Phys. Oceanogr.*, 21, 998-1017.
- Le Roy, Y.; M. Deschaux-Beaume.; C. Mavrocordatos; F. Borde (2009), "SRAL, a radar altimeter designed to measure a wide range of surface types," *Geoscience and Remote Sensing Symposium, 2009 IEEE International, IGARSS 2009*, vol.5, no., pp.V-445,V-448, 12-17.
- Lecomte, P., (1998), "The ERS Scatterometer instrument and the On-Ground processing of its data", *Proceedings of a Joint ESA-EUMETSAT Workshop on Emerging Scatterometer Applications-From Research to Operations (SP-424)*.
- Lee, P. H. Y., J. D. Barter, K. L. Beach, C. L. Hindman, B. M. Lake, H. Rungaldier, J. C. Shelton, A. B. Williams,

- R. Yee, and H. C. Yuen (1995), "X band microwave backscattering from ocean waves", *J. Geophys. Res.*, 100(C2), 2591–2611, doi:10.1029/94JC02741.
- Lee, P.H.Y., J.D. Barter, E. Caponi, M. Caponi, C.L. Hindman, B.M. Lake, H. Rungaldier (1996), "Wind-speed dependence of small-grazing-angle microwave backscatter from sea surfaces," *Antennas and Propagation, IEEE Transactions on*, vol.44, no.3, pp.333,340, Mar doi: 10.1109/8.486302
- Leifer, I., G. Caulliez, G. de Leeuw, (2006), "Bubbles generated from wind-steepened breaking waves: 2. Bubble plumes, bubbles, and wave characteristics". *J. Geophys. Res.*, 111, 16.
- Li, X. and X. Xu (2011). "Scattering and Doppler Spectral Analysis for Two-Dimensional Linear and Nonlinear Sea Surfaces". *Geoscience and Remote Sensing, IEEE Transactions on*, 49(2):603-611.
- Lin, C.C.; Betto, M.; Rivas, M.B.; Stoffelen, A.; de Kloe, J., (2012), "EPS-SG Windsscatterometer Concept Tradeoffs and Wind Retrieval Performance Assessment," *Geoscience and Remote Sensing, IEEE Transactions on*, vol.50, no.7, pp.2458,2472,doi: 10.1109/TGRS.2011.2180393.
- Loiselet, M., V. Kangas, I. Manolis, F. Fois; S. D'Addio, (2013), "MetOp Second Generation Payloads", *Living Planet Symposium, Edinburgh*.
- Long, D.G., P. Hardin, and P. Whiting. 1993. Resolution enhancement of spaceborne scatterometer data. *IEEE Transactions on Geoscience and Remote Sensing* 31(3): 700-715.
- Longuet-Higgins, M.S. (1963), "The effect of nonlinearities on statistical distributions in the theory of sea waves". *Journal of Fluid Mechanics*, 17(03):459-480.
- Madsen, S.N., (1989), "Estimating the Doppler centroid of SAR data", *Aerospace and Electronic Systems, IEEE transactions on*, vol 25, no.2, pp. 134-140.
- Magnusson, P.; Di Salvo, M.; Scarchilli, C., (2013), "A dual polarised slotted waveguide antenna for satellite based wind scatterometer instruments," *Antennas and Propagation (EuCAP), 2013 7th European Conference on*, vol., no., pp.3565,3568.
- Melville, W. K. and P. Matusov, (2002), "Distribution of breaking waves at the ocean surface", *Nature*, 417, 58 -63.
- Militskii, Y.A., V.Y. Raizer, E.A. Sharkov, V.S. Etkin, (1977),"Scattering of microwave radiation by foamy structures", *Rad. Eng. Electron Phys.*, Vol. 22, pp. 46-50.
- Milliff, R.F., W.G. Large, J. Morzel, G. Danabasoglu, and T.M. Chin, (1999): Ocean general circulation model sensitivity to forcing from scatterometer winds. *J. Geophys. Res.*, 104, 11,337-11,358.
- Monahan, E., and G. O'Muircheartaigh, (1980), "Optimal power-law description of oceanic whitecap coverage dependence on wind speed", *J. Phys. Oceanogr.*, 2094-2099.
- Monahan, E., and D. K. Woolf, (1989),"Comments on variations of whitecap coverage with wind stress and water temperature", *J. Phys. Oceanogr.*, 19,706-709.
- Mouche, A. A., B. Chapron, N. Reul, F. Collard (2008), "Predicted Doppler shifts induced by ocean surface wave displacements using asymptotic electromagnetic wave scattering theories," *Waves in Random and Complex Media*, vol. 18, issue 1, pag. 185-196.
- Mouche, A. A., F. Collard, B. Chapron, K. Dagestad, G. Guitton, J. A. Johannessen, V. Kerbaol and M. W. Hansen (2012), "On the use of Doppler Shift for sea surface wind retrieval from SAR", *IEEE Trans. Geosci. Remote Sens.*, vol. 50, no. 7.
- Neil, F. and S. A. Husain, (1971), "The deadliest tropical cyclone in history?".*Bulletin of the American Meteorological Society*, vol. 52 (6). pp. 438-444.
- Nie, D., M. Zhang, X.-P. Geng, and P. Zhou (2012), "Investigation on Doppler spectral characteristics of electromagnetic backscattered echoes from dynamic nonlinear surfaces of finite-depth sea", *Progress In Electromagnetics Research*, Vol. 130, 169-186.
- Ninnis, R. M., W. J. Emery, and M. J. Collins (1986), Automated extraction of pack ice motion from advanced very high resolution radiometer imagery, *J. Geophys. Res.*, 91(C9), 10725–10734, doi:10.1029/JC091iC09p10725.

- Nouguier, F., C. A. Guèrin, and B. Chapron (2009). "Choppy wave model for nonlinear gravity waves". *Journal of Geophysical Research (JGR)-Oceans*, 114(C09012):1-16.
- Nouguier, F., C. A. Guèrin, and B. Chapron (2010). "Scattering From Nonlinear Gravity Waves: The 'Choppy Wave' Model". *Geoscience and Remote Sensing, IEEE Transactions on*, 48(12):4184-4192.
- Nouguier, F., A. Guèrin, and G. Soriano (2011), "Analytical techniques for the Doppler signature of sea surfaces in the microwave regime II: Nonlinear surfaces," *IEEE Trans. Geosci. Remote Sens.*, Vol. 49, No. 12, 4920-4927.
- Papoulis, A. (1965), "Probability random variables and stochastic processes," pp. 153-162, McGraw-Hill, Boston.
- Peteherych, S., M. G. Wurtele, P. M. Woiceshyn, D. H. Boggs, and R. Atlas, (1984). First global analysis of SEASAT scatterometer winds and potential for meteorological research, NASA Conf. Publ. CP2303, 575-585.
- Pickard, G.L., W.J. Emery, (1989). *Descriptive Physical Oceanography: An Introduction*. Pergamon Press, Oxford, England.
- Pierson, W. J., and L. Moskowitz (1964), "A proposed spectral form for fully developed wind sea based on the similarity theory of S. A. Kitaigorodskii," *J. Geophys. Res.*, 69, 5181-5190, 1964.
- Plant, W. J. (1997), "A model for microwave Doppler sea return at high incidence angles: Bragg scattering from bound, tilted waves", *J. Geophys. Res.*, 102(C9), 21131-21146, doi:10.1029/97JC01225.
- Plant, J. W. (2002), "A stochastic, multiscale model of microwave backscatter from the ocean", *J. Geophys. Res.*, vol. 107, no. c9, 3120.
- Plant, W. J. and W. Alpers (1994), "An Introduction to SAXON-FPN", *J. Geophys. Res.*, 99 (C5), 9699-9703.
- Plant, W. J., W.C. Keller, R.A. Petitt, and E.A. Terray (1994). The dependence of microwave backscatter from the sea on illuminated area: Correlation times and lengths, *J. Geophys. Res.*, 99(C5), 9705-9723.
- Plant, W. J., W. C. Keller, V. Hesany, T. Hara, E. Bock, and M. A. Donelan (1999), "Bound waves and Bragg scattering in a wind-wave tank", *J. Geophys. Res.*, 104(C2), 3243-3263.
- Portabella, M., and A. Stoffelen, 2006. "Scatterometer Backscatter Uncertainty due to Wind Variability," *IEEE Trans. Geosc. & Remote Sensing*, Vol. 44, pp. 3356-3362.
- Portabella, M., A. Stoffelen, W. Lin, A. Turiel, A. Verhoef, J. Verspeek, and J. Ballabrera-Poy, (2012), "Rain Effects on ASCAT-Retrieved Winds: Toward an Improved Quality Control", *Geoscience and Remote Sensing, IEEE Transactions on*, vol.50, no.7, pp.2495,2506.
- Quazi, A., (1981), "An overview on the time delay estimate in active and passive systems for target localization," *Acoustics, Speech and Signal Processing, IEEE Transactions on*, vol.29, no.3, pp.527,533, doi: 10.1109/TASSP.1981.1163618.
- Raney, R. K., 1986, "Doppler properties of radars in circular orbits," *Int. J. Remote Sens.*, vol. 7, no. 9, pp. 1153-1162.
- Ren, Y.-Z., S. Lehner, S. Brusch, X.-M. Li, and M.-X. He, (2012), "An algorithm for the retrieval of sea surface wind fields using X-band TerraSAR-X data," *Int. J. Remote Sens.*, vol. 33, no. 23, pp. 7310-7336.
- Reul, N., and B. Chapron, (2003), "A model of sea-foam thickness distribution for passive microwave remote sensing applications", *Journal of geophysical research*, Vol.108.
- Rino, C. L., T. L. Crystal, A. K. Koide, H. D. Ngo, and H. Guthart (1991), "Numerical simulation of backscattering from linear and nonlinear ocean surface realizations," *Radio Sci.*, vol. 26, no. 1, 51-71.
- Rabaste, O.; Savy, L., (2014), "Mismatched filter optimization via quadratic convex programming for radar applications," *Radar Conference (Radar), 2014 International*, vol., no., pp.1,6, 13-17 Oct. 2014.
- Romeiser, R., and W. Alpers (1997), An improved composite surface model for the radar

- backscattering cross section of the ocean surface: 2. Model response to surface roughness variations and the radar imaging of underwater bottom topography, *J. Geophys. Res.*, 102(C11), 25251–25267
- Romeiser, R. and D. R. Thompson (2000). "Numerical study on the along-track interferometric radar imaging mechanism of oceanic surface currents". *Geoscience and Remote Sensing, IEEE Transactions on*, 38(1):446-458.
- Slade, R. (2009), RADARSAT-2 product description, MDA RN-SP-52-1238, 46 pp.
- Smirnov A. V. and V. U. Zavorotny (1995). Study of polarization differences in the Ku-band ocean radar imagery *J. Phys. Oceanogr.* 25 2215–28.
- Snoeij, P., E. van Halsema, J. Vogelzang, S. Waas, S. Zecchetto, H. et al. Janssen, (1992).VIERS-1 Final Report Phase 3.
- Soriano, G., M. Joelson, and M. Saillard (2006). "Doppler spectra from a two-dimensional ocean surface at L-band". *Geoscience and Remote Sensing, IEEE Transactions on*, 44(9):2430-2437.
- Stoffelen, A., and D. Anderson, (1997) "Scatterometer data interpretation: Estimation and validation of the transfer function CMOD4," *J. Geophys. Res.—Oceans*, vol. 102, no. C3, pp. 5767–5780, Mar. 15.
- Stoffelen, Ad, and Gerard Cats, (1991). The impact of SeaSat-A scatterometer data on highresolution analyses and forecasts: The development of the QEII storm, *Mon. Wea. Rev.*, 119, 2794-2802.
- Stoffelen, A., J. de Kloe, J. Johannessen, A. Mouche, F. Collard, B. Chapron, A. Recchia, V. Enjolras, F. Fois, C.C. Lin., (2011). Feasibility assessment of simultaneous ocean wind and current measurements. Presentation: IOVWST, , Annapolis, USA, FSU (int.).
- Stoffelen, A., A. Verhoef, J. Verspeek, J. Vogelzang, T. Driesenaar, Y. Risheng, C. Payan, G. De Chiara, J. Cotton, A. Bentamy, M. Portabella and G.J. Marseille (2013), "Research and Development in Europe on Global Application of the OceanSat-2 Scatterometer Winds", Document external project: 2013, NWP SAF report number: NWPSAF-KN-TR-022, OSI SAF report number: SAF/OSI/CDOP2/KNMI/TEC/RP/196, KNMI, 2013.
- Stoffelen, A. and M. Portabella, (2006). On Bayesian scatterometer wind inversion. *IEEE Transactions on Geoscience and Remote Sensing*, Vol. 44, 1523 – 1533, doi:10.1109/TGRS.2005.862502.
- Stoffelen, A., J. Vogelzang, (2011), "Wind bias correction guide", NWP SAF report, available at https://nwpsaf.eu/derivables/scatterometer/WindBiasCorrectionGuide_v1.0.pdf
- Stratton, J. A.; Morse, P. M.; Chu, L. J.; and Hutner, R. A. (1941). *Elliptic Cylinder and Spheroidal Wave Functions, including Tables of Separation Constants and Coefficients*. New York: Wiley.
- Tagawa, N., T. Moriya, K. Iwashita, M. Yoshizawa, 2004, "Multiplexed dual-chirp pulse compression method for ultrasonography," *Ultrasonics Symposium, 2004 IEEE* , vol.3, no., pp.2302,2305 Vol.3, 23-27.doi: 10.1109/ULTSYM.2004.1418301.
- Thorndike, A. S., and R. Colony (1982), Sea ice motion in response to geostrophic winds, *J. Geophys. Res.*, 87(C8), 5845–5852.
- Tokmakian, R., T. P. Strub, and J. McClean-Padman, (1990), "Evaluation of the maximum cross-correlation method of estimating sea surface velocities from sequential satellite images," *J. Atmos. Ocean. Technol.*, vol. 7, no. 6, pp. 852–865.
- Thompson, D. R. (1989), "Calculation of microwave Doppler spectra from the ocean surface with a time-dependent composite model". Kluwer Academic Publishers.
- Thompson, D.R., T.M.Elfohaily, B. Chapron, (1998), "Polarization ratio for microwave backscattering from the ocean surface at low to moderate incidence angles," *Geoscience and Remote Sensing Symposium Proceedings, 1998. IGARSS '98. 1998 IEEE International* , vol.3, no., pp.1671,1673 vol.3, 6-10.
- Toporkov, J. V. and G. S. Brown (2000). "Numerical simulations of scattering from time-varying, randomly rough surfaces", *IEEE Trans. Geophys. Remote Sensing*, 38:1616-1624.

- Toporkov, J. V. and M. A. Sletten (2007). "Statistical properties of low-grazing range-resolved sea surface backscatter generated through two-dimensional direct numerical simulations". *IEEE Transactions on Geoscience and Remote Sensing*, 45(5):1181-1197.
- Torres, R., P. Snoeij, D. Geudtner, D. Bibby, M. Davidson, E. Attema, P. Potin, B. Rommen, N. Floury, M. Brown, I. Navas Traver, P. Deghaye, B. Duesmann, B. Rosich, N. Miranda, C. Bruno, M. L'Abbate, R. Croci, A. Pietropaolo, M. Huchler, F. Rostan, (2012), "GMES Sentinel-1 mission", *Remote sensing of Environment*.
- Tsang, J.A. Kong and R.T. Shin, (1985), "Theory of microwave remote sensing", A Wiley-Interscience Publication.
- Tsang, L., C. H. Chan, K. Pak, H. Sangani, A. Ishimaru, and P. Phu, (1994). "Monte Carlo simulations of large scale composite random rough surface scattering based on the banded matrix iterative approach", *J. Opt. Soc. of Am.*, vol. 11, pp. 691-696.
- Uhlhorn, E.W. and P.G. Black, (2003), "Verification of remotely sensed sea surface winds in hurricanes," *J. Atmos. Oceanic Technol.*, pp. 99-116.
- Ulabay, F. T., R. K. Moore, A. K. Fung (1990), "Microwave Remote Sensing: Active and Passive, Volume II: Radar Remote Sensing and Surface Scattering and Emission Theory", Artech House, Norwood.
- Vachon, P. W., and J. Wolfe (2011), C-band cross-polarization wind speed retrieval, *IEEE Geos. Remote Sensing Lett.*, 8, 456-458.
- Valenzuela, G. R., (1978). Theories for the interaction of electromagnetic waves and oceanic waves. A review. *Bound. Layer Met.*, pages 61-85.
- Valenzuela, G. R. and M. B. Laing (1970), "Study of Doppler spectra of radar sea echo", *J. Geophys. Res.*, 75(3), 551-563.
- van Zadelhoff, G.-J., A. Stoffelen, P. W. Vachon, J. Wolfe, J. Horstmann, M. Belmonte Rivas. (2013), "Scatterometer hurricane wind-speed retrievals using cross-polarization", *Atmos. Meas. Tech. Discuss.*, 6, 7945-7984.
- van Zadelhoff, G.-J., A. Stoffelen, P. W. Vachon, J. Wolfe, J. Horstmann, and M. Belmonte Rivas (2014), "Retrieving hurricane wind speeds using cross polarization C-band measurements, *Atmos. Meas. Tech.*, 7, 437-449.
- Verhoef, A., M. Portabella and A. Stoffelen, (2011), High-resolution ASCAT scatterometer winds near the coast, *IEEE Transactions on Geoscience and Remote Sensing*, 2012, 50, 7, 2481-2487.
- Verhoef, A., M. Portabella, A. Stoffelen and H. Hersbach, (2008). CMOD5.n - the CMOD5 GMF for neutral winds, OSI SAF report, SAF/OSI/CDOP/KNMI/TEC/TN/165, available at <http://www.knmi.nl/scatterometer/publications/>
- Vogelzang, J., A. Stoffelen, A. Verhoef, J. de Vries and H. Bonekamp, (2009), Validation of two-dimensional variational ambiguity removal on SeaWinds scatterometer data, *J. Atm. Oceanic Technol.*, 7, 2009, 26, 1229-1245.
- Voronovich, A. (1994), "Small-slope approximation for electromagnetic wave scattering at a rough interface of two dielectric half-spaces". *Waves in Random and Complex Media*, 4(3):337-367.
- Voronovich A G 1999 Wave Scattering from Rough Surfaces 2nd edn (Berlin: Springer) p 236
- Voronovich, A. G. and V. U. Zavorotny (2001). "Theoretical model for scattering of radar signals in Ku- and C-bands from a rough sea surface with breaking waves", *Waves Random Media* 11, 247-269.
- Voronovich, A., and V. Zavorotny, (2011): "Depolarization of microwave backscattering from a rough sea surface: modeling with small-slope approximation", *Geoscience and Remote Sensing Symposium (IGARSS)*, 2033-2036, doi:10.1109/IGARSS.2011.6049530, 2011. 7954.
- Wang H., J. Zhu, M. Lin, X. Huang, Y. Zhao, C. Chen, Y. Zhang, H. Peng (2013), "First six months quality assessment of HY-2A SCAT wind products using in situ measurements", *Acta Oceanol. Sin.*, 0253-505X, Vol.32, pp.27-33.
- Wentz, F. J., (1999). A model function for the ocean-normalized radar cross section at 14 GHz derived

- from NSCAT observations *J. Geophys. Res.* 104 11 499–514
- Wentz, F. J., S. Peteherych, and L. A. Thomas (1984), A model function for ocean radar cross sections at 14.6 GHz, *J. Geophys. Res.*, 89(C3), 3689–3704, doi:10.1029/JC089iC03p03689.
- Wentz, F. J., and D. K. Smith (1999). A model function for the ocean-normalized radar cross section at 14 GHz derived from NSCAT observations, *J. Geophys. Res.*, 104(C5), 11499–11514.
- West, B. J., K. A. Brueckner, R. S. Janda, D. M. Milder, and R. L. Milton (1987), "A new numerical method for surface hydrodynamics". *J. Geophys. Res.*, C11:803-824.
- Wilson, J.J.W.; Anderson, C.; Baker, M.A.; Bonekamp, H.; Saldaña, J.F.; Dyer, R.G.; Lerch, J.A.; Kayal, G.; Gelsthorpe, R.V.; Brown, M.A.; Schied, E.; Schutz-Munz, S.; Rostan, F.; Pritchard, E.W.; Wright, N.G.; King, D.; Onel, U., (2010), "Radiometric Calibration of the Advanced Wind Scatterometer Radar ASCAT Carried Onboard the METOP-A Satellite," *Geoscience and Remote Sensing, IEEE Transactions on*, vol.48, no.8, pp.3236,3255.
- Wright, J. W. (1968), "A new model for sea clutter. *Antennas and Propagation*," *IEEE Transactions on*, 16(2):217-223.
- Wu, J., (2000), "Bubbles produced by breaking waves in fresh and salt waters", *J. Phys. Oceanogr.*, 30, 1809-1813.
- Zavorotny, V. U. and A. G. Voronovich (1998). "Two-scale model and ocean radar Doppler spectra at moderate-and low-grazing angles". *Antennas and Propagation, IEEE Transactions on*, 46(1):84-92.
- Zhang, Z., Y. Lu, H. Hsu (2007). "Detecting Ocean Currents from Satellite Altimetry, Satellite Gravity and Ocean Data", *Dynamic Planet, International Association of Geodesy Symposia*, Springer Berlin Heidelberg.
- Zhang, B. and Perrie, W., (2012): Cross-polarized synthetic aperture radar: a new potential measurement technique for hurricanes, *B. Am. Meteorol. Soc.*, 93, 531–541, doi:10.1175/BAMS-D-11-00001.1, 2011.7949,7953,7954,7959.
- Zhang, B., W. Perrie, and Y. He (2011), Wind speed retrieval from RADARSAT-2 quad-polarization images using a new polarization ratio model, *J. Geophys. Res.*, 116, C08008.
- Zhang, B., G. Zhang, W. Perrie, Y. He, (2014) "A new semi-empirical sea surface microwave backscatter model coupled with the rain effect", *Geoscience and Remote Sensing Symposium, IGARSS-2014*.
- Zhang, B., W. Perrie, P. Vachon, J. A. Zhang, E. W. Uhlhorn, and Y. He (2014), High resolution hurricane vector winds from C-band dual-polarization SAR observations, *J. Atmos. Oceanic Technol.*, 31, 272–286.

